

**Design of Low-Profile Multi-Band Microwave Antennas and Components
Using Metamaterial-Based Electromagnetic Bandgap Structures**

by

Braden P. Smyth

A thesis submitted in partial fulfillment of the requirements for the degree of

Doctor of Philosophy

in

ELECTROMAGNETICS AND MICROWAVES

Department of Electrical and Computer Engineering
University of Alberta

© Braden P. Smyth, 2023

Abstract

This thesis investigates applications of metamaterial-based electromagnetic bandgap structures, or MTM-EBGs. MTM-EBGs are uniplanar, compact, and often fully printable, making them ideal candidates for integration into planar topologies. This differs from many other metamaterial-based structures that have been proposed in the last couple of decades, many of which have shown great potential but have suffered from drawbacks including difficult integration into existing structures, poor operating characteristics, and expensive fabrication. Along with its useful physical and electrical properties, the recent development of MTM-EBG theory based on multiconductor transmission line techniques has rendered its properties predictable and designable, and this presents an excellent opportunity to fully explore how they can be used to improve performance and reduce the size of commonly used microstrip-based structures. In particular, embedding MTM-EBG unit cells directly into the metallic features of microstrip-based circuit components and antennas is an efficient way to produce multi-band operation without taking up any extra circuit board space. A general approach is taken that further allows the same technology to be used in a multitude of different applications. This is demonstrated with the design of many different circuit components, including dual- and tri-band microstrip stub filters, dual- and tri-band matching networks for arbitrary impedances, and a dual-band Wilkinson power divider. There are diverse uses in antenna applications as well; a dual-band antenna is first presented, followed by a simultaneously dual-band and dual-polarized antenna, as well as a GPS antenna with increased bandwidth. A tunable version of the dual-band dual-polarized antenna demonstrates further possibilities of what can

be achieved with the MTM-EBG. Most devices were fabricated for comparison to simulation and excellent agreement is consistently seen between both sets of results, further suggesting that the MTM-EBG is a versatile and extremely useful tool for creating the next generation of miniaturized and multi-functional microwave systems.

Preface

This thesis is an original work by B. P. Smyth, however, sections of it have previously been published by the author.

Section 4.5 is adapted from work first published by S. Barth, B. P. Smyth, J. A. Brown, and A. K. Iyer, “Theory and Design of Dual-Band Microstrip Networks Using Embedded Metamaterial-Based Electromagnetic Bandgap Structures (MTM-EBGs)”, *IEEE Trans. Antennas Propag.*, vol. 68, no. 3, 2020, pp. 1761-1772. The work on the Wilkinson power divider and associated data is my own (other sections of the work that are not primarily mine were excluded from this thesis), although S. Barth created the plot in Fig. 4.28 using data that I obtained. Part of the literature review from this publication was adapted for Section 2.3 of this thesis as well, particularly the discussion of multi-band couplers and power dividers; some of these references were first found by S. Barth and J. A. Brown. The remainder of Chapters 2 and 4 are original to this thesis.

The dual-band antenna forming section 5.2 was first published as B. P. Smyth, S. Barth, and A. K. Iyer, “Dual-Band Microstrip Patch Antenna Using Integrated Uniplanar Metamaterial-Based EBGs”, *IEEE Trans. Antennas Propag.*, vol. 64, no. 12, 2016, pp. 5046-5053. This work was primarily my own, with S. Barth assisting mainly in the MTM-EBG theory section. Plots from this work that may contain data from S. Barth are also reproduced in section 3.2 as Fig. 3.8 and Fig. 3.9.

The dual-band, dual-polarized antenna in section 5.3 was published as B. P. Smyth and A. K. Iyer, “Low-Profile Uniplanar Dual-Band and Dual-Polarized Microstrip Patch Antenna Using Embedded MTM-EBGs”, *IEEE Trans. Antennas Propag.*, vol.

69, no. 7, 2021, pp. 3645-3653.

Chapter 3 includes a background on the device fundamental to this thesis, the MTM-EBG. Parts of section 3.2 are adapted from work by S. Barth, particularly from [1, 2], and while this work takes inspiration from his theory, the techniques and data are otherwise my own.

Finally, Sections 4.4 and 4.5 are based on a paper that has been accepted for publication but remains in press at the time of the submission of this thesis. The paper, by B. P. Smyth and A. K. Iyer, is titled “Multi-Band Impedance Matching Using Microstrip-Embedded MTM-EBGs”, and is due to be published in the *IEEE Trans. Microw. Theory Techn.* later in 2023.

All of this work was completed through discussion, input, and collaborative brainstorming with my supervisor, Dr. A. K. Iyer.

“And Ilúvatar spoke to Ulmo, and said: ‘Seest thou not how here in this little realm in the Deeps of Time Melkor hath made war upon thy province? He hath bethought him of bitter cold immoderate, and yet hath not destroyed the beauty of thy fountains, nor of thy clear pools. Behold the snow, and the cunning work of frost! Melkor hath devised heats and fire without restraint, and hath not dried up thy desire nor utterly quelled the music of the sea. Behold rather the height and glory of the clouds, and the everchanging mists; and listen to the fall of rain upon the Earth!’”

- J. R. R. Tolkien, The Silmarillion

Acknowledgments

As a second year student, Professor Ashwin Iyer gave me an opportunity to enter the academic world, and for this I am truly grateful. He has guided me, advocated for me, and given me opportunities that I consider myself extremely fortunate to have had. He nurtures an environment of constant creative thinking and high quality research, creating space for me and many others to thrive. An endless source of wisdom beyond just electromagnetics, the many, many years of mentorship have left an indelible mark on formative years of my career path and life. I sincerely thank you.

We stand on the shoulders of giants, supported on either side by colleagues. I have many to thank. Dr. Justin Pollock, Dr. Stuart Barth, Dr. Sangamitro Das, Dr. Elham Baladi, Dr. Mitchell Semple, Robert Winter, Jacob Brown, Christopher Barker, and many others – the impact each of you had on my research and the grad school experience in general will not be forgotten.

My parents, Peter and Cheryl, have raised me not just to question the world around me but also to approach it appreciatively, genuinely, and with an open mind. For starting me on this path and encouraging me throughout the journey, I am grateful. I am also fortunate to be close to my siblings, Conor and Karina, Kiara, and Jenna, who have been available to talk or grab a drink when I needed a break. I am here because of you all.

Finally, to my wife Cassie, for her encouragement and belief in me, for putting up with me and keeping me sane during the long years as a grad student, even as you were working on your own graduate degree. I certainly couldn't have done it without you.

Table of Contents

1	Introduction	1
1.1	Motivation	1
1.2	Objectives	4
1.3	Outline	6
2	Background	7
2.1	Multi-Band Design Techniques	7
2.1.1	Overview	7
2.1.2	Metamaterials	12
2.1.3	Electromagnetic Bandgap Structures	15
2.1.4	MTM and EBG Unit Cells	18
2.2	Multi-Band Circuit Components	20
2.2.1	Stubs and Filters	20
2.2.2	Matching Networks	23
2.2.3	Power Dividers and Couplers	25
2.3	Multi-Band Antennas	27
2.3.1	Traditional Designs	27
2.3.2	Multi-Band Antennas With Mixed Polarization	29
2.3.3	MTM-Inspired Approaches	33
2.4	Challenges of Multi-Band Design	34
2.4.1	Layout and Fabrication	34
2.4.2	Design Considerations	35

2.4.3	Performance	36
3	The MTM-EBG	39
3.1	Development	39
3.1.1	TL-MTM Models	39
3.1.2	MTM-EBG Design	42
3.2	Analysis	50
3.2.1	MTL Properties	50
3.2.2	Periodic Analysis	54
3.2.3	Individual Unit Cell	57
3.3	Embedded MTM-EBG Unit Cells	60
3.3.1	Implementation	60
3.3.2	Multi-Band Devices	64
3.3.3	Alternate MTM-EBG Structures	65
3.4	Design Strategies	67
3.4.1	Effect of L and C	67
3.4.2	Simplified Design Procedure	71
3.4.3	Design Tools	73
3.5	Tunability	74
4	Multi-Band Circuit Components	76
4.1	Methodology	76
4.1.1	Embedded MTM-EBGs	76
4.1.2	Device Design	78
4.1.3	Choice of Substrate	79
4.2	Microstrip Stubs	79
4.2.1	Dual-Band Stub	79
4.2.2	Dual-Band Radial Stub	84
4.2.3	Tri-Band Stub	87

4.2.4	Additional Stub Properties	89
4.3	Dual-Band Matching Network	97
4.3.1	Approach	97
4.3.2	Optimization Algorithm	100
4.3.3	MTM-EBG Implementation	103
4.3.4	Summary of Procedure	105
4.3.5	Results	107
4.4	Tri-Band Matching Network	110
4.4.1	Design Steps	110
4.4.2	Results	112
4.5	Wilkinson Power Divider	115
4.5.1	Design	115
4.5.2	Results	119
5	Multi-Band Antennas	123
5.1	Antenna Design Methodology	123
5.1.1	Design	123
5.1.2	Considerations	125
5.2	Dual-Band Linear Patch Antenna	129
5.2.1	Design	129
5.2.2	Results	133
5.3	Dual-Band, Dual-Polarized Antenna	138
5.3.1	Theory	138
5.3.2	Implementation	140
5.3.3	Results	149
5.3.4	DBDPA with Matching Network	155
5.4	GPS Antenna	158
5.4.1	Bandwidth-Enhanced Antenna Design	159

5.4.2	Results	163
5.5	Tunable DBDPA	167
5.5.1	Tuning Mechanism	167
5.5.2	Bias Network	169
5.5.3	Results	170
6	Conclusion	174
6.1	Summary	174
6.2	Limitations	176
6.3	Future Considerations	179
	Bibliography	182
	Appendix A: Modeling the MTM-EBG with 2-Conductor Transmission	
	Lines	198
	Appendix B: MTM-EBG Host TLs	203

List of Tables

4.1	MTM-EBG Unit Cell Dimensions in Multi-Band Microstrip Stubs, Given in mm	82
4.2	Stub Filter 10-dB Bandwidths	86
4.3	Dimensions of MTM-EBG Unit Cells in Multi-Band Matching Net- works, Given in mm	105
4.4	Comparison of multi-band matching networks in recent literature. . .	115
4.5	Dimensions of MTM-EBG Unit Cells in WPD	119
4.6	Simulated and Measured S -Parameters of the Dual-Band WPD at Fre- quencies of Peak S_{21}	122
4.7	Proposed Dual-Band WPD compared to similar equal-power division dual-band devices in recent literature	122
5.1	Antenna design values (in mm) for the conventional patch antennas and the dual-band antenna. Refer to Fig. 5.2 for parameter descriptions.	131
5.2	Design values for the proposed antenna's two MTM-EBG regions, in mm.	133
5.3	Maximum antenna gain (in dBi), co-pol and cross-pol, from simulation.	136
5.4	Comparison of MTM-EBG antenna to other examples of multi-band patch antennas.	138
5.5	Dimensions of MTM-EBG Unit Cell in DBDPA	143
5.6	DBDPA Dimensions, not including the MTM-EBG.	146
5.7	DBDPA Properties	153

5.8	Comparison of Dual-Band, Dual-Polarized RF Antennas in Recent Literature	155
5.9	Matching Network Dimensions for DBDPA With Different Feed Positions.	157
5.10	Properties of GPS antenna with air dielectric.	165

List of Figures

2.1	π -network TL model that can be used to replace a TL segment of specified phase for dual-band operation. Reproduced from [12] ©2012 IEEE.	10
2.2	(a) T-network model that can replace a TL segment to produce dual-band operation. Reproduced from [13] ©2022 IEEE. (b) T-network model that can replace a TL segment for tri-band operation. Reproduced from [14] ©2022 IEEE.	10
2.3	Unit cell of a transmission line loaded with a series capacitor and shunt inductor. Reproduced from [21] ©2003 IEEE.	13
2.4	(a) Sievenpiper mushroom structure. Reproduced from [32] ©1999 IEEE. (b) Cross section of the mushroom structure, indicating periodicity, capacitance, and inductance. A shield conductor is included in the model since it is required for rigorous MTL analysis [15].	14
2.5	EBG application of a periodic array of holes beneath a microstrip TL to provide a strong bandgap. Reproduced from [43] ©1998 IEEE. . .	17
2.6	EBG application to reduce mutual coupling between patch antenna array elements. Reproduced from [44] ©2003 IEEE.	18
2.7	Microstrip stub geometries, shown in parallel with a transmission line. (a) Rectangular stub. (b) Radial stub. (c) Triangular stub. (d) Rhombic stub.	21

2.8	Dual-band stub filter using CRLH structure. (a) Fabricated structure and circuit model. (b) Reported S -parameters showing two clear filtering bands. Both reproduced from [81] ©2004 IEEE.	23
2.9	Dual-band matching network designs. (a) π -network model designed to operate at 2.4 GHz and 3.6 GHz. Reproduced from [84] ©2015 IEEE. (b) Another π -network model operating at 1.0 GHz and 1.8 GHz. Reproduced from [83] ©2018 IEEE. (c) Three-stub model operating at 0.9 GHz and 1.5 GHz. Reproduced from [85] ©2017 IEEE.	24
2.10	Circuit models of various dual-band power dividers and couplers. (a) Dual-band WPD circuit using T-network quarter-wave branches. Reproduced from [100] ©2008 IEEE. (b) Dual-band branch-line coupler employing π -network transmission lines. Reproduced from [111] ©2004 IEEE.	25
2.11	WPD design using CRLH TLs. (a) Proposed circuit for dual- or tri-band operation. (b) CRLH circuit used in the WPD. (c) Fabricated dual-band WPD for operation at 0.7 GHz and 1.5 GHz. All reproduced from [123] ©2011 IEEE.	26
2.12	Multi-band stacked GPS antenna. (a) Structure; (b) reported S -parameters and broadside gain. Both reproduced from [133] ©2007 IEEE.	29
2.13	Representative diagrams of arbitrary antennas depicting their radiated far-field frequencies and polarizations. Note that each of Polarization 1 and 2 may be linear or circular, depending on antenna geometry. . .	30
2.14	Multi-band patch antenna with embedded MTM unit cells. (a) Structure, showing NRI-TL sections embedded in patch; (b) S_{11} . Both reproduced from [171] ©2008 IEEE.	33

2.15	Circuit board cross-sections. (a) Common fabrication challenges include vias, lumped components that require soldering, multi-layer boards, and ground plane patterning. (b) Simple circuit board consisting of a patterned upper layer over a solid ground plane.	34
3.1	(a) CBCPW TL. (b) Truncated CBCPW. (c) Truncated CBCPW embedded in a microstrip TL.	44
3.2	Depiction of electric-field lines of the three TEM modes supported by the CBCPW MTL (microstrip-like, CPW-like, and CSL-like). Reproduced from [184] ©2020 IEEE.	45
3.3	(a) CBCPW host medium, and (b) host medium loaded with inductors and capacitors to form an MTM-EBG unit cell. The four constituent conductors that form the MTL model of this unit cell are labeled. Reproduced from [185] ©2021 IEEE.	46
3.4	Illustration of contradirectional coupling between a forward PPW mode and a backward CPW mode within an MTL.	47
3.5	Basic fully-printed MTM-EBG unit cell embedded in microstrip.	48
3.6	Symmetric model of MTM-EBG unit cell.	49
3.7	MTL circuit model of a single MTM-EBG unit cell.	51
3.8	Representative dispersion diagram of the MTM-EBG unit cell, showing analytical and simulated data. The bandgap region is shaded. Reproduced from [188] ©2016 IEEE.	56
3.9	Transmission of the PPW mode through one and three printed cells of the MTM-EBG. The shaded bandgap region corresponds to that of Fig. 3.8. Reproduced from [188] ©2016 IEEE.	58

3.10	(a) Profile view of MTM-EBG unit cell. Host medium consists of three conductors above a ground plane, loaded with series capacitors and shunt inductors. (b) Top view of MTM-EBG unit cell embedded in a microstrip, with strip inductors and interdigitated capacitors. Propagation direction is indicated. Reproduced from [193] ©2023 IEEE.	63
3.11	Two modes of operation for the MTM-EBG to enable multi-band operation. (a) Exploiting the equiphase point to incur the same phase at two different frequencies. (b) Employing the bandgap to transmit one frequency and reflect the other.	64
3.12	Comparison of unit cell with (a) capacitors in conductors 1 and 3, and (b) capacitor in conductor 2. (c) Dispersion diagram for unit cells with provided dimensions. A 1.524 mm Rogers 3003 substrate is used. . . .	68
3.13	MTM-EBG unit cell structure with dimensions and propagation direction indicated. L and C values are swept in Fig. 3.14 and Fig. 3.15, respectively. Rogers 3003 with a height of 1.524 mm is used as the substrate.	69
3.14	MTM-EBG unit cell dispersion and transmission properties for various L values. Based on the unit cell in Fig. 3.13, with $C = 0.5$ pF.	70
3.15	MTM-EBG unit cell dispersion and transmission properties for various C values. Based on the unit cell in Fig. 3.13, with $L = 0.2$ nH.	71
3.16	Effect of adding a 0.1 nF decoupling capacitor into conductor 2. (a) Unit cell designs, which are identical other than the capacitor in the central strip. (b) Dispersion properties.	75
4.1	MTM-EBG unit cell embedded in microstrip TL (top view) that transmits at f_1 and presents a bandgap at f_2 . Phase in each region of the TL is indicated.	78

4.2	Representative depiction of the design of a dual-band microstrip stub. Quarter-wavelength stubs at (a) f_1 and (b) f_2 are effectively combined into a (c) dual-band stub using an embedded MTM-EBG unit cell, which has a bandgap at f_1 and a specified phase at f_2	80
4.3	Dispersion diagram of MTM-EBG unit cell used for dual-band rectangular stub design, and S -parameters of a transmission simulation for a single unit cell. The predicted bandgap location is shaded. Reproduced from [193] ©2023 IEEE.	81
4.4	(a) Simulated dual-band bandstop stub filter, consisting of a stub of length $a = 8.05 \text{ mm}$ topped with an MTM-EBG unit cell with dimensions given in Table 4.1. (b) Fabricated stub filter.	83
4.5	Complex electric field magnitudes of the dual-band rectangular stub in a plane bisecting the substrate, plotted on a logarithmic scale, at (a) 2.4 GHz and (b) 5.8 GHz.	83
4.6	Measurement setup of the dual-band rectangular bandstop stub filter.	84
4.7	Simulated and measured S -parameters of the dual-band, rectangular bandstop stub filter. Operating frequencies are indicated by vertical black lines.	85
4.8	(a) Simulated and (b) fabricated dual-band bandstop stub filter with radial geometry, with $\alpha = 90^\circ$, $r = 9.29 \text{ mm}$, and $h = 1.90 \text{ mm}$. Dimensions of the MTM-EBG unit cells are provided in Table 4.1 . . .	86
4.9	Simulated and measured S -parameters of dual-band, radial bandstop stub filter. Operating frequencies are indicated by vertical black lines.	87
4.10	(a) Simulated layout and (b) fabricated tri-band stub, each with close-ups of the embedded MTM-EBG unit cells to show the $50 \mu\text{m}$ features. Reproduced from [196] ©2018 IEEE.	88
4.11	Dispersion diagram including all individual segments of the tri-band stub. Bandgaps for each unit cell are highlighted.	89

4.12	Complex electric-field magnitudes at tri-band stub resonances (left) versus corresponding conventional devices (right); excitation is at the right port. (a) 2.4 GHz resonance, (b) 3.6 GHz resonance, (c) 5.0 GHz resonance. Reproduced from [196] ©2018 IEEE.	90
4.13	S -parameters of the simulated and fabricated tri-band stub. Data reproduced from [196] ©2018 IEEE.	91
4.14	Comparison of tri-band stub response to conventional stub responses, as plotted near their respective resonances. Reproduced from [196] ©2018 IEEE.	92
4.15	Simulated and measured loss of dual-band rectangular stub filter, compared to conventional stub filters at the chosen operating frequencies.	92
4.16	Broadband response of dual-band rectangular stub.	93
4.17	(a) Model of frequency-dependent load consisting of a $100 - \Omega$ resistor over a gap of $l_r = 0.7 \text{ mm}$, a capacitive plate with dimensions of $w = 3.7 \text{ mm}$ by $l_c = 2 \text{ mm}$, and a via of diameter $d = 0.9 \text{ mm}$. (b) Fabricated load showing measurement plane and reference plane to which results are de-embedded. (c) Simulated and measured input impedance a distance of $c_1 = 10 \text{ mm}$ from the load. Reproduced from [193] ©2023 IEEE.	99
4.18	Representative depiction of microstrip dual-band matching network. A single-band double-stub tuner at (a) f_1 and (b) f_2 are effectively combined into a (c) dual-band double-stub tuner, enabled by embedded MTM-EBG unit cells that have a bandgap at f_1 but transmit with a designed phase at f_2 . Load impedance and the distance between the load and nearest stub, c_1 , are lumped into a frequency-dependent Z_L . Reproduced from [193] ©2023 IEEE.	101

4.19	MTM-EBG bandgap center frequency (solid red) and 10-dB insertion-loss bandwidth (dashed blue) as a function of printed capacitor length g_C . Insets show what the embedded MTM-EBG unit cell looks like for $g_C = 1.5 \text{ mm}$ and $g_C = 3.5 \text{ mm}$. This plot only applies to an MTM-EBG on the chosen substrate with the dimensions given in Table 4.3. Reproduced from [193] ©2023 IEEE.	104
4.20	(a) Simulation model and (b) fabricated dual-band matching network. MTM-EBG A dimensions are given in Table 4.3, and other dimensions are: $a_1 = 2.75 \text{ mm}$, $a_2 = 31.00 \text{ mm}$, $b_1 = 13.37 \text{ mm}$, $b_2 = 39.75 \text{ mm}$, $c_1 = 9.34 \text{ mm}$, and $c_2 = 12.67 \text{ mm}$. Reproduced from [193] ©2023 IEEE.	106
4.21	(a) Simulated and measured S_{11} of the dual-band matching network compared to single-band matching networks (one each for matching at 2.4 GHz and 5.8 GHz, each plotted only over a frequency range of interest). (b) Simulated loss in dual- and single-band matching networks. Reproduced from [193] ©2023 IEEE.	108
4.22	Complex electric field magnitudes of the dual-band matching network at frequencies of loss-causing resonances. Reproduced from [193] ©2023 IEEE.	110
4.23	(a) S_{11} and (b) loss for different lengths of a_2 in the dual-band matching network. Reproduced from [193] ©2023 IEEE.	111
4.24	(a) Layout of the tri-band matching network, where $a_1 = 10.8 \text{ mm}$, $a_2 = 15.5 \text{ mm}$, $a_3 = 23.0 \text{ mm}$, $b_1 = 12.5 \text{ mm}$, $b_2 = 21.1 \text{ mm}$, $b_3 = 27.5 \text{ mm}$, $c_1 = 4.9 \text{ mm}$, and $c_2 = 9.2 \text{ mm}$. Dimensions of MTM-EBG A and B are given in Table 4.3. (b) Fabricated device. Reproduced from [193] ©2023 IEEE.	113
4.25	(a) Simulated and measured S_{11} of the tri-band matching network. (b) Simulated loss. Reproduced from [193] ©2023 IEEE.	114

4.26	a) Dual-band WPD layout, with different MTM-EBG unit cells for the inner (containing MTM-EBG A) and outer (containing MTM-EBG B) branches. Paths for high-frequency (short dash) and low-frequency (long dash) power flow are indicated by arrows. b) General MTM-EBG unit cell layout used in the WPD branches. Reproduced from [184] ©2020 IEEE.	118
4.27	Dispersion diagrams for a) MTM-EBG A and b) MTM-EBG B, with design parameters for each given in Table 4.5. Highlighted regions indicate the bandgap and the horizontal (black) lines show the two operating frequencies. Solid (red) lines and dotted (blue) lines give the imaginary and real parts of the propagation constant, respectively. Reproduced from [184] ©2020 IEEE.	118
4.28	Simulated, experimental, and corrected simulated (including 7- μm over-milling in capacitive gaps) <i>S</i> -parameters of the dual-band WPD. The vertical (black) lines indicate the operating frequencies of 2.4 GHz and 5.0 GHz. Reproduced from [184] ©2020 IEEE.	120
4.29	Fabricated dual-band WPD. The inset magnifies MTM-EBG B, showing the 50 μm features. Reproduced from [184] ©2020 IEEE.	121
5.1	Schematic of microstrip patch antenna with embedded MTM-EBG region on the radiating edge for dual-band operation.	123
5.2	Top view of proposed dual-band antenna consisting of a microstrip-fed patch with MTM-EBG sections placed on the radiating edges. Reproduced from [188] ©2016 IEEE.	131

5.3	Simulated complex electric-field magnitudes (displayed on a logarithmic scale) shown at the resonance frequencies of a) the conventional 2.4 GHz patch, b) the MTM-EBG patch at 2.4 GHz, c) the conventional 5.0 GHz patch, and d) the MTM-EBG patch at 5.0 GHz. Reproduced from [188] ©2016 IEEE.	133
5.4	Simulated and measured S_{11} of the MTM-EBG patch: a) lower-frequency band and b) higher-frequency band. Simulation represents the originally designed antenna, while the corrected simulation curve takes into account fabrication errors in the printed antenna. Reproduced from [188] ©2016 IEEE.	134
5.5	Experimental setup of the antennas in an anechoic chamber. Inset: the fabricated MTM-EBG antenna. Reproduced from [188] ©2016 IEEE.	135
5.6	Simulated and measured normalized radiation patterns of conventional and dual-band antennas, with patterns recorded at the peak return loss frequency: a) lower-frequency conventional patch E-plane, b) lower-frequency conventional patch H-plane, c) lower-frequency MTM-EBG patch E-plane, d) lower-frequency MTM-EBG patch H-plane, e) higher-frequency conventional patch E-plane, f) higher-frequency conventional patch H-plane, g) higher-frequency MTM-EBG patch E-plane, h) higher-frequency MTM-EBG patch H-plane. Reproduced from [188] ©2016 IEEE.	137
5.7	Schematic of patch surrounded by a region of MTM-EBG unit cells, which transmit at a low frequency and have a bandgap at a high frequency. Resonant frequencies and feed points are indicated for both bands, as well as for the horizontal polarization and vertical polarization. This structure forms the DBDPA.	139

5.8	(a) Dispersion diagram for the MTM-EBG unit cell used in the DBDPA, and (b) S_{11} and S_{21} of a single unit cell. Operating frequencies are indicated by horizontal dashed lines, and the bandgap region is highlighted and labeled. Reproduced from [185] ©2021 IEEE.	141
5.9	Patch antenna with rounded corners, and feed pin location indicated. Constituent MTM-EBG unit cell with dimensions is inset. Reproduced from [185] ©2021 IEEE.	142
5.10	Complex electric field magnitudes (in V/m, logarithmic scale) in a plane bisecting the substrate at 3.6 GHz (left) and 5.8 GHz (right). Arrows indicate the excited feeds. Reproduced from [185] ©2021 IEEE.	144
5.11	Exploded feed structure of the proposed DBDPA. Each layer is separated by a dielectric sheet with drilled holes through which the pins pass. Reproduced from [185] ©2021 IEEE.	145
5.12	(a) Top and (b) bottom views of DBDPA. The middle ground plane can only be seen near standard SMA connectors on the top layer, and connecting feed pins are not visible. Reproduced from [185] ©2021 IEEE.	147
5.13	(a) Broadside gain of DBDPA at 3.6 GHz (LF) and 5.8 GHz (HF), for both co- and x-pol, and (b) E- and H-plane total 3-dB beamwidths at each frequency, versus ground plane size, L_g . The vertical dashed lines indicate the chosen ground size. Reproduced from [185] ©2021 IEEE.	148
5.14	(a) Top and (b) bottom views of the fabricated DBDPA. Reproduced from [185] ©2021 IEEE.	151
5.15	S-parameters of the DBDPA in each frequency band. Reproduced from [185] ©2021 IEEE.	152
5.16	Simulated and measured E- and H-plane gain patterns of the DBDPA for the a) 3.6 GHz resonance, and b) 5.8 GHz resonance. Reproduced from [185] ©2021 IEEE.	154

5.17	DPDPA with matching network for (a) a pin position from patch center $p_c = 4.1$ mm (Design A) and (b) $p_c = 5.6$ mm (Design B). The DBDPA is on the top layer, while the matching networks are on the bottom layer, below a ground plane.	156
5.18	Simulation results of the DBDPA with different pin feed locations p_c , both with and without a matching network. (a) $p_c = 4.1$ mm (Design A) and (b) $p_c = 5.6$ mm (Design B).	158
5.19	Side view of the GPS antenna structure, not to scale.	160
5.20	(a) Conventional view of GPS patch antenna above ground plane, and (b) top view with semi-transparent layers.	162
5.21	Close-up view of a segment of the GPS antenna, showing the MTM-EBG unit cells.	163
5.22	S -parameters of the of the GPS antenna, L1, L2, and L5 frequencies indicated by dashed vertical lines.	164
5.23	GPS gain patterns at (a) L1, (b) L2, and (c) L5.	166
5.24	Broadside RHCP and LHCP realized gain of the GPS antenna, with the three operating frequencies indicated by dashed vertical lines. . .	167
5.25	Tunable version of the DBDPA, using varactors in the MTM-EBG unit cells rather than interdigitated capacitors, and decoupling capacitors in the MTM-EBG strips.	168
5.26	Exploded view of the tunable DBDPA. The top layer includes the patch and DC shorting stubs, the bottom layer includes the microstrip feeds with the remainder of the bias network, and a ground plane with holes for the feed pins separate the layers.	170
5.27	S_{11} of the patch antenna for different varactor capacitances, C	171
5.28	(a) E- and H-plane gain patterns for various varactor capacitances C at the lower radiating frequency. (b) Gain patterns at upper frequency resonances.	173

A.1 (a) Simulation model of MTM-EBG unit cell on 60 mil Rogers 3003.
(b) S_{21} of the unit cell for various values of g . Also included are vertical lines indicating the lower bandgap edge predicted by MTL analysis. 199

A.2 (a) Possible circuit model of a single MTM-EBG unit cell incorporating TL coupling, created in Pathwave ADS. (b) S_{21} of the unit cell for various values of g . Vertical lines indicate the lower bandgap edge predicted by MTL analysis. 201

Abbreviations & Acronyms

AC Alternating current.

ADS Advanced design system (Pathwave software).

AMC Artificial magnetic conductor.

AR Axial ratio.

CBCPW Conductor-backed coplanar waveguide.

CBRS Citizens broadband radio service.

CPW Coplanar waveguide.

CRLH Composite right-/left-handed.

CSL Coupled slotline.

CSRR Complementary split-ring resonator.

DBDPA Dual-band dual-polarized antenna.

DC Direct current.

DGS Defected ground structure.

EBG Electromagnetic bandgap.

eMTC Enhanced machine type communication.

GPS Global positioning system.

HFSS High frequency simulation software (Ansys software).

IoT Internet of Things.

ISM Industrial, scientific, and medical.

LHCP Right-hand circularly polarized.

LTE Long-term evolution.

LTE-U Long term evolution unlicensed.

MMCX Micro-miniature coaxial.

MTL Multiconductor transmission line.

MTM Metamaterial.

MTM-EBG Metamaterial-based electromagnetic bandgap structure.

NFC Near field communication.

NRI Negative refractive index.

OC Open circuit.

PBG Photonic bandgap structure.

PCB Printed circuit board.

PEC Perfect electric conductor.

PMC Perfect magnetic conductor.

PPW Parallel plate waveguide.

RF Radio frequency.

RFID Radio frequency identification.

RHCP Right-hand circularly polarized.

RL Return loss.

SAS Spectrum access systems.

SC Short circuit.

SMA Subminiature version A.

SRR Split-ring resonator.

TEM Transverse electromagnetic.

TL Transmission line.

TL-MTM Transmission line metamaterial.

TM Transverse magnetic.

UC-EBG Uniplanar compact electromagnetic bandgap structure.

WiFi Wireless fidelity.

WiMAX Worldwide interoperability for microwave access.

WLAN Wireless local area network.

WPD Wilkinson power divider.

Chapter 1

Introduction

1.1 Motivation

Microwave systems have become increasingly important in modern life. Wireless devices communicating in the radio, micro-, and millimetre-wave spectra are found in all sorts of everyday items; individuals often keep a variety of devices that operate in these bands with them at all times. Smartphones are ubiquitous and connect to 3G, LTE (long-term evolution), and 5G networks, operate on Wi-Fi, and connect to other devices with Bluetooth. The phone may be communicating with a smart watch or wireless headphones, may transfer data to another phone through NFC (near field communication), or may be charging wirelessly.

Broader infrastructure facilitates these connections; 3G and, increasingly, 5G networks require massive public infrastructure to run, with different challenges in urban environments, where noise is an issue, compared to more rural settings, where power levels and coverage must be addressed. Some situations are more localized; a concert or sporting event where a large number of people are gathered faces a considerable challenge in overcoming noise constraints and bandwidth requirements.

Communications are hardly the only use for microwave and RF devices that are increasingly in demand. A range of sensing-related applications that are accurate, reliable, and comprehensive are appearing in various fields. Consider radio-frequency identification (RFID), which typically uses small passive or active tags to communi-

cate with a reader, for the identification of items or the sensing of the surrounding environment [3]; compare this to automotive radar, which uses a broad range of frequencies to identify obstacles around a vehicle and to react accordingly. Overlay this with other devices that form the Internet of Things (IoT), and complexity compounds substantially. Each of these applications and everything in between presents unique and interesting challenges to the microwave community.

A large part of the solution to these problems depends on the spectrum itself, which is strictly managed by national and international bodies. The radio, microwave, and, increasingly, mm-wave spectra are partitioned into bands that may be licensed or unlicensed (and may differ by region), and restrictions on device power levels and interference with other bands apply. Since the spectrum is a limited resource, however, more efficient use of the available spectrum is required to meet the demands of modern systems. For example, it is estimated that basic implementation of the IoT alone (which includes Bluetooth, Zigbee, LoRaWAN or SigFox in unlicensed bands, enhanced machine type communication (eMTC) and narrow-band IoT in licensed bands) requires about 76 GHz of the spectrum [4]. Spectrum sharing can reduce this to about 19 GHz, which is much more manageable but still a significant chunk of the finite frequency space available [4]. In part, this reduction depends on dynamic system access to more efficiently use the spectrum, rather than having fixed channel allocations [5].

New solutions to maximize use of the available spectrum are being implemented in many emerging protocols. As an example, the Citizens Broadband Radio Service (CBRS) covers a frequency range of 3550–3650 MHz and utilizes a spectrum access system (SAS), which dynamically allocates spectrum to various tiers of users [6]. The requirements of such a system are complex and yet stringent [7], and this puts demands on the hardware that must be used to operate in such an environment. Devices including antennas and the RF front end should be operable across the entire CBRS band to facilitate dynamic frequency assignment, and a user also has to report

position changes every 60 seconds. This requires a global navigation satellite system (GNSS) such as the global positioning system (GPS) in North America, a communication channel with the SAS, and the ability to dynamically adapt to the prescribed channel.

Improving usage of the spectrum and generally meeting the needs of burgeoning wireless industries requires technologies that present an improvement over the current infrastructure. Devices are required that outperform existing systems, as measured by any number of metrics. This could include increased bandwidth for higher data rates, or high selectivity to reduce interference. Antennas with higher directivity can be used to reduce system power or increase signal-to-noise ratio if the required transmission direction is known, as can an omni-directional antenna with higher radiation efficiency when greater spatial coverage is needed; the choice is application dependent. Many advantages arise from reducing power consumption and an increasing amount of devices aim to be completely batteryless. Along with improving individual system metrics, increased functionality is often required, such as the ability of devices to operate over several bands or perform several functions simultaneously. Smaller, multi-band, and multi-functional devices can render products cheaper, more mobile, and able to be embedded into everyday objects. The best new devices will present improvements in several of these areas simultaneously, and include other advantages not listed here. These improvements to individual microwave components form a critical contribution to realize the next generation of wireless devices, sensors, and systems.

This work aims to take a metamaterial (MTM)-based structure that inherently has some advantages for use in microwave systems, and using a systematic approach, demonstrate its integration into a variety of microwave applications for improved performance, particularly to render antennas and related circuit components multi-band. The approach is based on a well-developed theory and is general enough to be used for both circuit components and antennas, for dual- or tri-band applications at

nearly arbitrary frequencies. While many technologies have been proposed for specific applications, this work intends to develop a more general approach to rendering devices multi-band. In doing so, this thesis attempts to realize in practice some of the device improvements promised when modern MTM theory was first developed. Rapid and rigorous theoretical advancements suggested many practical and exciting implementations at that time, but these have not yet been widely adopted for commercial applications, due to difficulties such as ad-hoc design procedures, fabrication complexity and sensitivity, large sizes, and difficulty of using a given structure for multiple applications. This work presents a technology and theory with which many of these challenges can be overcome.

1.2 Objectives

The objective of this work is to use a recently developed technology known as the MTM-based electromagnetic bandgap structure, or MTM-EBG, to create a suite of multi-band circuit components and antennas that are compact, uniplanar, and practical for many applications and arbitrary frequencies. This particular structure has been developed with analytical and theoretical rigor, and while some advances are made in this regard, creating practical design strategies and guidelines is prioritized. This work intends to allow a designer to quickly begin using the MTM-EBG to create multi-band circuits for many applications, independent of structure, frequencies, or substrate, while providing them with design strategies, intuition, and data to simplify the process.

When MTMs were first introduced, theory was quickly developed with the promise of transforming electronics in the microwave regime; consider the broad range of novel properties and devices discussed in [8]. While new theories, technologies, and devices have been created as a result, there has been at times a haphazard quality to the body of research. Some developments have had excellent theoretical rigor without resulting in practical devices, while some excellent and novel structures have been proposed

without a strong theoretical foundation. More often, researchers have reverted to ad-hoc design methods or simplistic models that fail to encapsulate the full richness of a MTM-based structure, or is only applicable to specific situations.

A subset of MTMs, EBGs, have also been used extensively at microwave frequencies and many practical realizations have been demonstrated, for example in antenna applications [9]. While suffering from some similar drawbacks to the broader class of MTMs, they also tend to be large and difficult to integrate with existing devices. Their usage is therefore limited without compact realizations.

The MTM-EBG can be used to bridge these gaps for several reasons. It is rigorously designed, but the design process can be simplified when necessary, and analysis of the MTM-EBG can be completed independently from analysis of the device that it is embedded into. Standard design procedures for different circuit components and antennas can therefore still be used, and an independently designed MTM-EBG can be implemented into arbitrary devices to enable multi-band operation. The approach is general and works at nearly arbitrary frequencies, and since the MTM-EBG is uniplanar and electrically small, implementation is typically straightforward.

This work aims to demonstrate potential uses of the MTM-EBG by designing and creating the multi-band circuit components and antennas themselves. Demonstrating a variety of different components with the same technology serves to illustrate that this solution is truly general, and any design quirks that are unique to individual structures will be assessed and overcome, creating a blueprint for a designer of new devices to do the same. Practical design aspects will be the main focus since this thesis primarily aims to bridge the gap between theory and application, meaning that details of theoretical interest only are not strongly emphasized (but are discussed where necessary). By the end of this thesis, the reader should have an appreciation of how the MTM-EBG can be used to create general multi-band systems, and understand the design approach required to do so.

Multi-band devices in this work are designed for the sub-6 GHz frequency range,

which encompasses GPS frequencies, several ISM bands, Wi-Fi/WLAN, LTE/LTE-U, CBRS, and many 5G/IoT applications. This frequency range is currently receiving a vast amount of attention in the literature, and although MTM-EBG-based devices are not inherently limited to these bands, it is an important part of the spectrum to cover, particularly in light of the imminent deployment of 5G and beyond 5G networks.

1.3 Outline

This thesis starts with an investigation of methods by which devices can be rendered multi-band in Chapter 2. It investigates general multi-banding methods as well as approaches that use MTMs or EBGs, and a brief background for both of these structures is additionally provided. A literature review of multi-band circuit components and antennas follows with a focus on structures created in the past few decades, and current design and implementation challenges of such structures are investigated. Chapter 3 then investigates the MTM-EBG in detail, providing relevant background and a plethora of design details to enable use in planar structures. Using this information, Chapter 4 then endeavours to implement the MTM-EBG into a variety of circuit components for use in wireless systems to produce multi-band operation, including filters, matching networks and power dividers. Focus is shifted to antennas in Chapter 5, and patch antennas that are dual-band and/or dual-polarized are presented. Operation at various bands, antennas with integrated matching networks, patches with increased bandwidth, and tunable antennas are all demonstrated. The work is concluded, and future directions are discussed, in Chapter 6.

Chapter 2

Background

2.1 Multi-Band Design Techniques

2.1.1 Overview

Multi-band devices allow circuits to process multiple bands simultaneously, or improve performance of a single function by increasing available spectrum. Many different approaches to creating multi-band devices have been taken, and this chapter endeavours to discuss and classify these methods, providing designers with an overview of available techniques. The focus will be on passive planar circuit topologies and antennas, since these are ubiquitous in low-power microwave communications, and cheap to implement. Traditional approaches will be discussed first, before some recent enabling technologies are introduced. Advantages and disadvantages of the various methods will be discussed.

Regardless of the multi-banding technique, there are some important criteria that these devices strive to meet. Performance-based criteria (impedance matching, bandwidth, insertion loss, antenna gain, etc.) are typically compared to conventional devices at each operating frequency, with the goal of matching or exceeding that performance in each band. Additional functionality may also be added to the multi-band device, for example, simultaneous filtering or improved beam shape for an antenna. Doing this in the same amount of space as a conventional device presents a challenge, as more components or features are typically required. Fabrication cost is a related

issue; not only should size be minimized, but elements that are difficult to fabricate (e.g., vias) or that require additional steps or cost to include (e.g., chip components that require soldering) may vastly increase production cost and time, especially in mass-production scenarios. Creating a multi-band device that is capable of keeping size and cost down while maintaining performance is the goal of most design procedures.

Perhaps the most direct way to operate over several frequency bands is simply to operate over *all* frequency bands. Broadband structures have long been sought after and many have been designed, albeit often with drawbacks including size, complex structure, and/or performance across its bandwidth (especially since many bandwidths may be considered and are not always correlated; for example, a 10-dB return loss bandwidth for an antenna may be drastically different than its 3-dB gain bandwidth). It is also inefficient in many cases to operate over a broad frequency range when only small frequency bands in the range are actually required. Being more selective of operating bands can filter out unwanted bands, reducing noise and potentially interfering signals. Many broadband devices require additional filtering stages to remove these unwanted bands as a result. Some broadband devices will therefore be considered, but much more focus will be placed on multi-band components.

Creating broadband devices is typically difficult since most are inherently bandwidth-limited. On a large scale, bandwidth is limited by frequency-dependent material properties; for example, metals have a plasma frequency, and this makes visible light interact with them fundamentally differently than radio waves. This work will focus on the microwave regime, however, where it can usually be assumed that important material properties (permittivity, permeability, conductivity) are approximately constant as a function of frequency. For this work, therefore, it is not the materials themselves that limit bandwidth (at least in low-loss conditions), but the structure of the devices instead.

Some fundamental limits on bandwidth exist for all devices, for example, on

impedance matching bandwidth [10] or on antenna bandwidth as a function of size [11]. These limits exist in more extreme realms, and most microwave structures are not hampered by them. Instead, the bandwidth-limiting feature of most microwave devices is simply that a part of their structure requires a particular phase response, making its overall response frequency-dependent. For example, Wilkinson power dividers (WPDs) and quadrature hybrid couplers require quarter-wavelength transmission line (TL) segments, while microstrip patch antennas resonate at a half-wavelength size. These conditions are only valid over a small frequency range.

Most devices with strong frequency dependence are naturally multi-band, with higher-order harmonics providing additional operating frequencies. This is caused by TL segments exhibiting the same length-dependent conditions at harmonic or odd-harmonic frequencies, although performance is usually degraded to some extent in the higher-order bands. This is often observed as increased insertion losses or poorer matching, and compounding the problem is that the devices are large for their operating frequency, typically several multiples of $\lambda/4$ larger than they need to be for operation at the fundamental harmonic. These harmonic bands are also not typically useful; most standards (such as WiFi, WiMAX, or GPS) do not employ harmonically-related bands, and it is often advantageous to filter out these other bands instead. Additionally, non-linearities can cause intermodulation distortions in or near harmonic bands that can degrade system performance. Implementation of multi-band operation using harmonics is therefore not efficient or useful, and little design freedom is gained from this method.

A direct and more useful way to render devices multi-band is to replace the bandwidth-limiting segments with a different structure that meets the required phase condition at several frequencies. For example, a TL segment can be replaced with an equivalent circuit such as a π network that is capable of meeting the required phase condition at two frequencies, as shown in Fig. 2.1 [12]. The π -network can be analyzed using $ABCD$ parameters, and comparing the cascaded result to $ABCD$ parameters

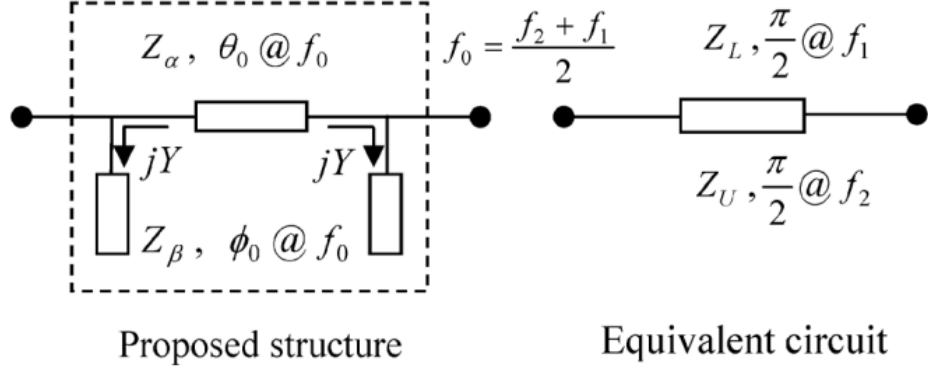


Figure 2.1: π -network TL model that can be used to replace a TL segment of specified phase for dual-band operation. Reproduced from [12] ©2012 IEEE.

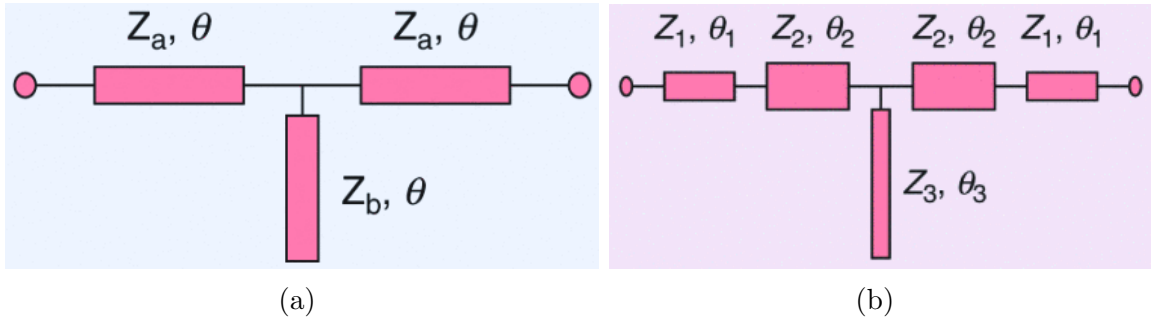


Figure 2.2: (a) T-network model that can replace a TL segment to produce dual-band operation. Reproduced from [13] ©2022 IEEE. (b) T-network model that can replace a TL segment for tri-band operation. Reproduced from [14] ©2022 IEEE.

of a desired network (for example, a quarter-wave transmission line segment) allows the formulation of design equations to produce dual-band operation [12, 13]. This approach increases complexity and circuit size and often has limitations (for example, the π -network can typically provide dual-band matching for a frequency ratio less than three [13]), but produces closed-form equations for the design of dual-band networks in cases where it is applicable.

A variety of circuits may be proposed to replace frequency-dependent transmission lines; another canonical example is the T-network shown in Fig. 2.2a, although other arbitrarily constructed circuits have been proposed and design equations formulated. To operate in more than two bands, more complicated networks are needed; consider Fig. 2.2b, which adds additional TL segments to the T-network to produce multi-

band operation [14]. Different proposed circuits may have different advantages and disadvantages, ranging from differences in circuit size and frequency ratios to controllability of bandwidth. The number of possible variations leads to this approach losing some appeal because it is unclear which circuit model provides the best option for a given application.

A second means of rendering circuits multi-band is to propose a circuit that can provide an overall multi-band response (rather than directly replacing the frequency-selective segment), and analyzing it to find conditions that allow multi-band operation [13, 14]. This can involve techniques such as the extended port, multisection circuits, or using coupled lines or resonators. Also often within this category is the use of MTMs or composite right-/left-handed (CRLH) materials, which will be explored separately in the following subsection.

In most cases, the analysis of MTM-based structures embedded in TLs (or TL-MTMs) employ equivalent-circuit and/or two-conductor TL models, although this has limited efficacy in cases where more than two conductors lie parallel to the direction of propagation, separated by a gap or slot. The efficacy of a traditional TL model may be limited to certain frequency regimes or ignore certain important scattering/coupling phenomena, which may otherwise be captured using a more rigorous multiconductor TL (MTL) analysis [2, 15–17]. TLs can be considered to be a special case of MTLs, and as such are missing information that MTL analysis includes.

A different approach to designing multi-band devices (using TL or MTL approaches) is in conjunction with dispersion engineering. Often used with MTM-based structures, it simply involves determining the dispersion properties of a material or structure and using/altering them to produce multi-band operation. This is a common technique with novel and periodic materials for which dispersion plots are commonly generated to conveniently represent their behaviour. New methodologies of achieving multi-band operation can be postulated and attained with these data, for example as in [18].

Many other multi-banding approaches have gained popularity over the last few decades using novel structures broadly classified as different types of MTMs. Many of these structures provide an electromagnetic bandgap (EBG) response when interfaced with usual circuits. These categories will be explored in further detail before examples of multi-band devices themselves are considered.

2.1.2 Metamaterials

The idea of intentionally creating structures, or “effective media”, by manipulating the properties of electrically small constituent particles arose in the mid-20th century, where sub-wavelength lattices were created to engineer bulk media properties including ϵ and μ [19, 20]. For microwave structures with wavelengths on the order of centimetres to metres, these media consist of electrically small but physically large constituent particles, and are therefore easily realizable.

With the freedom to engineer these constituent effective medium particles, it was discovered that they could be manipulated to produce *entirely new* material parameters that are not found naturally; for example, a material can be engineered to have a simultaneously negative permittivity and permeability, which gives rise to a negative refractive index (NRI). Materials such as this that have exotic or unique properties not found in nature are classified as MTMs, although they possess many other names as well, typically descriptive of specific properties of interest.

A particularly useful area of study that blossomed in the early 21st century involves integrating MTM structures into TLs. The canonical TL-MTM structure, depicted in Fig. 2.3, consists of a series capacitor and shunt inductor embedded into a standard two-conductor TL; lumped loading at sub-wavelength intervals in this way supports exotic properties such as left-handed propagation, in which the electric field, magnetic field, and Poynting vectors form a left-handed, rather than right-handed, triplet [21, 22]. This is also referred to as a *backward wave* structure since the direction of power flow is contra-directional to the direction in which phase is incurred.

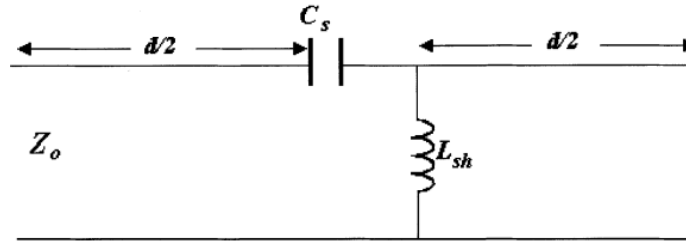


Figure 2.3: Unit cell of a transmission line loaded with a series capacitor and shunt inductor. Reproduced from [21] ©2003 IEEE.

The circuit model in Fig. 2.3 can be understood by comparison to a standard TL model. If $\mu \propto L_{series}$ and $\epsilon \propto C_{shunt}$ for a TL (or any right-handed media, including free space), then they can be reversed into the dual (or high-pass) configuration for left-handed operation, namely by having L_{shunt} and C_{series} . This effectively renders the traditional reactive components, and therefore the effective medium parameters, negative [23, 24], albeit with frequency dispersion in order to preserve causality.

TL-MTM models quickly became an extremely important tool for MTM characterization, and were used to verify many important properties. These approaches were applied to various areas including the creation of superlenses that overcome the diffraction limit [25, 26] or complex multiconductor systems supporting large bandgaps [15, 27, 28]. The term CRLH MTMs also arose to describe structures which contained both left-handed and right-handed circuit elements, producing dispersion curves with some unique features including various modal bandgaps and an infinite guided wavelength frequency [29–31]. A large body of theory was rapidly developed to describe MTMs in detail [8, 24, 31].

This work is interested in using MTM- and MTM-based structures in circuit components and antennas for multi-band operation, and aims to understand how their unique properties can be exploited through interaction with traditional materials and TLs. To better understand this, consider the Sievenpiper mushroom structure, shown in Fig. 2.4a, which is a simple structure that presents an easy visual representation of the fundamental MTM model, since it consists of a set of vias, providing shunt

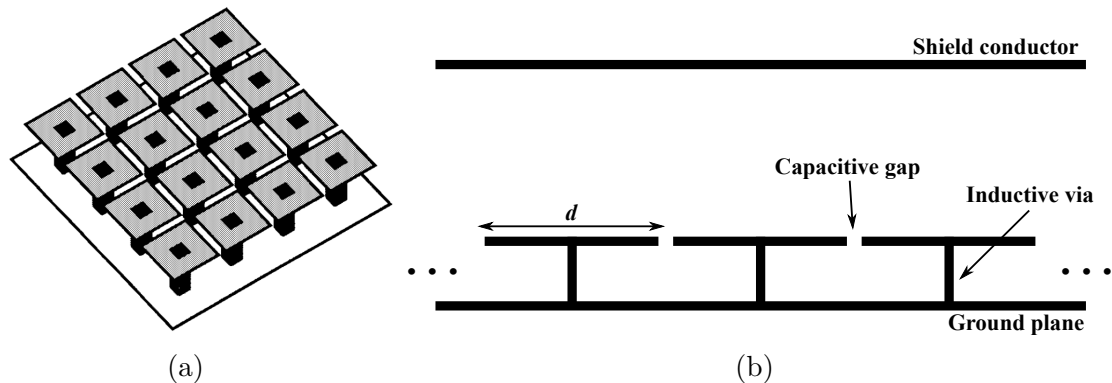


Figure 2.4: (a) Sievenpiper mushroom structure. Reproduced from [32] ©1999 IEEE. (b) Cross section of the mushroom structure, indicating periodicity, capacitance, and inductance. A shield conductor is included in the model since it is required for rigorous MTL analysis [15].

inductance, connected to plates that are separated by series capacitive gaps [32]. Initially introduced as a high-impedance surface (related to a corrugated metal sheet), it was further shown to behave in the long-wavelength limit as an NRI medium with a predictable band structure [15, 27].

Elek *et al.* [15] were able to demonstrate how the NRI properties of the Sievenpiper structure relate to the bandgap it produces by considering it to be a MTL consisting of a ground plane, a conductor plane with capacitive gaps (or “square patch plane”) connected to the ground conductor by vias, and a shield conductor (required to model propagation above the mushrooms and capture modal coupling effects); this model is shown in Fig. 2.4b. It is demonstrated that a backwards wave mode created by the effective medium in the long-wavelength limit contra-directionally couples to a forward parallel-plate waveguide (PPW) mode to produce a bandgap. Dispersion properties of the modes can be plotted independently to observe their right-handed and left-handed characteristics, while coupled-mode MTL analysis of the system gives a full dispersion diagram that predicts the observed bandgap properties with remarkable accuracy [15, 33]. Coupling of the modes is further described by the complex propagation constant in the bandgap region, and great insight into how such MTMs operate is provided by this example. Less rigorous 2-conductor transmission line models are

still used to describe most MTM-based structures, with accuracy often limited to a small frequency range.

The development of TL-MTMs over the last couple decades was heralded with many claims of what this new class of structures would be able to achieve. Some of these claims have proven over time to be overstated or difficult to realize in practice, generating debate and controversy on occasion (see [34], for example); however, plenty of evidence of the usefulness of TL-MTMs and proof of some of their more exotic properties have led to the continued development of many novel and improved devices. TL-MTMs have been widely applied to various new structures and devices, due largely to their easy ability to be integrated with traditional TL-based structures.

2.1.3 Electromagnetic Bandgap Structures

EBGs (or photonic bandgap structures (PBGs) in optics and many early microwave engineering papers [35, 36]) are artificial periodic structures that interact with electromagnetic waves to produce a bandgap [37, 38]. Periodicity is typically on the order of wavelengths, usually $\lambda/4$ to $\lambda/2$, rather than being strongly subwavelength as MTMs tend to be. Microwave-frequency EBGs can consist of periodic dielectric slabs [39, 40] or metallic features, although it is the function rather than structure that defines them. 2D EBGs or surfaces suitable for integration into microwave circuits will mainly be considered in this work.

While the design of EBGs precedes MTMs, the former are often considered to be a category of the latter, using the broadest definition of MTM. For example, the Sievenpiper mushroom structure is considered a canonical EBG, and yet can also be understood as a TL-MTM [15, 27], and some NRI or CRLH metamaterials can be viewed in context of EBG theory. Some periodic structures will act as an EBG at one frequency, and propagate a left-handed mode at others [9]. The distinction between EBGs and MTMs is therefore not always clear, and the terms EBG and MTM are often used to refer to the same structures [8]. This work generally considers MTMs

to be a class of artificial structures with novel or unusual properties, and it considers EBGs to be a class of structures within the very broad umbrella of MTMs that provide some sort of bandgap. This does not necessarily indicate that traditional MTM concepts are used to analyze or enable an EBG's functionality, so it is more correct to say that EBGs *may* fall into the category of MTMs, but for the sake of consistency, it is convenient to classify all EBGs as such.

A major difference in early development between EBGs and MTMs is that the practical aspects of EBGs were more immediately clear, such as their use in suppressing surface waves and acting as an artificial magnetic conductors (AMCs) that could be placed under antennas [32], and as a result, their development was often more application-driven than based on theory [37]. The complexity of some of the structures contributed to a less theory-driven approach as well [9]. Many EBG structures, as a result, were developed using numerical approaches or commercial software. Regardless, they have found applications in all sorts of areas crucial to modern-day technology, including GPS, Bluetooth, phased arrays, antenna ground planes, leaky wave radiation, and microwave circuit elements [8, 9, 37, 41, 42].

To describe a few examples in closer detail, consider a simple EBG consisting of a periodic array of apertures in the ground plane beneath a microstrip line [44]. A strong bandgap around 11 GHz is created by the large number of apertures that constitute the EBG with a periodicity of approximately half a guided wavelength. The aperture radius affects the bandgap strength and bandwidth, but it is the periodicity that determines the bandgap location. This is a typical use of an EBG, which operates effectively, but requires a large amount of space to implement.

A second example of an EBG application is to place the periodic structure between antenna array elements for surface-wave suppression, in order to reduce mutual coupling [44]. The structure used in this case is the Sievenpiper mushroom structure, a large array of which can be seen separating antenna elements in Fig. 2.6. While this structure is effective in reducing mutual coupling, note the similar drawbacks to the

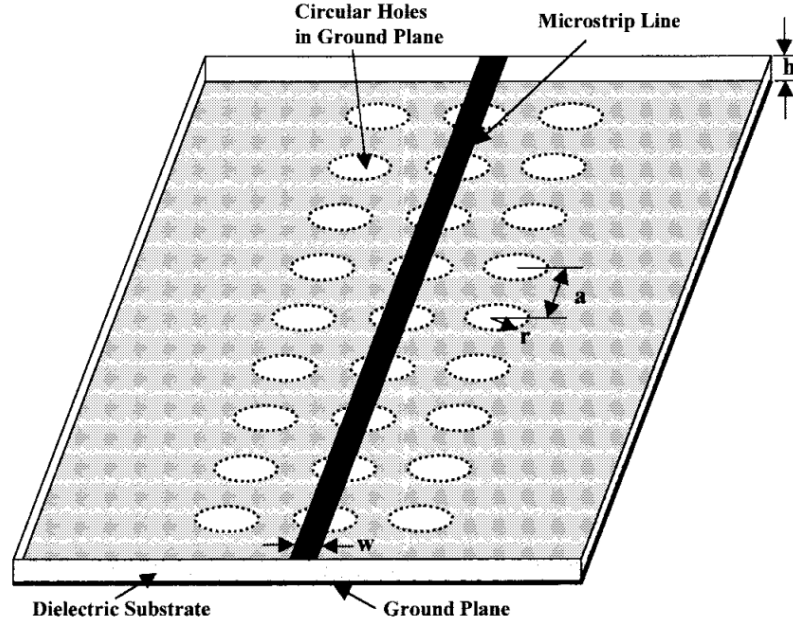


Figure 2.5: EBG application of a periodic array of holes beneath a microstrip TL to provide a strong bandgap. Reproduced from [43] ©1998 IEEE.

previous example: the EBG is large and requires many periods to implement. EBGs are typically introduced in this manner, near to or surrounding an existing structure to enhance operation, and often take up more space than the structure itself.

Methods to reduce the large size and difficult fabrication of EBGs have been in demand; for example, the Sievenpiper structure has undergone size reduction [45] and other geometric changes to remove the need for vias and enable easier fabrication [46], and it has been used for an increasingly diverse set of applications [47, 48]. Low-profile EBGs have made their way into various circuit and waveguide elements, and similar to TL-MTMs, the last couple decades have experienced a surge in useful devices augmented with these structures. They have not always been used explicitly for multi-banding purposes due to their principle drawback being size, but creating a small structure that acts as an EBG (which can be done with MTM principles) presents the opportunity to vastly expand their applicability, and many MTM-based approaches are capable of shrinking the size of EBGs. This work uses one such approach to apply MTM-based EBGs with an electrically small size into circuits for

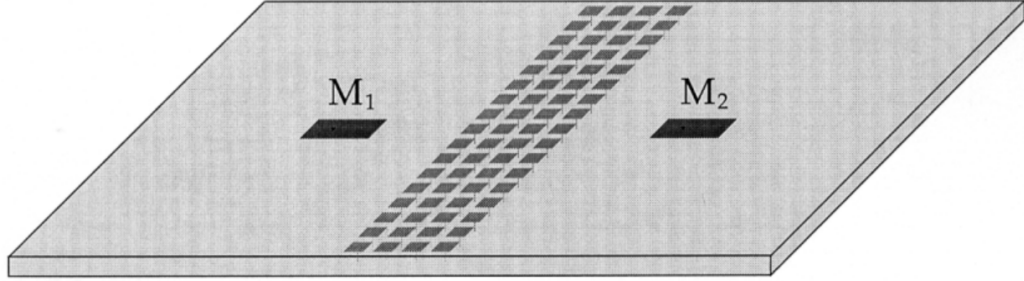


Figure 2.6: EBG application to reduce mutual coupling between patch antenna array elements. Reproduced from [44] ©2003 IEEE.

multi-band operation.

2.1.4 MTM and EBG Unit Cells

While MTM and EBG structures are inherently periodic, there are many cases in which metamaterial particles or unit cells are used individually. A common example of this is the split-ring resonator (SRR) [49], which can be placed in or adjacent to microwave antennas [50], TLs [51], and other devices. Other topologies that can be described as having MTM properties in a unit cell include defected ground structures (DGSs) [52], small sections of CRLH-loaded TLs, and others [53].

The use of single unit cells poses a challenge to designers, who may describe them as “metamaterial-inspired”, or shy away from the label of MTM and use one of the more functional terms instead. Truly, it is difficult to classify a single resonant structure as a “material” since it operates as a non-periodic “lumped” component, otherwise may be electrically large, and is certainly not rigorously amenable to homogenization. Other means are needed to describe how they operate. Structures like the SRR and complementary SRR (CSRR) are better described as resonators, while CRLH TLs can be analyzed with conventional circuit theory. Properties such as the left-handedness of the TL are not necessarily required to understand how these devices operate.

While these structures may not explicitly take advantage of the NRI aspect of MTMs, they can be described in terms of forwards and backwards modes coupling to

form a bandgap, as was briefly discussed in regard to the Sievenpiper structure earlier [15]. A complex mode arises as a result of this coupling, with the real part of the complex mode describing reflection rather than loss [54]. For a single unit cell, this can again be thought of as a resonant phenomenon rather than modal coupling, as the MTM loading (high-pass configuration) in the presence of TL loading (low-pass configuration) produces appropriate conditions to resonate at microwave frequencies [23].

Similarly, unit cells of an EBG may be resonant at some frequency where electric and magnetic stored energy are equal. The resonant frequency of the unit cell may be different than the operating frequency of the periodic structure if the periodicity is primarily what determines bandgap location (as was the case in regard to Fig. 2.5). The bandgap mechanism may therefore change for a single unit cell, or no bandgap may be produced at all.

Many single MTM or EBG unit cells that do produce a bandgap contain half-wavelength features and are easily understood to be resonant. In this case, a circuit model of a unit cell can be produced, albeit one that is accurate only over a limited frequency range. This may functionally still be considered an EBG if a bandgap is produced, even if periodicity is not required.

Understanding these structures as MTMs or EBGs often remains useful, despite questions of whether it truly represents their nature. These classification issues are semantic in nature but remain important in assessing the state-of-the-art and choosing an appropriate structure for a given application. In particular, it may be possible that the term MTM has become overly broad, and more specific terms describing functionality or structure (e.g., terms like EBG or high-impedance surface) are more useful. Describing structures as MTMs would better be reserved for effectively homogeneous media (although these structures remain difficult to fabricate), or as TL-MTMs when the same assumptions can be made. This purist definition, however, is seldom adhered to. This conversation is complicated by the inheritance of the suffix “meta” to

the burgeoning field of metasurfaces, which has roots in the MTM community and has precedence for adopting the term [55].

Despite this, concepts underlying these typically periodic structures are crucial to an enormous body of work in the microwave community, and continue to be used extensively today. While interest in volumetric MTMs using the homogeneous material approximation has waned, partially due to problems such as loss and sensitivity that has plagued such designs, easier structures to build and fabricate such as TL-MTMs are more commonly employed. Smaller or single-cell MTM unit cells have also increased in prevalence as the ability to implement them into compact, realistic microwave circuit components increases. The direction towards practicality has led to some extremely useful and interesting devices.

2.2 Multi-Band Circuit Components

2.2.1 Stubs and Filters

Now that methods of rendering planar microwave devices multi-band have been discussed, examples of such devices will be investigated. This discussion is sorted by device type rather than methodology since the latter may not always be clearly defined. Furthermore, it provides the opportunity to compare the performance of like devices. Microwave circuit components will be investigated first followed by planar antennas, and specifically, one of the simplest microstrip components will begin the investigation: the microstrip stub.

Microstrip stubs are a canonical element in high-frequency circuits and have a multitude of functions in modern microwave and mm-wave systems. Their simple design and fabrication ensures their ubiquity in modern communications applications either as individual components or as part of larger microwave components. Stubs are capable of producing effective RF short or open circuits, acting as simple filters, or providing a reactance that can replace lumped chip components, for example, in

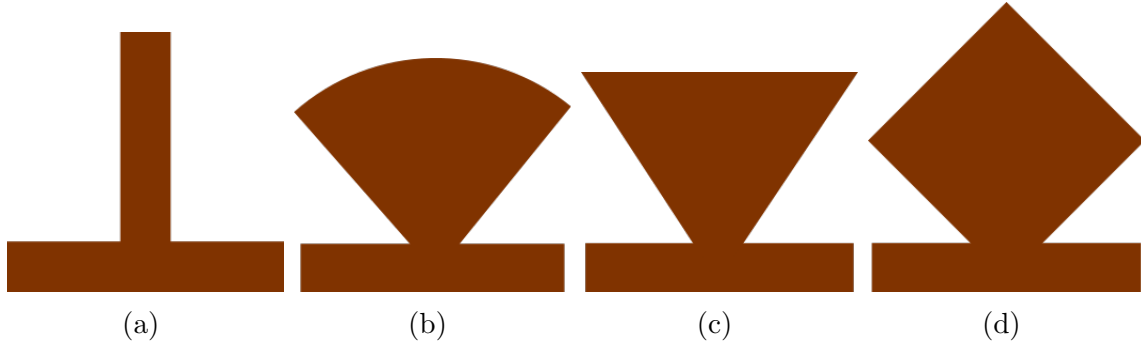


Figure 2.7: Microstrip stub geometries, shown in parallel with a transmission line. (a) Rectangular stub. (b) Radial stub. (c) Triangular stub. (d) Rhombic stub.

power-amplifier design or patch-antenna impedance matching applications [56]. However, they are fundamentally band-limited due to the fact that their input impedance is a periodic function of electrical length. Furthermore, as distributed components, they can take up a significant amount of space on a circuit board. As modern high-frequency electronics demand smaller systems to perform increasingly complex tasks, improving stubs has high applicability.

Multi-band operation is the ultimate goal in this thesis, but increased operational bandwidth can achieve the same end, and will first be discussed. To improve upon their small bandwidths and/or provide a lower impedance, several different stub geometries have been proposed, some of which are shown in Fig. 2.7. Traditional rectangular microstrip stubs have been flared into a radial geometry and used as a simple stub filter with improved bandwidth [57–60]; these stubs are commonplace. Similar to this is the triangular stub, which is slightly more compact and has been used in low-pass [61] and resonant band-pass filters [62]. Other bandwidth-enhancing geometries include coupled rhombic stubs [63] and log-periodic radial stubs [64].

Rather than changing geometry, combinations of stubs can be used to yield broadband operation. Examples of this include [65], in which a large number of stubs are used for low-pass filtering, or [66] where stubs enable optimal high-pass filtering. In each of these cases, additional stubs greatly increase the overall size of the structure,

although this can be mitigated somewhat by creative meandering of the stubs. Moderate bandwidth enhancement was observed in [67], where stub inverters in between quarter-length resonators provide some control of bandgap properties. Radial stubs have been used together with these multi-element systems to further enhance bandwidth at the expense of increased complexity and footprint, for example, to produce broadband filtering [68–70]. Some systems generate broadband operation through the combination of microstrip stubs with other elements, such as a spurline [71] or defected microstrip structure (DMS) [72]. DMSs can alternatively be used to improve in-band performance of stub-based systems [73]. The authors of [74] add slotline stubs as well as microstrip stubs into the ground plane of a substrate to increase bandwidth.

Multi-band rather than broadband stubs and stub-based filters are useful in applications where use of the entire broadband spectrum is not required. For these applications, stubs are often used in combination with other circuit elements or geometries to provide operation over various bands. Integration of stubs into microstrip loops to create multiple resonances in filtering is common, though generally produces small bandwidths [75, 76]. Stepped-impedance resonators in conjunction with radial stubs have reported dual-band operation [77], and similar methods have resulted in operation in up to five bands [78]. DMSs have also been employed with stubs to generate multi-band filtering [79, 80]. These systems are often narrowband and involve components that increase the size and cost of the circuit.

MTM-based approaches have been used to render stubs dual-band as well. As an example, an open-circuited stub with embedded series capacitors and shunt inductors forms a CRLH structure with phase conditions designed to produce a non-harmonic dual-band response [81]; the structure and filtering response are shown in Fig. 2.8. A more compact dual-band CRLH stub is presented in [82].

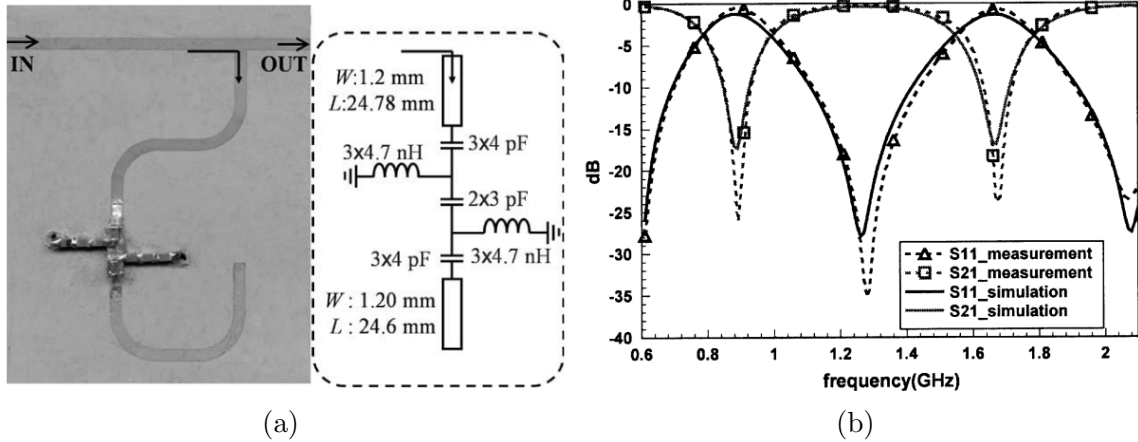


Figure 2.8: Dual-band stub filter using CRLH structure. (a) Fabricated structure and circuit model. (b) Reported S -parameters showing two clear filtering bands. Both reproduced from [81] ©2004 IEEE.

2.2.2 Matching Networks

A particularly common application of microstrip stubs is impedance matching, through the use of one or more stubs [56]. A variety of matching networks have been proposed with many designed for dual-band impedance matching. π -model approaches are employed in [83, 84] and realized with stubs of varying characteristic impedance, resulting in stubs of extreme widths. A third stub is added in [85] to avoid the need for TLs with extremely high or low impedance, and narrowband dual-band matching is achieved. The final layouts of these stub-based matching networks are shown in Fig. 2.9.

Applications of multi-band matching networks are varied, and include power amplifier circuits [86, 87] and antenna matching networks [88, 89]. A circuit is proposed and design equations obtained for matching to a frequency-dependent complex load in [90], while dual-band matching is achieved with a single stub and several TL segments in [91]; a similar approach is taken in [92], while [93] avoids the use of stubs altogether, and instead uses two cascaded transmission line sections.

Many of these systems are capable of matching to arbitrary frequency-dependent complex loads, and some are modeled on traditional designs such as single-stub tuning

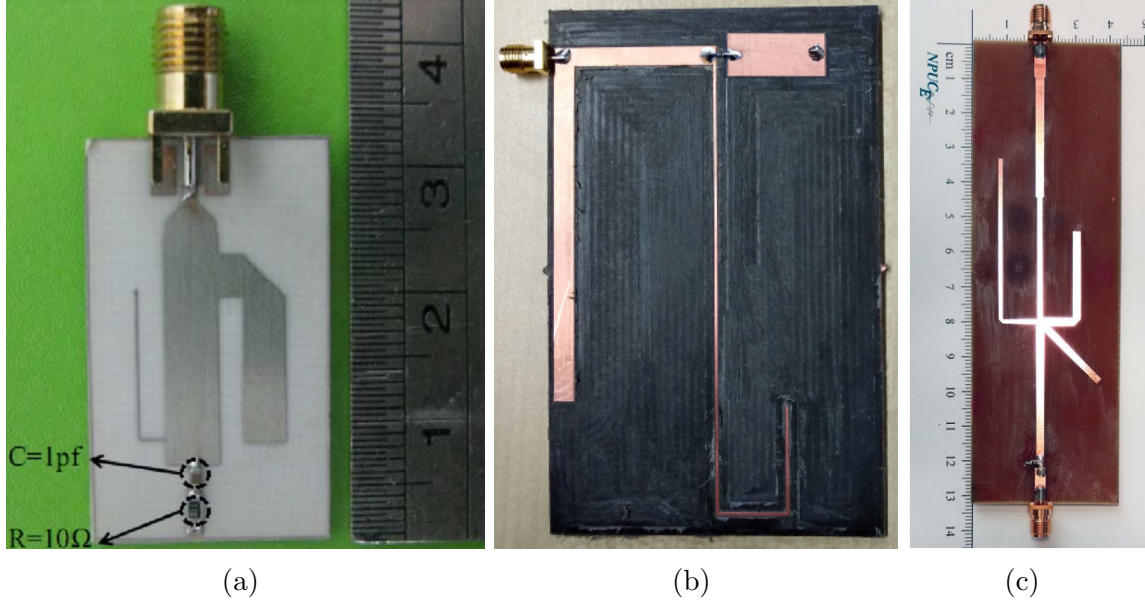


Figure 2.9: Dual-band matching network designs. (a) π -network model designed to operate at 2.4 GHz and 3.6 GHz. Reproduced from [84] ©2015 IEEE. (b) Another π -network model operating at 1.0 GHz and 1.8 GHz. Reproduced from [83] ©2018 IEEE. (c) Three-stub model operating at 0.9 GHz and 1.5 GHz. Reproduced from [85] ©2017 IEEE.

circuits [94]. Tri-band [95, 96] and quad-band [97] matching networks have also been proposed with microstrip implementation, typically involving large, multi-section circuits, but analysis in these cases is complicated or impossible for loads that are not purely real. A versatile matching network for n frequency bands, requiring n capacitors and n inductors, is presented in [98]. These networks have limitations on possible operating frequencies and suffer from other drawbacks such as narrow bandwidths or large footprints.

Another method inserts varactors into multi-stub systems to allow tuning over a wide frequency range [99], which is an active method but allows frequency-agile impedance matching. Active approaches can improve bandwidth drastically, but generally will not be focused on in this work.

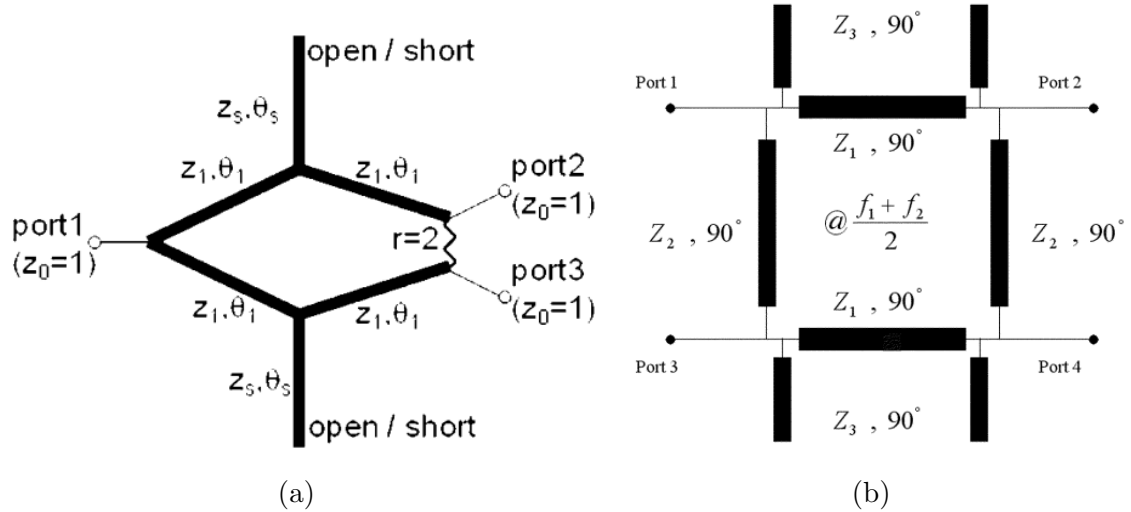


Figure 2.10: Circuit models of various dual-band power dividers and couplers. (a) Dual-band WPD circuit using T-network quarter-wave branches. Reproduced from [100] ©2008 IEEE. (b) Dual-band branch-line coupler employing π -network transmission lines. Reproduced from [111] ©2004 IEEE.

2.2.3 Power Dividers and Couplers

Various configurations of power dividers and combiners have been designed, each with different benefits and drawbacks. The WPD is one such 3-port device that relies on quarter-wavelength TL segments and a lumped resistor to ensure matching at all ports and isolation of the output ports [56]. It can be rendered dual-band through the inclusion of printed stubs in a T-configuration [100] (shown in Fig. 2.10a) or by combining stubs with a multi-section approach [101], where limits on possible frequency ratios apply. Other designs employ lumped surface-mount elements in combination with printed geometries, the operation of which is predicted with even/odd mode analysis and preserves the intended input impedance and isolation at all operating frequencies [102, 103]. Altering the port placement in a T-network [104], coupling TL segments within a device [105–107], using filter elements with appropriate dual-band phase [108], applying coupled stepped-impedance resonators [109], and exploiting signal interference along multiple distinct branches [110] are other means of producing a multi-band response.

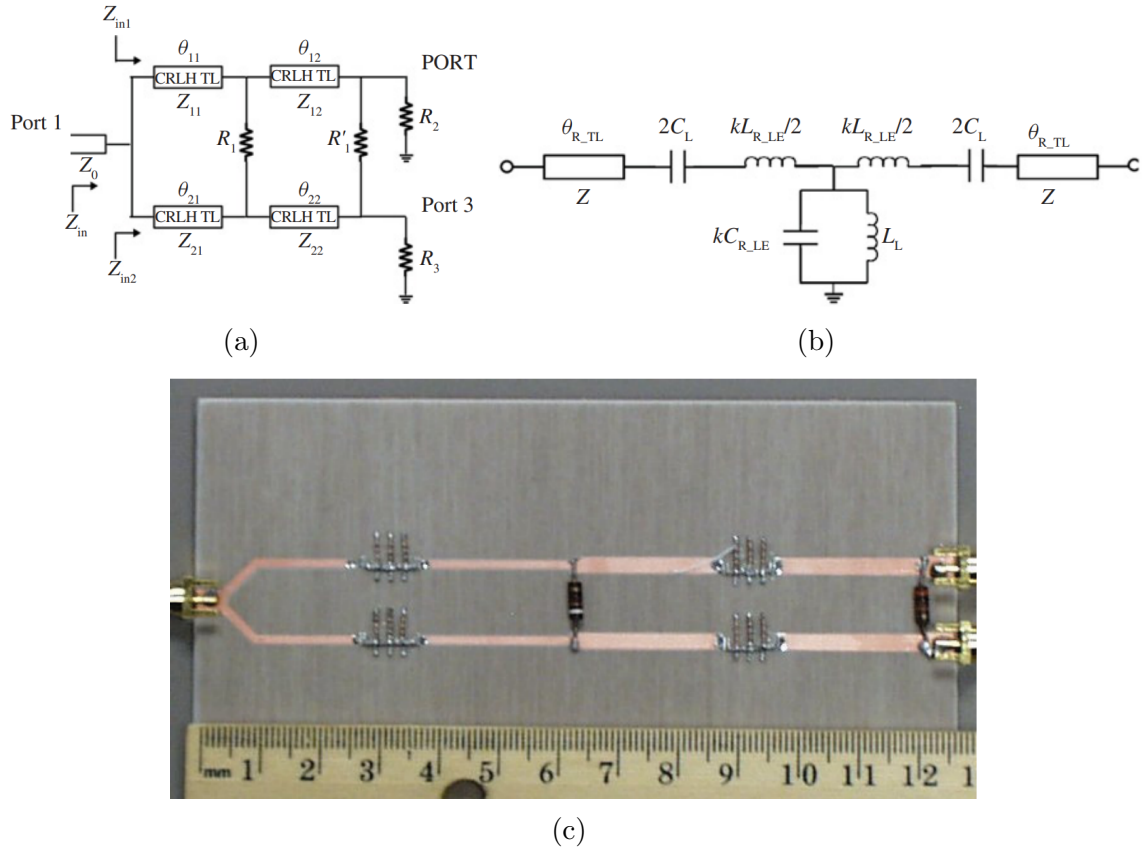


Figure 2.11: WPD design using CRLH TLs. (a) Proposed circuit for dual- or tri-band operation. (b) CRLH circuit used in the WPD. (c) Fabricated dual-band WPD for operation at 0.7 GHz and 1.5 GHz. All reproduced from [123] ©2011 IEEE.

Similar methods are used to render directional couplers dual-band by augmenting them with reactive elements in various configurations, with circuit analysis again used to develop appropriate design equations. Despite containing four quarter wavelength branches rather than two, π -networks [111–114], T-networks [115] (Fig. 2.10b), port extensions [116], stepped-impedance sections, [117], resonators [118, 119], and coupled branches [120] and TL segments [121, 122] have all been used to generate multi-band operation. These varied methods create the same phase condition at two uncorrelated frequencies for operation comparable to conventional devices, with some allowing the choice of important properties like bandwidth in each band, while others aim to simultaneously provide miniaturization.

MTM-based structures and principles have been used to enhance coupler and power

divider operation in many instances. MTM elements or resonators such as SRR and CSRR are often used to miniaturize couplers [124] or improve performance [125]; they may also enable dual-band operation by acting as CRLH materials away from resonance at the expense of limited bandwidth or increased insertion losses [53, 126]. Many other NRI or CRLH TL structures have been implemented in power dividers and combiners, but their unique geometries are generally not conducive to completely uniplanar implementations, resulting in more complex fabrication. Despite this, they often produce good performance over multiple bands and compact sizes. For example, an NRI TL with various printed and chip components takes a dispersion-engineering approach to achieve quad-band matching in [127], while other quad-band couplers are proposed in [128]. An example of circuit design using CRLH methods is shown in Fig. 2.11, which shows the equivalent circuit of the proposed structure as well as a break down of the CRLH unit cell used, before finally presenting a dual-band WPD based on this method (note that it is also used for tri-band operation) [123]. Even/odd mode analysis again extracts the properties of this circuit to create useful design equations. Further examples of MTM-based TLs show the design variability that is possible with this approach [81, 82].

2.3 Multi-Band Antennas

2.3.1 Traditional Designs

As the worldwide reliance on RF/microwave communication systems continues to rapidly increase, the need for smaller and multi-functional antennas correspondingly grows. Multi-resonant antennas are developed for a wide variety of applications, such as software-defined radio or multiple-input and multiple-output (MIMO) systems. Operation in multiple bands can be used to meet a variety of radio protocols simultaneously, while the use of orthogonal polarizations at the same frequency can increase channel capacity and combat the problem of multipath fading. Combined with the

fact that antennas are often the largest components of a system, improving antennas while maintaining a compact footprint is crucial to the development of modern communication infrastructure.

Creating multi-band antennas is generally more complex than creating multi-band circuits since there are many different figures of merit to consider. While most circuit components are characterized by S -parameters (from which conductor and dielectric loss can also be extracted), antennas have to consider excitation method as well as radiation patterns, including properties such as gain, antenna efficiency, polarization, and side lobe levels. These properties are sensitive not only to the antenna structure, but to the surrounding environment (including ground planes), antenna shape and size, and the resonant mode that is excited. They also have well-known trade-offs between impedance bandwidth, size, and gain [11]. There are a few more factors to consider in the design of multi-band antennas, and they will be considered with particular attention to planar structures once again, specifically microstrip patch antennas which are increasingly required for cellular communication, WLAN, GPS, automotive radar, and 5G applications. Some methods that will be considered to render them dual-band include the implementation of reactive loading, the use of slots or stubs, adding parasitic or stacked elements, or using embedded MTMs [129–131]. These methods will be investigated below.

Early multi-banding efforts introduced “stacked” patches [132], in which patches of different sizes are layered vertically with each underlying layer serving as the effective ground plane to the above patch, and each of which may be directly or parasitically excited. An example of this is a stacked and proximity-fed GPS antenna, shown in Fig. 2.12, designed to cover three GPS bands [133]. This particular patch was designed with a minimum 0 dB gain requirement for all bands, but suffers from poor matching and realized gain as a result.

A simpler arrangement involves parasitically exciting adjacent patches [134], allowing for a single-layer design; however, the parasitic coupling was found to be much

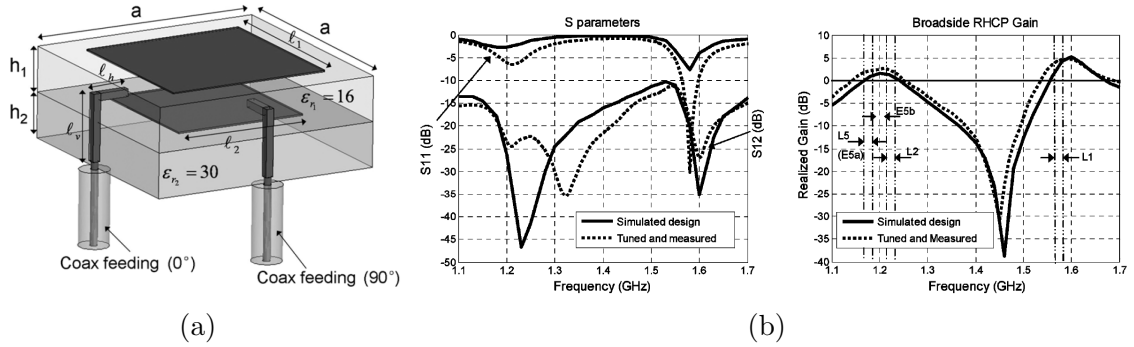


Figure 2.12: Multi-band stacked GPS antenna. (a) Structure; (b) reported S -parameters and broadside gain. Both reproduced from [133] ©2007 IEEE.

less effective in this orientation as compared to the stacked version. Exciting various cavity modes on asymmetric patches has been used [135], although this technique inherently requires that the excited modes have different field profiles, polarizations, and possibly different feeding mechanisms.

Many multi-band microstrip patch antennas are created simply by altering the patch topology [129, 136]. A popular method of exciting various modes in a fully planar structure employs slots etched into the patch or ground plane, but such approaches tend to be empirical and are, therefore, ill-equipped for systematic design [137–141]. Other designs employ loading with non-planar components such as vias [142, 143] while others, particularly those using frequency-dependent dispersive properties, achieve multi-band operation through the excitation of a number of different resonances [144–149]. These behaviours tend to come at the expense of some of the antenna properties, including gain and polarization purity. Moreover, the radiation patterns of these antennas do not typically resemble those of the fundamental patch mode for all radiating frequencies.

2.3.2 Multi-Band Antennas With Mixed Polarization

Antennas in the previous section tended to have the same polarization at all operating bands, but various combinations of antennas with multiple bands and mixed polarizations are possible. Fig. 2.13 depicts possible antenna configurations that produce such

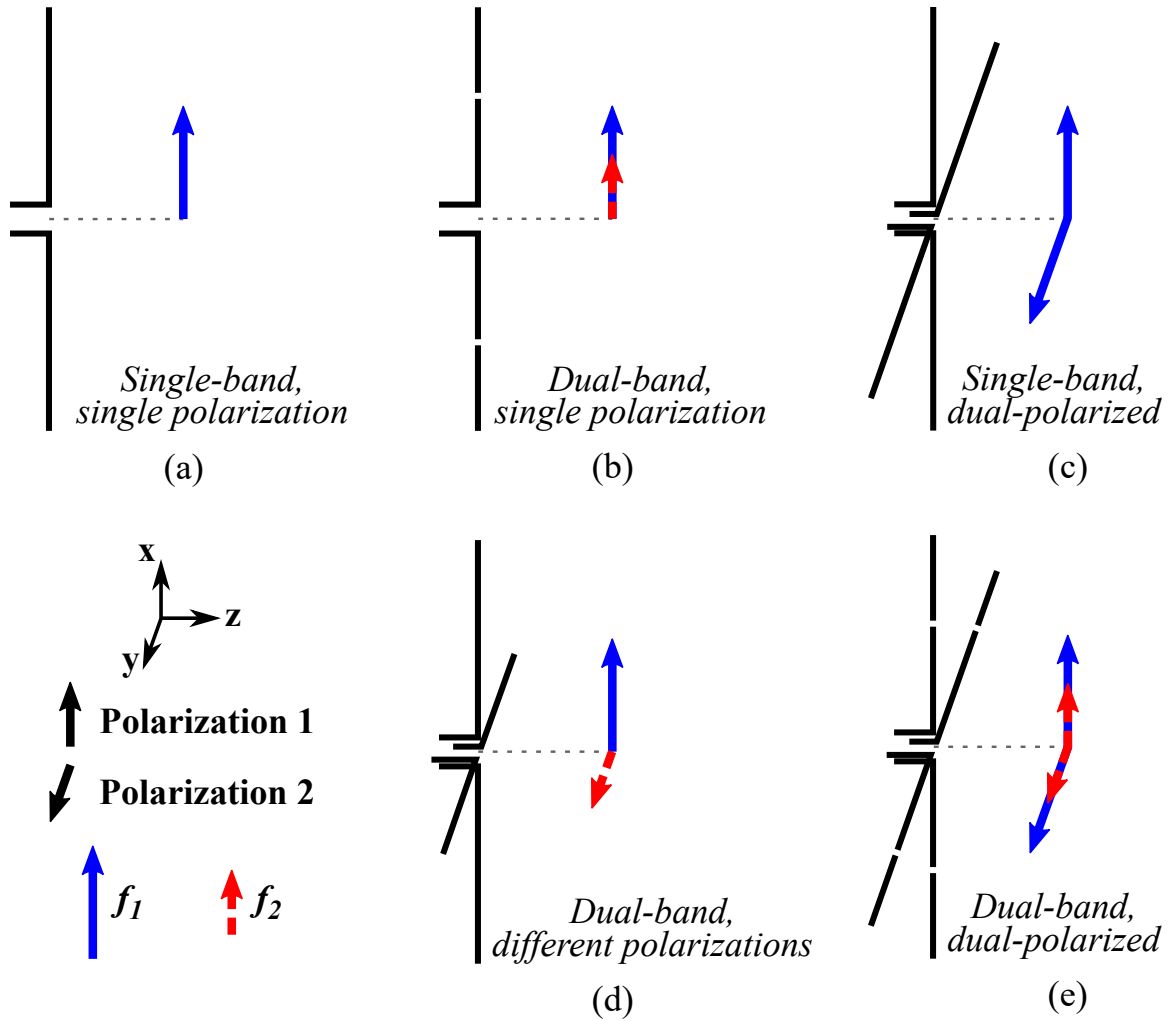


Figure 2.13: Representative diagrams of arbitrary antennas depicting their radiated far-field frequencies and polarizations. Note that each of Polarization 1 and 2 may be linear or circular, depending on antenna geometry.

varied operation (the previous section only considered antennas with the properties of Fig. 2.13b). Although the image schematically illustrates this with topologies resembling a dipole or crossed-dipole, this is intended to represent any possible antenna (wire, planar, etc.) that can be rendered multi-band or dual-polarized. Any frequencies may be represented by f_1 and f_2 , and polarizations 1 and 2 could indicate different linear polarizations, different circular polarizations, or a combination of the two. Regardless, this figure illustrates what is meant when referring to single-/dual-band and single-/dual-polarized antenna operation. Fig. 2.13 depicts dual-band operation, but the same concepts apply to antennas operating at even more frequencies, so the term “multi-band” will generally be used in place of “dual-band” for greater generality.

Antennas operating with multiple polarizations [Figs. 2.13(c)-(e)] may use a single feed to excite both polarizations, but they often require two independent feeds to provide the required excitations, which correspondingly separates the signal based on polarization (this also renders port isolation an important figure of merit). The implementation of multiple isolated feeds can be quite structurally complex [150, 151], although this is not always the case [152]. Antennas that operate with different polarizations in different bands (Fig. 2.13d) have been created in several ways [153–156], but these are typically not as highly sought after due to the aforementioned need for most antennas to operate with the same polarization for all resonances.

Multi-band antennas with different polarizations support one resonance at each frequency (Fig. 2.13d), but a more complicated class of antennas are simultaneously multi-band *and* dual-polarized, effectively supporting two resonances per operating frequency (Fig. 2.13e). The added functionality generally means that these antennas are more complex, but they also allow systems such as MIMO to operate efficiently over several channels. Any two modes may be excited at each frequency (although ideally all radiation would be the result of two similar orthogonal modes at each frequency, giving all bands and polarizations similar properties) and multiple feeds will typically be required, with one feed to either excite two polarizations at a single

frequency, or two frequencies for a single polarization. Note that these antennas as well as antennas with a single, different polarization at each frequency are often both called multi-band, dual-polarized antennas, but that term better represents the present category, in which multiple bands and both polarizations are excited simultaneously. This is represented in Fig. 2.13, where the designation of “dual-band, dual-polarized” is used exclusively to describe Fig. 2.13e.

Similarly to traditional dual-band antennas, some of the earliest planar multi-band and dual-polarized antennas employed stacked patches [157], achieving this operation by exciting various layers through some coupling mechanism [158–160]. Stacked patches continue to be used, despite the complexity of creating these antennas and exciting all four (for the dual-band, dual-polarized case) necessary resonances [161, 162], and these antennas have been designed up to mm-wave bands for 5G applications [163]. Three-dimensional structures that protrude from the plane in which the antenna is fed are used rather than multiple layers in [164], but this and other designs suffer from relatively poor performance, necessitating the use of arrays to achieve desired radiation characteristics [165]. Other designs use AMC’s to facilitate multi-resonant radiation; for example, [166] places a two-layer bowtie structure above an AMC, while [167] does the same with a modified circular dipole. The antenna in [168] requires a frequency selective surface above several aperture-fed patches to produce an overall dual-band, dual-polarized response. Other designs produce multiple resonances through the excitation of higher-order modes, which significantly affects pattern shape. This is observed in the dielectric resonator antenna in [169], while different modes of a planar structure are excited in [170]. These designs achieve dual-band and dual-polarized operation, but at the cost of increased complexity and often poor radiation characteristics in portions of the operating bands.

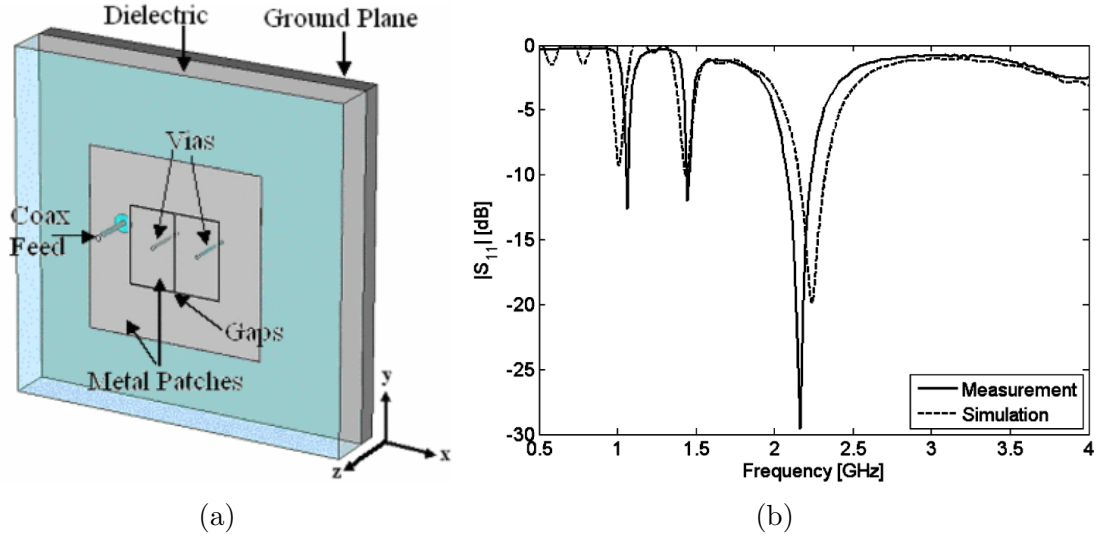


Figure 2.14: Multi-band patch antenna with embedded MTM unit cells. (a) Structure, showing NRI-TL sections embedded in patch; (b) S_{11} . Both reproduced from [171] ©2008 IEEE.

2.3.3 MTM-Inspired Approaches

More recently, MTM structures have been integrated into patch designs using NRI or CRLH approaches, and are often dispersion engineered for multi-band operation [146, 148, 149, 171]. Oftentimes, various modes are excited to enable multi-band radiation and as a result, radiation patterns and gain are usually inconsistent from one band to another [146, 148, 149, 171, 172]. However, the range of applications in which MTM-based antennas are found is extensive. Consider the patch antenna shown in Fig. 2.14, which has embedded unit cells of the Sievenpiper mushroom structure in the middle of the patch. Various modes are excited with this inclusion, resulting in three operating bands. The usual patch mode ($n = 1$) occurs at the highest frequency of 2.16 GHz and performs well, while the other modes ($n = -1$ with left-handed performance in the MTM region at 1.06 GHz and a monopolar $n = 0$ mode at 1.45 GHz) show reduced efficiency and gain [171].

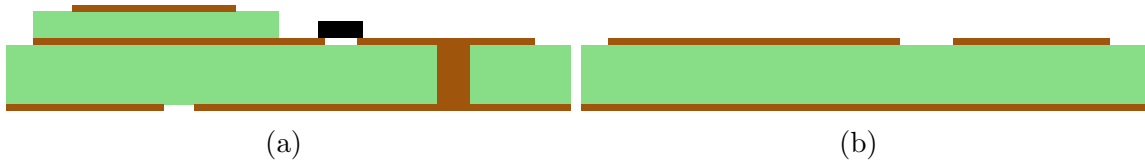


Figure 2.15: Circuit board cross-sections. (a) Common fabrication challenges include vias, lumped components that require soldering, multi-layer boards, and ground plane patterning. (b) Simple circuit board consisting of a patterned upper layer over a solid ground plane.

2.4 Challenges of Multi-Band Design

2.4.1 Layout and Fabrication

While multi-band circuits clearly provide an important function, they have some disadvantages as well. Some of these have been alluded to in reference to specific works, but they will be summarized briefly here.

Most canonical microstrip-based devices are uniplanar, consisting of a series of microstrip lines with specified lengths and widths (or characteristic impedances) above a uniform ground plane. It is advantageous to preserve uniplanarity, and many multi-band structures do this, although typically by forming a larger footprint overall, through the inclusion of stubs or multi-section TLs. Furthermore, these may require extreme impedances as well, resulting in inconvenient or impossible microstrip widths. The same problem can exist for planar resonators, since resonator sizes are functions of wavelength, and it tends to take extreme feature sizes to shrink them down.

Compactness can be preserved through the addition of lumped circuit components including surface-mount capacitors and inductors. This is particularly true for NRI or CRLH materials, which require sub-wavelength reactive loading. These increase the cost of a circuit and require an additional fabrication step to solder them in place, and they are generally only suitable for use in the sub-6 GHz regime, as many become self-resonant above this frequency range.

Even more difficult to fabricate are vias, which require drilling and through-hole plating (or the addition of metallic posts) and drastically increase production costs.

These circuits are no longer considered purely uniplanar, and similar costs are associated with other multi-layer fabrication techniques. The use of multiple substrates requires bonding of the layers and alignment of all features, and increases the material costs. While many useful multi-layer devices exist and are used in industry, production on a single layer presents significant fabrication and financial advantages.

Many of these physical challenges that increase fabrication cost and complexity are illustrated by a circuit board cross-section in Fig. 2.15a. Ideally, a circuit board would contain as few of these features as possible; Fig. 2.15b illustrates the relative simplicity of a board that only requires patterning of a single metallization layer. Other challenges that can arise are the use of air dielectrics or superstrates that require the suspension of one layer a precise height above another, or the fabrication of extremely fine features (for example, strips or gaps that are fractions of a mm in size) that are difficult to realize with conventional fabrication methods.

2.4.2 Design Considerations

Many of the matching networks and power dividers propose a circuit layout and develop design equations, then solve the equations for a particular set of frequencies or conditions. This is certainly useful in the design of any particular multi-band component, but lacks generality for use in other structures or circumstances. Furthermore, the design equations may be based on simplistic circuit models, missing some aspect of its operation such as parasitics, and a large amount of tuning may subsequently be required as a result.

Generality is better achieved for designs where a TL segment may be replaced by a multi-band counterpart, since the multi-banding technique is independent of circuit component. While very useful, this method presents the challenge that the circuit solutions may be physically difficult to realize, for example, in cases where large features or extreme TL impedances are needed. Some circuit models are devised with this in mind but it typically places limitations on the circuit properties, such as

on the ratio of operating frequencies that can be chosen.

Accuracy of such models is also important, since poor models require a large amount of tuning that can be time-consuming to complete. On the other hand, modeling every possible parasitic reactance, junction effect, and so on can, in many cases, render models overly complicated. A balance between accuracy (to limit tuning) and simplicity should be found, although increasing available computational power means means that accuracy is often favoured.

It is important to note that multi-band devices are rarely used in isolation, and often interface with other devices or systems. Multi-band operation requires that all individual components within the system are capable of operating in all bands. Diplexers can be used to separate signals first, but then a separate circuit is needed for each band; instead, rendering the entire system multi-band significantly reduces the number of components needed. This does, however, complicate implementation, first of all because several more complicated devices must interact, but also because there is generally not one best method with which to render different devices multi-band. Several techniques may be required to form a full multi-band system.

2.4.3 Performance

Multi-band devices are designed with the specific goal of enabling simultaneous operation at different frequency bands or for multiple applications of interest, but this may come at the expense of in-band performance. Many such devices introduce additional dissipative losses through the use of lumped circuit elements or resonators, which directly affects insertion and return loss levels. Replacing existing TL segments with multi-band versions also poses challenges such as maintaining impedance matching in the modified segment.

Antennas in particular can suffer from drawbacks including poor multi-band matching or gain, or drastically different operation in each frequency band. The latter may be intentional if a different application is demanded at each frequency, but typically

it is desirable to operate similarly across the spectrum.

A major drawback of most multi-band structures, particularly those that use MTM-based elements due to their typically dispersive nature, is bandwidth. Devices employing resonators with a high quality factor suffer similarly. This can be remediated with multi-resonant structures that merge narrowband responses into one usable band, but not every implementation is amenable to this method. For this reason, required bandwidth must be considered when choosing the multi-banding technology to employ.

For antennas, bandwidth often becomes an even more difficult constraint. Any reduction in antenna size fundamentally limits antenna impedance bandwidth [10], and many multi-band structures are based on size-reducing MTM structures, or have multiple resonances that do not each span the full antenna size. That being said, many structures intentionally aim for increased bandwidth and successfully achieve that end, but typically with a trade-off such as gain.

Methods have been developed to improve antenna bandwidth. The first thing to consider is the effect of the substrate. For planar patch antennas, increasing substrate height and reducing the effective dielectric constant both increase bandwidth [131, 173, 174], so while patches with air dielectrics may pose serious fabrication challenges, they are also better suited to applications where bandwidth is crucial. Related to this is the trade-off between antenna size and bandwidth, which trend in the same direction. Bandwidth can also be increased by choice of feed mechanism (aperture feeds produce the largest bandwidth over a single band, but are not well-suited to multi-band feeding) and impedance matching techniques [175]. Note that maximum antenna bandwidth does not occur with a perfect match to an antenna, but rather when the quality factor is slightly reduced [175]. Active circuits provide other means of increasing bandwidth that will not be explored further here [176, 177]. These considerations will be discussed in further detail in Chapter 5.

In some cases, reduced bandwidth (or increased selectivity) can be an advantage;

for example, this could be viewed as embedded filtering in an antenna. Even narrowband antennas still typically have to meet a minimum channel bandwidth to communicate with a given standard.

As with any microwave device, there are a number of other considerations that these multi-band circuits and antennas deal variably well with. Considerations such as sensitivity and tolerance to error, power handling capability, passive intermodulation, and integration with all front- or back-end passive and active components are all important parts of system design, and different components are optimized for different outcomes. While some designs undoubtedly operate better than others, an engineer is ultimately responsible for finding the appropriate trade-offs to meet as many of their system requirements as possible.

Chapter 3

The MTM-EBG

3.1 Development

3.1.1 TL-MTM Models

3.1.1.1 2-Conductor Models

The general approach to describe TL-MTMs is to view them as loaded, 2-conductor TLs. Consider the prototypical NRI TL, which consists of series capacitors and shunt inductors, the dual of a standard TL. This model is useful for simple loading of a one-dimensional transmission line and analytically expresses novel MTM properties. CRLH TLs, which generally include capacitors and inductors in both series and shunt (or high-pass and low-pass) configurations, are similarly described with 2-conductor models, often as standard transmission lines periodically loaded with reactive elements.

These models are extremely useful, and have shown great success in analyzing TL-MTMs. They can be used to predict dispersion properties and formulate effective medium models, and successfully enable the design of complex and novel devices. Simple circuit models enable easy analysis, whether it be for periodic structures or for single unit cells. However, the simple circuit models used generally describe simple structures. The Sievenpiper structure, for example, is a basic case of series capacitors and shunt inductors, but what happens if several reactive components are included in the top layer, or a more complex geometry is used, such as the stacked mushroom

structure in [178]? Similarly, no accurate 2-conductor TL model exists to describe the uniplanar compact EBG (UC-EBG) over more than a small frequency band [46, 179]. These limitations are not easy to address with these circuit models alone.

3.1.1.2 MTL Approach

While the 2-conductor transmission line is the standard model for most systems and in many cases provides an excellent approximation, it remains a special case of MTL theory, which generalizes TL theory to a system of N conductors [17]. The MTL approach has traditionally been used for purposes such as wire cross-talk and in devices such as the couplers [180], but it generally provides a means of describing complex, multi-conductor systems using a formulation similar to TL theory but in a matrix form. Using this approach to model MTMs is a recent development that has not been highly exploited to date, despite the great insights that it provides [2, 15].

There are several implications to using an MTL formulation, one of which is that it supports $N - 1$ independent transverse electromagnetic (TEM) modes. Each mode has an associated propagation constant and characteristic impedance, and modes may couple in cases where the field distributions are similar and they are phase-matched. Independent modes may have different wave velocities, and their combination forms a basis set describing the total voltages, currents, and fields in an MTL system. MTL theory rigorously describes these properties and interactions, and provides a more complete picture of dispersion properties in MTL systems than 2-conductor theories can.

This theory is useful in systems with complex geometries where several independent conductors are present and/or interconnected. TL-MTMs such as the shielded Sievenpiper structure have been described with MTL theory with great success [33, 181], which suggests that other structures can be described with the same approach.

Two domains are used when working with MTL structures: the terminal domain, which describes voltages and currents on the several different conductors indepen-

dently, and the modal domain, in which TEM modes (each of which has a unique propagation constant) are described. The two different descriptions of the MTL ultimately describe the same phenomena, and diagonalization procedures for the matrices involved allow for the conversion from one domain to the other [17]. Generally, this work will focus on the modal domain since bandgap properties in regard to specific modes are required. This is, again, a key property of MTL analysis: modal coupling and phase properties are critical to understanding propagation in these systems, and traditional 2-conductor TL theory is unable to capture these details, despite its relevance to many systems.

The MTM-EBG is such a structure that does not lend itself to 2-conductor analysis, and it has been shown extensively that MTL analysis can produce a detailed and accurate dispersion diagram, accounting for all modes, all coupling between modes, and bandgap locations that result [1, 2, 182]. This thesis does not attempt to develop fundamentally new analysis tools for the MTM-EBG since it has already been done in great detail, and with great accuracy; however, it does intend to expand on the function and use of the MTM-EBG, as analyzed in this way. Key results from previous works will be summarized in this chapter for the sake of completeness, but special focus will be taken on interpreting how the resulting structures can be used practically, and what tools can help verify operation and simplify the design procedure. Application considerations tend to outweigh theoretical rigor when using the MTM-EBG (for example, more interest is taken in the properties of a single unit cell than of the properties of an infinite cascade of unit cells), with the intent of providing maximum utility to designers of multi-band or unique circuit elements and antennas. Regardless, a theoretical basis is required to appreciate and understand operating principles of the MTM-EBG, so a brief background will first be provided.

3.1.2 MTM-EBG Design

3.1.2.1 Nomenclature

The MTM-EBG is the particular structure on which this thesis is based, the reasons for which will be developed throughout the course of this chapter. Considering the perspective taken that EBGs in the microwave region are simply a class of MTMs with a particular function, this name merits further explanation. The MTM part comes from the fact that TL-MTM principles are explicitly used to conceptualize and design the structure; concepts such as left-handed or backwards wave propagation are used to describe its operation, and properties including a negative index of refraction can be discussed in this context [1]. While this work will avoid an overly rigorous discussion of these concepts in the interest of taking a more application-based approach to the MTM-EBG, they remain essential to its conception and analytical modeling of its operation. Many of these details can be found in previous work by S. Barth [1, 2, 182].

The second half of the name stresses functionality. Based on MTM principles, this structure presents a strong bandgap to a mode of interest, and hence acts as an EBG. It differs from many EBGs in that it does not have to be periodic to provide a bandgap, it is not resonant at frequencies of operation, and simple TL-based circuit models cannot accurately capture its full dispersion properties. However, its bandgap properties are explicitly used to render devices multi-band, and this is explicitly reflected in the name of the structure.

3.1.2.2 Properties

The goal of this work is to implement MTM-EBG unit cells into planar devices to improve their performance, specifically by making them multi-band. The MTM-EBG is an ideal structure to achieve this for several reasons.

Firstly, it is capable of interacting with microstrip or parallel-plate waveguide (PPW) modes, which is critical for use in microstrip-based circuit elements and patch

antennas, which support similar transverse field profiles. The MTM-EBG can then be embedded directly into these devices without taking up any additional space on the circuit board. This requires a high degree of compactness, which implies that the MTM-EBG must also be electrically small since many devices contain quarter- or half-wavelength electrical lengths into which the MTM-EBG must be placed. The MTM-EBG must be far smaller than the guided wavelength to be implemented in this compact area and enable the same amount of phase to be incurred at different frequencies. It must also be small in the direction transverse to propagation in order to be embedded into microstrip TLs.

The properties of the MTM-EBG must be well known for it to be applied to a wide range of devices. Bandgap and phase properties are important for different designs, and both properties must be finely tuned in order to achieve operation at the intended frequencies. For devices where operating frequencies are widely spaced, its frequency response must be predictable over a wide frequency range.

Finally, the MTM-EBG has a simple structure that allows inexpensive and easy implementation with various fabrication methods. It is uniplanar and via-less to simplify construction, and the use of discrete lumped loading components can also be avoided so that the structure is fully printed, meaning that fabrication can be completed in a single step that is no more complicated than printing any conventional device in the same way.

How the MTM-EBG was designed to have these properties and specifics of its operation will be discussed throughout this chapter. First introduced by Barth and Iyer in [2] and developed further in several subsequent works [1, 182], it has since been shown to be a one-dimensional version of the UC-EBG [46, 183], which can also be analyzed as an MTL structure supporting several modes. This work will focus specifically on the one-dimensional MTM-EBG, however, since its properties are sufficiently useful to render a wide range of devices multi-band. Its structure contains a well-developed theory and richness of application to merit its own extensive

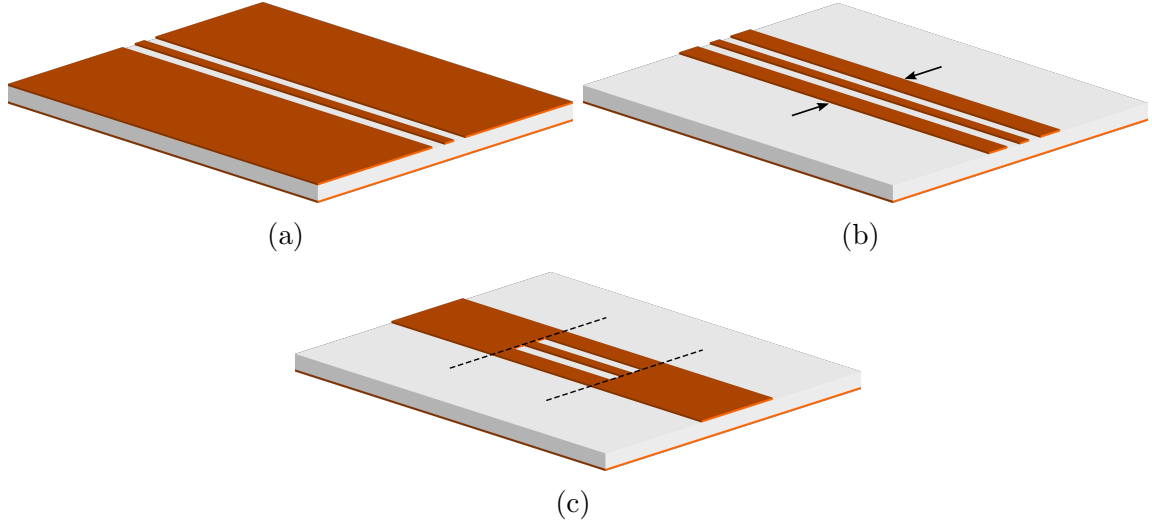


Figure 3.1: (a) CBCPW TL. (b) Truncated CBCPW. (c) Truncated CBCPW embedded in a microstrip TL.

investigation in this thesis.

3.1.2.3 Host Medium

A host medium describes an unloaded MTL, which is presently assumed to be infinite in length along the direction of propagation, with electrically small gaps in between adjacent conductors, similar to a 2-conductor transmission line. The host medium in this case is chosen to be the conductor-backed coplanar waveguide (CBCPW) for an important reason: it consists of three uniplanar conductors above a solid ground plane, as shown in Fig. 3.1a in a printed configuration (any low-loss substrate may be used between the upper and lower layers). Not only does this allow for simple fabrication on standard substrates, but it also allows the MTL to be easily embedded into other simple 2-conductor TLs, such as the PPW or microstrip TL. The process of embedding into the latter is illustrated in Fig. 3.1; the CBCPW must first be truncated to the width of the microstrip, and a finite-length section can be interfaced between input and output lines. The utility of this will be discussed in detail throughout this work.

An MTL consisting of N conductors generally supports $N - 1$ TEM (or quasi-TEM if the substrate is inhomogeneous) modes. The CBCPW MTL therefore supports

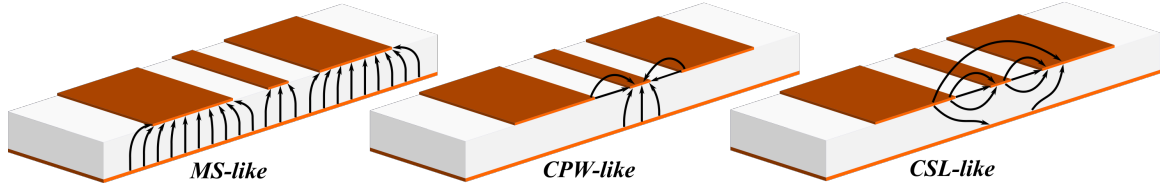


Figure 3.2: Depiction of electric-field lines of the three TEM modes supported by the CBCPW MTL (microstrip-like, CPW-like, and CSL-like). Reproduced from [184] ©2020 IEEE.

three quasi-TEM modes, the field distributions of which are shown in Fig. 3.2. Two modes are primarily of interest: the CBCPW mode, which is characterized by a potential on the central strip conductor (2) while all others (0, 1, and 3) are effective grounds, and a PPW mode, where all three upper conductors (1, 2, and 3) are equipotential, and the conductor backing (0) is the ground. The third supported mode is a coupled slotline (CSL) mode, but this exhibits odd symmetry around the central strip (different potentials on conductors 1 and 3), and as a result is neither excited in the applications in this work nor couples with the other “even” modes, and so does not need to be discussed further here.

Scattering allows even modes to couple when they are phase-matched since they have similar field distributions around conductor 2. This important property is naturally described with MTL theory, but some form of loading or discontinuity is required to enable such scattering and provide interesting and useful dispersion properties. The chosen loading scheme with this host medium gives insight into the origin of the MTM-EBG, and is critical to how it ultimately operates.

A section of the truncated CBCPW is presented in Fig. 3.3a, with the constituent conductors labeled from zero (reference conductor) to three. The MTM-EBG is based on this host medium partially due to one important property: all reactive loading can occur between the top three conductors, *in a single plane*. Consider the loading configuration shown in Fig. 3.3b (for which the host medium section is assumed to be periodic or embedded in a 2-conductor TL, where the capacitors will be terminated in series to another conductor rather than simply remaining open-circuited). Since all

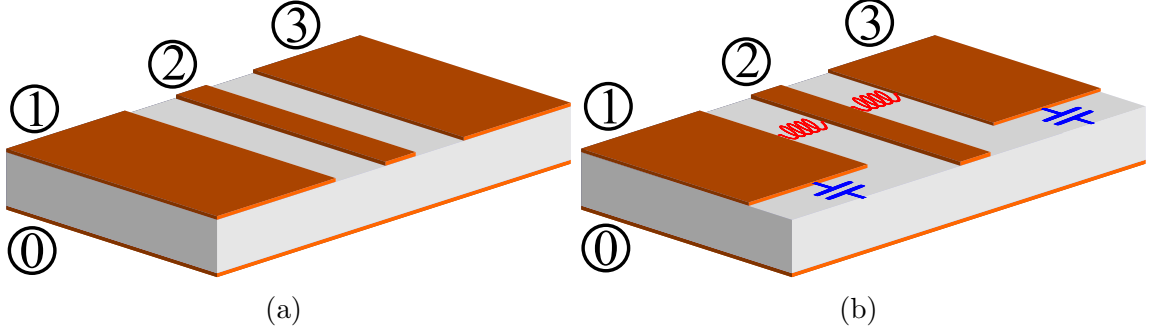


Figure 3.3: (a) CBCPW host medium, and (b) host medium loaded with inductors and capacitors to form an MTM-EBG unit cell. The four constituent conductors that form the MTL model of this unit cell are labeled. Reproduced from [185] ©2021 IEEE.

loading lies in the upper plane, fabrication is greatly simplified; expensive components such as vias or complex multi-layered configurations are not required to realize this structure.

3.1.2.4 Loading

While the host medium is continuous in the direction of propagation, periodic loading affects the dispersion properties of the overall structure. A periodic arrangement of a unit cell with the particular loading scheme presented in Fig. 3.3b is considered to be the MTM-EBG. Specifically, this is the one-dimensional MTM-EBG since interest is only taken in propagation along the direction perpendicular to a cross-section of the host medium. Note that a two-dimensional version of the MTM-EBG is the UC-EBG [46, 183].

Loading of the MTM-EBG is inspired by MTM principles, so to achieve left-handed/backwards-wave operation, a TL-MTM requires shunt inductive and series capacitive loading. For an MTL structure, however, not all propagating modes will necessarily be loaded equally, so the loading should be discussed with respect to propagating modes. Consider the loading scheme in Fig. 3.3b, where inductors bridge across from conductor 2 to conductors 1 and 3, and capacitors are placed in series in conductors 1 and 3. The first even mode to consider is the microstrip-like or PPW

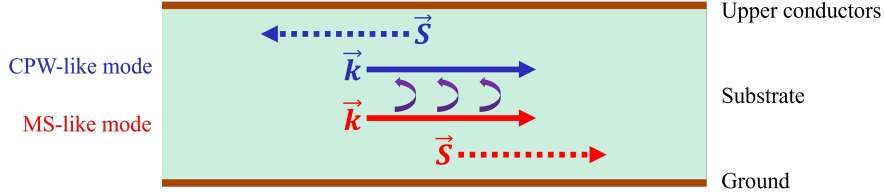


Figure 3.4: Illustration of contradirectional coupling between a forward PPW mode and a backward CPW mode within an MTL.

mode, in which conductors 1, 2, and 3 are equipotential. The inductors will have no effect on this mode since no current flows through them. The capacitors will have some effect on propagation (e.g., reduce phase velocity) but conductor 2 remains electrically connected so a low-frequency cutoff is not anticipated, and backward-wave propagation cannot be achieved.

Consider this loading scheme in the context of the CPW-like mode. In this case, conductors 1 and 3 are considered grounds along with conductor 0, so the inductors act as shunt elements to ground. Combined with series capacitors, MTM-like loading is obtained, and backwards-wave propagation is expected over some frequency range. This implies that the direction of power flow for the CPW mode in this range is anti-parallel to direction in which phase is incurred.

Where the forward PPW-like mode and the backward CPW-like mode are phase-matched, contradirectional coupling will occur, as illustrated in Fig. 3.4. This is observed as a reflection of power, resulting in strongly suppressed forward power flow over the length of a unit cell. A strong bandgap response in the coupled-mode system is thus produced, consisting of both complex-mode and evanescent frequency regions, where propagation is strongly reactively attenuated. Geometric features and loading values of the unit cell determine the precise position and size of the bandgap, with loading being the most important attribute to enable this functionality. Dispersion engineering is required in the coupled-mode system so that the isolated modes interact to produce a bandgap in a predictable frequency range, and the phase response over the rest of the spectrum should be predicted as well. This particular loading scheme

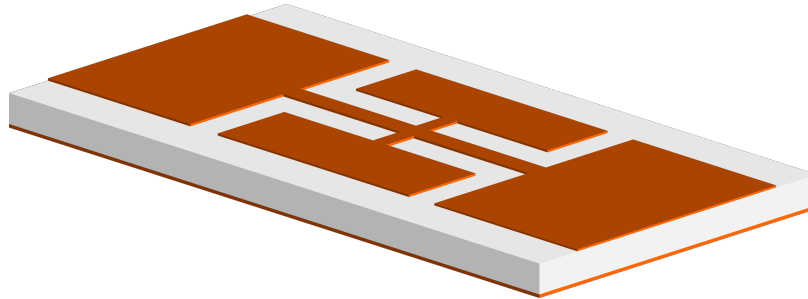


Figure 3.5: Basic fully-printed MTM-EBG unit cell embedded in microstrip.

is also critical to a uniplanar design, since loading the CPW mode rather than the PPW is what allows all loading to be achieved in the top metallization layer of the MTL.

Loading of the MTM-EBG unit cell in this scheme may be physically realized in various ways. Capacitors can take various forms, the most basic of which is a lumped chip capacitor that can be placed across a capacitive gap; similarly, chip inductors can be used, though their values are more limited. This requires chip components to be soldered into place, which is typical of many circuits but has some drawbacks. Lumped components increase costs, they complicate the fabrication procedure, and their maximum operating frequencies are constrained by their self-resonance frequencies (typically several GHz). To mitigate these drawbacks, the MTM-EBG cells can be designed for minimal reactive loading to enable the use of fully printed lumped elements, such as strip inductors and gap capacitors. This creates a unit cell that is completely printable as in Fig. 3.5, shown embedded in a microstrip TL for simplicity even though several unit cells could be cascaded. To realize larger reactance values more complex structures such as interdigitated or parallel-plate capacitors may be used, depending partially on fabrication methods and tolerances, but the basic overall structure will not change.

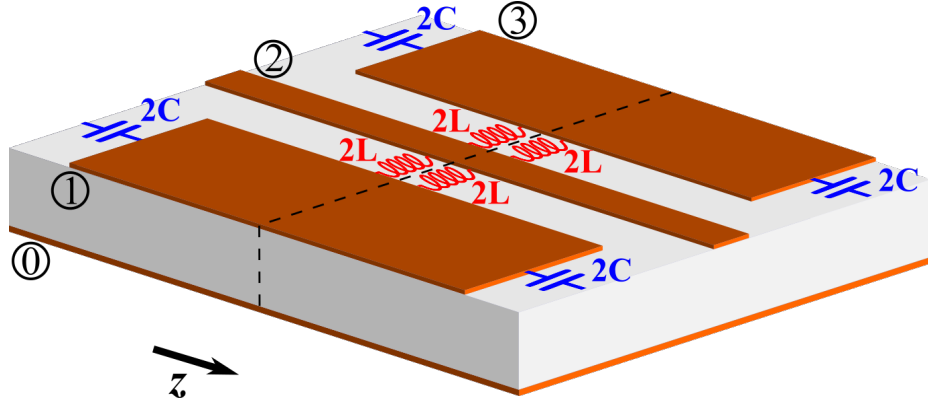


Figure 3.6: Symmetric model of MTM-EBG unit cell.

3.1.2.5 Reference Plane

It may be noticed that there is a difference between the proposed MTM-EBG unit cell in Fig. 3.3b and Fig. 3.5: symmetry. The former places capacitors on one side of the unit cell, while the latter has four gap capacitors, two on either end of the unit cell. Historically, the MTM-EBG has been presented symmetrically [1], either with inductors placed in the center of the unit cell as shown in Fig. 3.6, or shifted half a period with the capacitors nearer the center and the inductors on the unit cell edges. Loading periodic structures symmetrically is typical, and provides some advantages; for example, it is possible to predict Γ and X -points of the unit cell without a full dispersion analysis, and instead by setting boundary conditions on a half-cell [33, 186]. Furthermore, the dispersion equation of the MTM-EBG discussed below is simplified by using the symmetric structure.

It should be recognized that this does not present the most efficient practical loading scheme. It is apparent that the central inductors can be combined in parallel so that only two inductors, each with half the required inductance, are needed. This is true as well for the capacitors; in an infinite cascade of unit cells, two capacitors will be in series in conductors 1 and 3, meaning that only a single capacitor of half the capacitance could replace them. For this reason, loading values of $2L$ and $2C$ are used, so that the overall loading of the MTM-EBG unit cell in this circuit model and

the asymmetric model is the same.

Both MTM-EBG models describe identical structures, as long as an infinite cascade of unit cells are assumed. However, consider the case in which a finite number of unit cells are cascaded in the direction of propagation (z -direction). While the capacitors can be combined between adjacent unit cells, the first and last unit cell in the chain require a capacitor of $2C$. It is inconvenient to introduce a different capacitor into an otherwise uniform set, and will also be more difficult to realize in a printed manner, since twice the capacitance is required. It is therefore convenient to combine both capacitors (and inductors) into as few components as possible in the circuit model so that, upon physical realization, all implemented lumped elements will be uniform and minimized. This motivates practical consideration of the loading scheme in Fig. 3.3b, and it will be used in all realized configurations. Generally, then, a symmetric model will be used when analyzing the dispersion properties of an MTM-EBG, but an asymmetric model will be implemented in practice. An awareness of the fact that all loading values will be halved when transitioning from the symmetric model to the practical model is required.

3.2 Analysis

3.2.1 MTL Properties

3.2.1.1 Host Medium Properties

The MTM-EBG MTL equivalent circuit model is shown in Fig. 3.7, where a symmetric version of the structure is considered. Its $N = 4$ conductors are numbered, starting with zero; the zeroth conductor can be considered the reference conductor (and physically corresponds to the ground plane beneath the other three co-planar conductors). It can be broken down into six cascading segments: capacitors, host medium of length $l/2$, inductors, inductors, host medium, and capacitors. Properties of each segment can be analyzed, starting with the host medium.

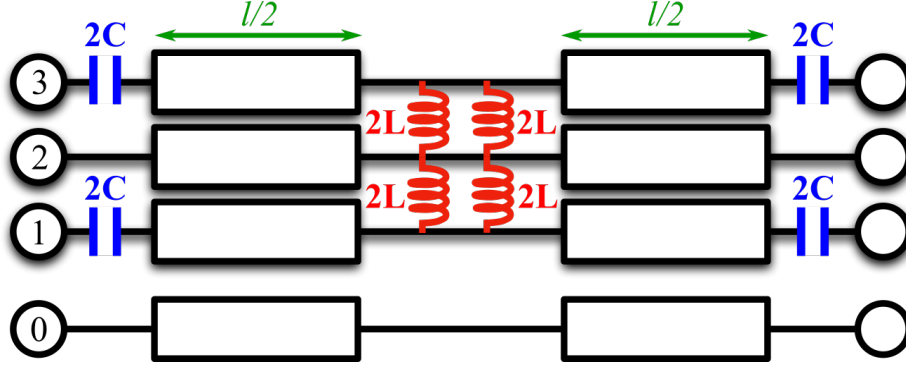


Figure 3.7: MTL circuit model of a single MTM-EBG unit cell.

Similarly to a 2-conductor TL, per-unit-length parameters can be calculated from analysis of a cross-section of the MTL, and are a function of geometry and substrate permittivity [17]. The per-unit-length matrices are used to calculate properties of the MTL, particularly propagation constants of characteristic impedances of the modes which will be found in the terminal domain; all of these matrices are of size $N - 1$. These matrices can be determined analytically in simple cases, but in practice are difficult to solve exactly, particularly for the quasi-TEM host medium that forms the MTM-EBG. Instead, numerical methods will be used to determine the propagation constant and characteristic impedance matrices of the host medium. This is done by solving the static transverse fields of the host medium, for example with a finite-element-method (FEM) solver, and producing impedance and admittance matrices in the terminal domain, $[Z]$ and $[Y]$ respectively. Then, the propagation constants and characteristic impedance matrices are determined from the relations [17]:

$$[\gamma] = ([Y][Z])^{\frac{1}{2}} \quad (3.1)$$

$$[Z_0] = [Z][\gamma]^{-1} \quad (3.2)$$

Each of these matrices can be diagonalized to transform from the *terminal domain* to the *modal domain*, which allows the propagation constants and characteristic impedances for each mode to be determined [187]. The diagonalization process involves using an eigenmode solver to determine the modal properties (e.g., the modal

propagation constants $[\gamma_M]$) along with a diagonalization matrix $[T_D]$, as it solves the equation

$$[\gamma_M] = [T_D][\gamma][T_D]^{-1} \quad (3.3)$$

The same procedure is applied to the characteristic impedance matrix, and these quantities are used to characterize the host medium.

In anticipation of the loading of the host medium, a transmission matrix (analogous to the ABCD matrix in 2-conductor TLs) is defined. It relates voltages and currents at the input terminal of the MTL to voltages and currents at the output terminal, making a square matrix of size $2(N - 1)$. The transmission matrix $[T]$ is generally defined as

$$\begin{bmatrix} \vec{V} \\ \vec{I} \end{bmatrix} = [T] \begin{bmatrix} \vec{V}' \\ \vec{I}' \end{bmatrix} = \begin{bmatrix} [A] & [B] \\ [C] & [D] \end{bmatrix} \begin{bmatrix} \vec{V}' \\ \vec{I}' \end{bmatrix} \quad (3.4)$$

where the unprimed voltage and current are defined at the input terminal and the primed voltage and current represent the output terminal (note that current is defined to travel into the input terminal, and out of the output terminal). The transmission matrix is written in the form of ABCD submatrices, each of which is a square matrix of size $N - 1$. For a segment of the host medium of length $l/2$, the transmission matrix takes the form:

$$[T_H] = \begin{bmatrix} \cosh([\gamma]l/2)^T & -[Z_0] \sinh([\gamma]l/2) \\ -\sinh([\gamma]l/2)[Z_0]^{-1} & \cosh([\gamma]l/2) \end{bmatrix} \quad (3.5)$$

Knowing the modal propagation constant and characteristic impedance matrices, this transmission matrix can be determined with the hyperbolic trigonometric terms written as [1, 17]:

$$\cosh([\gamma]l/2) = \frac{1}{2}[T_D] \left(e^{[\gamma_M]l/2} + e^{-[\gamma_M]l/2} \right) [T_D]^{-1} \quad (3.6)$$

$$\sinh([\gamma]l/2) = \frac{1}{2}[T_D] \left(e^{[\gamma_M]l/2} - e^{-[\gamma_M]l/2} \right) [T_D]^{-1} \quad (3.7)$$

3.2.1.2 MTM-EBG Transmission Matrix

Transmission matrices can also be determined for lumped components in the MTL. The process for doing this is similar to that of determining ABCD parameters in a 2-conductor TL. Consider the transmission matrix equation in (3.4). Each element in the transmission matrix T_{ij} can be defined as:

$$T_{ij} = \frac{P_i}{Q_j} \Big|_{Q_k=0 \text{ for } k \neq j} \quad (3.8)$$

where

$$P = \begin{bmatrix} \vec{V} \\ \vec{I} \end{bmatrix}, Q = \begin{bmatrix} \vec{V}' \\ \vec{I}' \end{bmatrix} \quad (3.9)$$

From the circuit model for the MTM-EBG in Fig. 3.7, transmission parameters are required for the capacitive and inductive segments in order to determine the full transmission parameters of a unit cell. Using the definition in (3.8), these capacitive ($[T_C]$) and inductive ($[T_L]$) transmission matrices for this particular arrangement of reactive elements, i.e., 2 series capacitors in conductors 1 and 3 or two parallel inductors between conductor 2 and conductors 1 and 3, are given by:

$$[T_C] = \begin{bmatrix} 1 & 0 & 0 & \frac{1}{j\omega 2C} & 0 & 0 \\ 0 & 1 & 0 & 0 & 0 & 0 \\ 0 & 0 & 1 & 0 & 0 & \frac{1}{j\omega 2C} \\ 0 & 0 & 0 & 1 & 0 & 0 \\ 0 & 0 & 0 & 0 & 1 & 0 \\ 0 & 0 & 0 & 0 & 0 & 1 \end{bmatrix} \quad (3.10)$$

$$[T_L] = \begin{bmatrix} 1 & 0 & 0 & 0 & 0 & 0 \\ 0 & 1 & 0 & 0 & 0 & 0 \\ 0 & 0 & 1 & 0 & 0 & 0 \\ \frac{1}{j\omega 2L} & \frac{-1}{j\omega 2L} & 0 & 1 & 0 & 0 \\ \frac{-1}{j\omega 2L} & \frac{1}{j\omega L} & \frac{-1}{j\omega 2L} & 0 & 1 & 0 \\ 0 & \frac{-1}{j\omega 2L} & \frac{1}{j\omega 2L} & 0 & 0 & 1 \end{bmatrix} \quad (3.11)$$

Note that changes to the loading can easily be reflected in these matrices. For example, if an MTM-EBG unit cell were to be designed an added capacitor in conductor 2 that was aligned with the other capacitors in conductors 1 and 3, $[T_C]$ would require an adjustment ($T_{C,25} = 1/j\omega 2C$, the rest of the matrix remains the same) while the other transmission matrices $[T_H]$ and $[T_L]$ remain unchanged. In this regard, the MTM-EBG geometry in Fig. 3.7 is chosen due to particular advantages and properties it provides, but related configurations are just as easily accounted for, and sometimes required.

Finally, the overall transmission matrix $[T_{MTM-EBG}]$ is simply a cascade of the the constituent transmission matrices. The six segments of the MTM-EBG given in Fig. 3.7 are cascaded to form:

$$[T_{MTM-EBG}] = [T_C][T_H][T_L][T_L][T_H][T_C] \quad (3.12)$$

3.2.2 Periodic Analysis

3.2.2.1 Bloch's Theorem

The MTM-EBG is a periodic structure and can be analyzed using Bloch's Theorem, which states that the voltage and current at unit cell n must be identical to the voltage and current at unit cell $n + 1$, except with a phase delay due to a finite propagation time [38]. This boundary condition can be represented as:

$$\begin{bmatrix} \vec{V}_n \\ \vec{I}_n \end{bmatrix} = [T_{MTM-EBG}] \begin{bmatrix} \vec{V}_{n+1} \\ \vec{I}_{n+1} \end{bmatrix} = \begin{bmatrix} [A] & [B] \\ [C] & [D] \end{bmatrix} \begin{bmatrix} \vec{V}_n \\ \vec{I}_n \end{bmatrix} e^{-\gamma_B d} \quad (3.13)$$

In this equation, γ_B represents the Bloch propagation constants, and the MTM-EBG transmission matrix is written in the form of the ABCD matrix, where each submatrix is a 3×3 quadrant of the overall transmission matrix. For a non-trivial solution of this eigenvalue equation to exist, the following determinant of the system must be zero (note that $[I]$ is the identity matrix).

$$\det \left(\begin{bmatrix} [A] & [B] \\ [C] & [D] \end{bmatrix} - [I]e^{-\gamma_B d} \right) = 0 \quad (3.14)$$

This determinant can be simplified substantially due to the symmetry of the structure (for example, symmetry and reciprocity of the transmission matrix ensures that $[A] = [D]^T$), [1, 2] which results in:

$$\det ([A] - [I] \cosh(\gamma_B d)) = 0 \quad (3.15)$$

This forms the dispersion relation for the MTM-EBG.

3.2.2.2 Dispersion Diagram

Calculation of the complex Bloch propagation constants produces $N - 1 = 3$ values at each frequency corresponding to the three TEM modes that are supported by the host medium, and takes into account modal coupling as it occurs between the modes. The resulting dispersion diagram, therefore, may have many curves, and can include real ($\gamma_B = \alpha$), imaginary ($\gamma_B = \beta$), or complex ($\gamma_B = \alpha + j\beta$) propagation constants. An example of this is presented in Fig. 3.8, where several modes are observed. Note also that the imaginary parts of the dispersion curves agree well with eigenmode simulation results in HFSS for the same unit cell; this will be assumed to be true for the remainder of presented results, as it has been demonstrated previously [1].

Modes can, on occasion, be difficult to distinguish from one another, since they often couple and are not as well-defined in terms of modal voltages and currents as in the unloaded host medium (although comparing associated eigenvectors to the expected voltage distribution gives a good idea of what modes an eigenvalue is associated with). For example, the voltage on conductors 1-3 for a PPW-like mode with some coupling to a CPW mode will not be perfectly equal. They can be distinguished by recognizing the modes in regions where they are not strongly coupled and then following the traces into coupled regions, or by recognizing properties of the modes; for example, a CSL mode will not couple with other modes, so is easy to recognize (and it is not included in Fig. 3.8 as a result). Isolated modes can also be plotted individually for comparison [184].

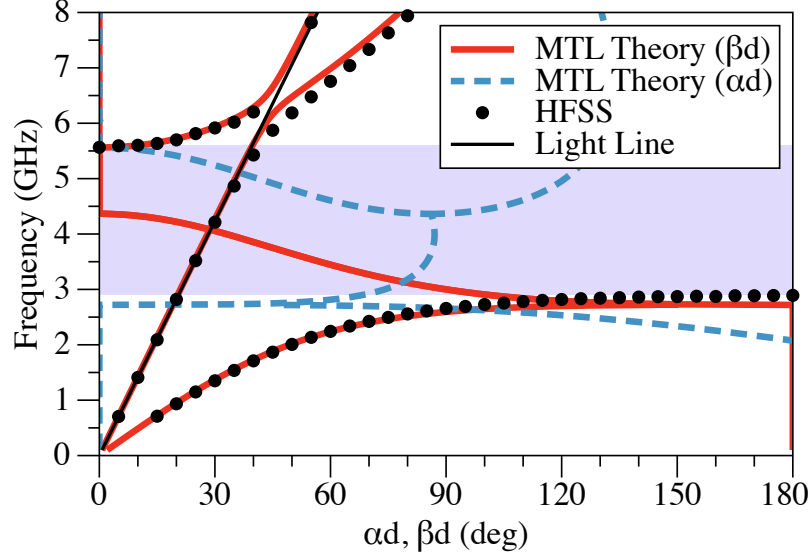


Figure 3.8: Representative dispersion diagram of the MTM-EBG unit cell, showing analytical and simulated data. The bandgap region is shaded. Reproduced from [188] ©2016 IEEE.

The CPW mode has MTM-based loading, so its curve is “backwards”, or has a negative slope in the dispersion diagram. However, its strong coupling with the PPW mode makes it more useful to discuss a coupled PPW/CPW mode rather than distinguishing the two; this coupled mode is primarily responsible for the solid red lines in Fig. 3.8. A bandgap in this coupled mode from approximately 2.9 GHz to 5.5 GHz is observed, and highlighted in purple. A complex mode is present within the bandgap region, which represents the contradirectional coupling that occurs. Note that when a bandgap region is discussed in this work, it always refers to a bandgap in the coupled PPW/CPW mode, since this is the bandgap that an interfacing PPW wave will observe.

A full dispersion curve is shown here for completeness, but in future dispersion diagrams, only the imaginary part of the PPW/CPW mode will be shown, for simplicity and clarity. This will clearly outline the MTM-EBG’s bandgap location and indicate phase that guided waves will incur when transmitting. This is sufficient detail for the applications in this work.

3.2.3 Individual Unit Cell

While dispersion analysis of the MTM-EBG assumes an infinite array of unit cells, only a finite number of unit cells can realistically be used. Ideally, a single, electrically small unit cell will have the same properties as the infinite array; this would provide the greatest utility since it would allow control over propagation in the smallest possible area. In practice, it has been shown that a single unit cell produces the phase [189] and strong bandgap [185] predicted by theory, albeit with a reduced bandwidth that approaches the theoretical prediction for a large cascade of unit cells [188].

Consider the dispersion of the MTM-EBG unit cell with dispersion properties shown in Fig. 3.8. The coupled system of even modes is presented, and the PPW bandgap is highlighted. Fig. 3.9 compares S_{11} and S_{21} through both a single cell and a cascade of three unit cells. Both cases produce a strong bandgap, but a wider bandwidth is generated in the three unit cell case. In fact, the bandgap edges are observed to approach the analytical prediction as the number of cells is further increased. However, even a single unit cell is clearly capable of producing a strong bandgap in the predicted region. As for the transmitting regions of the MTM-EBG, the fact that the phase response through a single unit cell matches that predicted by the dispersion diagram is clearly demonstrated in [189].

It is difficult to classify exactly what the MTM-EBG is when just a single unit cell is present, since it is not a homogeneous MTM, is not a periodic EBG, and it does not contain any obvious half-integer wavelength resonances. The term MTM-EBG remains a good description based on its design principles and functionality, but a question remains whether a better model exists to describe the operation of a single unit cell.

This question is not obvious. Calling the MTM-EBG a simple resonator is difficult to justify since power is reflected from the unit cells and little stored energy

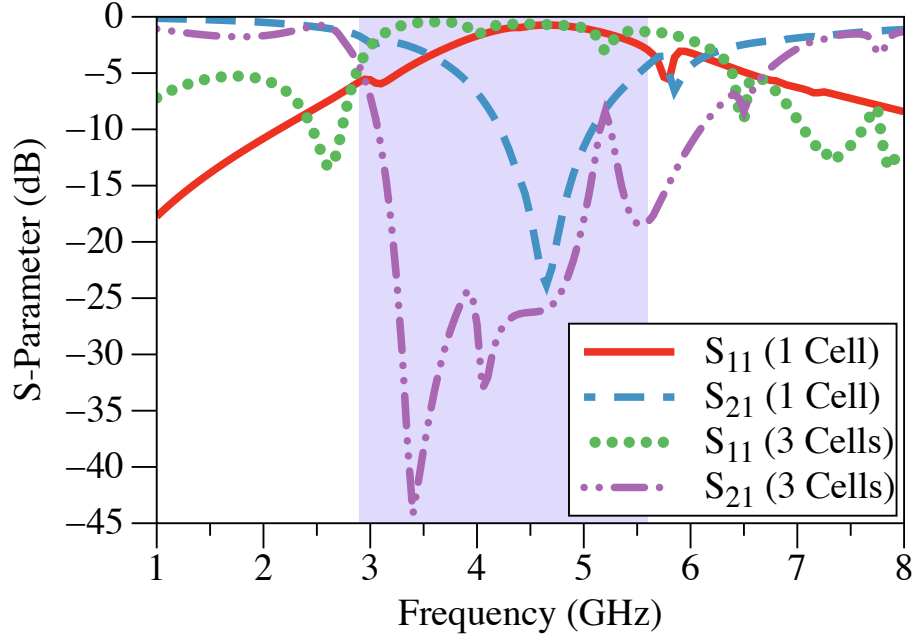


Figure 3.9: Transmission of the PPW mode through one and three printed cells of the MTM-EBG. The shaded bandgap region corresponds to that of Fig. 3.8. Reproduced from [188] ©2016 IEEE.

is observed; this will become apparent in later chapters, where field plots of several MTM-EBG unit cells in their bandgap region are observed. Furthermore, the physical size of the MTM-EBG is often electrically small. The resonance would have to come from the reactive loading itself, and while this is undoubtedly critical to the bandgap formation, it is difficult to draw direct comparisons between the loading values and bandgap frequency. Furthermore, if the resonance was solely due to the loading elements, then changing the unit cell size would not have an impact on the bandgap location; however, a simple test shows that this is not the case.

Filter theory provides another possible lens with which to analyze the MTM-EBG. Filters may use a single element or a number of cascaded elements to produce a specific filter response, with selectivity increasing with filter order. The MTM-EBG shares some properties with filters in that an increase in number of elements creates a steeper rolloff and stronger bandgap, as Fig. 3.9 demonstrates. However, the MTM-EBG does this in an extremely compact space with few lumped reactances. Better

modeling of all parasitic reactances in the MTM-EBG may allow it to be analyzed as a filter, but the MTM-EBG is structurally quite different from a conventionally anticipated filter design, and how it would be modeled as such is not obvious.

Dispersion engineering of the MTM-EBG generally provides a different focus than filter theory. As analyzed in this work, the MTM-EBG can be designed for different bandgap locations and bandwidths based purely on cell geometry and loading, and phase information in the passband is maintained. Filter theory allows for control of bandgap properties instead, including rolloff and bandgap strength. It may assume a cascade of individual, unique filters that couple to produce this response, which the dispersion engineering approach is not well-equipped to do. For the devices to be presented in this work, however, dispersion engineering provides a clear design advantage, since interest is taken in the passband and bandgap response, and specific bandgap properties do not need to be highly engineered. Combined with the fact that the ability of filter theory to model the MTM-EBG is questionable, the filter approach will not be pursued further.

Any 2-conductor model, as previously discussed, will be unable to capture coupling effects between the various conductors of the MTM-EBG, although modeling the coupling with lumped elements will approach the MTL model as the number of elements increases. This does not provide any significant advantages over the MTL model. While it can safely be concluded that such a model lacks accuracy compared to what has been established so far, verification of this is provided in Appendix A, which compares results of a circuit simulator to the analytical model and a full-wave simulation.

It is clearly difficult to find a simple and succinct theory of MTM-EBG operation *except* with MTL analysis, and while it may be argued that periodic analysis is a poor way to represent the properties of a single non-periodic unit cell, it does a better job of predicting its bandgap and phase properties than other available methods. Using the analytically derived dispersion properties, the remainder of this chapter will focus

on practical use of the MTM-EBG to enable multi-band operation.

3.3 Embedded MTM-EBG Unit Cells

3.3.1 Implementation

MTM-EBGs were originally introduced for the suppression of noise in parallel-plate waveguide environments [2], but this work intends to focus on their application in microstrip-based multi-band devices, including circuit elements and antennas. Its viability as a general-purpose solution depends on many factors, including physical properties, which have been mentioned: the MTM-EBG is uniplanar and can be completely printable, making it easy and inexpensive to fabricate.

The fact that a single unit cell alone can provide a strong bandgap is important, but not sufficient on its own; a key to using the MTM-EBG in resonant devices in particular is that the single unit cell is also electrically small. Embedding an MTM-EBG into a segment of set electrical length would be impractical if the MTM-EBG unit cell has a similar or larger electrical length. MTM-EBG unit cells that incur a phase of less than 20° in parts of its passband while still maintaining a strong bandgap at nearby frequencies are realizable, and this allows electrically small TL regions to effectively be reconfigured as a function of frequency.

The small unit cell sizes allow MTM-EBG unit cells to be embedded directly into microstrip or PPW segments, effectively giving that TL section a frequency-dependent bandgap. However, the MTM-EBG unit cell also operates in its passband region, so impedance matching becomes an important consideration. That good impedance matching is ensured can be found from considering the MTM-EBG modes. A PPW-like (or microstrip-like) field configuration propagates through the MTM-EBG, and when coupled to the backward CPW mode, the bandgap in the PPW mode arises. This also implies that the propagating mode in the MTM-EBG unit cell is PPW-like, and therefore, has a similar field profile and therefore characteristic impedance to the

TLs in which it is embedded [184, 189]. This leads to inherent impedance matching, which is most easily observed from transmission simulations of MTM-EBG unit cells, many plots of which are included in this work. Noting that this is true, it will be assumed for the remainder of this thesis.

Viability finally depends on having a versatile design procedure, which is particularly important in tailoring specific MTM-EBG unit cells for various implementations. The analytical design procedure is key to this, since MTM-EBG unit cells will need to be designed to have particular phase and bandgap properties. There is no guaranteed method to produce the desired properties, however; instead, a general design procedure is given as follows.

The design process consists of choosing host-medium dimensions (i.e. the widths of conductors 1-3) such that a unit cell (or integer number of unit cells) has the same overall width as the microstrip or PPW geometry into which it will be embedded. The length of the unit cell should be chosen to be approximately the same length as the TL section that it replaces, although it will ultimately be slightly shorter than this as the loaded unit cell will be more dispersive than the standard TL it replaces. All geometrical features should be chosen to be large enough to allow fabrication with available techniques.

It is then loaded with series capacitance and shunt inductance to get the desired properties, with minimal inductance typically being chosen for simple printed realization, and capacitance largely determining the bandgap location. Capacitance should be kept small as well if possible, to allow for a printed realization. Tuning of reactive values and geometric feature sizes allow a design that meets all properties to be achieved. For general trends showing the effect that changing any given property of the MTM-EBG has on its bandgap, the reader is referred to Table I from [190], or to some of the plots below. These figures should provide the reader intuition into tuning of the MTM-EBG.

Finally, a single-cell transmission simulation will ensure that the desired properties

are achieved. In this work, this is done with a full-wave FEM solver, Ansys HFSS, using lumped L and C values that agree with the analytical model. In the case of creating a fully printed version of the MTM-EBG, the inductors and capacitors in the simulation model can be replaced with strip inductors and interdigitated capacitors (interdigitations are usually needed to produce the required capacitance, but gap capacitors could also be used in some cases, or parallel-plate capacitors in multi-layer designs). The inductance of the strip inductors can be estimated using empirical formulas found in [191] and the design of interdigitated capacitors can be guided by [192]. Thereafter, parametric tuning is used to achieve the previously designed L and C values by simulating this unit cell and comparing its performance to the lumped-element simulation. Lumped loading could be used instead, but rendering the unit cell fully printed enables single-step fabrication, and allows the MTM-EBG to be used at higher frequencies than discrete chip components alone would allow.

An example of the unit cell geometry, as designed with the analytical code, is shown in Fig. 3.10a. On the given substrate, geometry of the upper three conductors is chosen, as well as loading element values. This is then implemented as in Fig. 3.10b, which shows the top of the MTM-EBG unit cell in fully printed form, embedded in a microstrip TL. Dimension labels shown in this image will be used continuously throughout this work. The fully printed version is limited in the possible capacitances and inductances that can be achieved, and this is also dependent on how small of a gap or interdigitations can be fabricated. Regardless, most structures in this work achieve a fully-printed realization, and further discussion of limitations will be included as needed.

A final note on this structure is that when embedded in a TL such as in Fig. 3.3b, parasitic inductance is introduced at the transition between the PPW/microstrip and the MTM-EBG unit cell nearer to the inductor. The parasitic inductances introduced are in parallel with the strip inductors of width d_3 , and can be on the same scale. There may be cases in which the parasitic inductance is sufficient for unit cell opera-

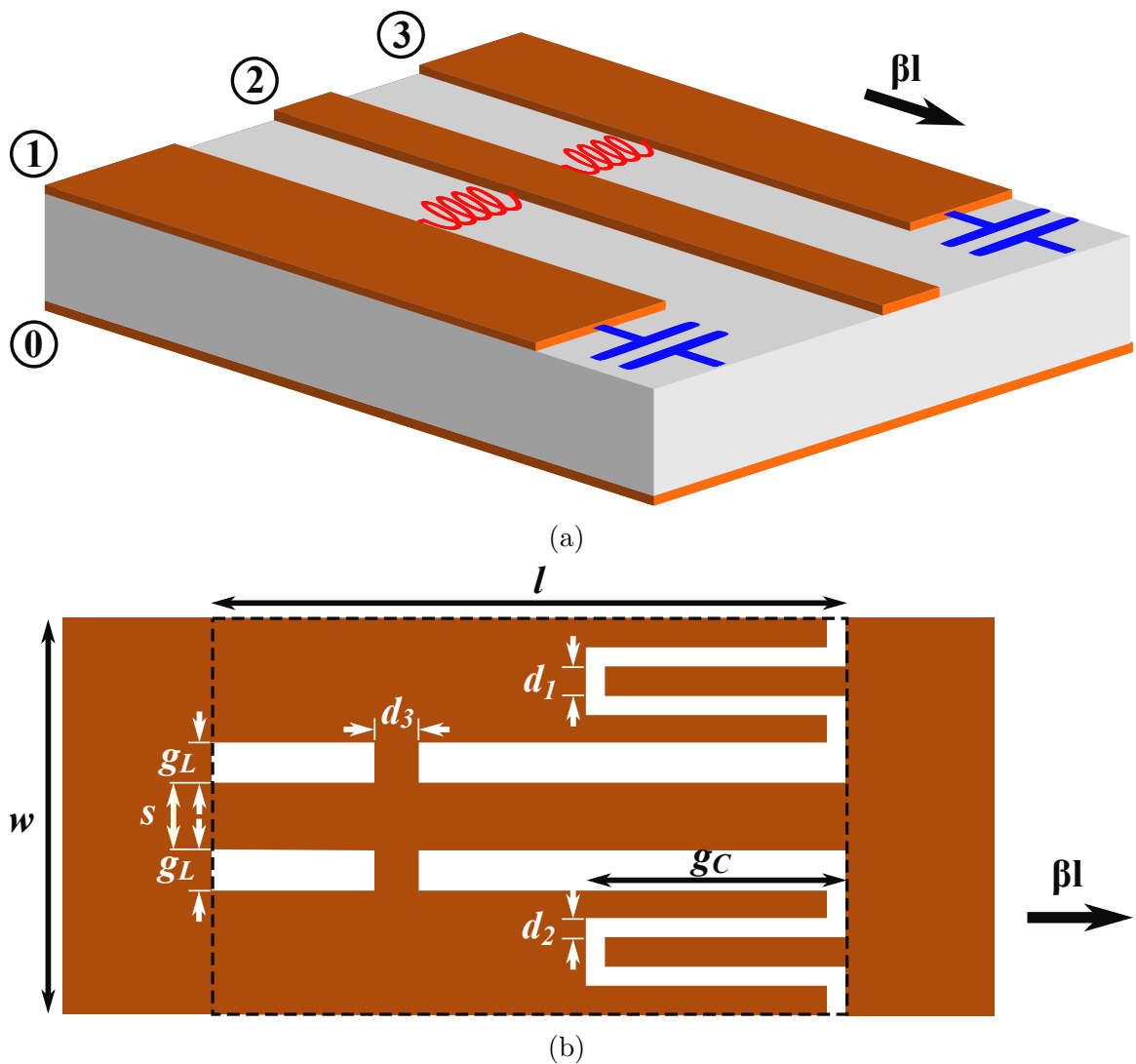


Figure 3.10: (a) Profile view of MTM-EBG unit cell. Host medium consists of three conductors above a ground plane, loaded with series capacitors and shunt inductors. (b) Top view of MTM-EBG unit cell embedded in a microstrip, with strip inductors and interdigitated capacitors. Propagation direction is indicated. Reproduced from [193] ©2023 IEEE.

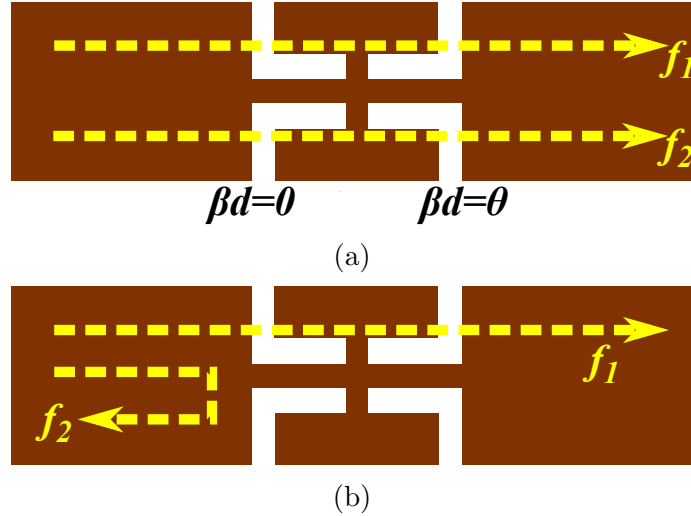


Figure 3.11: Two modes of operation for the MTM-EBG to enable multi-band operation. (a) Exploiting the equiphase point to incur the same phase at two different frequencies. (b) Employing the bandgap to transmit one frequency and reflect the other.

tion, and the strip inductors are not required at all. This case will be discussed as it arises, but note that it only applies to a single unit cell embedded in a TL, as other situations (multiple unit cells, or a unit cell that interfaces with a TL on one side only) will not have the same parasitic inductance.

3.3.2 Multi-Band Devices

Dispersion properties of MTM-EBG unit cells are manipulated to allow multi-band operation, with the bandgap location and unit cell phase both important. There are two primary ways to make a device multi-band. One is by recognizing that on either side of the bandgap, equiphase points exist such that a section of MTM-EBG would have the same phase at two different operating frequencies, as demonstrated in [184]. This approach involves replacing a section of TL with frequency-dependent length with a section of MTM-EBG that achieves this electrical length at both operating frequencies, and is illustrated in Fig. 3.11a. This is an effective approach, but suffers from some drawbacks: operation occurs in dispersive regions on either side of the bandgap resulting in narrow bandwidths, and only dual-band operation is possible.

A second, more robust approach is focused on in this thesis, which involves rendering TL lengths frequency-dependent through operating alternately in the transmission and bandgap regions of the MTM-EBG. The MTM-EBG can be considered to act as an open circuit (OC) when it is in its bandgap region, which will effectively reflect nearly all power incident on it. At a different frequency in which the MTM-EBG is transmitting with a known phase, the power will pass through this TL segment, allowing completely different routing of the signal and different operation as a result. This approach tends to produce narrowband solutions in most cases as well, but also has the advantage that the use of multiple different MTM-EBG unit cells can enable more than two operating bands. This approach presents design challenges where it is desirable for power to pass through the MTM-EBG at both frequencies, but details of this approach will be discussed extensively in the coming chapters, and demonstrated for a variety of practical devices.

In either case, the MTM-EBG unit cells will be embedded into an existing design of a single-band device to render it multi-band. This means that the device and MTM-EBG can be designed independently, which is advantageous because design equations usually exist for conventional, single-band devices, and the MTM-EBG has a well-understood and independent design procedure as well.

3.3.3 Alternate MTM-EBG Structures

The standard MTM-EBG unit cell, shown in Fig. 3.10, is used in most structures in this work, but it is not the only possible configuration of the MTM-EBG. Other options will be discussed here.

3.3.3.1 Physical Geometry

The host medium used in this work typically consists of a thin, low-loss substrate with a uniform ground plane on the bottom and three conductors on the top surface of the substrate. This is advantageous in that it is uniplanar and easily fabricated,

and it can interact well with other planar structures. Any substrate can be used, but it is typically easier to use substrates with lower permittivities, since the MTM-EBG unit cell features can be larger. This is because the MTM-EBG unit cell is typically the same width as the TL it is interfacing with. In microstrip configurations, the TL narrows as permittivity increases, thereby reducing the required MTM-EBG width simultaneously. Printed capacitors, however, may not shrink proportionately since the fringing fields are largely in air; they will therefore become more difficult to implement. The unit cell may be able to remain sufficiently wide for use in PPW environments, such as its integration into patch antennas.

While most applications use the simple planar setup for the MTM-EBG, there are cases where it is advantageous to alter the geometry. Consider the fact that antenna bandwidth can be enhanced by reducing a substrate permittivity or increasing the substrate height [130]. In this case, it may be beneficial to use an air dielectric and mount an antenna with embedded MTM-EBG unit cells above a ground plane, perhaps on a thin substrate for structural support. Analytically, this is not much different than the standard case; the host medium properties will change, but analysis remains the same otherwise. However, this increased complexity in the geometry has other advantages. Mounting the upper three conductors of MTM-EBG unit cell on a thin substrate allows both sides of the substrate to be used, for example by implementing parallel-plate capacitors rather than interdigitated versions, which allows for a much higher printed capacitance to be achieved. Furthermore, small vias in the upper substrate could be introduced in the strip inductors to drastically increase the achievable inductance.

The conductors are not even required to be coplanar; as long as the host medium properties can be determined and the desired L and C connections between conductors established, the MTM-EBG is capable of conforming to various topologies that different devices may have.

Generally, the host TL is not required to be PPW or microstrip-like, as long as

modal coupling can be enabled. For a discussion on MTM-EBG integration into other TL types including stripline, CPW, and coaxial, see Appendix B.

3.3.3.2 Loading Schemes

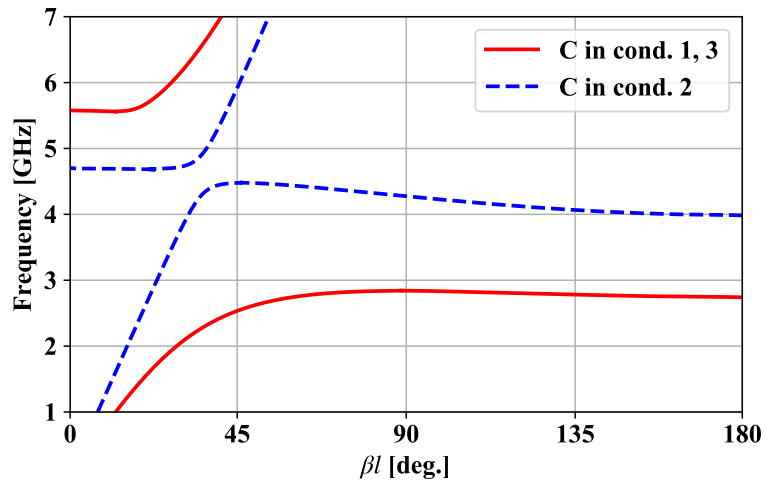
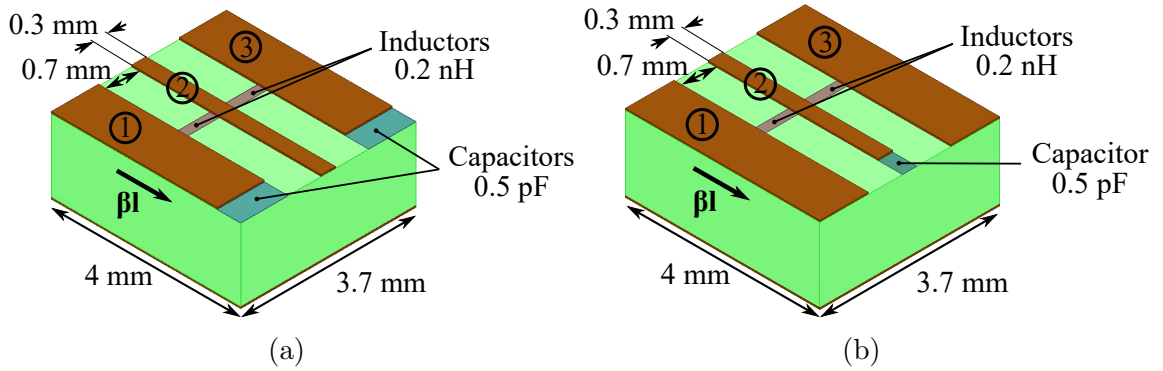
The MTM-EBG need not be loaded in the precise way discussed so far. While the production of a bandgap based on contradirectional modal coupling requires this configuration generally, some tweaks could be made. For example, a capacitor could be in the central strip (conductor 2) instead of the CPW grounds (conductors 1 and 3), or capacitors could be placed in all three conductors. The choice of loading is reflected in the transmission matrices of the loading elements ($[T_C]$ and $[T_L]$), and is easily accounted for.

Consider a comparison of having capacitors with capacitance C in the usual locations (conductors 1 and 3, Fig. 3.12a), versus having a single capacitor with the same C in the central strip (conductor 2, Fig. 3.12b) alone. Dispersion properties for this case are presented in Fig. 3.12c. It is observed that while a broad bandgap is produced in the former case, an extremely narrow bandgap results in the latter. This is likely due to decreased modal coupling as the fields around the central strip, which are normally well-matched for the two modes, are disturbed. This small change in loading scheme is therefore advantageous in cases where a narrow bandgap is preferred [184, 190].

3.4 Design Strategies

3.4.1 Effect of L and C

Physical dimensions of an MTM-EBG unit cell are critical to determining its properties; the strip width, capacitive gap size, and overall width are all crucial in determining the host medium parameters, and length describes the periodicity of the MTM-EBG during analysis. However, these properties tend to be limited by the geometry into which the MTM-EBG is implemented. For example, an MTM-EBG



(c)

Figure 3.12: Comparison of unit cell with (a) capacitors in conductors 1 and 3, and (b) capacitor in conductor 2. (c) Dispersion diagram for unit cells with provided dimensions. A 1.524 mm Rogers 3003 substrate is used.

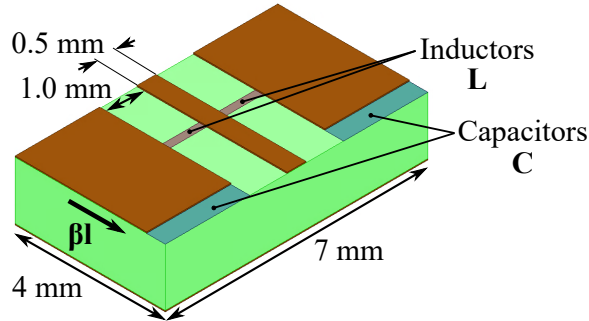


Figure 3.13: MTM-EBG unit cell structure with dimensions and propagation direction indicated. L and C values are swept in Fig. 3.14 and Fig. 3.15, respectively. Rogers 3003 with a height of 1.524 mm is used as the substrate.

in a TL should have the same width as the TL, and if printed capacitors are to be used, the CPW grounds should be as large as possible to provide room to implement them. There is usually some room to adjust these physical dimensions, but there is much more freedom to affect the unit cell's properties by changing reactive loading, particularly if it is implemented in lumped form. The effects of changing these properties, therefore, merit special consideration. The unit cell shown in Fig. 3.13 will be used to investigate these effects.

Unit cell inductance L generally has a small effect on the phase or bandgap properties of an MTM-EBG unit cell. What it does do to the isolated CPW mode is give it a steeper negative slope, but in terms of the coupled mode, this is primarily observed as a marginal increase in bandgap bandwidth and a slight downshift of the bandgap. Phase in the passband remains relatively unchanged, so the effect of changing L is, overall, not substantial. All of these effects are observed in Fig. 3.14, which compares the dispersion properties (based on analysis) to the transmission properties (based on simulation) of a single unit cell. As expected, the bandgap of the single unit cell is smaller than predicted, as expected, and only marginally shifted for a wide range of L values, which are swept from 0.2 nH to 2.0 nH.

Due to its minimal effect, it is generally advantageous to use as small as possible of an L value in order to easily realize it in printed form. In fact, in many cases,

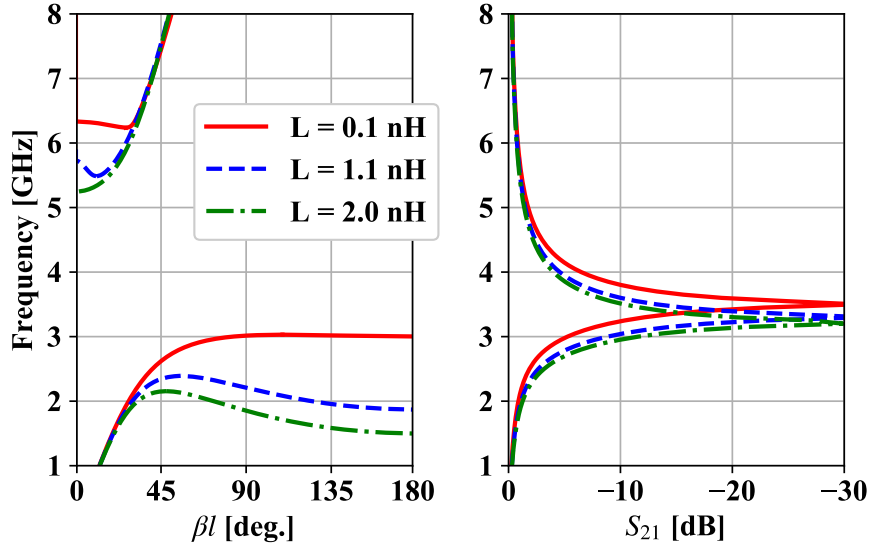


Figure 3.14: MTM-EBG unit cell dispersion and transmission properties for various L values. Based on the unit cell in Fig. 3.13, with $C = 0.5 \text{ pF}$.

L is chosen to be in the 0.1 nH-0.3 nH range, where it can be realized as a simple strip inductor between the central strip of the MTM-EBG and the CPW grounds. This implementation is simple, easy to implement, and generally has a minor effect on dispersion properties.

Unlike L , the unit cell capacitance C has a major effect on the bandgap location of the MTM-EBG. As shown in Fig. 3.15, increasing C rapidly shifts the bandgap downwards, with a 0.4 pF change in capacitance resulting in a bandgap downshift of about 2 GHz for this unit cell, and this is the best way to set a bandgap location once physical dimensions are chosen. As the bandgap central frequency decreases, so does bandwidth; other parameters must be adjusted again if a specific bandwidth is required, or else a different loading scheme could be chosen. Implications of this are that at higher frequencies, small capacitances are required and can be easily printed; for example, $C = 0.2 \text{ pF}$ may be sufficient for a given unit cell to produce a bandgap in the 5 GHz range. To get a bandgap closer to 1 GHz, however, a C value of around 1-2 pF will be required, which may either require substantially more space to

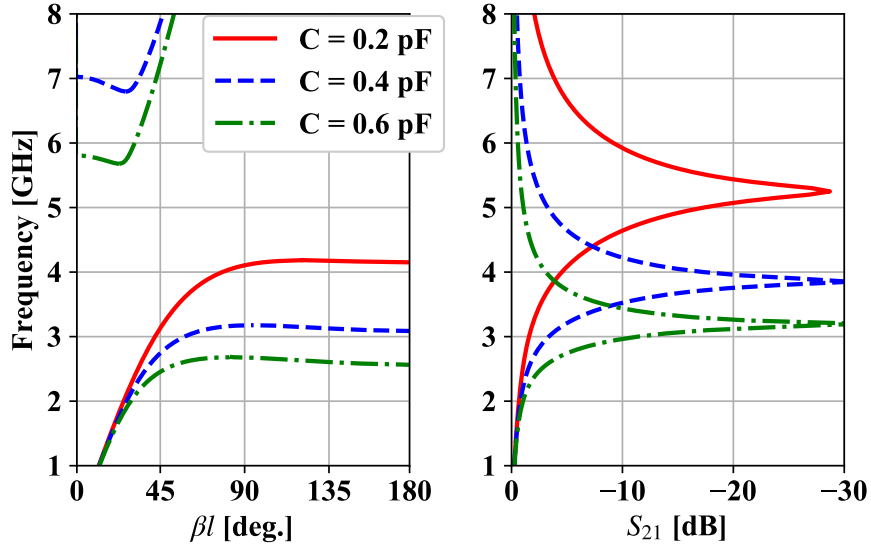


Figure 3.15: MTM-EBG unit cell dispersion and transmission properties for various C values. Based on the unit cell in Fig. 3.13, with $L = 0.2 \text{ nH}$.

create in printed form, or may necessitate the use of lumped components as frequency decreases. Regardless, using C to effectively set the bandgap location is a valuable design tool to create an MTM-EBG with desired properties.

3.4.2 Simplified Design Procedure

While many variations of the MTM-EBG unit cell are used, there are similarities between them, particularly for unit cells on the same substrate and using the same loading element geometries, such as interdigitated capacitors. For any of the circuit element devices, for example, an MTM-EBG unit cell will be embedded into a (typically) 50Ω microstrip TL which limits the possible host-medium geometry, and capacitor value will primarily determine the bandgap location, which is between 1 GHz and 6 GHz for all devices in this work.

The design of an MTM-EBG unit cell typically involves the following steps:

- Determine host medium parameters from simulation.
- Using analytical process, choose unit cell length l , inductance L , and capacitance

C to produce required dispersion properties.

- Simulate single unit cell with lumped reactive elements and verify properties.
- Systematically convert lumped elements into printed elements, ensuring properties of the unit cell do not change.

The resulting MTM-EBG unit cell can now be embedded into the structure of choice.

For subsequent designs with similar physical properties, some of these design steps can now be skipped, even if the MTM-EBG requires a bandgap in a different location.

Consider the following simplified design procedure:

- Take simulation results of similar unit cell with fully printed features.
- Adjust unit cell length l to change the phase of the unit cell at the required operating frequency.
- Change the bandgap location by adjusting the parameter that controls the printed unit cell capacitance, g_C .

A unit cell with desired properties can rapidly be produced in this way, keeping in mind that the last two steps may have to be done iteratively.

This approach is not suitable when MTM-EBG geometry changes substantially, for example in a multi-layer design that uses parallel-plate capacitors, or when the MTM-EBG host medium changes substantially (e.g., a much wider unit cell is required in a patch antenna than in a microstrip), since in these cases an analytical approach finds the required solution much more directly, and with less tuning. However, it is certainly an approach a designer could take when designing multiple unit cells, or it can even be used to create a design chart, an example of which will be included in Chapter 4.

3.4.3 Design Tools

The simulations included so far use full-wave solver Ansys HFSS. This provides accurate simulations, but can take several minutes to simulate an MTM-EBG unit cell, particularly with fully printed features. A design requiring a large amount of capacitance in printed form becomes inefficient to simulate, so it is important that analytical code is accurate, to reduce iterations and tuning of the unit cell. In simulations where many MTM-EBG unit cells are required, for example in practical circuit elements or antennas, simulations may take on the order of hours or even days to complete.

One way to speed up the process is to simulate with printed features on the final structure only, and complete most simulations with assigned reactive sheet impedances instead. This can greatly reduce simulation time, but it requires a thorough understanding of how to convert from such models into realistic designs. Overall, however, full-wave solvers are the most accurate means of completing these simulations, and typically few design iterations are needed due to the strong analytical nature of the MTM-EBG, which makes the long simulation times tolerable.

In some cases, an MTM-EBG unit cell or cells are interfaced with TLs in which the TL is tuned, while the MTM-EBG does not need to be. For example, at frequencies where an MTM-EBG is in its bandgap region, other parts of the circuit such as TL length on either side of the MTM-EBG may require tuning. In this case, it can be more efficient to export the S-parameters of a single unit cell, and integrate them into a microwave circuit solver, such as Pathwave ADS. Treating the MTM-EBG as a black box allows its position in a TL system that can easily be handled by such solvers to be altered rapidly, and quick iterations of the system can optimize its performance. This method was used particularly with multi-band circuit elements that contain many MTM-EBG unit cells, such as the tri-band matching network discussed in Chapter 4.

While the first and most important tool is the analytical description of the MTM-EBG, circuit solvers and full-wave simulators can render design rapid and accurate.

Many different designs are a result of this, with excellent agreement to measurements throughout this thesis.

3.5 Tunability

The ability of the capacitors alone in the MTM-EBG unit cell to drastically shift bandgap location suggests that a capacitively tunable version of the MTM-EBG could be implemented. On its own this presents interesting possibilities, such as a tunable filter created from the insertion of a unit cell directly into a simple TL [190]; however, embedded in devices such as antennas, this is more complex, as a shift in bandgap location does not necessarily correspond to the desired change in antenna resonant length. This particular problem will be explored in detail in Chapter 5. Suffice for now to acknowledge that tunability presents an array of new opportunities for MTM-EBG implementation.

Tuning can be achieved in many ways, for example mechanically, electrically, or with ferroelectric substrates. Mechanical tuning of the MTM-EBG has been demonstrated in [190], and provides an excellent solution for a small number of unit cells arranged in a convenient orientation so that they can all be tuned simultaneously. When this is not the case, or when the large space taken up by the tuning mechanism is prohibitively large, electrical tuning through varactors provides a better solution. This is typically much cheaper and easier to implement than a ferroelectric substrate as well. For these reasons, electrical tuning will be the only method used in this work.

The possibility of tuning is raised here because it has implications on MTM-EBG design. Varactors cannot simply take the place of the usual capacitors in conductors 1 and 3, since conductor 2 will short them out at DC (where the inductors will act as short circuits). Some sort of capacitor will need to be added to conductor 2 as well to ensure that the varactors can be properly biased.

Consider Fig. 3.16. Two dispersion curves are shown, corresponding to two illustrated unit cells: the solid red lines represent a typical MTM-EBG unit cell, while

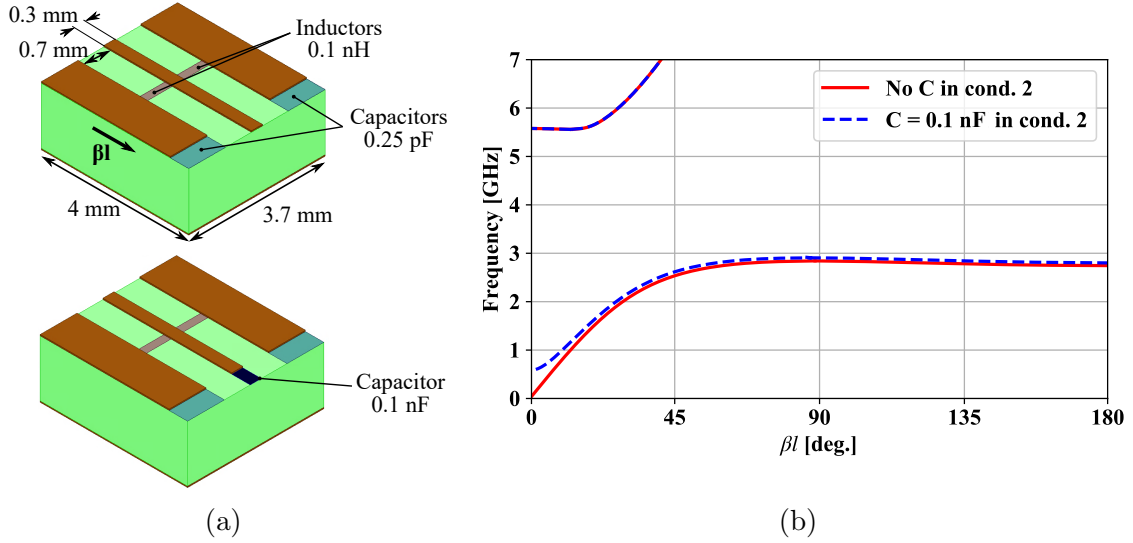


Figure 3.16: Effect of adding a 0.1 nF decoupling capacitor into conductor 2. (a) Unit cell designs, which are identical other than the capacitor in the central strip. (b) Dispersion properties.

the dashed blue line depicts the same unit cell but with an additional capacitor in conductor 2. This additional capacitor is three orders of magnitude larger than the capacitors in conductors 1 and 3, and acts as a DC decoupling capacitor; notice that makes the MTM-EBG act as a DC OC, but has almost no other effect on the dispersion properties of the unit cell. Even larger capacitors would have less of an effect, and the low-frequency Γ -point would approach zero. This demonstrates that decoupling capacitors can easily be used with little effect on the MTM-EBG design to allow a varactor to be biased, and thus electrical tunability can be achieved.

Chapter 4

Multi-Band Circuit Components

4.1 Methodology

4.1.1 Embedded MTM-EBGs

As has been established, an MTM-EBG can be used as a section of microstrip with two possible frequency-dependent states; it has a transmitting, or “on”, state, where it transmits with some phase Θ , and a bandgap, or “off”, state, where all power is reflected. These two states occur at different frequencies, in between which the MTM-EBG unit cell will have regions of partial transmission and reflection. Generally, for multi-band circuit elements, successive frequency bands are spaced far enough apart that it can be assumed to be working in one of the two switch states. The effects of partial transmission or reflection will be observed in some cases, and these will be discussed as they appear; otherwise, the MTM-EBG will be assumed to be fully transmitting or fully reflecting at frequencies of interest.

Multi-band circuit elements use the MTM-EBG in its two states to effectively superimpose multiple circuits, each operating at different frequencies, which are designed with traditional methods. Physical dimensions of any microstrip-based circuit containing TLs change as a function of frequency, so superimposing multiple circuits means changing the properties of TL segments to provide the correct phase at each frequency. Within those frequency-dependent segments is where MTM-EBG unit cells enable multi-band operation; when embedded in the TLs, their state at each fre-

quency (and phase response when in the transmitting state) allows the TL properties to change drastically as a function of frequency, thus preserving the desired electrical properties at each.

MTM-EBG unit cells are designed to be embedded directly into the constituent TL segments of circuit elements. In terms of designing such a unit cell, this immediately provides a constraint on the width of the unit cell as transmission lines tend to be narrow. Exact dimension depends on usual properties of the TL, including substrate permittivity, thickness, and the characteristic impedance. Regardless, this limits the ability to implement printed capacitance and inductance in the MTM-EBG, based purely on spatial constraints. These loading values should therefore be designed to be as small as possible. This is easier at higher frequencies but becomes a challenge as the desired bandgap location decreases in frequency, since a lower bandgap typically corresponds to a larger capacitance.

Despite this, all proposed devices in this chapter use fully printed MTM-EBG unit cells. When possible, a minimum feature size of 0.2 mm is maintained, but some devices use 50 μm features to produce more capacitance in a smaller area. While laser milling provides the ability to fabricate these features, other fabrication methods may not. Lumped capacitors could alternatively be used in these cases.

In some cases, the idea of extending the capacitive region outside of the width of the transmission line was explored to increase capacitance further. This was successful in lowering the MTM-EBG bandgap frequency without providing any substantial mismatch in the TL, and will be discussed in more detail when required below.

A final comment on embedding MTM-EBG unit cells into transmission lines is that a single unit cell is typically used. This is because frequency-dependent devices typically demand a specified phase condition to be met, for example to incur 90° through a particular constituent TL. For the MTM-EBG to achieve this phase condition, possibly in combination with some standard microstrip TL at one or both frequencies, it will typically need to incur less phase, or in other words, it needs to be electrically

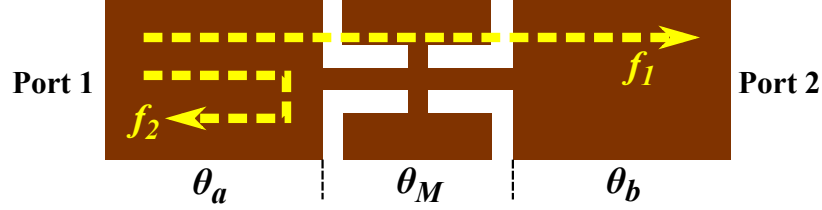


Figure 4.1: MTM-EBG unit cell embedded in microstrip TL (top view) that transmits at f_1 and presents a bandgap at f_2 . Phase in each region of the TL is indicated.

small. This is easier to achieve with a single unit cell than with two or more, with the tradeoff being a reduced bandgap size and rolloff.

4.1.2 Device Design

All circuit elements in this chapter utilize the bandgap properties of the MTM-EBG unit cell at one frequency and the transmission properties at another to obtain multi-band operation (for a case where transmission at both operating frequencies is used, see [184]). Design of such devices then becomes quite straight forward. Consider an MTM-EBG embedded in a TL segment that transmits with a phase Θ_M at f_1 and presents a bandgap at f_2 . According to Fig. 4.1, the phase between ports 1 and 2 amounts to $\Theta_a + \Theta_M + \Theta_b$ at f_1 , while f_2 reflects power back to port one with a phase of $2\Theta_a$, assuming that the MTM-EBG operates as a pure OC. Port 2 may be an actual port, but could also be an OC in the case of a microstrip stub, and Θ_a and/or Θ_b may be zero. This extremely simple accounting of phases from each constituent microstrip and MTM-EBG section provides the basis for a variety of devices presented in this section, and can be expanded in the similar way to microstrip lines with more than one different embedded MTM-EBG unit cell to provide different operation at several frequencies. The analysis can further be simplified by assuming that an MTM-EBG at f_1 transmits with approximately the same phase as an underlying microstrip, which is a good assumption as long as f_1 and f_2 are spaced a reasonable distance apart (i.e., f_1 is operating far from the dispersive region near the bandgap).

Once an MTM-EBG unit cell has been embedding into a structure minor tuning

is typically required for a few reasons. One is that the MTM-EBG does not act as a pure OC, but can be modeled as a small reactance (typically inductive) instead. Secondly, parasitics are introduced by the connection to the adjoining TL. Tuning for both these effects is typically minor, and can easily be accounted for in simulations.

4.1.3 Choice of Substrate

Many factors complicate the decision of choosing a substrate for the coming applications. For practical purposes a commonly-used substrate is preferred, as well as one with well-defined properties and low losses at microwave frequencies. It should be available and amenable to most types of fabrication.

Higher-permittivity substrates (e.g., ϵ_r around 6 to 10) are often preferred for circuit elements, since they provide miniaturization. This can be a disadvantage for MTM-EBG-based devices, however, since narrower trace widths are required to achieve the same characteristic impedance as permittivity increases. Since MTM-EBG unit cells are embedded into the constituent microstrip TLs, this further reduces its physical size, which can render fabrication more challenging, or lumped reactances more difficult to implement in the space.

The chosen substrate that meets these requirements is Rogers RO3003, which has a relative permittivity $\epsilon_r = 3$ and a loss tangent $\tan \delta = 0.0010$. A substrate height of 60 mils was used, and it is clad in 1 oz rolled copper (or 1/2 oz copper in some cases, but this will be indicated). This substrate allows wide enough 50Ω microstrip lines to support an embedded MTM-EBG unit cell, and is high-performance otherwise. It is suitable for nearly all applications in this work and will be used throughout.

4.2 Microstrip Stubs

4.2.1 Dual-Band Stub

To clearly show the design principles of stubs with embedded MTM-EBG unit cells, a rectangular stub for use in a dual-band bandstop filter at 2.4 GHz and 5.8 GHz will be

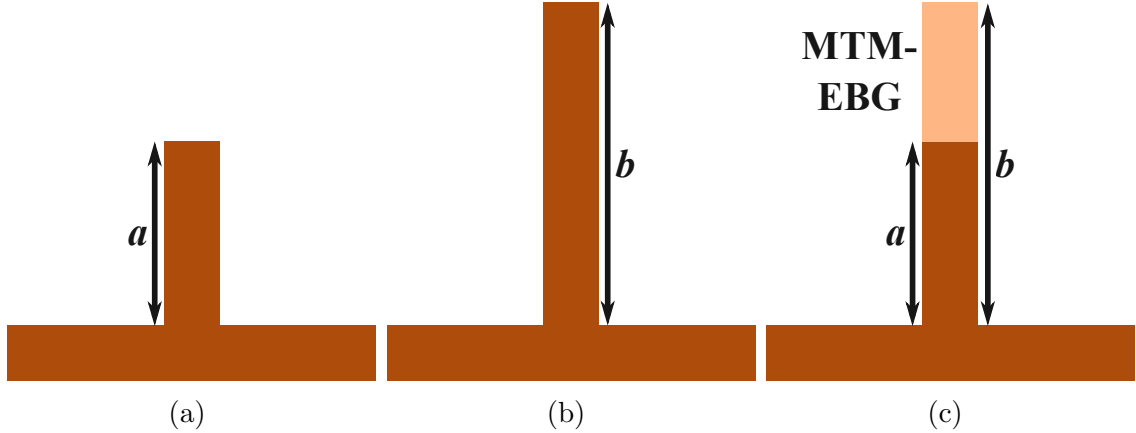


Figure 4.2: Representative depiction of the design of a dual-band microstrip stub. Quarter-wavelength stubs at (a) f_1 and (b) f_2 are effectively combined into a (c) dual-band stub using an embedded MTM-EBG unit cell, which has a bandgap at f_1 and a specified phase at f_2 .

demonstrated. A conventional stub connected in parallel with a microstrip line acts as a bandstop filter for the frequency at which it is a quarter wavelength in length; on the chosen substrate with a microstrip of 50Ω characteristic impedance, the required microstrip stub length is 19.5 mm at 2.4 GHz and 7.6 mm at 5.8 GHz. Both of these resonances will be achieved in a single microstrip stub with an embedded MTM-EBG, and the total stub size will be smaller than a conventional stub at 2.4 GHz.

The MTM-EBG unit cell is designed such that it produces a bandgap at 5.8 GHz, and transmits at 2.4 GHz. The phase of the MTM-EBG is designed to be equivalent to the phase difference between the two stub lengths at 2.4 GHz, meaning that the unit cell replaces this section of microstrip entirely (i.e., additional stub length at 2.4 GHz beyond the MTM-EBG unit cell is not required). This concept is illustrated in Fig. 4.2, where the ability of an MTM-EBG to enable two effective lengths is illustrated. Note that this picture is an accurate representation of electrical lengths, but the physical length of the dual-band stub b in Fig. 4.2c will be shorter than the physical length of the single band stub in Fig. 4.2b, since the MTM-EBG is more dispersive than the length of microstrip it replaces.

The dispersion properties of this unit cell are presented in Fig. 4.3 along with the

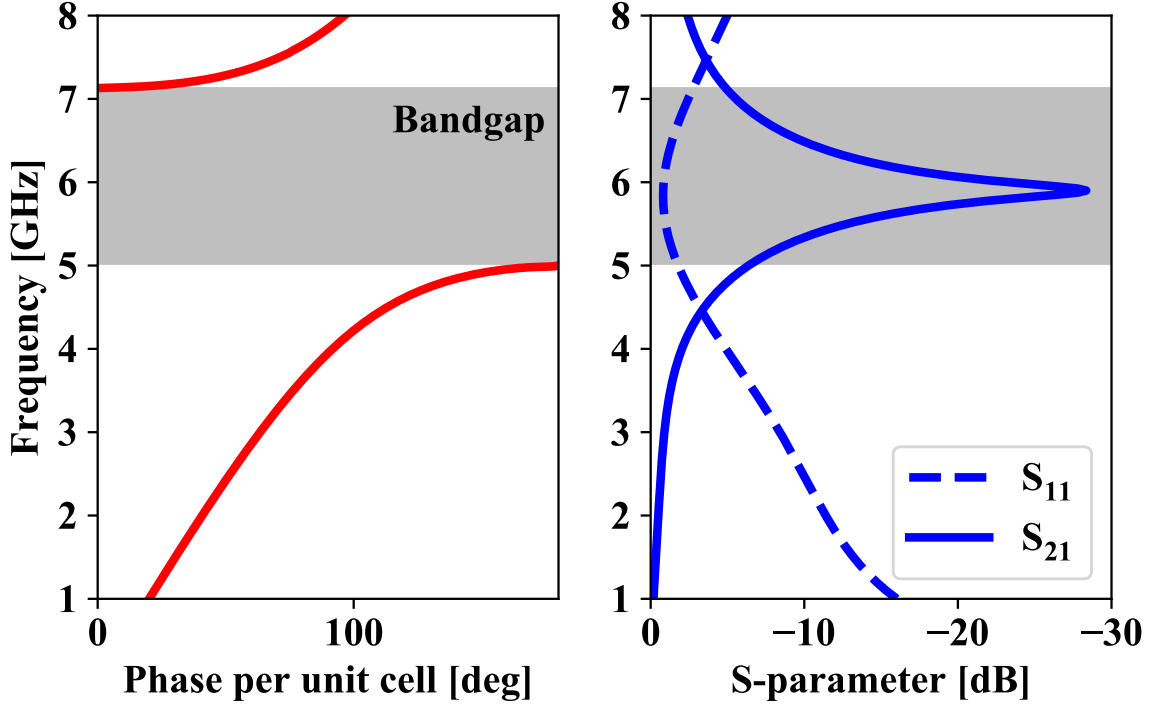


Figure 4.3: Dispersion diagram of MTM-EBG unit cell used for dual-band rectangular stub design, and S -parameters of a transmission simulation for a single unit cell. The predicted bandgap location is shaded. Reproduced from [193] ©2023 IEEE.

transmission parameters of a single unit cell, where it is seen that a strong bandgap is maintained at 5.8 GHz, even though the MTM-EBG bandgap bandwidth is reduced as compared to the theoretical result. Minor adjustment of geometric features of the stub are required to account for parasitics and ensure the stub has the correct phase at each frequency, and this involves marginal adjustments to the stub length a , the MTM-EBG length l , and the printed capacitor length g_C . Dimensions of the fully-printed unit cell that achieves the desired stub filtering response are given in the first column of Table 4.1 (corresponding to dimension labels in Fig. 3.10b), and the simulated and fabricated dual-band, bandstop filters are shown in Fig. 4.4.

To observe the bandgap properties of the MTM-EBG unit cell, simulated complex electric field magnitudes are presented in Fig. 4.5. A quarter-wavelength standing-wave resonance is observed at each frequency as a null is produced at the microstrip junction, and the MTM-EBG clearly shows strong bandgap behaviour at the higher

Table 4.1: MTM-EBG Unit Cell Dimensions in Multi-Band Microstrip Stubs, Given in mm

	DB Rect. Stub	DB Rad. Stub	TB Stub, MTM-EBG A	TB Stub, MTM-EBG B
l	8.00	5.40	2.70	3.90
w	3.70	6.28 ^a	3.74	3.74
s	0.60	0.30	0.20	0.20
g_C	2.47	1.52	1.11	1.35
g_L	0.40	0.60	0.50	0.50
d_1	0.25	0.26 ^a	0.05	0.05
d_2	0.20	0.20	0.05	0.05
d_3	0.40	0.20	0.10	0.10

^a Average value

frequency; this confirms that it is operating as intended. The dual-band filter was fabricated and measured with an Agilent PNA-X Network Analyzer, the setup of which is shown in Fig. 4.6, and S -parameters of the dual-band filter are presented in Fig. 4.7. Simulation and measurement data for the stub filter show excellent agreement and demonstrate strong insertion losses, well over 20 dB at each design frequency. The 10-dB bandwidths are fairly narrow in each band due to the MTM-EBG being more dispersive than an equivalent length of microstrip, and a comparison to the bandwidths of conventional stubs is presented in Table 4.2. The dual-band filter, however, maintains large enough bandwidths to cover multiple channels in each band, rendering it useful for many applications.

The dual-band filter is, in total, 16.05 mm in length, which is 17.7% shorter than a conventional microstrip stub filter at the lower operating frequency. Embedding the MTM-EBG unit cell into the stub not only provides added functionality, but also reduces the stub footprint and can be fabricated in exactly the same way. Therefore, the dual-band stub provides many advantages over the canonical design for applications

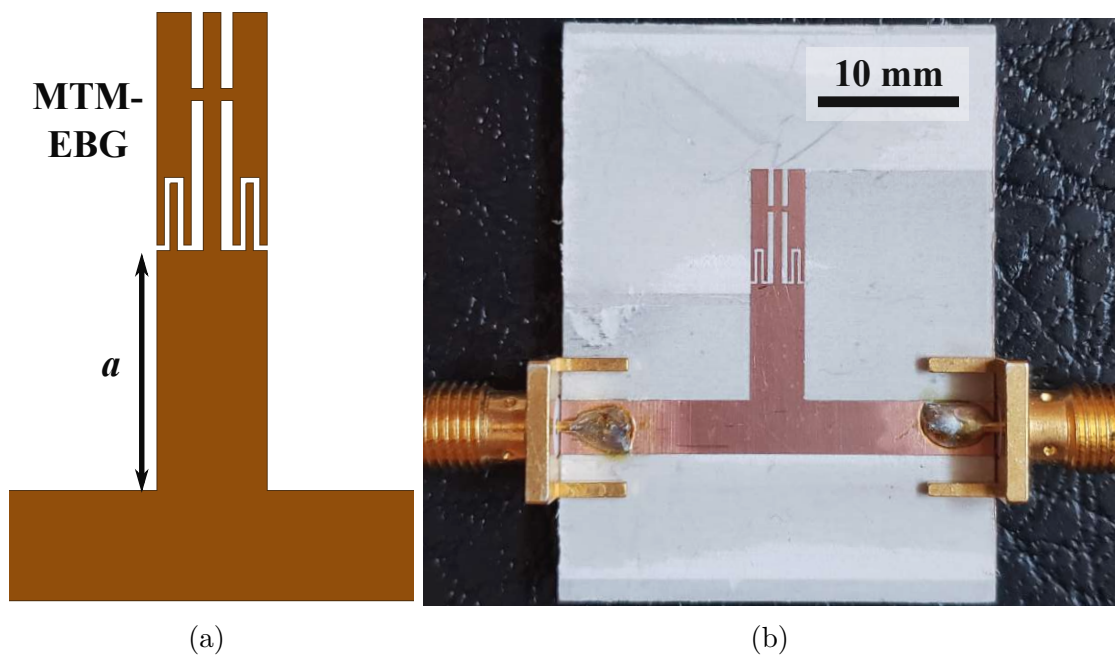


Figure 4.4: (a) Simulated dual-band bandstop stub filter, consisting of a stub of length $a = 8.05 \text{ mm}$ topped with an MTM-EBG unit cell with dimensions given in Table 4.1. (b) Fabricated stub filter.

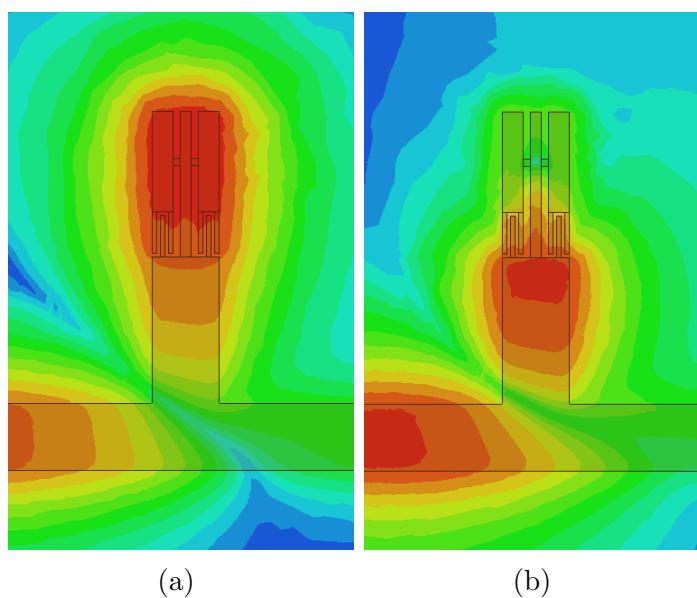


Figure 4.5: Complex electric field magnitudes of the dual-band rectangular stub in a plane bisecting the substrate, plotted on a logarithmic scale, at (a) 2.4 GHz and (b) 5.8 GHz.

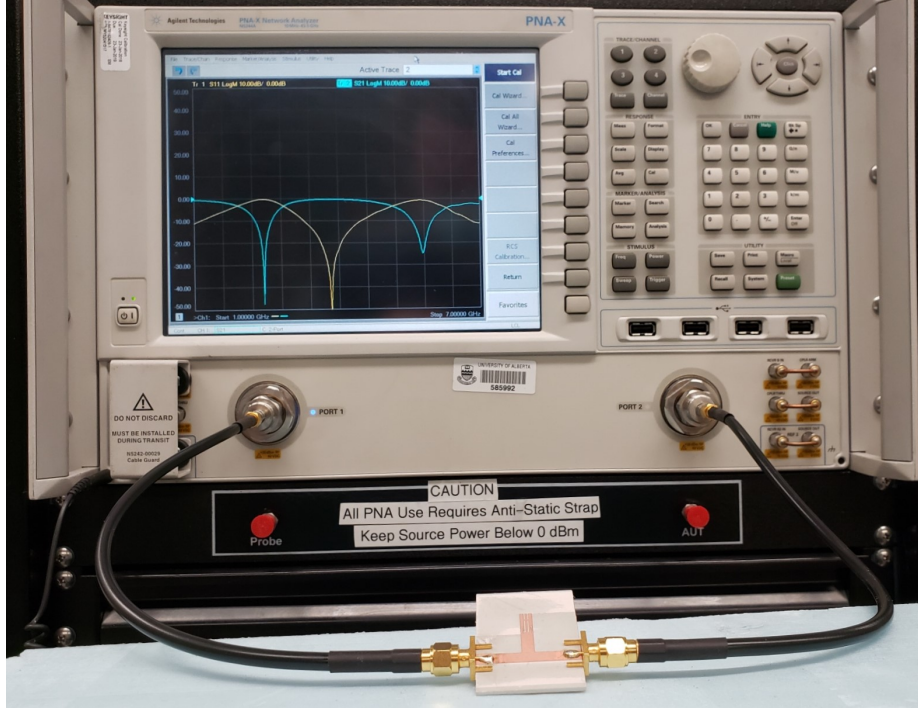


Figure 4.6: Measurement setup of the dual-band rectangular bandstop stub filter.

in which a mild reduction in bandwidth can be tolerated.

4.2.2 Dual-Band Radial Stub

In cases where larger stub bandwidths are desired, radial stubs that are flared with some angle α can be used with largely the same approach. An MTM-EBG unit cell that has a bandgap at 5.8 GHz and a specified phase to account for the difference in conventional stub radii is needed. In this case, however, the radial stub has a large arc length, so three MTM-EBG unit cells are placed azimuthally along the curve, and the geometry of the unit cell becomes radial. The unit cell properties are still modeled with the rectangular circuit model, and previous works show that this remains a good approximation [2, 194, 195]. A small amount of additional tuning is required as a result.

The simulated and fabricated dual-band radial bandstop stub is shown in Fig. 4.8, with all MTM-EBG dimensions given in Table 4.1. The total length of the dual-band stub is 12.0% shorter than a conventional radial stub at the lower operating

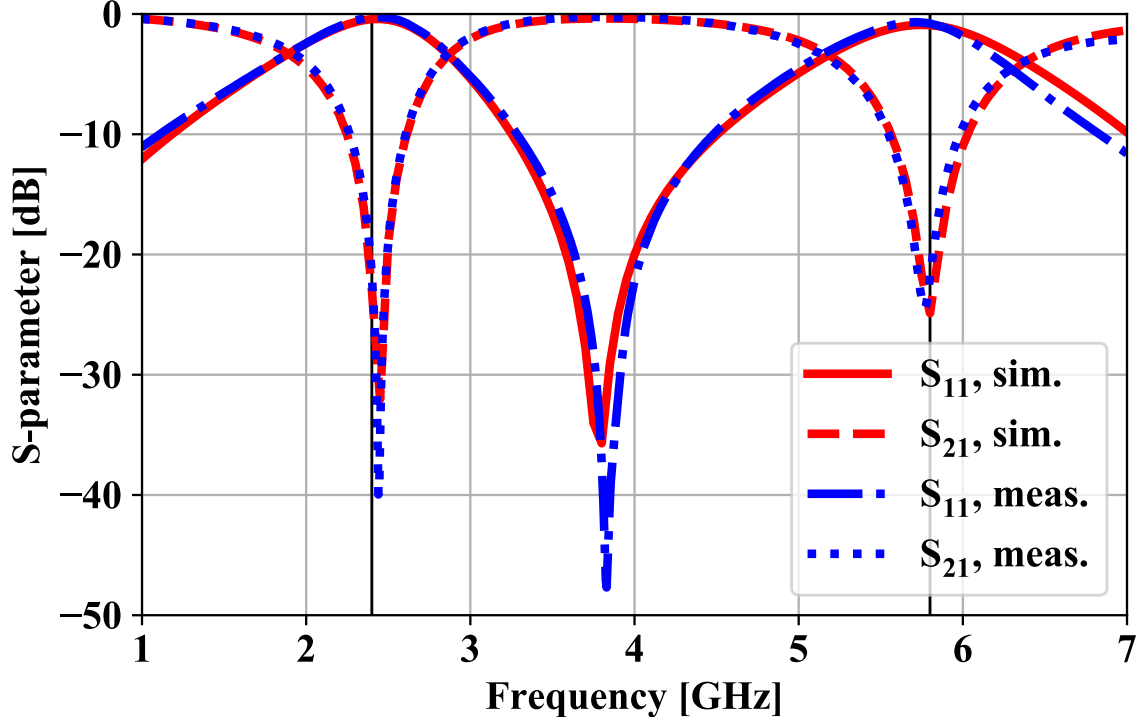


Figure 4.7: Simulated and measured S -parameters of the dual-band, rectangular bandstop stub filter. Operating frequencies are indicated by vertical black lines.

frequency. Notice that while features such as the unit cell width and capacitive teeth extend radially outward, the capacitive gap in between the teeth (d_2) is left at a constant width of 0.2 mm for consistent fabrication.

S -parameters of the dual-band radial stub filter are presented in Fig. 4.9, and once again, excellent agreement is observed between simulation and measurement. Strong bandstop responses are produced at the two operating frequencies with larger bandwidths than in the dual-band rectangular case, particularly in the lower band; the bandwidth around 2.4 GHz is more than doubled, showing an increase of 131.6%. Filtering bandwidth around the higher operating frequency is partially dependent on the MTM-EBG bandgap size (since the MTM-EBG must produce a bandgap over the whole filtering bandwidth to preserve the shorter effective stub length), so the bandwidth increase is less dramatic. Regardless, significant bandwidth improvement of 33.9% is observed. The bandwidths of the radial stub are included in Table 4.2 for comparison, and in cases where dual-band filtering is required, bandwidth of the

Table 4.2: Stub Filter 10-dB Bandwidths

Stub	BW at 2.4 GHz	BW at 3.6 GHz	BW at 5.8 GHz
Single-band Rect. ^a	518 MHz/21.6%	715 MHz/19.9%	978 MHz/16.9%
Single-Band Rad. ^a	1235 MHz/51.5%	1382 MHz/38.4%	1496 MHz/25.8%
Dual-Band Rect.	365 MHz/15.2%	N/A	469 MHz/8.1%
Dual-Band Rad.	845 MHz/35.2%	N/A	628 MHz/10.8%
Tri-Band Rect.	320 MHz/13.3%	131 MHz/3.6%	299 MHz/6.0% ^b

^aDifferent stub simulated at each frequency. ^bBW given at design frequency of 5.0 GHz

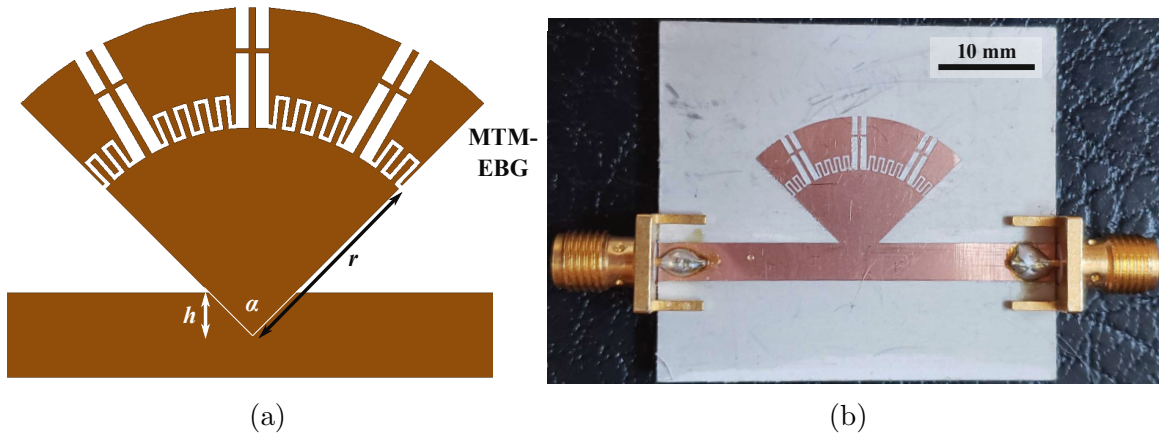


Figure 4.8: (a) Simulated and (b) fabricated dual-band bandstop stub filter with radial geometry, with $\alpha = 90^\circ$, $r = 9.29 \text{ mm}$, and $h = 1.90 \text{ mm}$. Dimensions of the MTM-EBG unit cells are provided in Table 4.1

application determines which stub geometry should be used.

Finally, note that the small notch near 4.1 GHz is a result of a weakly-excited transverse resonance across the radial stub (the distance from the leftmost to rightmost vertices approximates a guided half-wavelength). As expected, this is not observed in the rectangular stub case, and only results in a small amount of loss at that frequency. It could be shifted by adjusting the stub angle α if need be.

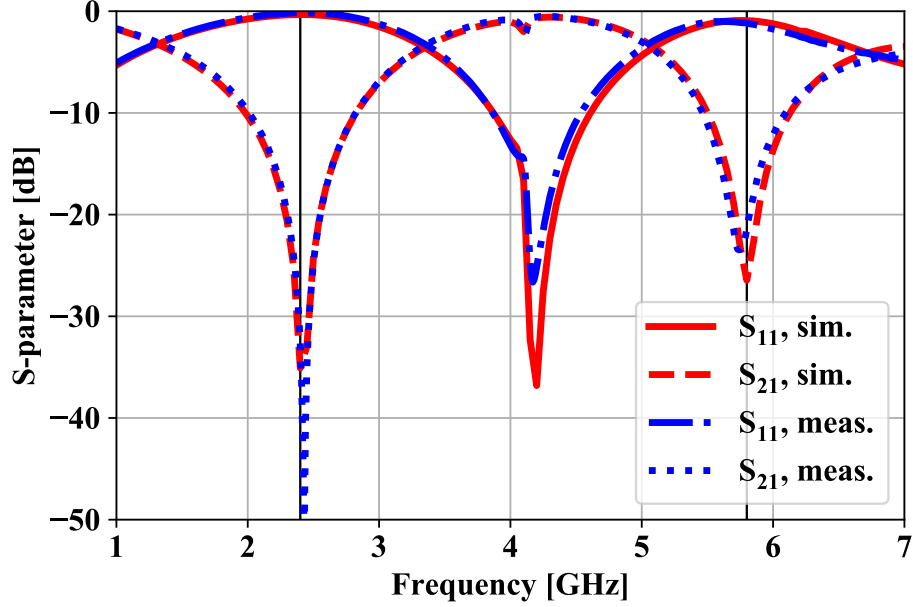


Figure 4.9: Simulated and measured S-parameters of dual-band, radial bandstop stub filter. Operating frequencies are indicated by vertical black lines.

4.2.3 Tri-Band Stub

While the use of a single MTM-EBG unit cell renders a bandstop stub filter dual-band, two embedded unit cells enable tri-band operation (or, generally, N unit cells facilitate operation in $N + 1$ bands). The tri-band design shown in Fig. 4.10 will demonstrate this by acting as a filter at 2.4 GHz, 3.6 GHz, and 5.0 GHz simultaneously. This design also tackles the challenge of creating large printed capacitances in small MTM-EBG unit cells by creating interdigitations with a $50 \mu\text{m}$ feature size. This could not be achieved with chemical etching or physical milling, but can be achieved with laser milling. Specifically for this fabrication, an LPKF Protolaser U3 laser milling system was used, which can achieve a minimum feature size nearly down to $10 \mu\text{m}$. Note that 1/2-oz rolled copper ($17 \mu\text{m}$ thickness rather than the $35 \mu\text{m}$ thickness used in previous designs) was used on the R03003 substrate to reduce the amount of copper required to be etched from the capacitive gaps.

Two MTM-EBG unit cells are used: MTM-EBG A, which has a bandgap at 5.0 GHz, and MTM-EBG B which has a bandgap at 3.6 GHz. The way in which

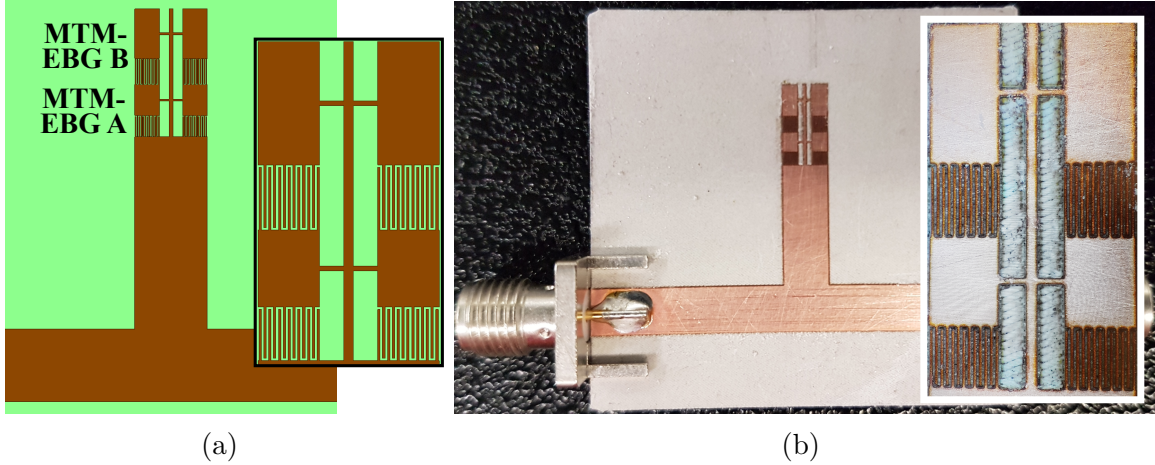


Figure 4.10: (a) Simulated layout and (b) fabricated tri-band stub, each with closeups of the embedded MTM-EBG unit cells to show the $50 \mu\text{m}$ features. Reproduced from [196] ©2018 IEEE.

the bandgap locations as well as phase properties of each unit cell result in a quarter-wavelength of phase at each operation frequency is demonstrated in Fig. 4.11. This dispersion diagram shows curves for each of the MTM-EBG unit cells as well as for the stub itself, and operating frequencies are indicated by dashed horizontal lines. As expected, both MTM-EBG unit cells are in their bandgap region at the higher operating frequency, and the microstrip region of the stub (which is $a = 9.9 \text{ mm}$ in length) incurs the required 90° of phase. At 3.6 GHz, MTM-EBG B remains in its bandgap region, but the stub and MTM-EBG A incur 67° and 23° of phase respectively, for a total of 90° . Both MTM-EBG unit cells transmit at 2.4 GHz, and they combine with the stub to produce the third 90° phase condition. Dimensions of the MTM-EBG unit cells (after minor tuning) can be found in Table 4.1.

Complex electric field magnitudes are presented in Fig. 4.12 to again confirm that both MTM-EBGs are providing the expected bandgap response, and this is compared to the fields of respective conventional stubs. Despite the small MTM-EBG lengths, three individual resonances are clearly supported. Miniaturization of the stub is apparent in Fig. 4.12a as well, since tri-band filtering is achieved with a stub that is 15.4% shorter than a conventional stub at the lowest frequency.

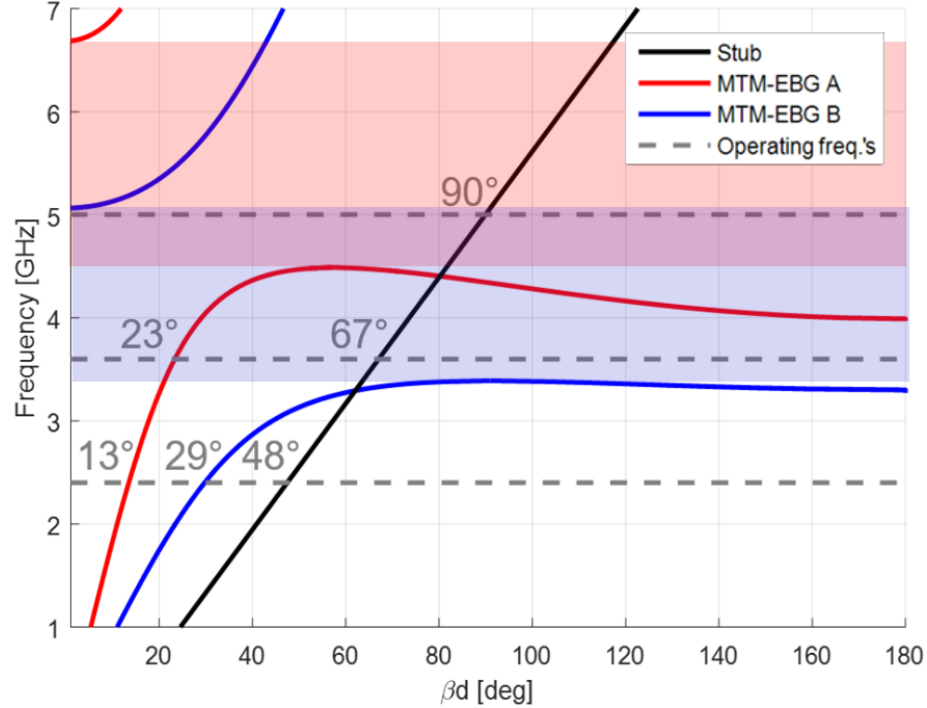


Figure 4.11: Dispersion diagram including all individual segments of the tri-band stub. Bandgaps for each unit cell are highlighted.

Agreement in S -parameters between the simulated and measured results is evident in Fig. 4.13. Three stop bands centred at the given operating frequencies are clearly visible, each demonstrating insertion loss better than 20 dB and return loss below 1 dB. The fabricated device displays a slight frequency shift (below 2.2%) that is likely the result of some substrate debris in between the small capacitive digits. Fig. 4.14 compares S -parameters for three respective conventional stubs and the tri-band device; it is apparent that the MTM-EBG-based device exhibits higher selectivity as compared to the individual single-band devices, and exact bandwidths are included in Table 4.2.

4.2.4 Additional Stub Properties

Some further stub filter properties merit discussion. Many of these concepts can easily be transferred to other MTM-EBG-devices as well, so while these filters act as

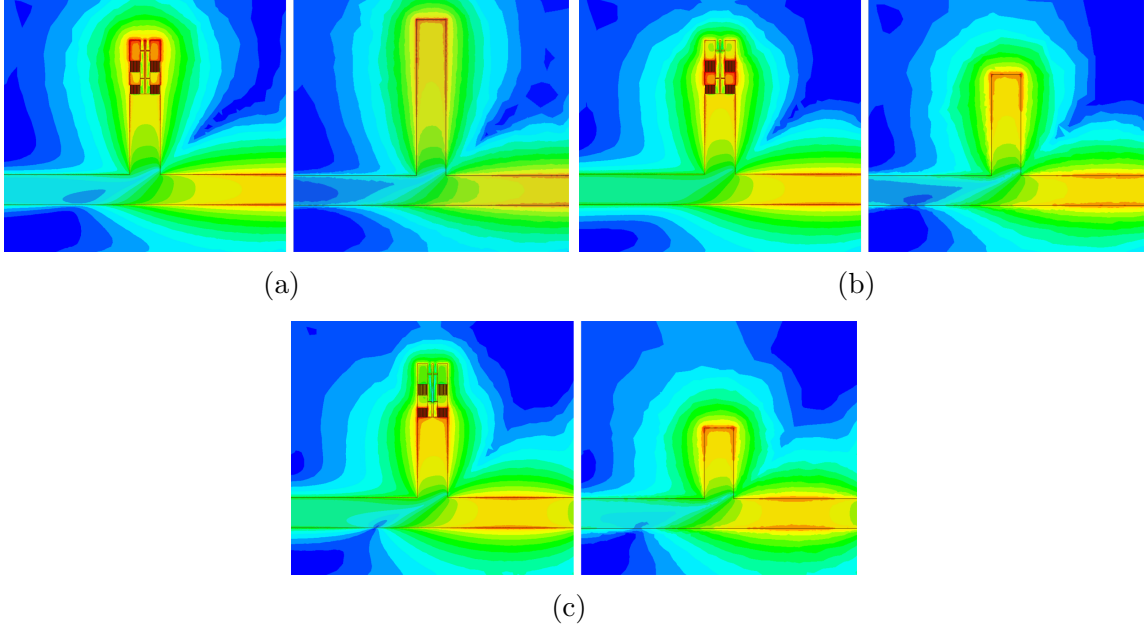


Figure 4.12: Complex electric-field magnitudes at tri-band stub resonances (left) versus corresponding conventional devices (right); excitation is at the right port. (a) 2.4 GHz resonance, (b) 3.6 GHz resonance, (c) 5.0 GHz resonance. Reproduced from [196] ©2018 IEEE.

a good example, these ideas can be taken more generally.

4.2.4.1 Loss in Resonant Structures

Field profiles of these multi-band stub filters show that a resonant length is observed at each operating frequency. When transmitting, the MTM-EBG unit cells have strong fields throughout, and in their bandgap region, some strong fields are observed penetrating into the MTM-EBG unit cells' capacitors, while fields throughout the cell are small but non-zero. With strong fields existing in the MTM-EBG and in particular in proximity to its finer features, it is worth investigating whether this significantly contributes to any dissipative loss.

Simulated and measured loss is shown for the dual-band rectangular stub filter in Fig. 4.15, calculated with the standard power loss definition of

$$P_L = 1 - |S_{11}|^2 - |S_{21}|^2. \quad (4.1)$$

Note that all realistic material losses (conductor and dielectric) are included in simu-

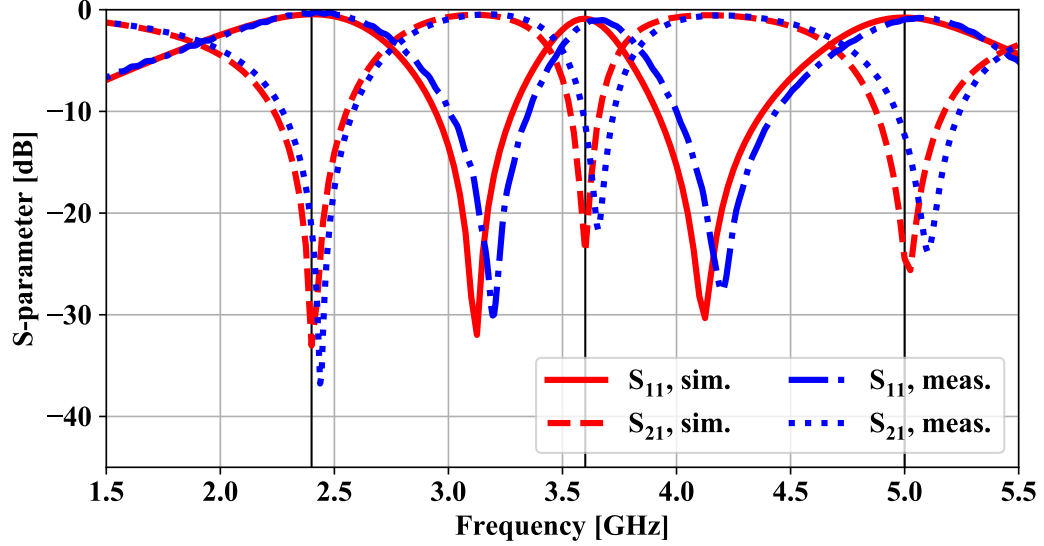


Figure 4.13: S -parameters of the simulated and fabricated tri-band stub. Data reproduced from [196] ©2018 IEEE.

lation. For the most part, especially under 5 GHz, losses in the dual-band stub filter are comparable to those in the standard filters, at below 10% of the total power. Interestingly, measured losses are even lower than simulated in this range, indicating that losses are slightly overstated in the simulation models. Loss increases near the upper filtering resonance in all cases, and this is particularly true for the measured data which begins to diverge from measurements; however, the likely candidate for the disagreement is the subminiature version A (SMA) connectors used, which are only rated up to 6 GHz.

While loss in the dual-band case is not insignificant, it is comparable to conventional stubs and it can be concluded that the presence of MTM-EBG unit cells does not substantially increase dissipative losses in the system, even with strong fields present in the MTM-EBG. This is true whether or not the MTM-EBG unit cells are transmitting or in their bandgap region. Similar results are observed for all multi-band stub filters in this work.

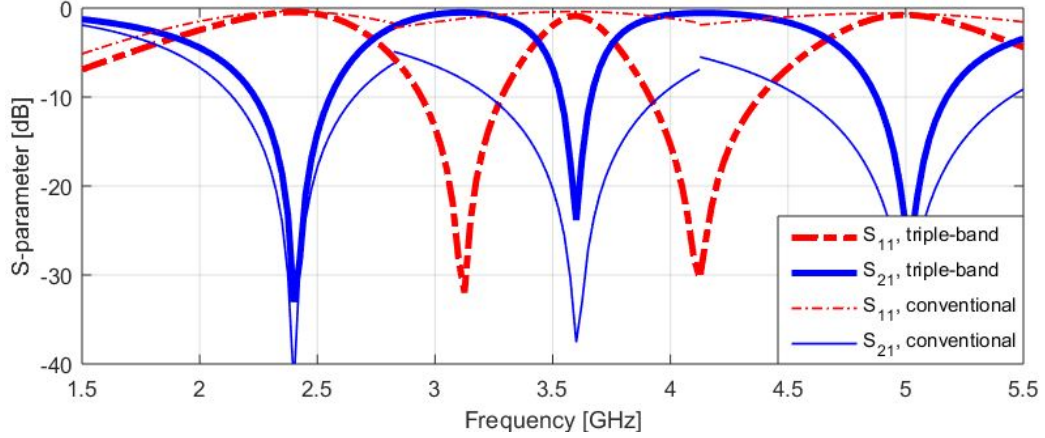


Figure 4.14: Comparison of tri-band stub response to conventional stub responses, as plotted near their respective resonances. Reproduced from [196] ©2018 IEEE.

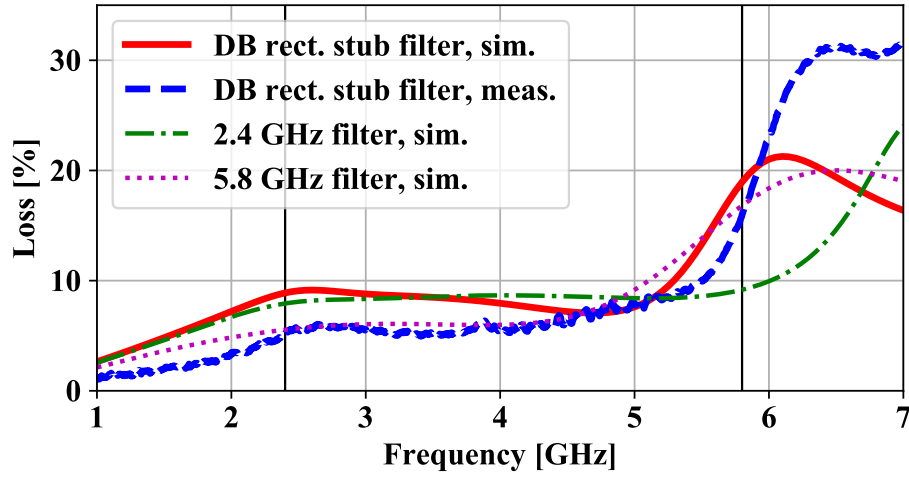


Figure 4.15: Simulated and measured loss of dual-band rectangular stub filter, compared to conventional stub filters at the chosen operating frequencies.

4.2.4.2 Harmonic Bands

The focus of all presented stubs has been to create a quarter-wavelength resonance at each of the desired operating frequencies. Discussion of harmonic bands has been neglected since this is not the primary intended function of the devices, but it merits discussion. For a standard microstrip stub, filtering is expected at all odd harmonics (or near to the odd harmonics in a realistic case); for example, an HFSS simulation of a stub that is a quarter wavelength at 2.4 GHz shows that additional filtering bands are produced at 7.0 GHz, 11.1 GHz, 15.0 GHz, and so on. A stub that is a quarter

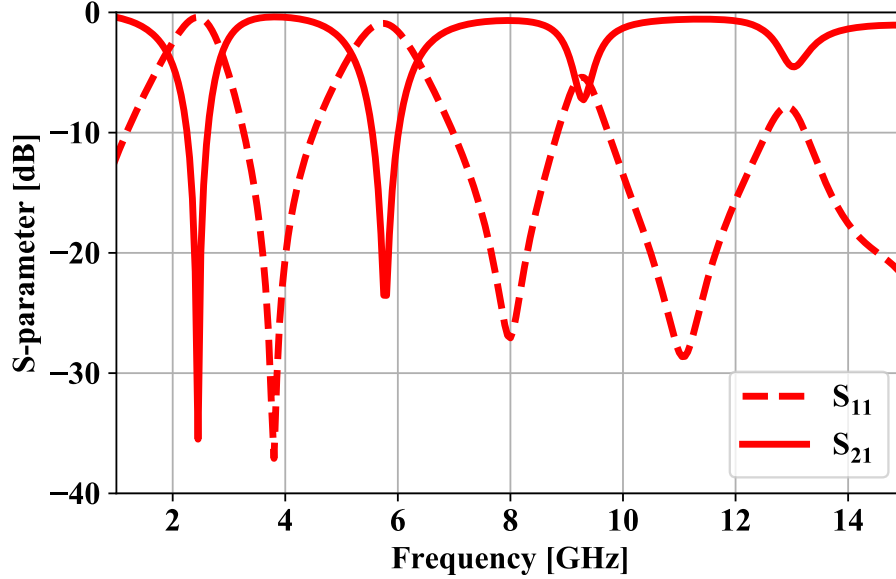


Figure 4.16: Broadband response of dual-band rectangular stub.

wavelength at 5.8 GHz, by contrast, has no harmonic bands below 15 GHz. Now, what happens for a dual-band stub that operates at both 2.4 GHz and 5.8 GHz?

Consider the broadband response of the dual-band rectangular stub presented in Fig. 4.16. The designed first-order filtering bands are observed at the two intended operating frequencies, and then weak filtering bands at 9.3 GHz and 13.1 GHz are additionally observed. Note that neither of these higher bands are harmonics of the design frequencies. That is to be expected, since the dispersion of the MTM-EBG is not uniform, but contains a non-periodic bandgap instead, around which it is dispersive. In other words, no harmonics related to the 5.8 GHz band are to be expected since the MTM-EBG unit cell would require a periodic bandgap for this to be the case, and dispersion of the MTM-EBG unit cell at 2.4 GHz (which is evidently a factor since the overall stub length is shorter than a conventional stub alone) causes the upper bands to shift from their expected harmonic locations.

In some applications, these properties could be extremely useful. Consider as an example the design non-linear devices, such as power amplifiers, in which intermodulation distortion is a problem and needs to be filtered out. An appropriately dispersive MTM-EBG-based stub filter could theoretically be used to transmit at the operating

frequency while simultaneously filtering out the higher-order intermodulation products that can occur at or near harmonic bands, thereby improving performance. Alternatively, a frequency may be filtered out (for example, an unwanted band received by a broadband antenna), but its harmonic band will still be received.

Another simple application of the MTM-EBG that takes advantage of its non-harmonic properties would be to implement single-band filtering directly into a TL that is being used for broadband applications with an embedded unit cell directly in the main TL. Such a simple device would provide filtering at the desired frequency, but not at the harmonics. This contrasts with other resonant filtering devices such as the SRR, in which harmonics will have to be considered at higher frequencies.

4.2.4.3 Bandwidth

The issue of bandwidth can easily become convoluted to discuss since the term may refer to several different parts of the structure. The bandgap bandwidth of the MTM-EBG unit cell itself is one context in which the term is used; this refers explicitly to the bandwidth for which the MTM-EBG is reflecting power (or in its bandgap region). This bandwidth is obtained from dispersion diagrams for an infinite cascade of unit cells, or with transmission simulations for a finite number of unit cells, in which case a 10-dB bandwidth is usually defined. Bandgap bandwidth of the MTM-EBG is designable from dispersion analysis, and can be chosen to be large or small based on physical dimensions and loading; a single unit cell will have a smaller bandgap bandwidth that is related to this, but approaches it as a large number of cascaded unit cells are used.

Oftentimes in this work, bandwidth to refers to the frequency range over which a device operates to a given specification. For example, the stub filters have a 10-dB bandwidth over which they reflect power, or an antenna might have a reflection or gain bandwidth to meet some specification. The overall device bandwidth may be related to the bandgap bandwidth of a constituent MTM-EBG unit cell, but is not

required to be. The relation between the two, in fact, can be fairly complex, especially since the design process is intentionally simplified to focus on two primary operating frequencies, rather than two frequency bands.

To determine the relationship between MTM-EBG bandgap bandwidth and device bandwidth, consider the dual-band rectangular stub, starting with the 2.4 GHz band. A single-band rectangular stub has a 10-dB device bandwidth of 518 MHz/21.6% around this frequency, while the dual-band stub filter observes a device bandwidth of 365 MHz/15.2%. The MTM-EBG is transmitting at this frequency, so its bandgap would only cause a reduction in device bandwidth if these two quantities overlap. The dispersion diagram in Fig. 4.3 suggests that this is not the case, as the lower edge of the MTM-EBG 3-dB bandgap bandwidth is found above 4 GHz, well above the upper edge of the 10-dB device bandwidth, at 2.61 GHz. The reduction in bandwidth is caused instead by the fact that the MTM-EBG unit cell is more dispersive than the underlying microstrip at this frequency, which inherently causes a reduction in device bandwidth. Further from the MTM-EBG bandgap, the dispersion more closely approaches that of a microstrip, so this leads to a general principle in cases where the MTM-EBG transmits at one of the operating frequencies: *the further the spacing is between operating frequencies, the more device bandwidth can be obtained at a frequency where the MTM-EBG is transmitting*. Of course, increased dispersion also manifests as a smaller physical size, so there is a trade-off between circuit size and bandwidth. Given that the MTM-EBG is embedded into the circuit to render it multi-band, however, miniaturization is primarily achieved by realizing dual-band operation in the space of a single-band device, and any miniaturization due to dispersion is typically secondary.

The 5.8 GHz band of the rectangular stub can now be considered. This is the band in which the MTM-EBG does observe a strong, though not uniform, bandgap. Its bandgap bandwidth is now a limiting factor of the device bandwidth, since the device will only operate as expected over this range. Ideally, the MTM-EBG bandgap

bandwidth should be larger than the bandwidth of a conventional device, so that the dual-band version has the potential to achieve a similar bandwidth. In practice, however, a conventional stub filter at 5.8 GHz was simulated to have a bandwidth of 978 MHz/16.9%, while the dual-band stub filter has a device bandwidth of 469 MHz/8.1%. This large difference merits further investigation.

First, a look at the dispersion diagram shows that the conventional device bandwidth is well covered by an infinite cascade of MTM-EBG unit cells, while a transmission simulation shows that the strength of the bandgap varies widely over that range. The stub filter was optimized for operation at 5.8 GHz so the MTM-EBG has its strongest bandgap at that frequency, but it falls to below the 10-dB insertion loss mark quickly, so significant reflections off the MTM-EBG will occur beyond that mark. A way to model this, as discussed, is to think of the MTM-EBG in its bandgap region as a lumped impedance rather than as an OC; alternatively, being aware of what the MTM-EBG bandgap bandwidth is can lead to an estimation of what the maximum device bandwidth will be as a result.

Confirmation that the MTM-EBG bandgap bandwidth limits the device bandwidth around 5.8 GHz comes from the radial stub filter. The radial stub filter bandwidth around 5.8 GHz is 10.8%, which is not a huge increase over the rectangular stub at this frequency, which has a bandwidth only 2.7% lower. By comparison, the difference in bandwidth between conventional rectangular and radial stubs at this frequency is 8.9%. Around the lower band, which is not limited by the MTM-EBG bandgap bandwidth, conventional devices see a 29.9% increase in bandwidth with a change in geometry from rectangular to radial, while the dual-band versions see a more comparable 20.0% bandwidth increase. Clearly, the MTM-EBG bandgap bandwidth plays a significant role in the device filtering bandwidth around 5.8 GHz.

This effect is magnified for the tri-band stub. The middle band has a narrow bandwidth, but this is to be expected, since the MTM-EBG has a narrower bandgap bandwidth as its center frequency is shifted down. MTM-EBG B has a bandgap

at 3.6 GHz, so this is the unit cell that limits the filtering bandwidth around this frequency.

General conclusions can be drawn from this study, allowing the question of bandwidth to require less rigorous consideration for future devices. First, when the MTM-EBG is in its bandgap region, its bandgap bandwidth tends to limit device bandwidth. When it is transmitting, the device bandwidth will be more comparable to that of its conventional counterpart. This approximation becomes more accurate for operating frequencies that are further separated. Additionally, the MTM-EBG may constrain device bandwidth substantially as its bandgap frequency is lowered, since its bandgap bandwidth reduces commensurately.

4.3 Dual-Band Matching Network

4.3.1 Approach

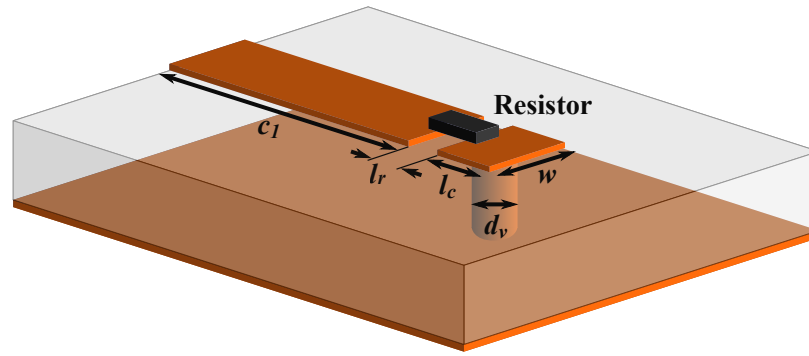
The stubs presented so far are resonant stubs for filtering applications, chosen as a simple example where the ability of the MTM-EBG to enable dual-band behaviour is clear. While this is useful in many applications, it is by no means the only or even primary use of microstrip stubs; they also act as distributed reactive elements when not operating at resonance, which makes them amenable to applications such as impedance matching. This section will focus on the use of non-resonant multi-band stubs; the chosen example is the stalwart double-stub tuner, where two stubs separated by some fixed distance are used to match to an arbitrary input impedance. Dual-band operation will again be achieved using stubs with embedded MTM-EBG unit cells. A rigorous design procedure for the matching network is also developed, and minimization of dissipative loss in the system is examined. The versatility of this approach is further demonstrated in the subsequent section with the design of a tri-band matching network.

A dual-band double-stub tuner using embedded MTM-EBGs will be designed to

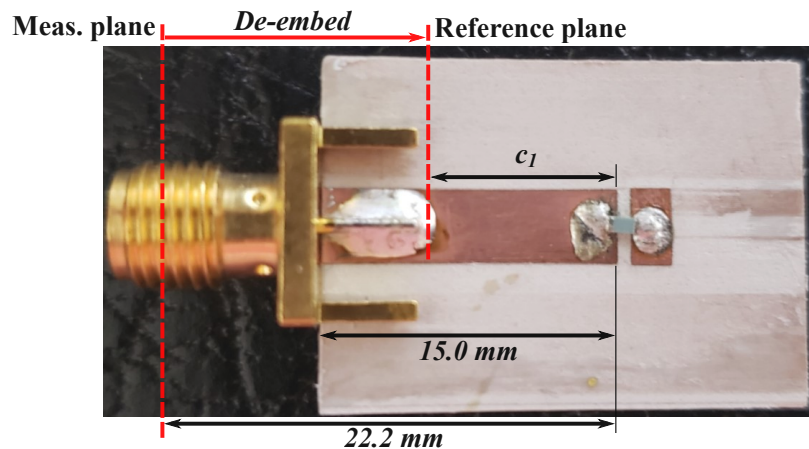
match a $50\ \Omega$ system impedance to an arbitrary, frequency-dependent load. The arbitrarily chosen load consists of a $100\ \Omega$ resistor in series with a capacitive pad that is $w = 3.7$ mm wide by $l_c = 2$ mm long, with a $d_v = 0.9$ mm diameter metallic via in the center that provides inductance. The load is modeled in Fig. 4.17a, while Fig. 4.17b shows a fabricated structure that is used to extract the load impedance for comparison to simulation. The fabricated load is measured with a PNA-X, and results are de-embedded from the measurement plane (the location where the SMA connector dielectric begins) to the reference plane [197]. The real and imaginary parts of the input impedance a distance of $c_1 = 10$ mm from the gap beneath the resistor is shown in Fig. 4.17c; the reason for presenting the impedance at this location will become apparent in the following subsections, as this is the impedance for which matching will ultimately be sought.

Matching to this load with a traditional double-stub tuner at one frequency is well understood, and a solution can be obtained through the use of a Smith Chart or with closed-form equations [56]. Two possible stub-length solutions exist for a given load impedance and stub separation distance, with the choice of solution typically being decided as the one with a smaller footprint. It is possible to have a load impedance fall in a “no-solution” region for which matching is not possible, although if the distance between the load and first stub is not fixed, the load impedance can always be transformed through some TL length into a region where solutions can be found, i.e. by changing c_1 .

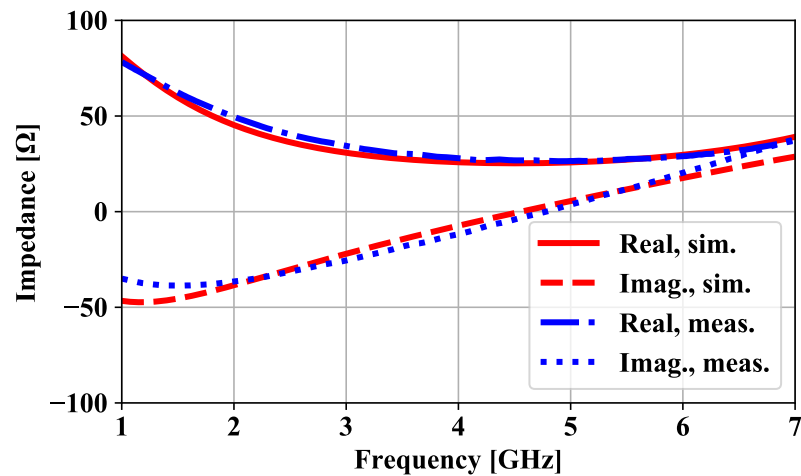
Creating a dual-band matching network requires two single-band solutions to be superimposed, as enabled by embedded MTM-EBG unit cells. Generally, each solution will be matched to a different impedance, as observed in Fig. 4.17c. The arbitrary load impedance (dependent on c_1), the many possible single-band solutions, and MTM-EBG design renders the creation of a dual-band matching network a complex problem. A systematic approach to all parts of this problem, resulting in an optimized solution, must be developed.



(a)



(b)



(c)

Figure 4.17: (a) Model of frequency-dependent load consisting of a $100\text{ }\Omega$ resistor over a gap of $l_r = 0.7\text{ mm}$, a capacitive plate with dimensions of $w = 3.7\text{ mm}$ by $l_c = 2\text{ mm}$, and a via of diameter $d = 0.9\text{ mm}$. (b) Fabricated load showing measurement plane and reference plane to which results are de-embedded. (c) Simulated and measured input impedance a distance of $c_1 = 10\text{ mm}$ from the load. Reproduced from [193] ©2023 IEEE.

4.3.2 Optimization Algorithm

Dual-band matching to the frequency-dependent load is sought at 2.4 GHz and 5.8 GHz. Single-band solutions must be found at each frequency, and then a double-stub tuner must be designed and rendered dual-band through the use of MTM-EBG unit cells. Since it is only the stubs that contain embedded MTM-EBG unit cells, both solutions must have the same distance between the load and first stub (c_1) and the same stub separation distance (hereafter called c_2).

For any given c_1 value, the load impedance must be in the solution region at each frequency. The value of c_2 is typically chosen to be either $\lambda_g/8$ or $3\lambda_g/8$ (where λ_g is the guided wavelength), since these distances result in a matching network that is less frequency-sensitive [56]. For a dual-band network with arbitrary operating frequencies this will not typically be possible, so a c_2 value that optimizes bandwidth in both bands should be found.

Another constraint arises from the fact that stub lengths at each frequency should be sufficiently different to allow an MTM-EBG unit cell to be embedded in that space. For example, assume that the single-band solutions determine the stub nearest to the load must be a_1 in length at the higher frequency, and a_2 in length at the lower frequency. If $a_2 > a_1$, then an MTM-EBG unit cell must be designed to provide a bandgap at the higher frequency and transmit at the lower frequency to effectively provide the correct stub length at each (or vice versa if $a_1 > a_2$). The difference in stub length $|a_2 - a_1|$ must, therefore, be above a threshold that allows the required MTM-EBG to be embedded in that space. The same applies to the stub nearer to the generator; if the stub lengths at the higher and lower frequency are b_1 and b_2 respectively, then $|b_2 - b_1|$ must also be larger than the determined threshold. What this threshold should be is a design choice; the amount of space that an MTM-EBG unit cell takes up depends on the bandgap frequency, whether printed or lumped capacitors are used, and what the minimum fabricated feature size is.

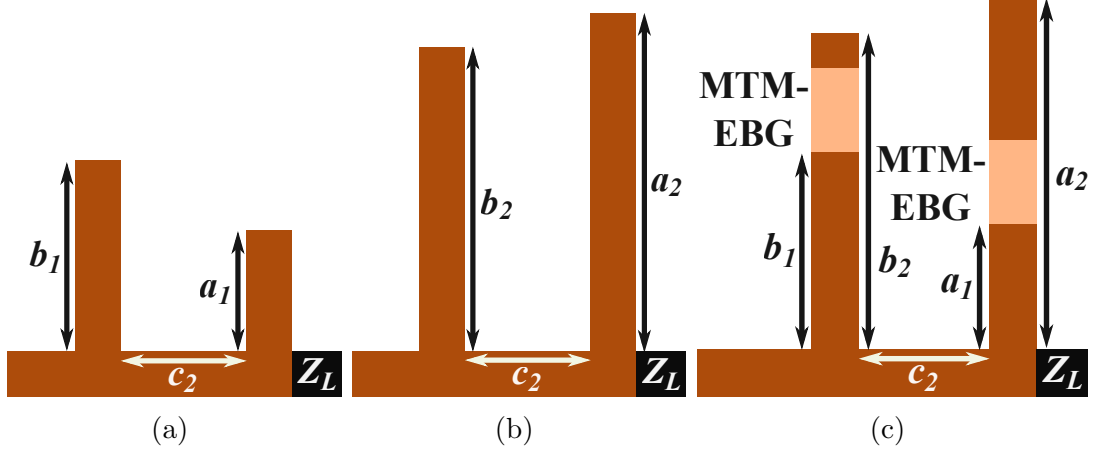


Figure 4.18: Representative depiction of microstrip dual-band matching network. A single-band double-stub tuner at (a) f_1 and (b) f_2 are effectively combined into a (c) dual-band double-stub tuner, enabled by embedded MTM-EBG unit cells that have a bandgap at f_1 but transmit with a designed phase at f_2 . Load impedance and the distance between the load and nearest stub, c_1 , are lumped into a frequency-dependent Z_L . Reproduced from [193] ©2023 IEEE.

While the constraint on the difference in stub length may seem restrictive, it is typically not difficult to overcome. For a given c_1 and c_2 , two solutions are available at each frequency, resulting in four possible combinations of solutions. Out of these combinations, it is likely that at least one meets the threshold for both stubs. A representative depiction of solutions that meet these requirements are shown in Figs. 4.18a and 4.18b, while Fig. 4.18c schematically demonstrates how MTM-EBG unit cells can be embedded to effectively render the double-stub tuner dual-band.

Note that the circuit operating at the lower frequency may not have the longer stubs, since the stub lengths are not resonant and may be anything between 0 and λ_g (although the lower frequency *tends* to have longer stubs since λ_g is larger at this frequency). It is also possible that the solution at one frequency has one longer stub and one shorter stub as compared to the solution at the other frequency. The optimization code allows for this possibility, and it is easily accommodated for by ensuring that any embedded MTM-EBG unit cell has a bandgap at the appropriate frequency required to facilitate this.

Taking these various restrictions into consideration, a large solution space still remains. Since closed-form equations provide solutions to the double-stub tuner for any choice of load impedance and stub separation distance, an algorithm can be written to determine an optimal solution within this space. The algorithm sweeps through values of c_1 and c_2 in small increments (from 0 to λ_g at the higher operating frequency), and finds the single-band solutions (if they exist) at both frequencies for each increment. Four solution combinations result at each step. A threshold for $|a_2 - a_1|$ and $|b_2 - b_1|$ is determined, and any solution that does not exceed both of these thresholds is discarded. A set of possible solutions for the given load arises.

Out of the possible solution set, the optimal solution is determined to be the one with the largest bandwidth in the searched parameter space (although for cases where specific bandwidths, return losses, or physical constraints are specified, a different optimization parameter can just as easily be used). This is achieved by first finding the frequency response of each of the possible solutions using circuit theory in combination with simulated values for the frequency-dependent load, de-embedded as necessary to the proper c_1 length. The 10-dB return loss bandwidth for each solution can then be determined, and the solution that provides the highest combined bandwidth while maintaining a minimum fractional bandwidth around each operating frequency is chosen.

The parameters fed into this algorithm can be adjusted in cases where they do not produce a solution, but in the large solution space available, this would mainly occur in cases where the stub difference threshold or minimum fractional bandwidth parameters are extreme. A more advanced optimization algorithm could also be used, but since all calculations are based on closed-form equations, a simple brute-force algorithm like the one described is quick and easy to implement.

The algorithm was run to find a solution for the dual-band matching network at 2.4 GHz and 5.8 GHz with the load impedance response that is shown in Fig. 4.17. The stub difference threshold was set to 6 mm, and fractional bandwidths of at least 25%

in each band were required. The optimal solution has values of $c_1 = 10$ mm (the load impedance is plotted at this reference plane in Fig. 4.17c) and $c_2 = 14.37$ mm. The stub lengths for the optimal solution at 5.8 GHz are determined to be $a_1 = 4.07$ mm (stub nearest to load) and $b_1 = 14.69$ mm (stub nearest to generator), and stub lengths at 2.4 GHz are $a_2 = 31.98$ mm and $b_2 = 36.55$ mm. The stub difference threshold is well exceeded in each case. The predicted 10-dB return loss bandwidth is 39.6% (950 MHz) and 29.0% (1680 MHz) at 2.4 and 5.8 GHz, respectively.

4.3.3 MTM-EBG Implementation

Now that complementary single-band solutions have been found, MTM-EBGs must be inserted into each of the stubs to produce an integrated dual-band matching network. The MTM-EBG unit cells should be the same width as the microstrip (3.7 mm in this case) and be shorter than the stub length difference threshold (6 mm). Since the MTM-EBG in each stub requires the same bandgap frequency, the same unit cell can be used for simplicity.

A fully printed MTM-EBG unit cell that meets these requirements can be found from Fig. 4.19, where the bandgap center frequency and 10-dB insertion-loss bandwidth is given as a function of capacitor length g_C . The unit cell is 4 mm in length, and all other dimensions of the unit cell are provided in the first column of Table 4.3. Fig. 4.19 shows that reducing capacitance (i.e., reducing g_C) results in the bandgap center frequency shifting upwards, and the absolute bandwidth correspondingly increasing. The strength of the bandgap remains nearly constant, with peak insertion loss between 26 dB and 28 dB. Note that since the unit cell is embedded into a microstrip, either end of the unit cell appears shorted; however, this actually provides, parasitically, the required inductance between the three MTM-EBG conductors, which is in parallel with the strip inductors seen in previous designs. Since the unit cell is electrically small, the strip inductors can be lumped in with the parasitic inductance of the short (which is of a similar magnitude), and thus are not

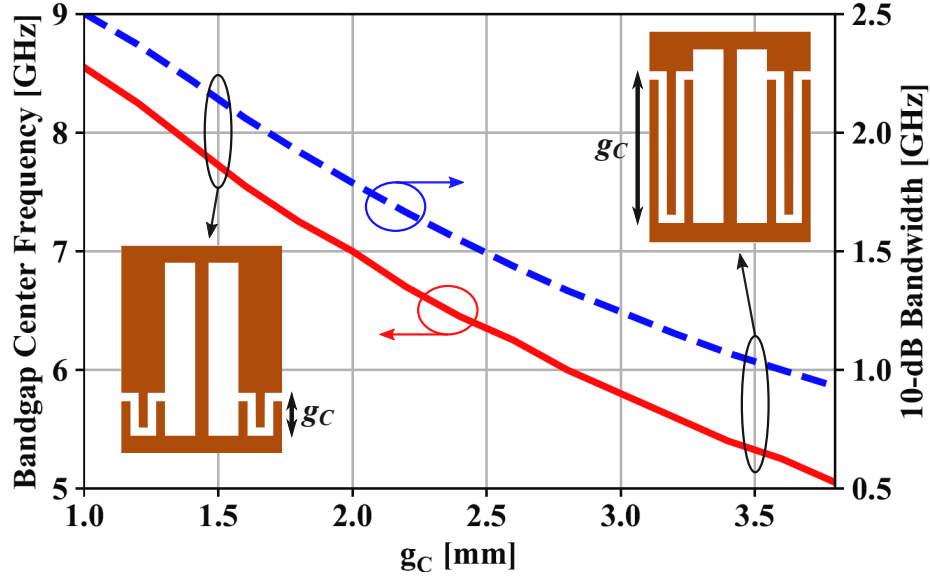


Figure 4.19: MTM-EBG bandgap center frequency (solid red) and 10-dB insertion-loss bandwidth (dashed blue) as a function of printed capacitor length g_C . Insets show what the embedded MTM-EBG unit cell looks like for $g_C = 1.5 \text{ mm}$ and $g_C = 3.5 \text{ mm}$. This plot only applies to an MTM-EBG on the chosen substrate with the dimensions given in Table 4.3. Reproduced from [193] ©2023 IEEE.

independently required in the unit cell design.

Inset in Fig. 4.19 are images of what the unit cell looks like for some different g_C values. Since g_C cannot exceed the length of the unit cell itself, this particular unit cell design is unable to provide a bandgap below approximately 5 GHz. For the present design, a bandgap at 5.8 GHz is needed, so this unit cell (with $g_c = 3 \text{ mm}$) is sufficient. In cases where lower-frequency bandgaps are needed, three options become available: i) reduce the size of the capacitive interdigitations to increase capacitance; ii) use discrete lumped capacitors rather than printed elements; or iii) redesign the unit cell (and, if necessary, the stub difference threshold) so that there is space for larger printed capacitors.

The MTM-EBG with the appropriate bandgap location can now be embedded into the matching network. It is placed at the end of the shorter stubs of length a_1 and b_1 , so that they remain the correct electrical length at the operating frequency of 5.8 GHz. For operation at 2.4 GHz where the MTM-EBG transmits, appended microstrip lines

Table 4.3: Dimensions of MTM-EBG Unit Cells in Multi-Band Matching Networks, Given in mm

	MTM-EBG A	MTM-EBG B
l	4.00	6.00
w	3.70	3.70
s	0.30	0.30
g_C	3.00	5.25
g_L	0.70	0.70
d_1	0.20	0.20
d_2	0.20	0.20

incur the remainder of the required phase. The dual-band double-stub tuner with embedded MTM-EBG unit cells is depicted in Fig. 4.20a.

All that remains at this stage is to tune the structure. The main reason that tuning is required is that the analytical description of the double-stub tuner used in the design algorithm does not include T-junction parasitics, and simple T-junction models that can be included in the analysis do not provide a sufficient increase in accuracy to render tuning unnecessary. The T-junctions are just as easily tuned out after the initial dual-band design. A simple way to do this is to reduce the length of each transmission line leading into a T-junction by some distance x . This amounts to reducing c_1 by x and c_2 by $2x$, where the value of x is on the order of 0.7 mm for the present design, and ensures that the matching bands occur at the designed frequencies. Further tuning of a_1 , a_2 , b_1 , and b_2 can fine-tune the results, but the tuning is minor, below $0.04\lambda_g$ at the higher operating frequency. Dimensions of the final dual-band matching network design are provided in the caption of Fig. 4.20.

4.3.4 Summary of Procedure

To summarize the design process for a dual-band matching network in full:

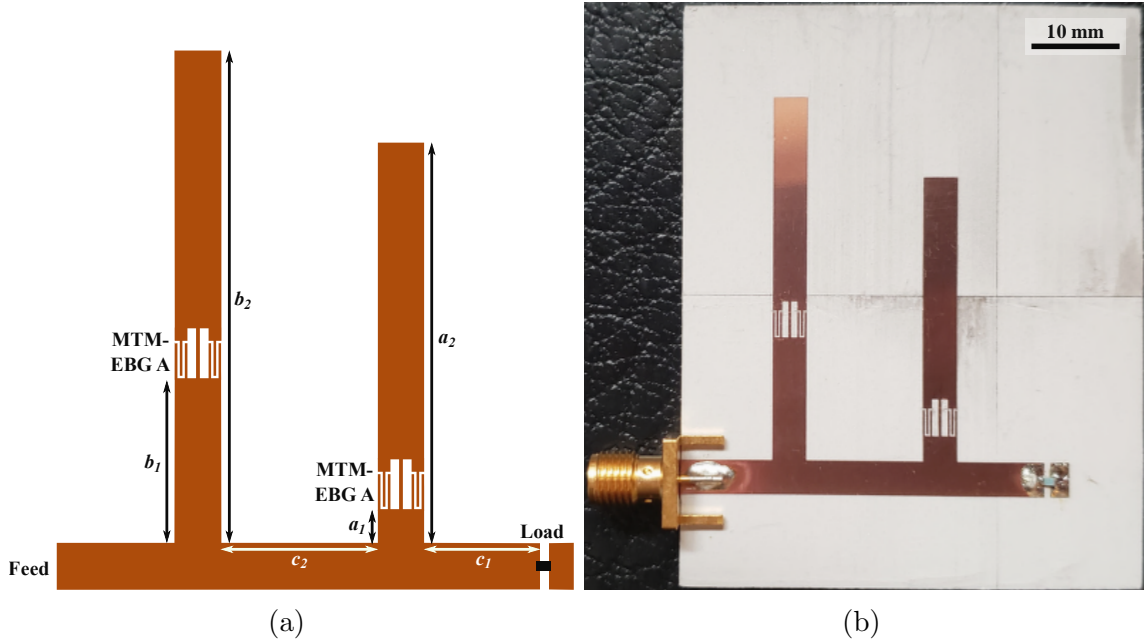


Figure 4.20: (a) Simulation model and (b) fabricated dual-band matching network. MTM-EBG A dimensions are given in Table 4.3, and other dimensions are: $a_1 = 2.75 \text{ mm}$, $a_2 = 31.00 \text{ mm}$, $b_1 = 13.37 \text{ mm}$, $b_2 = 39.75 \text{ mm}$, $c_1 = 9.34 \text{ mm}$, and $c_2 = 12.67 \text{ mm}$. Reproduced from [193] ©2023 IEEE.

1. Establish (e.g., by way of specification) the frequency-dependent load impedance, and the two frequencies to which it must be matched. Choose a substrate.
2. Use an algorithm to determine viable solutions, i.e., solutions at each frequency with the same c_1 and c_2 that have a minimum difference in stub length $|a_2 - a_1|$ and $|b_2 - b_1|$ based on the realistic size of an MTM-EBG unit cell.
3. Restrict viable solutions to ones that meet a minimum bandwidth requirement around each frequency, determined with circuit analysis. Choose a single solution out of these to optimize a particular trait of the system, e.g., largest combined bandwidth, or smallest circuit size.
4. Design an MTM-EBG unit cell with required bandstop properties and physical dimensions, using the same unit cell for both stubs if possible. A design table or graph like the one in Fig. 4.19 may be used.

5. Embed the MTM-EBG unit cell into the stubs at the required positions.
6. Simulate and tune the final structure to produce dual-band impedance matching around both desired operating frequencies.

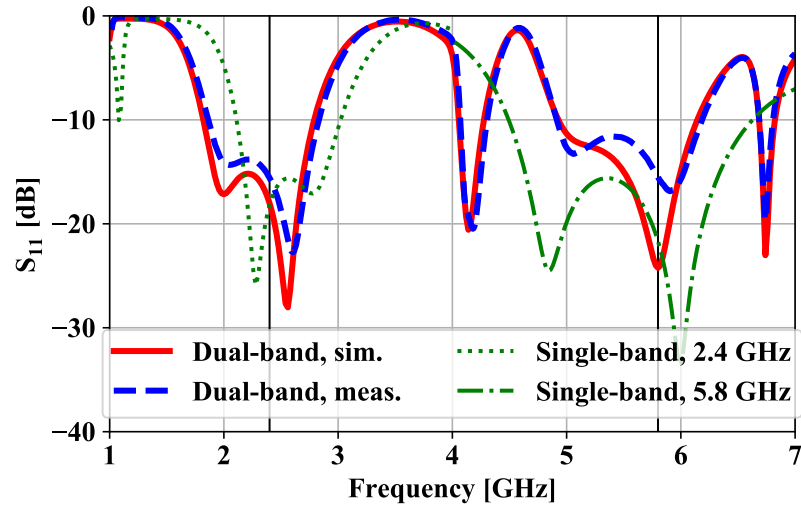
4.3.5 Results

4.3.5.1 S-Parameters

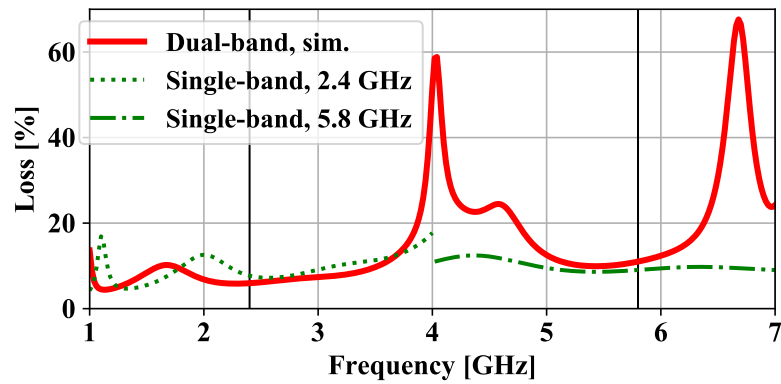
The final matching network was fabricated, as shown in Fig. 4.20b, and measured. Simulation and measurement results are presented in Fig. 4.21a, where very good agreement is observed, particularly above the -10 dB S_{11} level. For comparison, simulated matching networks of the single-band double-stub tuners are overlaid around their corresponding operating frequencies. Matching bands of the dual-band network present -10-dB bandwidths of 44.3%/1063 MHz and 22.1%/1284 MHz in the lower and higher bands, respectively. These bandwidths are similar to those predicted analytically, although a reduction in the upper band occurs since the predicted response is only valid within the bandgap bandwidth of the MTM-EBG A unit cell. Large bandwidths are otherwise preserved, in contrast to the resonant bandstop stub filters.

4.3.5.2 Loss Mechanisms and Mitigation

Two narrow bands that also appear to exhibit strong matching are additionally observed, one at 4.14 GHz and the other at 6.74 GHz. The origin of these features merits further investigation, specifically to determine whether the power is successfully delivered to the load in these bands, or if some resonant feature is causing dissipation instead; S_{11} alone does not distinguish these cases. As such, dissipative loss in the network is investigated in simulation. It is observed by comparing the net power flowing through a plane perpendicular to the direction of propagation at different points in the system. Consider a plane near the source; net power through this plane indicates power that makes it into the network, which may either be delivered to the load



(a)



(b)

Figure 4.21: (a) Simulated and measured S_{11} of the dual-band matching network compared to single-band matching networks (one each for matching at 2.4 GHz and 5.8 GHz, each plotted only over a frequency range of interest). (b) Simulated loss in dual- and single-band matching networks. Reproduced from [193] ©2023 IEEE.

or dissipated by loss. Subtract from this the net power through a plane next to the load (which gives the power delivered to the load), and the value that remains is the loss; this is then normalized to the total input power, and reported as a percentage. For the dual-band network, this loss value is given in Fig. 4.21b, where it is found that loss in the matching bands of the dual-band network is comparable to loss in single-band networks, around 10%. Note that realistic conductor and dielectric losses were modeled in these simulations.

What is also notable from this comparison is that loss spikes dramatically around resonant features corresponding to low reflection in the 4.14 GHz and 6.74 GHz bands. This indicates that a majority of power is not being delivered to the load at these frequencies, but is rather dissipated. As a result, the low S_{11} in these bands cannot be attributed to matching. The mechanism behind the loss is discovered by investigation of the complex electric field magnitudes at these two frequencies, shown in Fig. 4.22. A standing wave is observed at 4.14 GHz above the MTM-EBG unit cell in the stub on the left that corresponds approximately to $\lambda_g/2$ at this frequency, while a standing wave occurs in the upper part of the stub on the right at 6.74 GHz, corresponding to a length of λ_g . In each case, the MTM-EBG is partially transmitting, allowing the standing waves to form and to ultimately dissipate power.

It is important to ensure that these lossy resonances do not interfere with matching bands, and since their source is known, this can easily be achieved. Consider the resonance at 6.74 GHz. If the length of the stub nearer to the load (which supports the dissipative resonance) changes slightly, the resonance should shift correspondingly, and this is demonstrated in Fig. 4.23. It is observed that as the stub length increases, the resonance and loss peak shift downwards, eventually causing loss in the matching band and effectively shrinking it. The amount of loss decreases nearer to 5.8 GHz as the MTM-EBG presents a stronger bandgap and thereby limits the amount of power coupling into the resonance, but the effect is still detrimental. Finally, notice that the change in stub length only has a minor effect on the matching band around

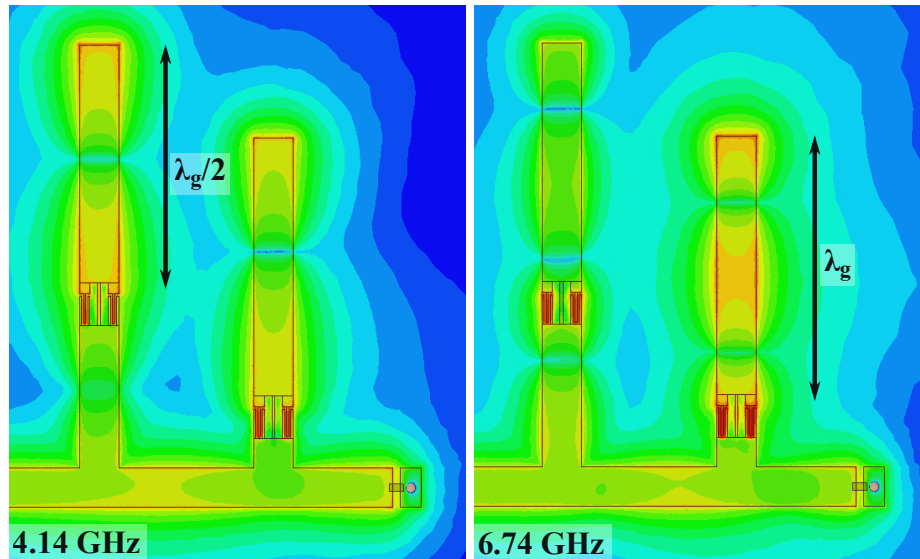


Figure 4.22: Complex electric field magnitudes of the dual-band matching network at frequencies of loss-causing resonances. Reproduced from [193] ©2023 IEEE.

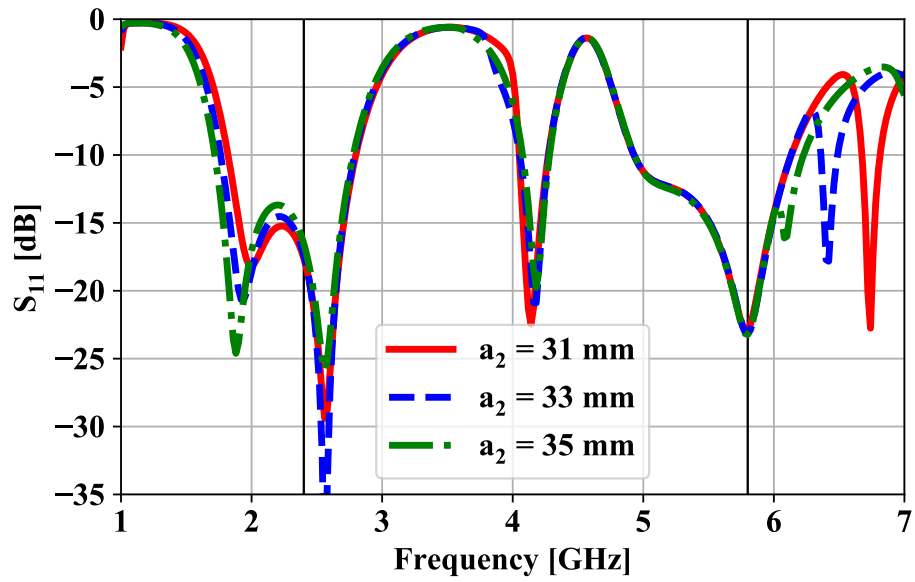
2.4 GHz, since the change in stub length is electrically small near this frequency. It can therefore be ensured that the spikes in dissipative loss are shifted away from the matching bands.

4.4 Tri-Band Matching Network

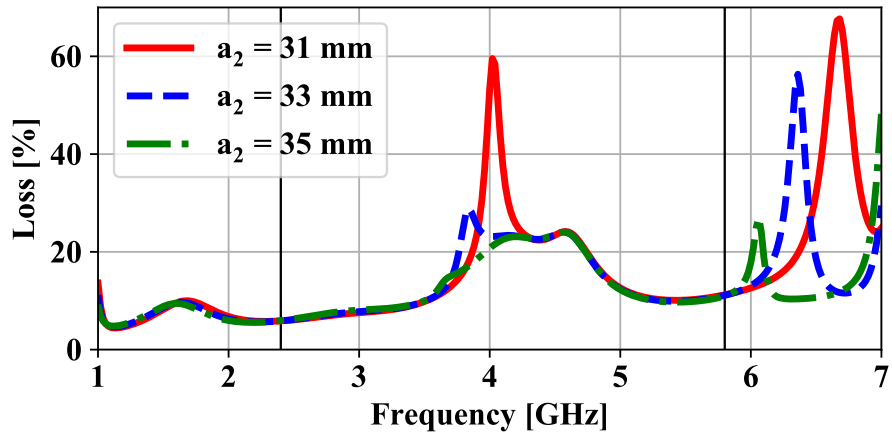
4.4.1 Design Steps

The concept behind the dual-band matching network can be expanded to by adding a second MTM-EBG unit cell to each stub, rendering them, and therefore the entire network, tri-band. As with stubs themselves, N unit cells in each stub results in $N + 1$ possible operating frequencies, although the solution space in the optimization algorithm shrinks as it may become difficult to fit all MTM-EBG unit cells into the stubs. The design procedure used in the dual-band case still applies anyways, with logical modifications to support tri-band operation. The design procedure is adjusted accordingly, and is carried out as follows:

1. Specify the problem: tri-band matching at 2.4 GHz, 3.6 GHz, and 5.8 GHz on Rogers 3003, designed to match to the load shown in Fig. 4.17.



(a)



(b)

Figure 4.23: (a) S_{11} and (b) loss for different lengths of a_2 in the dual-band matching network. Reproduced from [193] ©2023 IEEE.

2. Modify the algorithm to determine viable tri-band solutions, i.e. solutions at each frequency with the same c_1 and c_2 that have a minimum difference in stub lengths $a_1/a_2/a_3$ and $b_1/b_2/b_3$ of 6 mm.
3. Find solutions achieving a minimum fractional bandwidth around each frequency of 18%. Choose a solution where combined bandwidth is maximized.
4. Design two MTM-EBG unit cells with required bandstop properties and physical dimensions, using the same unit cells where possible for both stubs. In this case, unit cell A is the same as in the dual-band case, where unit cell B has a bandgap at 3.6 GHz.
5. Embed the MTM-EBG unit cell into the stubs at the required positions.
6. Simulate and tune the final structure to produce tri-band impedance matching around all desired operating frequencies.

The tri-band matching network produced by this procedure is shown in Fig. 4.24, and MTM-EBG dimensions are provided in Table 4.3.

4.4.2 Results

4.4.2.1 *S*-parameters

Simulated and measured S_{11} of the tri-band matching network are shown in Fig. 4.25a. Three bands are clearly observed with excellent agreement between the simulated and measured data. A -10 dB S_{11} bandwidth of 16.8%/402 MHz is observed around 2.4 GHz, while the 3.6 GHz band has a bandwidth of 237 MHz/6.6%; this is limited by the bandgap of MTM-EBG B, which is small compared to that of MTM-EBG A (following the trend in Fig. 4.19). The highest band has a broad bandwidth of 25.2%/1462 MHz, although loss spikes near the bottom of the band (see Fig. 4.24b); it is therefore more accurate to consider the matching band to start at the S_{11} local maximum at 5.42 GHz, which gives a matching bandwidth value of 18.3%/1061 MHz.

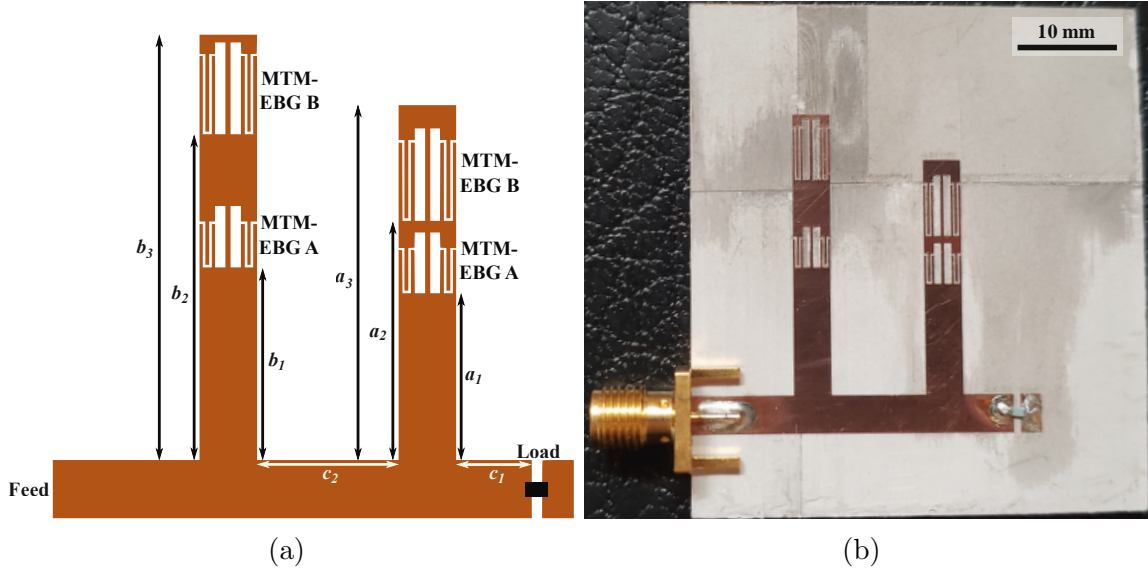
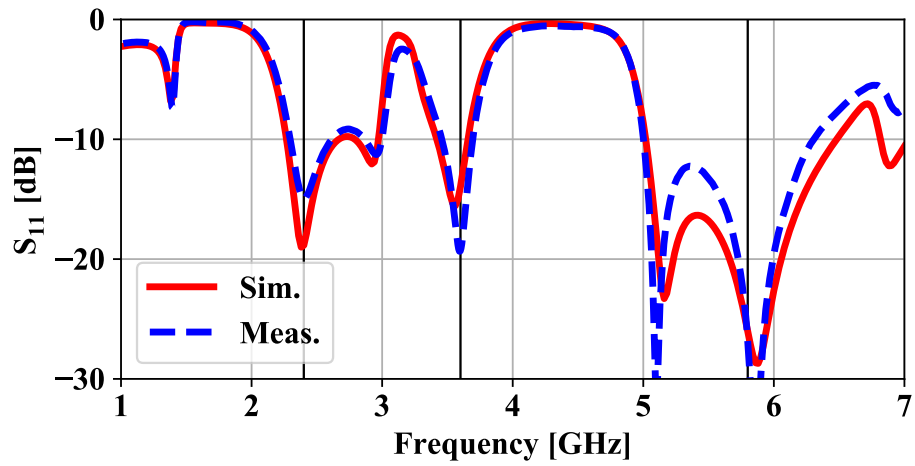


Figure 4.24: (a) Layout of the tri-band matching network, where $a_1 = 10.8 \text{ mm}$, $a_2 = 15.5 \text{ mm}$, $a_3 = 23.0 \text{ mm}$, $b_1 = 12.5 \text{ mm}$, $b_2 = 21.1 \text{ mm}$, $b_3 = 27.5 \text{ mm}$, $c_1 = 4.9 \text{ mm}$, and $c_2 = 9.2 \text{ mm}$. Dimensions of MTM-EBG A and B are given in Table 4.3. (b) Fabricated device. Reproduced from [193] ©2023 IEEE.

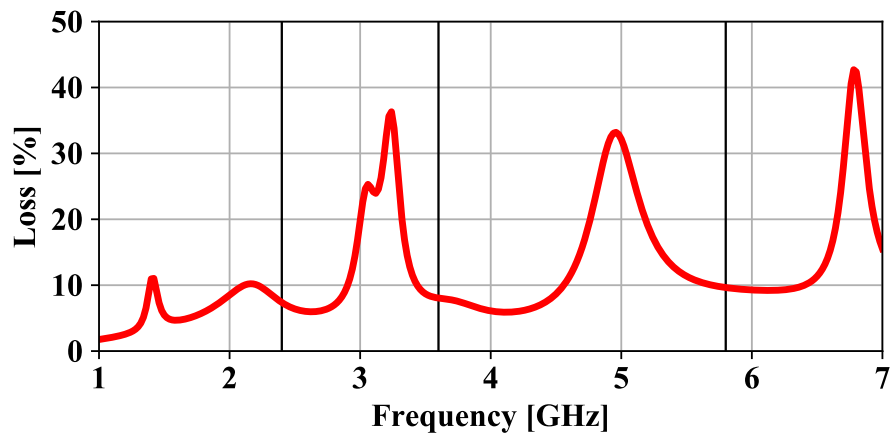
4.4.2.2 Loss

Loss in the network as shown in Fig. 4.24b demonstrates that while the middle band appears quantitatively similar in terms of S_{11} to the 4.14 GHz resonance in the dual-band case, it does not experience a high level of loss, making this truly a matching band. The other operating frequencies also have loss comparable to conventional devices, despite some high losses in regions between bands.

The tri-band design serves to further outline the merits of using non-resonant stubs with embedded MTM-EBG unit cells for multi-band matching, and demonstrates the wide applicability of this approach. Again, note that implementation of the tri-band matching network also does not require an increase in circuit board space as compared to a conventional double-stub tuner with this particular layout. The ability to embed so much additional functionality in a similar amount of space without greatly increasing fabrication complexity is a key element of these MTM-EBG-stub-based structures.



(a)



(b)

Figure 4.25: (a) Simulated and measured S_{11} of the tri-band matching network. (b) Simulated loss. Reproduced from [193] ©2023 IEEE.

Paper	Year	Bands	Frequencies [GHz]	Load	10-dB BW [%]	Substrate ϵ_r	Area [mm ²]	Area [λ_g^2] ^a
[84]	2015	2	2.4/3.6	complex	4/3	3.55	22×12	0.33×0.18
[90]	2015	2	1.00/2.42	complex	11/5	4.7	120×155	0.87×1.12
[85]	2017	2	0.9/1.5	complex	7/5	4.35	110×30	0.69×0.19
[91]	2020	2	1.0/2.5	complex	34/28 ^b	4.35	85×15	0.59×0.10
[95]	2016	3	1.0/2.0/2.5	real	44/16/7	3.48	80×100	0.50×0.62
[96]	2017	3	1.8/2.4/5.8	real	28/18/7	2.2	70×70	0.62×0.62
[97]	2017	4	1.5/2.45/3.5/4.5	real	8/7/5/2	2.33	18×73	0.14×0.56
This work (DB)	2021	2	2.4/5.8	complex	44/21	3	29×44	0.40×0.61
This work (TB)	2021	3	2.4/3.6/5.8	complex	17/7/25	3	21×31	0.29×0.43

^a λ_g is the wavelength in a bulk medium of corresponding ϵ_r at the lowest operating frequency. ^b 15-dB bandwidth reported.

Table 4.4: Comparison of multi-band matching networks in recent literature.

4.4.2.3 Comparison to Other Matching Networks

The matching networks in this work are compared to other multi-band matching networks in the recent literature in Table 4.4. All other matching networks are fabricated on a single printed circuit board (PCB) layer, although some use shorted stubs or vias for matching purposes, which complicates fabrication. Simulated results are compared in all cases for consistency. The comparison shows that the proposed multi-band matching networks operate comparably to other designs while maintaining some advantages over each, such as remaining compact, being able to match to complex loads, and presenting a larger matching bandwidth than most designs. Furthermore, the present work offers superior versatility, as the multi-band matching networks are suitable for matching to two, three, or even more frequency bands.

4.5 Wilkinson Power Divider

4.5.1 Design

Adding MTM-EBG unit cells into terminated OC stubs is intuitive, in that the stub possesses a different electrical length at each frequency of interest. Many devices

require power to transmit through the section of specified electrical length, and this poses a greater challenge. Consider the WPD, a three-port device based on two quarter-wavelength transmission line sections of impedance $\sqrt{2}Z_0$ between ports 1 and 2 and ports 1 and 3, respectively, as well as a fixed $2Z_0$ resistor between ports 2 and 3 [56]. With the usual system impedance of 50Ω , the quarter-wavelength transmission lines segments have a width of 2.13 mm, and a 100Ω resistor separates the two branches. The branch lengths of conventional WPDs are calculated to be 20.10 mm and 9.65 mm, respectively, for the lower and higher operating frequencies. As with other devices, the MTM-EBG should create the necessary frequency dependence to simultaneously achieve both of these solutions.

To render this device dual-band, the quarter-wavelength transmission lines should provide the required phase of 90° at both frequencies. There are two ways to achieve this: the first uses equi-phase points supported by the MTM-EBG on either side of the bandgap to render the quarter-wave section dual-band. This method has been used to render a quadrature hybrid coupler and impedance transformer dual-band [184].

The second method of making a device dual-band is more similar to the approach used for the stubs, and will be demonstrated here. This involves using MTM-EBGs to allow signals at frequencies f_1 and f_2 to travel along separate paths. Importantly, a path that transmits f_1 must reflect f_2 and vice versa, so that the signals are separated; then, the phase response for each frequency can be individually tailored before the signals are recombined. The quarter-wave segment of the WPD is divided into two paths to achieve this [198]. Each path requires “gateway” MTM-EBG unit cells at each end to allow transmission of signals at one frequency but prevent propagation of signals at the other. Furthermore, these MTM-EBGs, along with any TL segment that also contributes to total branch length, provide a total phase of 90° for the signal it is transmitting. Both the bandgap and passband response of the MTM-EBG are critical to the functionality of the device, and the MTM-EBG unit cells must be

electrically small to be embedded in a short ($\lambda_g/4$) and relatively high-impedance ($\sqrt{2}Z_0$) microstrip.

The dual-band WPD, designed to operate at 2.4 GHz and 5.0 GHz, is presented in Fig. 4.26a. The two possible signal paths are indicated. Signals at 2.4 GHz are directed along the outer (long-dash line) paths, while 5.0 GHz signals take the inner (short-dash line) paths. Correspondingly, MTM-EBG A possesses a bandgap at 2.4 GHz, while MTM-EBG B has a bandgap at 5.0 GHz. The phase incurred in each branch can be accounted for by adding up the phase through each section along the appropriate path. Specifically, along the outer branch in Fig. 4.26a, the 90° phase must be incurred through a combination of the microstrip between the two embedded MTM-EBG B unit cells (40.2° at 2.4 GHz), the small MS segments that connect Port 1 and Port 2/3 to MTM-EBG B (28.0°), and the MTM-EBG B unit cells themselves (10.9° each). The inner branch consists of MS segments (39.0° at 5.0 GHz) and MTM-EBG A (51.0°). Dispersion diagrams of both MTM-EBG unit cells designed to meet these specifications are given in Fig. 4.27, with the operating frequencies (horizontal black lines) and bandgap regions (shaded) indicated.

The MTM-EBG unit cells themselves require substantial loading which is difficult due to their small size, but they are still designed to be fully printed. To facilitate this, $50\ \mu\text{m}$ feature sizes were used (RO3003 with 1/2-oz rolled copper was used to facilitate fabrication of these small features), and the unit cell structure shown in Fig. 4.26b was employed. Meandered inductors were implemented in MTM-EBG A to obtain a greater inductance, and the capacitor was flared out beyond the width of the unit cell. This was found to have a minimal effect on the impedance or performance generally of the MTM-EBG unit cell.

Whereas the presented WPD is dual-band, more bands may be added theoretically added through the inclusion of additional branches. Two distinct MTM-EBG unit cell designs are required for every additional branch, with each unit cell possessing a bandgap to prevent signals at other operating frequencies from entering the new

Table 4.5: Dimensions of MTM-EBG Unit Cells in WPD

Parameter	MTM-EBG A	MTM-EBG B
l	4.90 mm	2.00 mm
w	2.13 mm	2.13 mm
s	0.10 mm	0.10 mm
g_L	0.60 mm	0.50 mm
g_C	2.55 mm	1.10 mm
d	0.05 mm	0.05 mm
h_L	2.00 mm	0.05 mm
x_1	0.15 mm	0.10 mm
x_2	0.58 mm	0.68 mm

branch. For N arbitrary operating frequencies, $2(N - 1)$ different MTM-EBG unit cells are required. Practically, such a design would be easier to achieve with lumped elements, since the branches and MTM-EBG unit cells are very compact.

The dual-band WPD was simulated and tuned, and resulting dimensions of the MTM-EBG unit cells are given in Table 4.5. The approximate loading values of the printed capacitors and inductors in MTM-EBGs A and B, respectively, are $L_A = 2.5$ nH, $C_A = 1.9$ pF, $L_B = 1.3$ nH, and $C_B = 0.8$ pF.

4.5.2 Results

Simulation results of the dual-band WPD are shown in Fig. 4.28 (red solid curves) and detailed in Table 4.6. Insertion losses of 3.42 dB and 3.92 dB at 2.4 GHz and 5.0 GHz, respectively, are seen, while return loss and isolation remain better than 17 dB at the operating frequencies. Performance at both operating bands is comparable to that of the well-known conventional microstrip-based divider, but with narrower bandwidths. Once again, this is to be expected due to the limited bandgap bandwidths and operation in dispersive regions of the MTM-EBG unit cells. How-

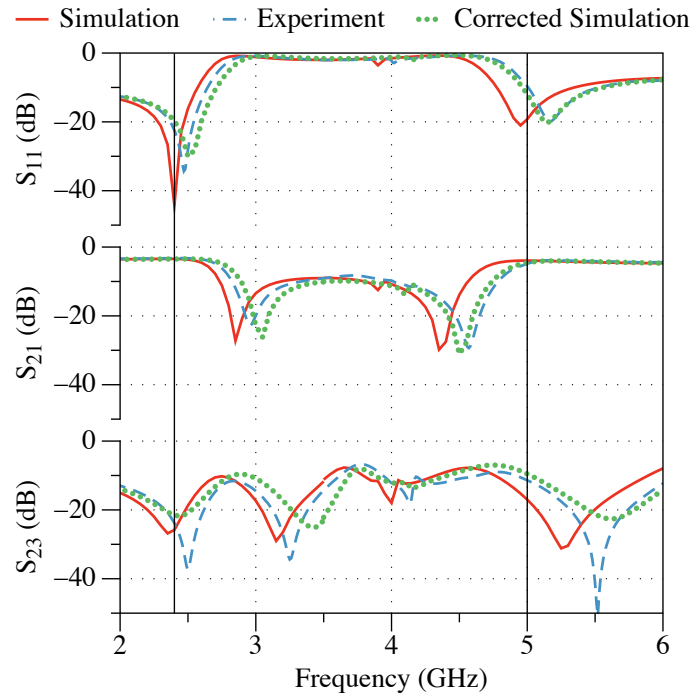


Figure 4.28: Simulated, experimental, and corrected simulated (including $7\text{-}\mu\text{m}$ over-milling in capacitive gaps) S -parameters of the dual-band WPD. The vertical (black) lines indicate the operating frequencies of 2.4 GHz and 5.0 GHz. Reproduced from [184] ©2020 IEEE.

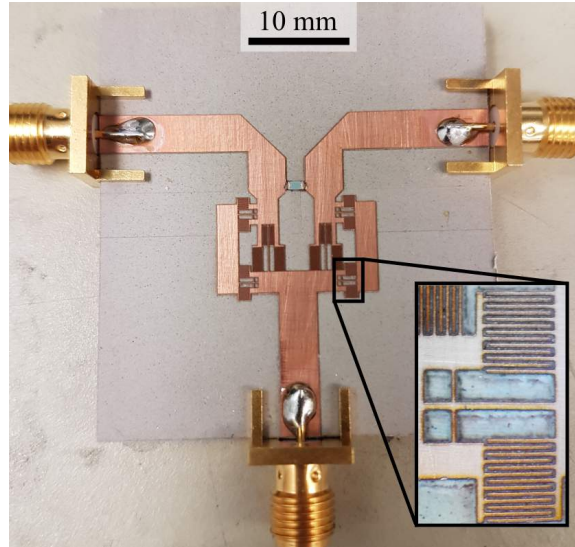


Figure 4.29: Fabricated dual-band WPD. The inset magnifies MTM-EBG B, showing the $50\ \mu\text{m}$ features. Reproduced from [184] ©2020 IEEE.

ever, the power divider bandwidths are still suitable for applications such as indoor WiFi, for which channels have a specified maximum bandwidth of 160 MHz.

The fabricated dual-band WPD is shown in Fig. 4.29, and experimentally obtained S -parameters are presented along with the simulated results in Fig. 4.28 (blue dash-dotted curves). Whereas simulated and measured data demonstrate generally good agreement, a frequency shift of under 4% is observed for both operating bands. The measured insertion losses, given in Table 4.6 and recorded at the shifted operating frequencies, report values very similar to those simulated. Upon inspection using a microscope, it was determined that the capacitive gap widths (d) were over-milled by approximately $7\ \mu\text{m}$, which is within the tolerance specifications of the U3 laser-milling system. When incorporated into the simulations (green dotted “corrected simulation” curves), the agreement is noticeably enhanced. To avoid over-milling in the fine features of future designs, either larger features sizes could be demanded or else surface-mount elements employed, the latter of which would require some additional fabrication steps but simplify unit-cell design. This WPD design is compared to other proposed multi-band power dividers in Table 4.7, which shows that it exhibits

Table 4.6: Simulated and Measured S -Parameters of the Dual-Band WPD at Frequencies of Peak S_{21}

Parameter	Simulated		Measured	
	2.40 GHz	5.00 GHz	2.45 GHz	5.15 GHz
S_{11} (dB)	-44.18	-19.22	-30.14	-19.59
S_{21} (dB)	-3.42	-3.92	-3.23	-3.86
S_{23} (dB)	-25.83	-17.01	-28.85	-14.56

Table 4.7: Proposed Dual-Band WPD compared to similar equal-power division dual-band devices in recent literature

	$f_1/f_2/\dots$ [GHz]	$ S_{11} $	$ S_{21} $	$ S_{23} $	Circuit Size
This Work	2.45/5.15	30.1/19.6	3.23/3.86	28.9/14.6	$0.20 \lambda_g \times 0.13 \lambda_g$
[100]	1.0/2.0	22.8/19.4	3.17/3.27	30.1/23.4	$0.20 \lambda_g \times 0.49 \lambda_g$
[101]	1.0/2.7	28.0/22.0	3.1/3.3	39.0/28.0	Not Reported
[103]	1.0/1.8	25/43	3.1/3.2	26.0/32.0	$0.31 \lambda_g \times 0.17 \lambda_g$
[110]	1.32/2.44/3.56/4.68	22.0/30.0/30.0/18.0	3.43/3.75/4.09/4.75	15.0/27.0/30.0/25.0	$0.45 \lambda_g \times 0.54 \lambda_g$
[199]	2.5/5.4	39.1/25.1	3.2/3.5	39.7/33.5	$0.23 \lambda_g \times 0.17 \lambda_g$
[200]	0.9/3.5	16/31	3.1/3.2	26/24	$0.18 \lambda_g \times 0.16 \lambda_g$

comparable performance with a very compact footprint, with all sizes reported in terms of the MS-like mode's guided wavelength λ_g for a fair comparison with respect to choice of substrate.

Chapter 5

Multi-Band Antennas

5.1 Antenna Design Methodology

5.1.1 Design

The design of a dual-band microstrip patch can be compared, in a way, to the design of the resonant stub filters (of course, there are plenty of extra considerations with an antenna - input impedance, radiation properties, gain, etc.). Consider a basic, half-wavelength microstrip patch antenna. Embedding an MTM-EBG unit cell onto the radiating edge of the patch provides it with two resonant lengths: a lower frequency resonance when the MTM-EBG is transmitting, and a higher-frequency resonance when the MTM-EBG is in its bandgap region. A simple, microstrip-fed version of this patch is represented in Fig. 5.1, with the MTM-EBG on the right side of the patch. At the most basic level, this concept is the basis of this chapter.

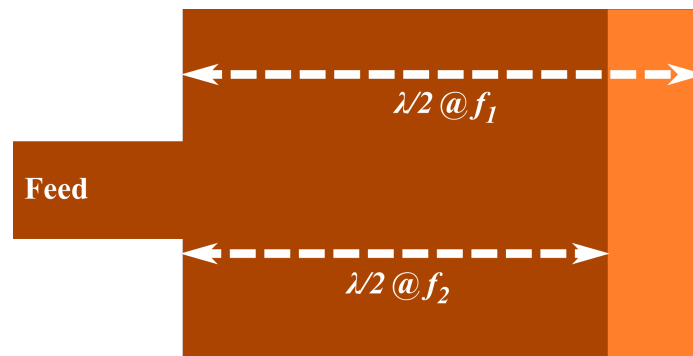


Figure 5.1: Schematic of microstrip patch antenna with embedded MTM-EBG region on the radiating edge for dual-band operation.

Another way to look at this is with the standard patch antenna cavity model [174]. The MTM-EBG allows the perfect magnetic conductor (PMC) boundary on the radiating edge of the antenna to effectively be shifted as a function of frequency, allowing the fundamental transverse magnetic (TM_{10}) mode to be supported at two independent frequencies (for a rectangular patch). The fact that the same mode is excited for both frequencies implies that they will have similar radiation patterns. The patch is dual-frequency, but single-mode; this contrasts with many multi-band antennas in the literature, which rely on the excitation of various modes and produce drastically different radiation properties in different bands.

Furthermore, effectively superimposing two antennas onto each other allows the same area to support both resonances, and neither is greatly miniaturized or created through extreme loading of the patch, either of which would affect key antenna parameters. The antenna becomes slightly miniaturized at the lower frequency due to the dispersion of the MTM-EBG, but not to the extent that gain or input impedance are significantly reduced. Miniaturization comes mainly from the fact that a single antenna can support two different TM_{10} modes, so a single antenna is needed rather than multiple antennas. Due to their superposition, they can typically both be excited with the same, simple feed as well.

The creation of these antennas involves choosing the operating frequencies and designing an MTM-EBG unit cell that provides a bandgap at the higher operating frequency while incurring the desired phase at the lower operating frequency to produce a resonance in both bands. Location of the MTM-EBG unit cells (e.g., determining which patch edge or edges they should be placed on) has an effect on matching and radiation properties, and these will be explored for various antenna designs. Traditional patch antenna design challenges must simultaneously be considered, such as ground plane size and feed mechanism. These will be explored, and implemented in different ways, for the antennas to come.

This work goes beyond the combination of two antennas into a simple dual-linear-

polarized antenna. While based on the same design concepts, circular polarization is also explored, as well as a tri-band antenna design for GPS frequencies. A dual-band and simultaneously dual-linearly-polarized antenna (i.e., an antenna that supports four independent and isolated TM_{10} modes in the same amount of space) is also demonstrated, which poses a number of different design challenges. A tunable version of this antenna is ultimately presented. The fundamental principles of antenna design remain the same in all cases, but each presents unique challenges.

5.1.2 Considerations

5.1.2.1 Feed Mechanisms

The goal of this section is to develop simple, uniplanar, and compact antennas, and to meet this goal, a simple feed design is also required. A few basic methods are commonly used for feeding microstrip antennas, and perhaps the simplest is a microstrip feed, in which a patch is fed by a microstrip on the same plane as the antenna. This allows for easy fabrication and integration with connecting microstrip circuitry such as feed networks, but presents the disadvantages of rendering the patch asymmetrical and allowing the feed to contribute spurious radiation, particularly if the substrate is thickened to improve patch bandwidth [130]. To match a microstrip feed to the antenna, either a matching network (often stub-based) is required, or the feed can be inset into the antenna such that the input impedance at resonance matches the characteristic impedance of the feed.

Pin feeds, in which a pin passes through a hole in the ground plane and connects to an antenna directly, are another simple way of feeding an antenna. The pin itself may come directly from a coaxial cable or be implemented as a via to a circuit layer below the ground plane. While this increases fabrication complexity in comparison to a microstrip feed, it has advantages of not affecting the antenna geometry at all, and keeping the feed shielded from the antenna so that it has a minimal impact on radiation properties [131], even with an extensive feed network (assuming that the ground

plane is large). The location beneath the antenna at which the pin passes through the ground plane determines impedance matching, and this method is relatively simple and compact to implement.

Similar to using pin feeds in that the feed and patch are separated by a ground plane is aperture coupling, which is even simpler to realize. Aperture coupling leaves a small gap, which may be a variety of shapes, in the ground plane through which power is resonantly coupled to feed the antenna. Although this can result in greater bandwidth than either of the other feeding methods [130], the aperture should be resonant at or near the antenna operating frequency, and that makes this method unsuitable for multi-band applications. As a result, microstrip and pin coupling were employed in this work rather than aperture coupling. Direct-contacting feeds were also preferred to other non-contacting feed types such as proximity coupling.

Baluns were not required for these structures as unbalanced currents were generally not a major issue for most of the presented designs. The only exception came in the design of a dual-band antenna where an unshielded microstrip to end-launch SMA connector was required, but the effects of this were fairly minor and will be presented below. In general, however, baluns are not required, which assists in minimizing design complexity and antenna size.

5.1.2.2 Return Loss

For most antennas in this section operation is considered to be across a 10-dB return loss bandwidth, unless otherwise indicated. Achieving good return loss at both frequencies is an important consideration of this work, and presents some challenges. It is addressed in different ways, depending on the feed type. For linearly-polarized antennas, the MTM-EBG unit cells help facilitate matching in each frequency band, while dual-linear-polarized or circularly polarized antennas often require high levels of symmetry in the radiator, and feed location becomes the primary method of enforcing impedance matching. There is an optimal feed location where the reflection

coefficient will be minimized since the feed will match to a 50Ω input impedance enforced by the patch resonance, although this location may be different for each resonance. (Note that the choice is often made not to insert the feed at a location of perfect matching, but rather at the location that maximizes bandwidth [175]; for a 50Ω system impedance, this means the pin should be located at a position where the antenna input impedance is closer to 60Ω . Regardless of the choice, however, an optimal pin location can be found.)

5.1.2.3 Operating Frequencies

How far apart frequencies can be spaced is a question of matching. Since there is an optimal pin position to feed each operating frequency, two superimposed TM_{10} resonances with similar frequencies will have similar optimal pin positions; thus, an average pin position that accommodates both resonances can be chosen. As the spacing between operating frequencies increases, so does the difference in optimal pin location. The compromising pin position will match more poorly to each resonance as the optimal location diverges, thus reducing impedance matching and bandwidth. However, adding a matching network that ensures power is delivered to the antenna at both operating frequencies can accommodate the difference in pin position and allow the operating frequencies to be widely spaced. Therefore, the restriction is only a serious problem in cases where a matching network cannot be used, and otherwise, a multi-band matching network was presented in the previous chapter that can ensure good matching for a patch antenna regardless of pin position. Examples of patch antennas with integrated matching networks will be demonstrated in this chapter.

Different problems arise as frequencies become closely spaced. If f_1 and f_2 are in close proximity, the resonant cavity will be a similar size at both frequencies. Physically, this raises the problem of requiring extremely small MTM-EBG unit cells that may be difficult to realize. As discussed previously, methods exist to reduce MTM-EBG length such as using lumped components or other compact capacitor

types, and this mitigates the problem to some extent, as will be seen later in the design of a GPS antenna. A second solution would be to make the resonant cavity an extra half-wavelength in length at the lower frequency to give plenty of room to embed MTM-EBG unit cells, but this involves exciting a TM_{20} mode at this frequency, which will have different radiation properties. Regardless, a second problem remains: the approximation that an MTM-EBG unit cell transmits power at one frequency and presents a bandgap at the other does not apply for closely-spaced frequencies, since in practice, the transmission response of a finite number of MTM-EBG unit cells, and especially a single unit cell, has a gradual band edge. As a result, only partial transmission and reflection would be observed at each of the closely-spaced frequencies. These techniques, therefore, are more suited to widely spaced frequencies - or at least, frequencies spaced sufficiently far apart enough that the MTM-EBG unit cell is not operating near its band edge.

5.1.2.4 Radiation properties

Most MTM-EBG-based antennas presented in this section are designed for linear polarization, or dual-linear-polarization if two feeds are introduced to excite orthogonal linear polarizations along different axes of the patch. The two-feed configuration can easily be converted to circular polarization with quadrature-phase inputs. Such a feed can be realized by dividing an input signal with a wideband or multi-band quadrature hybrid coupler (such as the MTM-EBG-based version presented in [184]). Axial ratio (AR) is used to quantify the polarization purity, and circularly polarized antenna have a defined AR bandwidth such as $AR < 3 \text{ dB}$ (some applications with more stringent demands will define an AR bandwidth for which $AR < 2 \text{ dB}$ or less). For the MTM-EBG-based antennas in this work, the broadside AR bandwidth with the quadrature-phase inputs is typically larger than the narrow -10 dB reflection coefficient bandwidth, so circular polarization can effectively be produced.

Circular polarization could also be achieved with a single feed and an altered

patch geometry, for example with slots or chamfered corners [174]. A challenge of this approach is ensuring that circular polarization is produced in both bands despite limited flexibility in creating frequency-dependent enabling features. AR bandwidth may be smaller than reflection coefficient bandwidth in this case, which can contribute to significant polarization losses at one or both operating frequencies. As a result, these methods of rendering the patches circularly polarized require more investigation and optimization, and are left for future work.

Patch antennas are resonant, and similar excited modes will have similar properties. Since all operating frequencies of an MTM-EBG-based multi-band antenna rely on the same fundamental cavity mode, it can be expected that the patch antennas will have the same properties at each resonance, and furthermore that these properties will be similar to conventional patches. Broadside radiation is therefore observed at all frequencies with a similar shape in the E- and H-planes, while backlobes depend largely on ground plane size.

The antennas also produce similar gain to conventional patches, although minor gain reductions can be expected. At the lower frequencies, this can be attributed to a slight reduction in patch size due to dispersion of the MTM-EBG unit cells. At higher frequencies, an MTM-EBG unit cell in its bandgap region stores some amount of energy in its capacitors, and with realistic materials this contributes to losses, resulting in a slight reduction in gain and efficiency. Overall, however, very comparable performance to conventional patch antennas is expected. All of these properties will be explored thoroughly in this chapter.

5.2 Dual-Band Linear Patch Antenna

5.2.1 Design

The first patch antenna to be designed is a dual-band linear patch fed by a microstrip TL, similar to the design concept shown in Fig. 5.1 but with a feed inset distance used

for impedance matching. Standard patch antenna design equations are used to determine patch length and width, and feed inset distance is determined to match to the 50Ω microstrip feed [174]. Patch length primarily determines the patch resonance, so this is the parameter that will be made frequency-dependent through the use of MTM-EBG unit cells. Patch width on the other hand plays a role in determining the input impedance profile of the antenna, and has a corresponding effect on bandwidth as well. This parameter must be the same for both frequencies to superimpose the two designs, so a compromising width must be chosen; this will affect the feed inset location as well. To get around this limitation, future designs could use the recently-developed 2D MTM-EBG unit cell that suppresses power flow along both of its axes; this is related to the UC-EBG, and has recently been established with similar analytical rigor as the MTM-EBG [183].

Feed inset distance depends on the input impedance of the patch antenna as a function of location. The input resistance of a patch is typically approximated as a cosine squared function, [174] although for microstrip-fed antennas it has been shown that dependence on a cosine to the fourth power provides a more accurate representation [201, 202]. In either case, input resistance at resonance is maximized at the patch edge and decreases to zero near the center of the patch; the antenna feed location should be chosen accordingly. MTM-EBG unit cells can be employed to improve matching at both operating frequencies by not simply adding them to one side of the patch to affect its resonant length, but by placing them on *both* resonant edges. Combined, they allow the patch to have two resonant lengths, and the unit cell on the feed side renders the feed inset parameter frequency-dependent as well, providing the freedom to effectively match both bands.

The patch is designed to operate at 2.5 GHz and 5.0 GHz on the same substrate used in the previous section: 60 mil Rogers 3003, clad in 1/2-oz rolled copper. As a basis for comparison, corresponding conventional higher-frequency and lower-frequency patch antennas were designed with parameters l_p , w_p , and i_p (see Fig. 5.2) chosen to

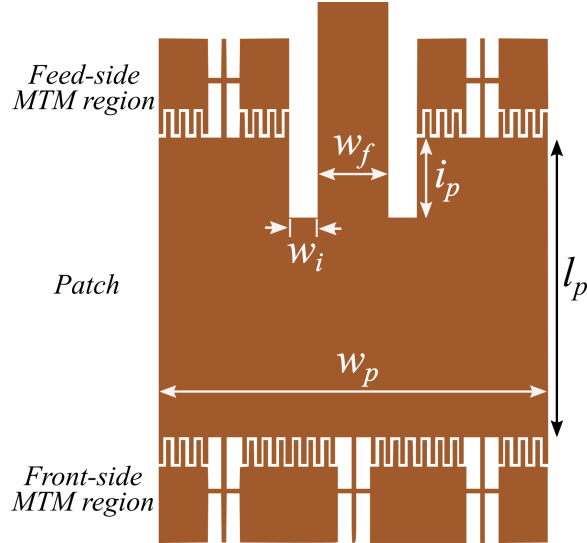


Figure 5.2: Top view of proposed dual-band antenna consisting of a microstrip-fed patch with MTM-EBG sections placed on the radiating edges. Reproduced from [188] ©2016 IEEE.

Table 5.1: Antenna design values (in mm) for the conventional patch antennas and the dual-band antenna. Refer to Fig. 5.2 for parameter descriptions.

	Conv. Low Freq.	Conv. High Freq.	Dual-band
l_p	35.15	16.67	16.80
w_p	43.32	21.21	21.00
i_p	10.40	4.80	4.50
w_i	2.00	2.00	1.62
w_f	3.76	3.76	3.76

achieve resonance at the above frequencies – the design parameters are given in Table 5.1. Inset length was determined by design equations in [174], and tuned to adjust for changes in patch width. The width of the patches are set to be the same, and a width similar to the optimal width for the higher-frequency antenna was chosen. Other widths could have been chosen as well, for example, something more similar to the optimal width at the lower frequency, but this results in a high-frequency antenna that is much wider than it is long, causing higher-order transverse modes to be excited and high levels of cross-polarization. The narrower patch instead causes a slight reduction in gain at the lower frequency due to its overall smaller size.

With the single-band antenna parameters set, MTM-EBG unit cells can finally be designed. First, an MTM-EBG unit cell is designed for the feed side of the patch to enable good matching at both frequencies. The difference in inset length is expressed as an electrical length, and an MTM-EBG cell is designed from its dispersion diagram to have this phase at the lower frequency. The remaining difference in electrical length between the two patches is encompassed by an MTM-EBG unit cell that is embedded in the opposite edge of the patch. Of course, both MTM-EBG unit cells must have a bandgap at the higher operating frequency. The resulting dual-band patch is shown in Fig. 5.2, and now electrically resembles each of the individual patches at their respective operating frequency. The result of this process, as described in the next section, is a well-matched, fully printed antenna that operates in a standard TM_{10} patch mode for both frequencies. Additionally, due to the dispersive nature of the MTM-EBG, the patch is moderately miniaturized at the lower frequency, with respect to the conventional low-frequency patch.

Dimensions of the dual-band patch are provided in Table 5.1, while remaining dimensions of the two MTM-EBG unit cell designs are given in Table 5.2 (capacitance for each unit cell was designed to be 0.54 pF, but the unit cells end up having slightly different capacitor lengths g_C due to minor parametric tuning). The width of the MTM-EBG unit cells were constrained to provide an integer number of unit cells on each patch edge, and dimensions were kept at or above 0.2 mm for ease of fabrication. PCB chemical etching was the chosen method of fabrication for this antenna, and the minimum dimension of 0.2 mm nears the limits of what can be achieved with such a method. Plots of the complex electric field magnitude in a plane through the centre of the substrate at the two resonances in Fig. 5.3 provide compelling evidence that the patch operates as intended; the MTM-EBG unit cells clearly demonstrate a strong bandgap at 5.0 GHz, as expected.

Table 5.2: Design values for the proposed antenna's two MTM-EBG regions, in mm.

	Front side	Feed side
l	5.90	5.50
w	7.00	7.00
s	0.20	0.20
g_L	0.80	0.80
g_C	1.70	1.60
d_1, d_2, d_3	0.20	0.20

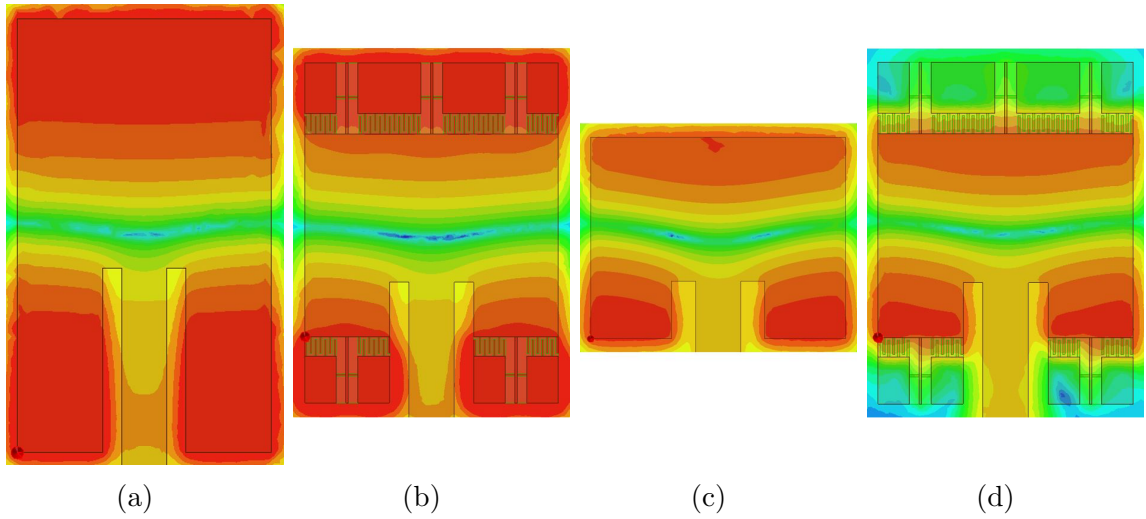


Figure 5.3: Simulated complex electric-field magnitudes (displayed on a logarithmic scale) shown at the resonance frequencies of a) the conventional 2.4 GHz patch, b) the MTM-EBG patch at 2.4 GHz, c) the conventional 5.0 GHz patch, and d) the MTM-EBG patch at 5.0 GHz. Reproduced from [188] ©2016 IEEE.

5.2.2 Results

5.2.2.1 S -parameters

The dual-band MTM-EBG antenna shown above was simulated, fabricated, and measured. S_{11} data shown in Fig. 5.4 demonstrates that the MTM-EBG antenna is well matched, exhibiting a return loss better than 10 dB in all cases although for a narrow bandwidth. The narrow bandwidth can be attributed both to the dispersive nature of the MTM-EBG unit cells when compared to underlying patch regions, and to the fact that the matching location for the microstrip feed is near the center of the patch,

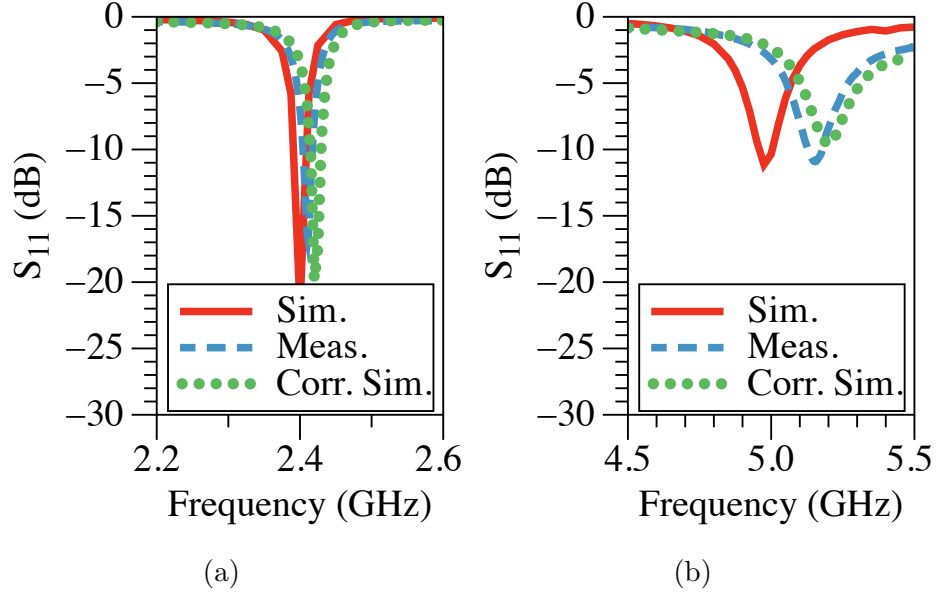


Figure 5.4: Simulated and measured S_{11} of the MTM-EBG patch: a) lower-frequency band and b) higher-frequency band. Simulation represents the originally designed antenna, while the corrected simulation curve takes into account fabrication errors in the printed antenna. Reproduced from [188] ©2016 IEEE.

where input resistance varies more rapidly as a function of frequency.

The operating frequency is shifted up for the higher-frequency resonance by about 3% in the fabricated structure. Inspection of the fabricated prototypes under a microscope suggested that this up-shift may be attributed to an over-etching of the capacitor interdigitations and inductive strips of the two MTM-EBGs by approximately 18-22% (i.e. both features were approximately $40\ \mu\text{m}$ narrower than intended). These imperfections, caused by the chemical etching process in the fabricated antenna seen inset in Fig. 5.5, were then incorporated into the simulations, and the corrected S_{11} data (also included in Fig. 5.4) show much better agreement with measurement. Other antenna designs presented in this thesis are laser-milled to reduce the likelihood of this sort of fabrication error.

5.2.2.2 Radiation Properties

Radiation patterns of the dual-band patch antenna were determined through measurement in an anechoic chamber, the setup for which is shown in Fig. 5.5, and

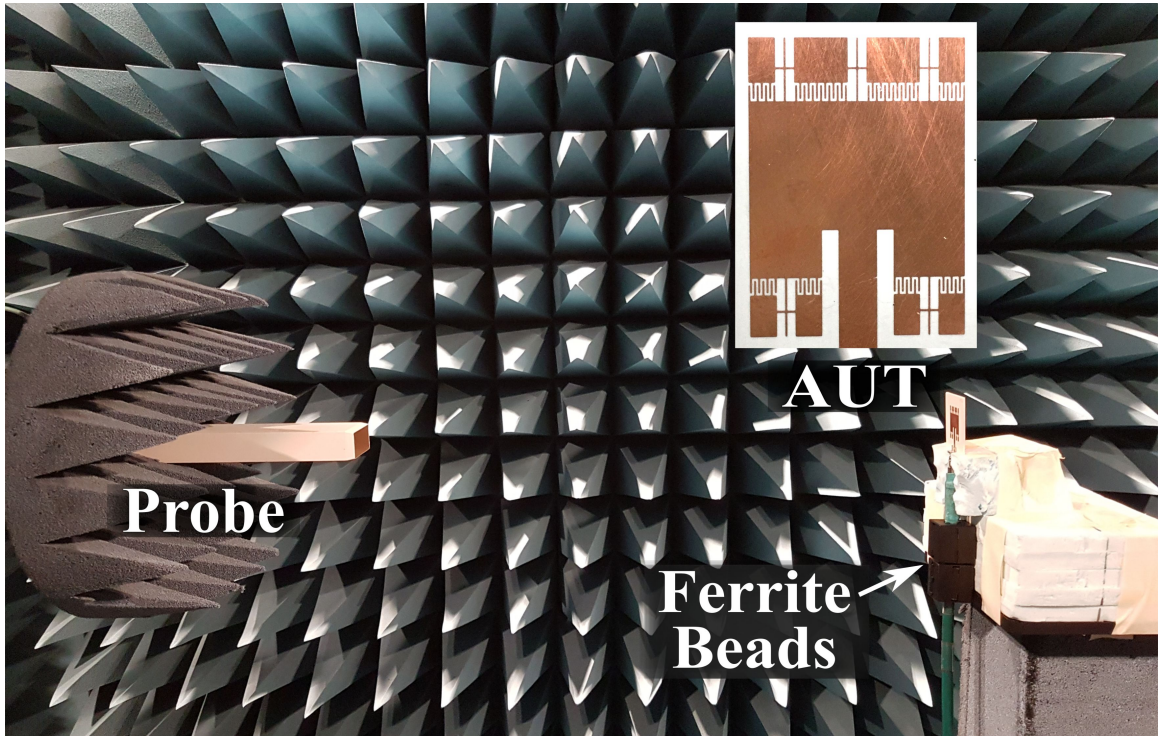


Figure 5.5: Experimental setup of the antennas in an anechoic chamber. Inset: the fabricated MTM-EBG antenna. Reproduced from [188] ©2016 IEEE.

compared to simulation. Conventional patched were also fabricated and measured for comparison. Antenna measurements initially showed high cross-polarization, and a combination of simulations and rigorous measurements suggested that this was due to radiation from unbalanced currents along the coaxial feedline. A solution to this for the lower-frequency resonances was to attach ferrite beads to the feedline; this directly contributed to a reduction in cross-polarization. The ferrite beads were not rated for 5 GHz but when attached very close to the antenna still contributed to the reduction of cross-polarization, if to a lesser extent than at the lower frequency. Therefore, they were included in all measurements of the antennas.

Overall, simulated and measured radiation patterns (normalized to the maximum co-polarized radiation intensity) exhibit excellent agreement, as shown in Fig. 5.6, and many of the finer details such as small lobes and nulls are present in both cases.

Table 5.3: Maximum antenna gain (in dBi), co-pol and cross-pol, from simulation.

	Max. co-pol	Max. cross-pol
Conv. Low-Freq	5.3	-23.2
Conv. High-Freq	7.6	-13.0
MTM-EBG Low-Freq.	2.6	-27.5
MTM-EBG High-Freq.	6.6	-13.7

There are only two notable disagreements; the first is a null in the back-fire direction of every antenna which is attributed to blockage due to the metallic mounting apparatus in the anechoic chamber. The other major disagreement is seen in the back lobes of the H-planes for the higher frequency resonances, where measurement shows significantly higher radiation intensity than simulation. Since both the conventional and MTM-EBG antennas exhibit this behaviour, it could be a result of the continued existence of unbalanced currents on the feed line, which maintain a presence due to the less-than-optimal performance of ferrite beads at this frequency. Overall however, the measurements both successfully verify the simulation results and confirm that the MTM-EBG antenna produces patterns that are very similar to those of the corresponding conventional patch antennas; in other words, the presence of an MTM-EBG that is either transmitting or in its bandgap region does not significantly affect the radiation pattern of the antenna.

The simulated maximum total gains (which generally occur at broadside for co-pol, but peaking at side lobes for cross-pol; see radiation patterns in Fig. 5.6) are compared in Table 5.3. While the higher-frequency gain of the MTM-EBG patch antenna is within 1 dB of that of the conventional patch, the lower frequency gain is approximately 2.7 dB below that of the conventional patch. While the MTM-EBG patch antenna still remains an effective radiator at this frequency, the degradation in performance is likely due to small scattering losses in the fine features of the MTM-EBG and to the decrease in electrical size of the antenna [203].

A comparison of this antenna with a sample of other multi-band antennas found

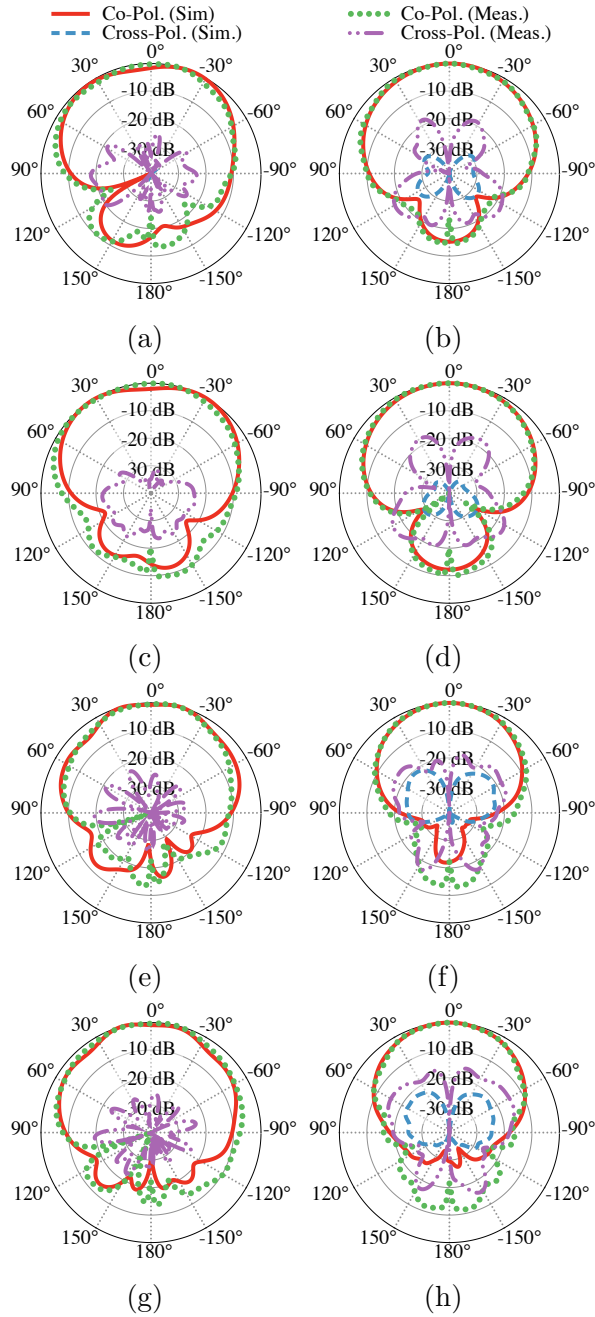


Figure 5.6: Simulated and measured normalized radiation patterns of conventional and dual-band antennas, with patterns recorded at the peak return loss frequency: a) lower-frequency conventional patch E-plane, b) lower-frequency conventional patch H-plane, c) lower-frequency MTM-EBG patch E-plane, d) lower-frequency MTM-EBG patch H-plane, e) higher-frequency conventional patch E-plane, f) higher-frequency conventional patch H-plane, g) higher-frequency MTM-EBG patch E-plane, h) higher-frequency MTM-EBG patch H-plane. Reproduced from [188] ©2016 IEEE.

Table 5.4: Comparison of MTM-EBG antenna to other examples of multi-band patch antennas.

	Op. Freq. (GHz)	6dB BW (%)	Gains (dBi)	Feature	Patch Size (mm)	Substrate ϵ_r
[139]	3.70/4.95/5.50	12.2/9.1/7.2	8.2/8.0/7.9	uniplanar	35.5×26.0	1.00
[146]	1.08/1.94/2.40	0.8/2.3/2.2	1.9/0.6/6.2	stacked	44.0×44.0	2.20
[147]	2.45/5.80	26.1/17.2	5.2/-0.3	uniplanar	32.0×28.0	1.38
[149]	3.66/5.3/5.8/7.03	3.8/4.9/1.74/1.1	7.41/7.7/5.55/1.0	uniplanar	28.0×25.7	2.20
MTM-EBG	2.4/5.2	1.9/3.6	2.6/6.6	uniplanar	28.2×21.0	3.00

in the literature is presented in Table 5.4. In terms of performance, it can be seen that the MTM-EBG antenna is comparable to these other antennas, demonstrating improvements variously in different categories. Since this antenna has a systematic design procedure, however, it may be better-suited to a broader array of applications as it offers great flexibility in choosing the operating frequencies. Further antenna designs in this chapter will illustrate the design flexibility that the MTM-EBG provides.

5.3 Dual-Band, Dual-Polarized Antenna

5.3.1 Theory

The microstrip-fed, dual-band antenna is advantageous in many ways, but even more functionality can be extracted from a similar footprint by superimposing another, orthogonally polarized antenna into the same space. The result is a simultaneously dual-band and dual-polarized antenna (DBDPA), which effectively supports four independent resonances in the space of a single antenna. Confusion may be caused by the fact that some antennas in the literature are designated dual-band and dual-polarized when the two bands simply support different polarizations, but to clarify, each band of the DBDPA supports *both* polarizations simultaneously.

A DBDPA requires four radiating resonances, and all four should ideally have similar radiation characteristics. For resonances of the same frequency but orthogonal linear polarizations, this is achieved by ensuring that the patch exhibits 90° rotational

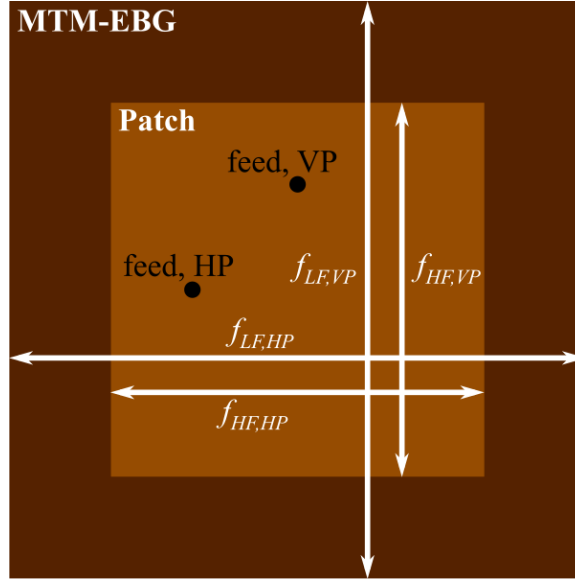


Figure 5.7: Schematic of patch surrounded by a region of MTM-EBG unit cells, which transmit at a low frequency and have a bandgap at a high frequency. Resonant frequencies and feed points are indicated for both bands, as well as for the horizontal polarization and vertical polarization. This structure forms the DBDPA.

symmetry and that this symmetry remains unbroken by the feed mechanism. Attaining similar radiation properties at two frequencies is typically a more complicated task, particularly to ensure that the half-wavelength cavity mode (TM_{10} mode) is excited at both frequencies. A single feed must also be able to excite both resonances for a single polarization, and these feeds must be well-isolated from each other, despite their close proximity.

These design constraints are all achieved by embedding MTM-EBG unit cells into a pin-fed square patch antenna, which will be described in detail below. Importantly, the antenna meets these requirements while remaining printable and smaller than a conventional square patch operating at the lower frequency. This antenna is designed to be pin-fed, and the feeding pins connect to a microstrip feed on a layer below the patch ground plane. The shielded arrangement isolates the radiating element from the feed and enables the use of different substrate permittivities, if necessary, for surface-wave suppression on the antenna side and feed miniaturization below.

The DBDPA will be designed around frequency bands for WiFi and fixed wireless

LTE and LTE-U radio platforms, centered on 3.6 GHz and 5.8 GHz. Choosing different bands than the previous antenna also serves to highlight the freedom in choice of frequency bands since the MTM-EBG can be robustly dispersion-engineered to enable nearly arbitrary selection of these operating frequencies, within the limits described previously. Feeding both bands is slightly easier in the pin-fed case as well, since a pin feed is less intrusive on the antenna structure, and matching is simplified as a result. The proposed DBDPA will be constructed on Rogers RO3003, clad in 1-oz rolled copper.

5.3.2 Implementation

5.3.2.1 Design

The concept of the DBDPA is based on the combination of conventional pin-fed square patches, facilitated by MTM-EBG unit cells. In this section, design of the patch itself will be considered; the following sections will discuss the feed structure and ground plane. Conventional square patches can easily be designed with a cavity model of the patch, and should be approximately half a wavelength in size [174]. On Rogers 3003, patches with lengths of 23.5 mm and 14.2 mm radiate at 3.6 GHz and 5.8 GHz, respectively. The difference in length between these patches is 9.3 mm, which, assuming each patch is exactly $\lambda_g/2$ at its respective operating frequency, translates to 71.2° at 3.6 GHz. Therefore, if a series of MTM-EBG unit cells are arranged circumferentially around a 14.2 mm patch such that they have a bandgap at 5.8 GHz and provide a phase of 35.6° at 3.6 GHz (since they will be on both sides of the patch), then dual-band, half-wavelength resonances will be present along both axes, at both frequencies. This concept is illustrated schematically in Fig. 5.7, which indicates the resonant cavities of all frequencies and polarizations.

The band structure of the required MTM-EBG is presented in Fig. 5.8a, where the bandgap location at 5.8 GHz and correct phase at 3.6 GHz are observed. The single-cell transmission simulation in Fig. 5.8b confirms that a strong bandgap is produced at

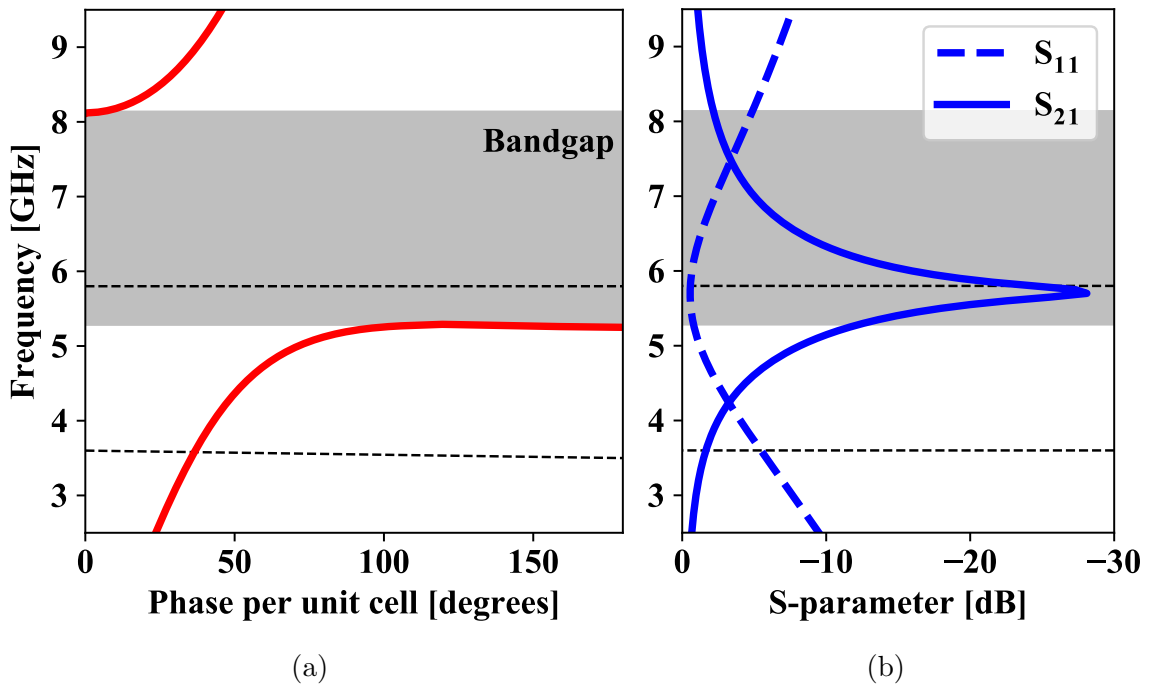


Figure 5.8: (a) Dispersion diagram for the MTM-EBG unit cell used in the DBDPA, and (b) S_{11} and S_{21} of a single unit cell. Operating frequencies are indicated by horizontal dashed lines, and the bandgap region is highlighted and labeled. Reproduced from [185] ©2021 IEEE.

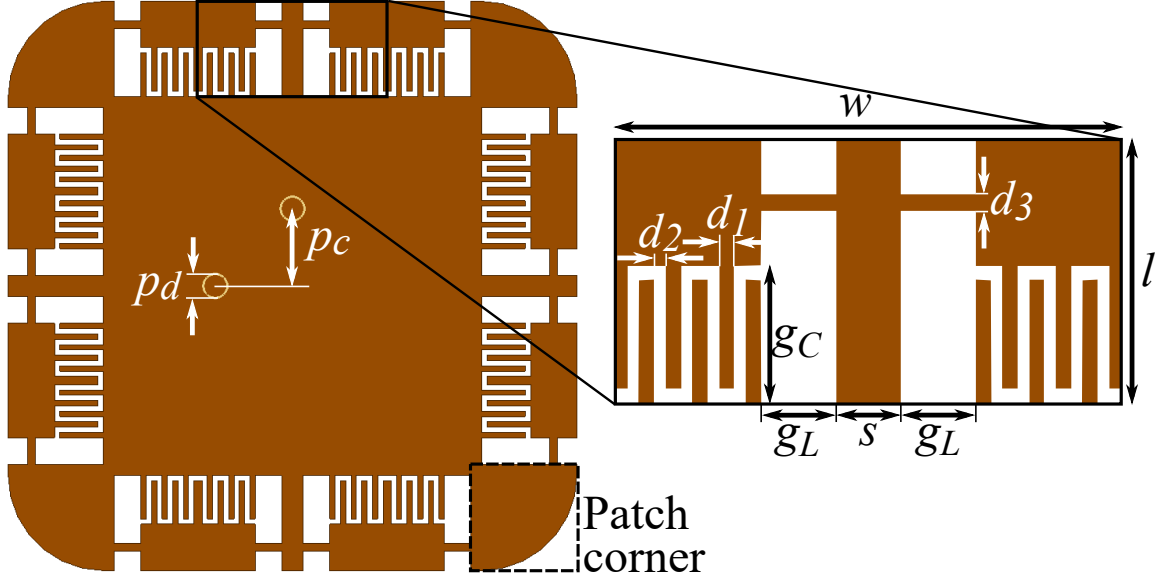


Figure 5.9: Patch antenna with rounded corners, and feed pin location indicated. Constituent MTM-EBG unit cell with dimensions is inset. Reproduced from [185] ©2021 IEEE.

5.8 GHz, while transmission occurs at 3.6 GHz. Two unit cells are placed along each edge of the patch, with interdigitated capacitors and strip inductors of approximately 0.4 pF and 0.3 nH, respectively, replacing each discrete lumped loading element to ensure the antenna can be fully printed. A minimum feature size of 0.2 mm was again chosen which offers the possibility of fabricating the antenna using several common methods, although laser milling was chosen for this device. Minor tuning of the MTM-EBG is required once it is embedded into the antenna, and this is done through slight modifications of the capacitor length (g_C) and to the length of the unit cell itself (l). The final structure is presented in Fig. 5.9, along with an inset of the MTM-EBG; corresponding dimensions are provided in Table 5.5.

Fig. 5.10 shows the simulated complex magnitude of the electric fields at each resonance for the vertical polarization excited by the indicated feed, and this confirms that fields are more contained in the central region of the patch at the higher frequency, while they pass throughout the full structure at the lower frequency. Characteristic TM_{10} patterns are observed at each frequency. It should be noted that, although

Table 5.5: Dimensions of MTM-EBG Unit Cell in DBDPA

Parameter	Value	Parameter	Value
l	3.58 mm	g_C	1.83 mm
w	7.10 mm	d_1	0.20 mm
s	0.80 mm	d_2	0.20 mm
g_L	1.00 mm	d_3	0.30 mm

not discernible in Fig. 5.10, some energy is stored in the capacitors, in particular at 5.8 GHz where they help create the MTM-EBG bandgap; however, this does not greatly affect the radiation properties of the patch.

After embedding MTM-EBG unit cells along each side of the patch, the question of how to design adjoining corner regions (as indicated in Fig. 5.9) remains. Three possible options were considered: leaving the square region free of all copper, filling it entirely with copper, or transitioning with rounded corners, the last of which is shown in the figure. All three corner options resulted in similar radiation properties, but the rounded corners produced the least cross-polarization by a small margin. As such, this option was chosen.

It should be emphasized that the design cannot tolerate asymmetries. Since the patch relies on orthogonal excitations, any asymmetry will cause a difference in pattern shape of one polarization compared to the other, and introduce higher levels of cross-polarization to one or both. Additionally, asymmetries will disrupt a uniform half-wavelength resonance that enforces port isolation (the mechanism for this will be discussed shortly), and will allow power to easily couple from one feed to the other. Asymmetries could include slots, pins, or stubs on the patch itself, parasitic elements to improve bandwidth, or the feed structure.

This completes the design of the patch itself. The antenna is very compact; its total footprint is 21.36 mm², which is 17% smaller in area than a conventional square

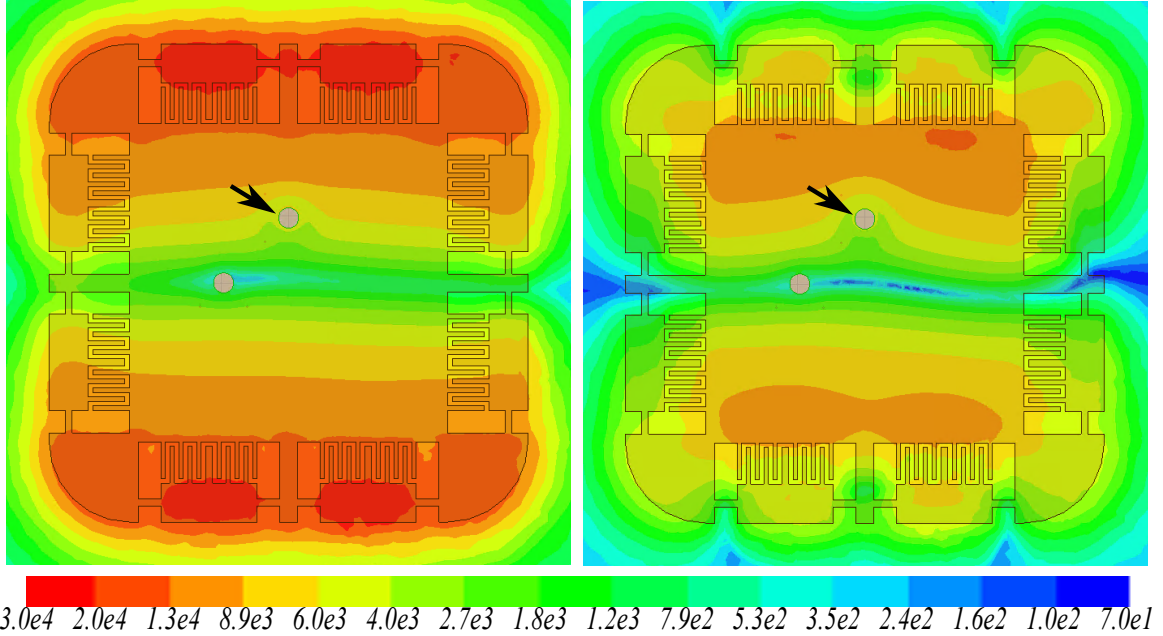


Figure 5.10: Complex electric field magnitudes (in V/m, logarithmic scale) in a plane bisecting the substrate at 3.6 GHz (left) and 5.8 GHz (right). Arrows indicate the excited feeds. Reproduced from [185] ©2021 IEEE.

patch on the same substrate at the lower operating frequency.

5.3.2.2 Feed Design

The proposed DBDPA cannot be fed directly with a microstrip in the same plane as the patch, since this would break the symmetry of the structure. Pin feeds were chosen instead, and this was preferred to aperture-coupled feeds due to their greater bandwidth, providing better matching in both bands. A pin for each polarization of diameter $p_d = 0.90$ mm is offset from the centre of the patch by a distance of $p_c = 2.90$ mm, as indicated in Fig. 5.9. These pins are able to impedance match at both frequencies since the optimal feed location for each resonance is near this position already ($p_c = 3.3$ mm and 2.4 mm for the conventional 3.6 GHz and 5.8 GHz patches, respectively). It is observed in Fig. 5.10 that each pin lies in the null of the orthogonal resonance, where the input resistance for this mode is zero; this ensures that high isolation between ports is achieved at each operating frequency, even though the two feeds are physically close together.

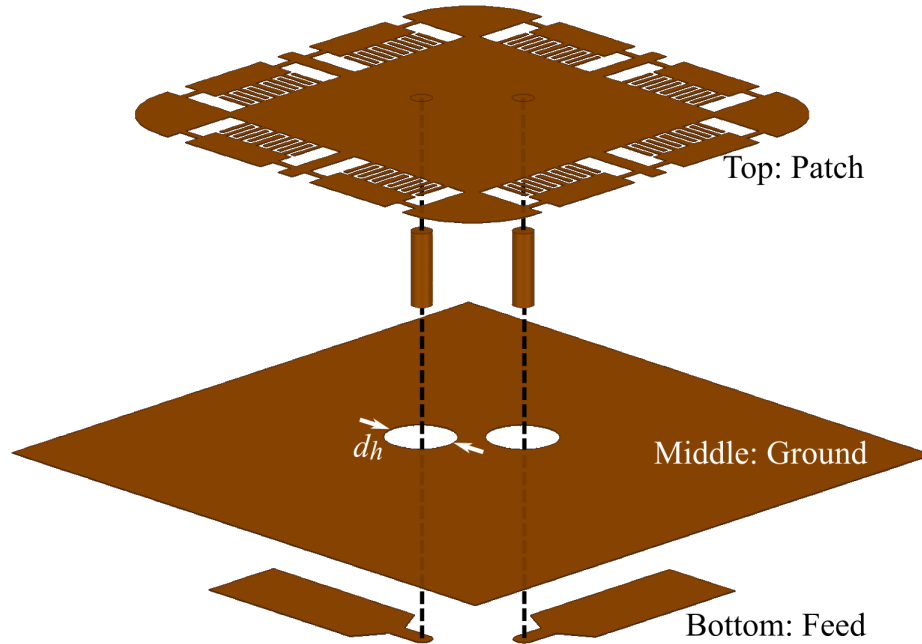


Figure 5.11: Exploded feed structure of the proposed DBDPA. Each layer is separated by a dielectric sheet with drilled holes through which the pins pass. Reproduced from [185] ©2021 IEEE.

The pin could be the central conductor of a coaxial cable, so that the entire structure consists of a single dielectric layer with a conductor backing that contains a small aperture through which the pin passes. A cable of small diameter, such as micro-miniature coaxial (MMCX), would be required to ensure that both feeds can be attached at the optimal feeding locations, since the diameter of other connectors such as SMAs would require the pins to be separated by a far greater distance. However, a pin-to-microstrip arrangement was preferred for two reasons. Firstly, a microstrip below the patch ground plane is isolated from the radiating element, allowing a different substrate to be used for feed miniaturization, and enabling planar array feed networks such as that in [189] to be integrated. Secondly, the microstrip can easily be matched to an SMA connector from the bottom layer, which facilitates proper measurement calibration with standard equipment. Regardless, either feed structure could be chosen for a given application.

The pin-to-microstrip feed is pictured in Fig. 5.11, where the pin connection of

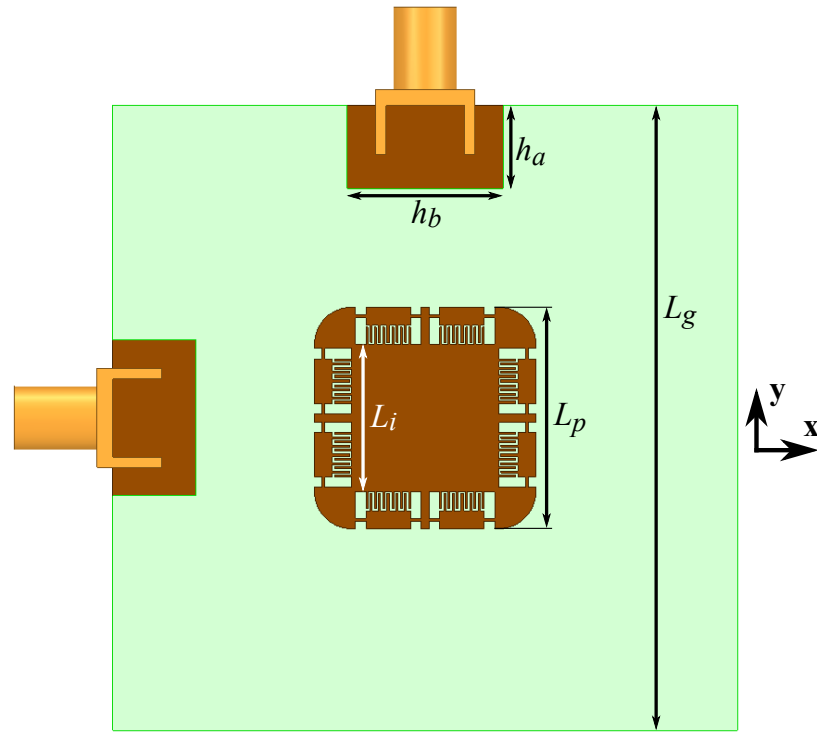
Table 5.6: DBDPA Dimensions, not including the MTM-EBG.

Parameter	Value	Parameter	Value
L_p	21.36 mm	p_a	1.86 mm
L_i	14.20 mm	w	3.70 mm
L_g	60.20 mm	h_a	8.00 mm
p_c	2.90 mm	h_b	15.00 mm
p_d	0.90 mm	α	30°
d_h	3.00 mm		

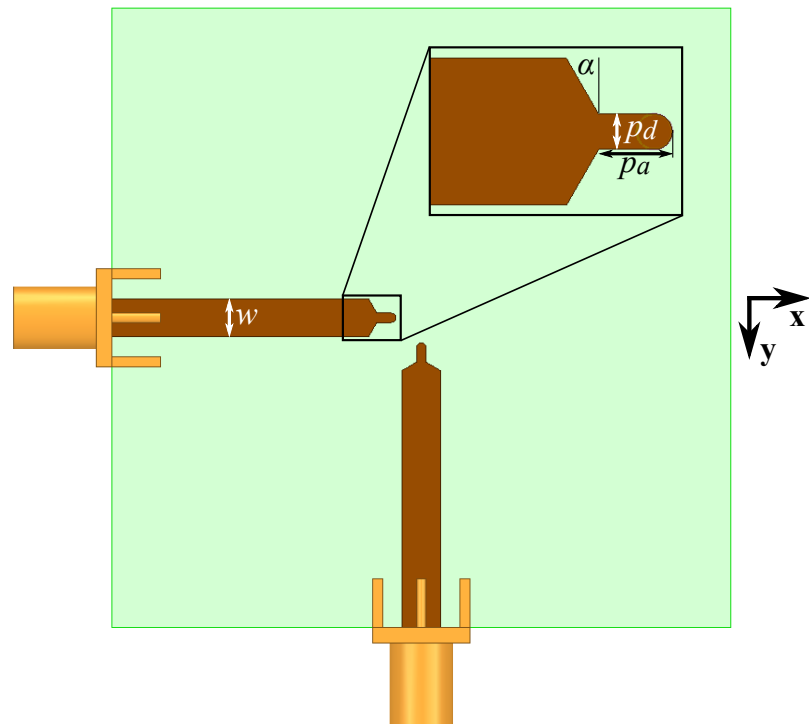
the patch and microstrip through a circular aperture in the ground plane can be seen. The top layer consists of the patch alone, while a middle layer is a solid ground plane with two holes through which the pins pass. 50- Ω microstrip lines on the bottom layer are linearly tapered towards the the pins, electrically connecting the top and bottom layers. The tapered microstrip structure has been tuned for optimal matching, and was found to match very well to conventional square patches in both bands. A good reflection coefficient for the DBDPA, presented below in Fig. 5.15, confirms that power is effectively being coupled from the feed into the patch. The two substrate layers of the structure, which are to be placed back to back, are shown in Fig. 5.12, and dimensions are provided in Table 5.6. Note that the microstrip lines are terminated in end-launch SMA connectors, which require a cutout of the top substrate to accommodate the SMA legs.

5.3.2.3 Ground Plane

The remaining design question involves the size of the ground plane, L_g . This requires a closer look at the antenna radiation characteristics (which will be shown in full shortly), since the ground plane can affect both gain and pattern shape. Furthermore, since some applications may require specific ground plane sizes, either for compactness or due to the presence of a larger conductor behind the antenna, performance as a

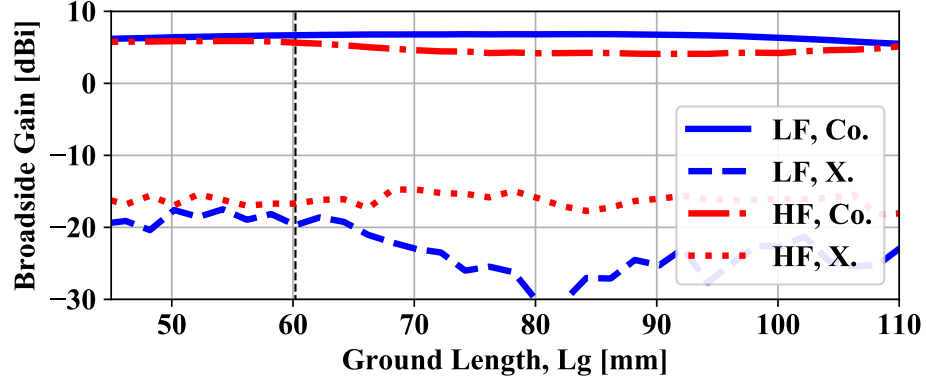


(a)

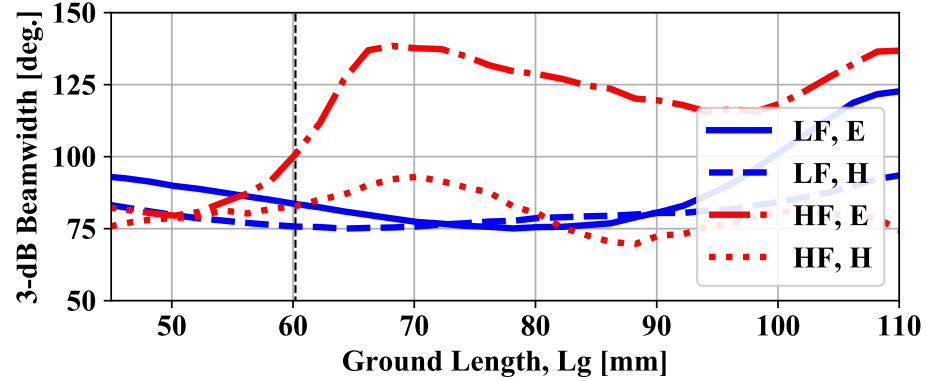


(b)

Figure 5.12: (a) Top and (b) bottom views of DBDPA. The middle ground plane can only be seen near standard SMA connectors on the top layer, and connecting feed pins are not visible. Reproduced from [185] ©2021 IEEE.



(a)



(b)

Figure 5.13: (a) Broadside gain of DBDPA at 3.6 GHz (LF) and 5.8 GHz (HF), for both co- and x-pol, and (b) E- and H-plane total 3-dB beamwidths at each frequency, versus ground plane size, L_g . The vertical dashed lines indicate the chosen ground size. Reproduced from [185] ©2021 IEEE.

function of ground plane size is important to study. Note that in the following studies, the patch is always centered on the ground plane, regardless of size.

The effect of ground plane size on gain is plotted in Fig. 5.13a, and it is observed that broadside (co-polarized) gain remains fairly constant across of wide range of possible ground sizes, particularly at 3.6 GHz. At 5.8 GHz, there is a difference of about 2 dB between maximum and minimum gain values. Broadside cross-polarization levels remain more than 19 dB below co-polarization levels for all ground plane sizes.

Fig. 5.13b plots the E- and H-plane 3-dB beamwidths as a function of ground plane size. It is observed that the slight reduction in broadside gain at 5.8 GHz corresponds to wider E-plane beamwidths, indicating that the reduced gain is due to a change

in beam shape rather than some form of loss, but the patterns otherwise remain fairly constant in shape as ground plane size increases. This indicates that while the pattern changes slightly for different ground planes, it still remains patch-like and is not greatly affected by the choice.

A patch with $L_g = 60.2$ mm is chosen, and this size is indicated by a vertical line on both plots in Fig. 5.13. This size is chosen for several reasons, although most importantly because it is near the maximum gain at 5.8 GHz, and presents similar pattern shapes at both frequencies. Implementation constraints were considered as well; if the ground size gets too small, the SMA connectors get closer to the patch and the cutout region begins to interfere with the patch itself. Furthermore, other parameters such as front-to-back ratio are improved with a larger ground plane, so making the ground as large as possible (without reducing the gain significantly at 5.8 GHz) optimizes performance. This completes the design of the proposed DBDPA.

5.3.3 Results

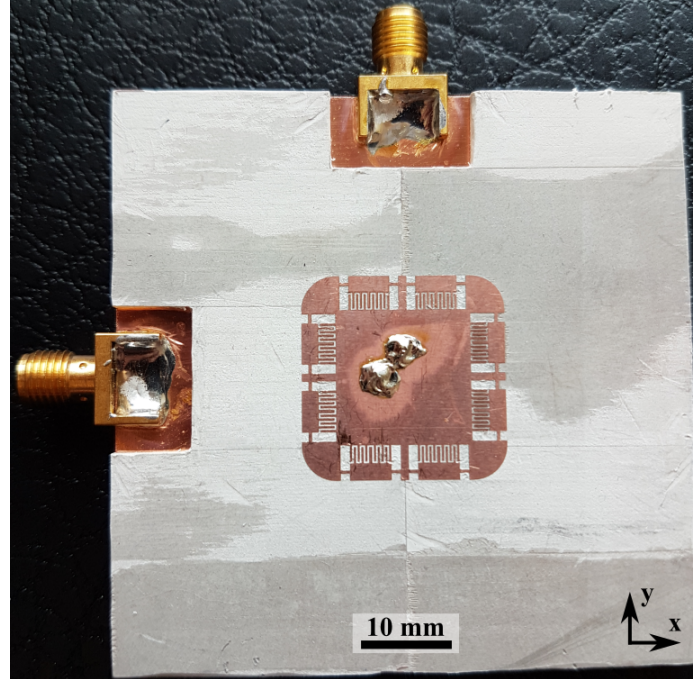
5.3.3.1 S-parameters

The DBDPA described above was simulated with Ansys HFSS, and then fabricated on Rogers 3003 using an LPKF Protolaser U3 laser milling system to pattern the copper. The antenna was fabricated in two parts and then assembled, rather than using a more complicated three-layer system; however, recall that only a single board would be needed if MMCX feeds were chosen rather than the pin-to-microstrip configuration. In this fabrication, one substrate includes the patch itself with a ground beneath it, and the other contains the microstrip feed structure, also above a ground plane. Circular apertures were etched into each ground plane for the feed pin to pass through, and the pin hole itself was drilled. The boards were then placed back to back such that the pin holes were aligned, and a 0.9-mm diameter wire was fed through the holes and soldered into place on each side. This provided some structural stability to the boards and ensured they were pressed tightly together, but for added mechanical stability

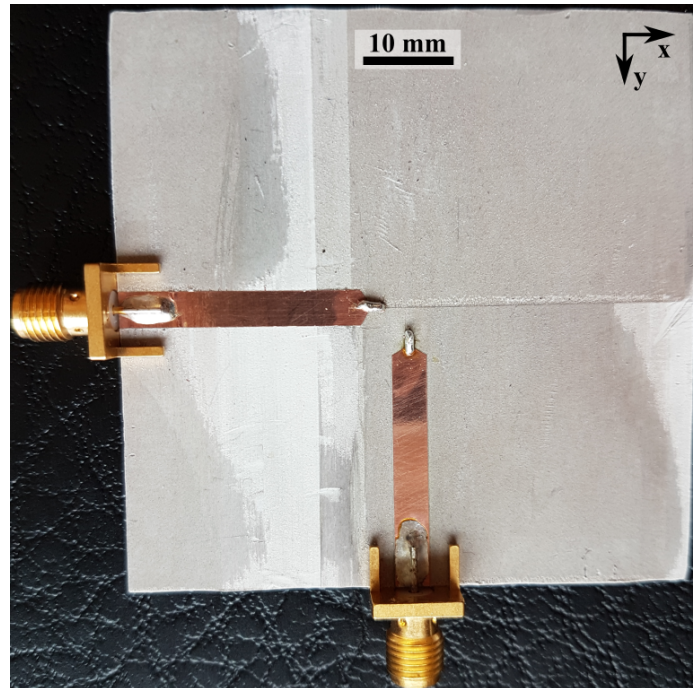
during measurements, the edges of the boards were taped together as well. The fabricated structure, after assembly, is pictured in Fig. 5.14, which can be compared to the simulated model in Fig. 5.12.

The fabricated antenna shows slight discolorations, and this is caused by regions where the laser etching singed the substrate (or the glue bonding the substrate and copper), which occurred either because minute differences in copper height or slight flexing of the board that caused the copper to etch away slightly more quickly in some regions. It has little to no effect on measurement results. One laser property that does affect the results, however, is a very slight over-etching of the metallic features due to the finite laser beam waist (about $12\ \mu\text{m}$). While this generally has an insignificant effect on the performance of a device, it does cause a very slight reduction in capacitance in the capacitive gaps, and causes up to a 0.6% frequency shift in the upper band [184, 196]. To counter this, the fabricated antenna has a capacitor length $d_1 = 1.85\ \text{mm}$, rather than the 1.83 mm used in simulation. This ensures the DBDPA will operate in the intended bands.

A vector network analyzer was employed to find the reflection coefficient of the antenna, as well as port-to-port isolation; the results of both simulation and measurement are presented in Fig. 5.15, and symmetry of the antenna ensures that reflection coefficient at both ports is the same. The simulated and measured curves appear to be in very good agreement; S_{11} is similar both in terms of shape and magnitude. While the upper frequency band shows nearly perfect agreement between the measured and simulated data, the lower band experiences a 0.4% frequency shift. Despite this, S_{11} remains well under $-10\ \text{dB}$ at the desired operating frequency. $-10\ \text{dB}$ bandwidths of the antenna are around 50 MHz at each frequency; these small values are characteristic of MTM-EBG-based devices, due to their dispersive nature. However, for applications such as WLAN, 20-40 MHz channels are commonly used, so this selectivity can be advantageous. Isolation in both bands exceeds 24 dB, and maximum isolation exists near the resonances due to the strong null produced at the orthogonal



(a)



(b)

Figure 5.14: (a) Top and (b) bottom views of the fabricated DBDPA. Reproduced from [185] ©2021 IEEE.

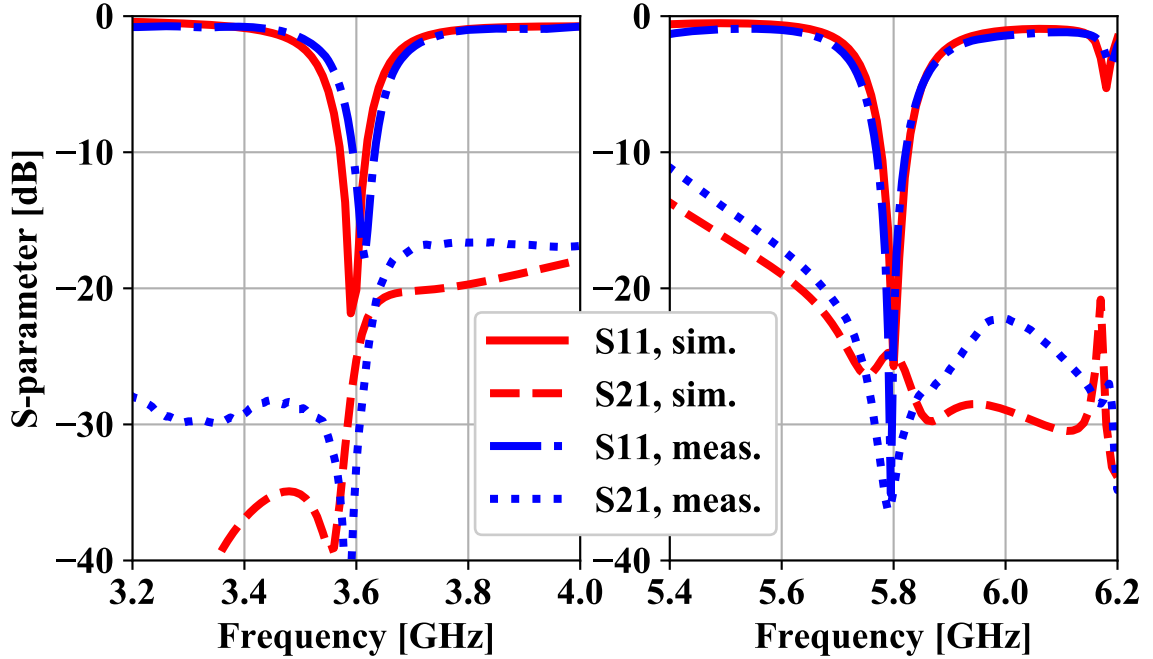


Figure 5.15: S-parameters of the DBDPA in each frequency band. Reproduced from [185] ©2021 IEEE.

feed’s location. Specific values related to the S -parameters can be found in the first three rows of Table 5.7.

5.3.3.2 Radiation Properties

To determine gain, the DBDPA was placed in an anechoic chamber and directly measured with calibrated standard-gain horns. The simulated and measured gain patterns for the E- and H-planes are presented in Fig. 5.16, and important quantities related to these results fill the remainder of Table 5.7. While the patterns for one polarization are shown, symmetry ensures that the patterns of both polarizations are identical in simulation, and identical within the limits of fabrication and measurement tolerances in practice. Similar gain patterns are observed for both frequencies, as was intended in the design, confirming that a standard patch-like TM_{10} mode is effectively radiating in each band. Measurement results show a very similar pattern shape, with some minor differences in cross-polarization being attributed to spurious radiation from the cables and connectors. The reduced gain observed in measurements of

Table 5.7: DBDPA Properties

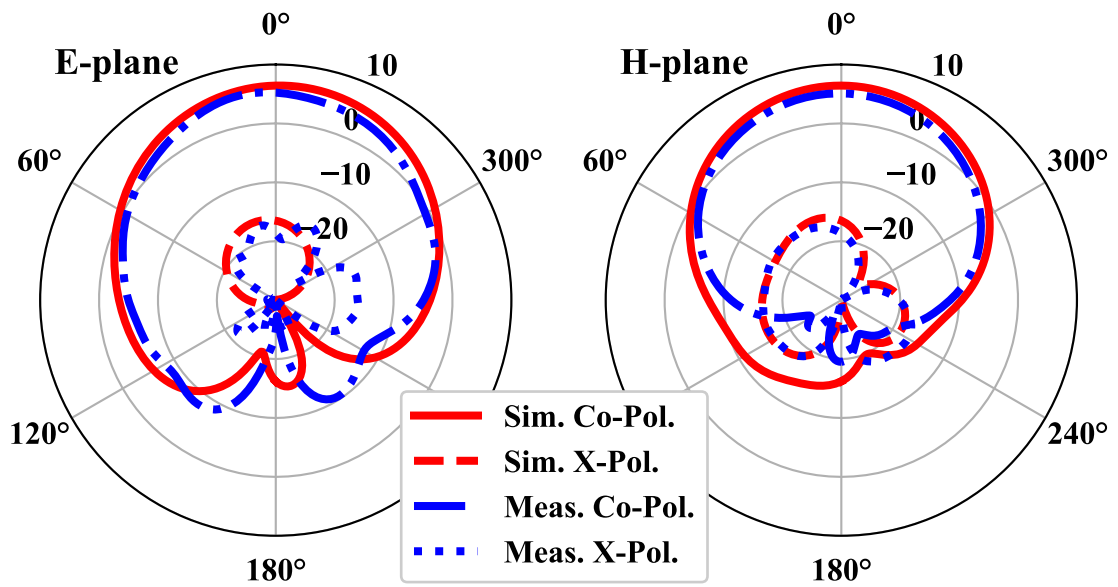
	3.6 GHz,	3.6 GHz,	5.8 GHz,	5.8 GHz,
	sim.	meas.	sim.	meas.
Peak RL	21.8 dB	17.8 dB	25.7 dB	35.1 dB
10-dB Bandwidth	50 MHz	41 MHz	49 MHz	52 MHz
Efficiency	0.87	N/A	0.79	N/A
Isolation	25.3 dB	33.0 dB	24.4 dB	34.8 dB
20-dB Iso. BW ¹	500 MHz	430 MHz	550 MHz	510 MHz
Broadside Gain	6.4 dBi	5.3 dBi	5.3 dBi	4.7 dBi
Max. x-pol., E	-16.3 dBi	-15.8 dBi	-24.3 dBi	-19.1 dBi
Max. x-pol., H	-15.6 dBi	-16.5 dBi	-12.8 dBi	-11.3 dBi
3-dB Beamwidth, E	85.6°	75.0°	100.8°	99.6°
3-dB Beamwidth, H	75.7°	60.6°	82.8°	79.3°
Front-to-Back	22.6 dB	30.0 dB	12.0 dB	13.0 dB

¹ As seen in Fig. 5.15; actual isolation BW is larger.

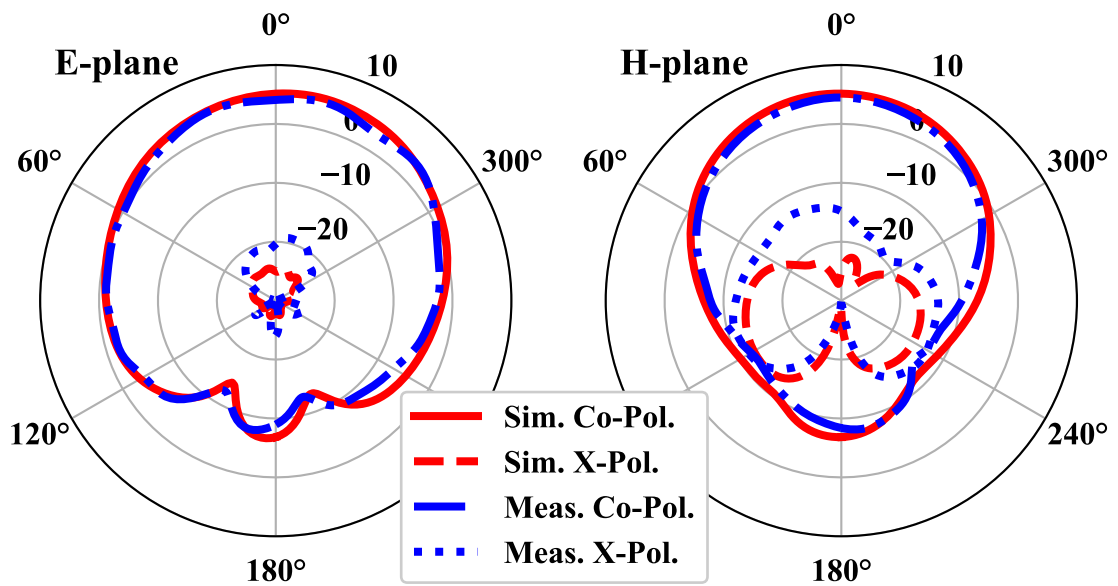
0.6 dBi to 1.1 dBi is largely caused by tolerances inherent to direct gain measurements, including those associated with standard gain horn calibration and the sensitivity of near-to-far-field transformations on measurement geometry and setup.

The DBDPA presents a simulated efficiency of 87% at 3.6 GHz, and 79% at 5.8 GHz. For the given substrate permittivity and height, efficiencies under 90% and 85% are predicted at these two frequencies, respectively, for a conventional patch [130], which indicates that dissipative losses within the patch are minimal. This is another indication that MTM-EBG devices do not greatly increase loss in a system, and operation compares well to conventional devices at the frequencies of interest as a result.

Simulated results of the proposed antenna are compared to various recent works in Table 5.8. In each category (with the exception of bandwidth), its performance is



(a)



(b)

Figure 5.16: Simulated and measured E- and H-plane gain patterns of the DBDPA for the a) 3.6 GHz resonance, and b) 5.8 GHz resonance. Reproduced from [185] ©2021 IEEE.

Table 5.8: Comparison of Dual-Band, Dual-Polarized RF Antennas in Recent Literature

	[165]	[168]	[170]	[166]	[167]	This Work
Centre Freq.'s [GHz]	0.92/1.8	10/12	2.45/3.5	2.4/5.4	1.38/1.57	3.6/5.8
RL [dB]	22/37	30/30	12/17	19/16	15/16	22/26
10-dB Bandwidths [%]	14.1/24.7	7.3/7.76	16.5/18.6	15.6/9.3	2/1	1.4/0.8
Isolation [dB]	45/43	NA	21/24	24/27	NA	33/35
Max. Gain [dBi]	11.8/7.0	7.7/8.5	3.2/5	7.2/7.3	2/7	6.4/5.3
Max. Cross-Pol. [dBi]	NR	-5/-12	-17/1	-13/-13	-11/-12	-15.6/-12.8
Beamwidth, E. [°]	63/85	80/55	various modes	80/50	various modes	86/101
Beamwidth, H. [°]	56/44	70/60	various modes	80/50	various modes	76/83
Front-to-Back	21.2/23.1	18/16	NA	22/20	NA	22.6/12.0
Antenna LxWxH [λ_0] ¹	0.51x0.26x0.06	1.76x0.43x0.25	0.32x0.23x0.01	0.35x0.35x0.09	0.22x0.22x0.03	0.26x0.26x0.02

¹ *Free-space wavelength*

comparable to or better than several of the presented antennas. It is perhaps structurally most comparable to [170] which employs a single dielectric sheet, but this antenna has varied performance as a function of polarization, and radiation is not constant across the spectrum as various modes contribute. Some electrical characteristics of [166] are similar to the proposed antenna, but this AMC-backed stacked design is difficult to fabricate and requires a large and complex feed mechanism. Advantages of the proposed DBDPA are therefore apparent for applications requiring small bandwidths, as it demonstrates good performance in both bands and polarizations while following a well-understood and versatile design procedure, and maintains a uniplanar, compact layout.

5.3.4 DBDPA with Matching Network

A drawback of the DBDPA design is that the pin position is fixed at both frequencies, and as discussed earlier, this limits the potential separation of operating frequencies. In fact, even the chosen frequency bands are expected to suffer from minor mismatches due to the chosen pin location, since it is not optimal in either band.

A solution to the impedance matching problem was presented in Chapter 4 with the double-stub matching network. This can easily be applied to the DBDPA to

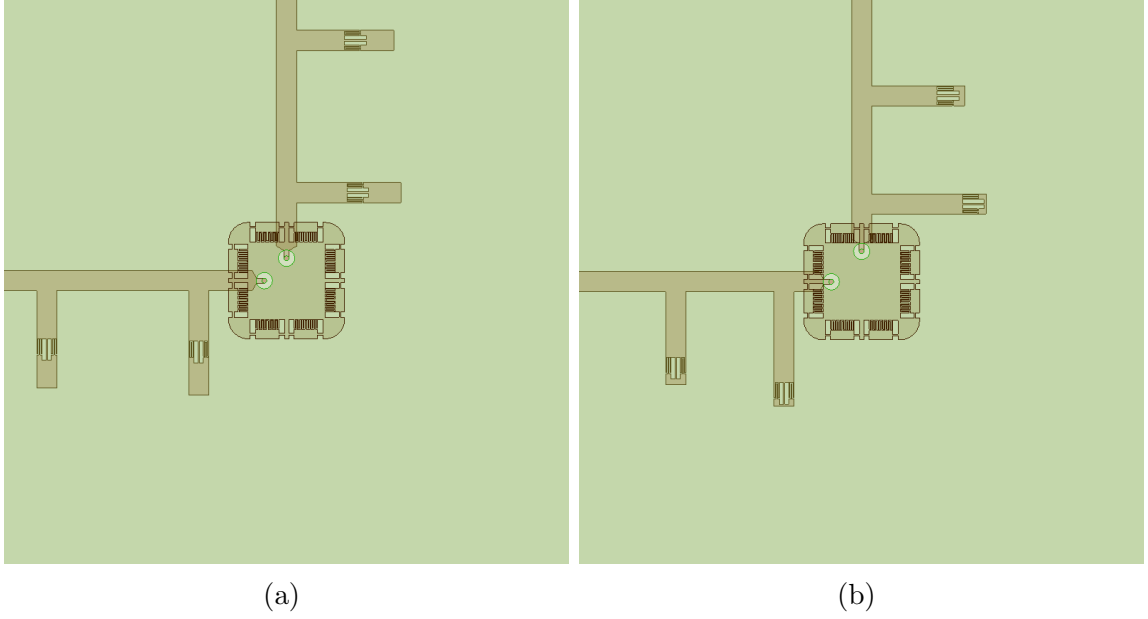


Figure 5.17: DPDPA with matching network for (a) a pin position from patch center $p_c = 4.1$ mm (Design A) and (b) $p_c = 5.6$ mm (Design B). The DBDPA is on the top layer, while the matching networks are on the bottom layer, below a ground plane.

demonstrate a) that impedance matching can indeed be achieved for any feed location even if it is not inherently matched at both frequencies already, b) that the double-stub matching network can easily be adapted to any matching problem, and c) that MTM-EBGs are well-suited to enable fully multi-band networks, as two radically different applications are combined for a dual-band system.

To demonstrate this, the same DBDPA as was presented in the previous section is fed in two different non-optimal locations, each one getting closer to the patch edge and presenting different levels of matching. S -parameters are presented in each case, and input impedance can be extracted at each port. Then, following the design procedure outlined in Chapter 4, a dual-band matching network is designed to maximize power delivered to the antenna.

While the optimal pin location was determined to be $p_c = 2.9$ mm, two different pin locations are chose: Design A sets $p_c = 4.1$ mm while Design B has pin location $p_c = 5.6$ mm. The change in pin location is not huge, but brings the pin feed successively closer to the patch edge, as shown in Fig. 5.17. These images also show

Table 5.9: Matching Network Dimensions for DBDPA With Different Feed Positions.

Parameter	Design A	Design B
p_c	4.10 mm	5.60 mm
a_1	9.24 mm	16.7 mm
a_2	19.15 mm	21.04 mm
b_1	8.76 mm	12.06 mm
b_2	17.86 mm	17.09 mm
c_1	7.98 mm	4.62 mm
c_2	24.2 mm	16.24 mm

the appropriate feed network that was designed for each patch. While these images are one-dimensional and show the outlines of both the patch and feed network in the correct orientation, recall that the patch is on the top substrate layer, while the feed network lies below a ground plane that separates the two layer. Dimensions of the feed network are included Table 5.9, with dimensions corresponding to those given in Fig. 4.20a. The MTM-EBG unit cell used in both matching network designs is also the same as the unit cell used for the dual-band matching network, since a bandgap in the same location is required.

S -parameter results for Designs A and B are presented in Fig. 5.18. The reflection coefficient is presented for the unmatched case as well as the case where a matching network is present. It is clear that as the pin moves away from the optimal location matching progressively gets worse, but it is restored almost entirely when the matching network is included. Design A presents 10-dB bandwidths of 47 MHz and 52 MHz while Design B shows 46 MHz and 54 MHz bandwidths, each around the upper and lower operating frequencies, respectively. These bandwidths are comparable to those achieved with the inherently matched pin, which indicates that good matching could be achieved for an antenna regardless of feed position; or, more generally, that this matching technique is applicable to a wide range of antenna designs. These results

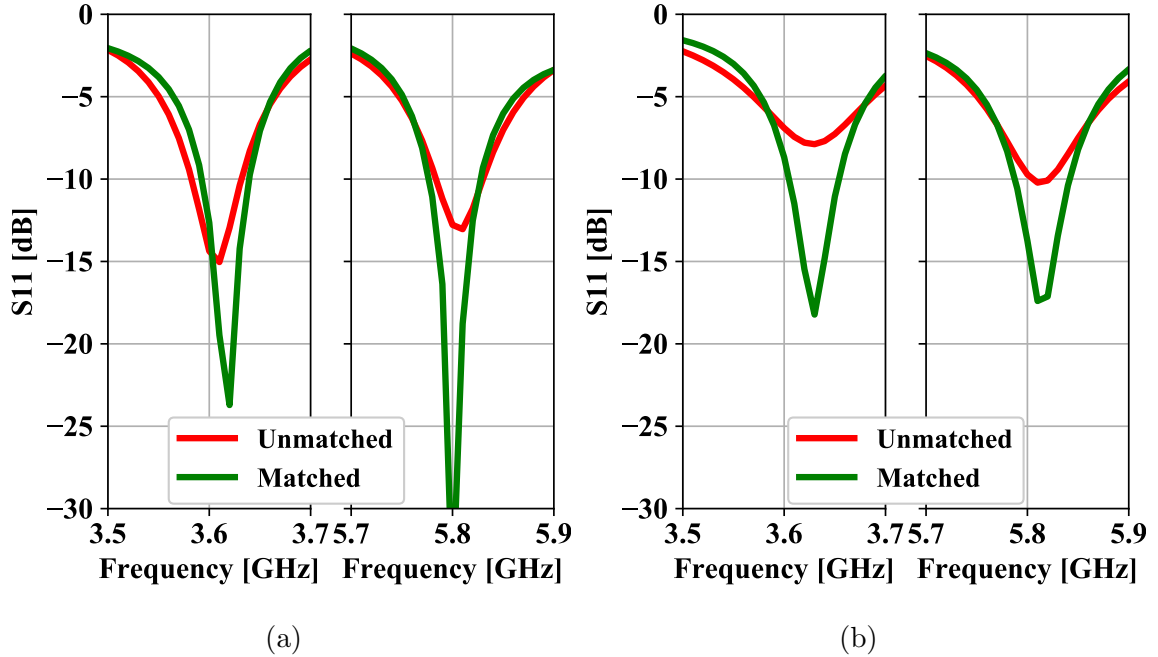


Figure 5.18: Simulation results of the DBDPA with different pin feed locations p_c , both with and without a matching network. (a) $p_c = 4.1$ mm (Design A) and (b) $p_c = 5.6$ mm (Design B).

also support the idea that bandwidth is limited by the MTM-EBG dispersion properties rather than poor impedance matching, since even with the matching network, bandwidth is not substantially increased compared to the original case.

5.4 GPS Antenna

The design of multi-band GPS antennas provides some challenges as compared to the DBDPA, although it is fundamentally very similar; it consists of a patch antenna with a ring of MTM-EBG unit cells on the outer edge that enable multi-band operation. The GPS antennas presented here will aim for tri-band operation, specifically at GPS L1 (center frequency of 1575.42 MHz), L2 (1227.60 MHz), and the recently-introduced L5 (1176.45 MHz) frequency bands. These bands are spaced substantially closer together than the frequencies chosen for the DBDPA, particularly L2 and L5. This challenge can be tackled in several ways: broadband operation to cover all bands (not likely achievable with MTM-EBG-based approaches), tri-band operation

which requires two different MTM-EBG unit cell rings [195], or dual-band operation with increased bandwidth, so that the lower band covers L2 and L5 simultaneously. The dual-band case also presents the advantage of covering the European Galileo navigation system bands E5a (1176.45 MHz) and E5b (1207.14 MHz), which lie on or between L2 and L5. The dual-band version will be investigated as it presents the important challenge of increasing antenna bandwidth.

In terms of implementation, a GPS antenna must meet certain criteria. GPS antennas require right-hand circularly polarized (RHCP) radiation, rather than simply linear polarization. A two-pin feed can still be used to realize this, but with each pin fed simultaneously with a phase difference of 90° . Overall, the system only needs one input signal, with a quadrature hybrid coupler dividing power to each feed. This can again be achieved in a printed form (using a multi-band or broadband coupler) or else with coaxial cables that connect to a coupler; the latter was chosen for these designs. The quadrature coupler was not included in simulation, but coaxial feeds with the appropriate phase condition were used. The goal of this section will be to produce a GPS antenna that has matching greater than 10 dB at each operating frequency and realized broadside gain as high as possible.

5.4.1 Bandwidth-Enhanced Antenna Design

A dual-band GPS antenna that covers three GPS bands must have an impedance bandwidth of at least 51.15 MHz in its lower band, which is the separation between L2 and L5; this translates to a minimum of 4.3% bandwidth around an intermediate frequency. This requires a substantial bandwidth enhancement of the MTM-EBG-based antenna as compared to the dual-band patch antenna or DBDPA, which are on the order of 1%. Some ways the bandwidth of a patch antenna can be improved are by lowering the substrate permittivity, and increasing the substrate height [130, 174]. Using an air dielectric can achieve both of these goals, and although this complicates fabrication, it is worthwhile if a useful GPS antenna can be produced.

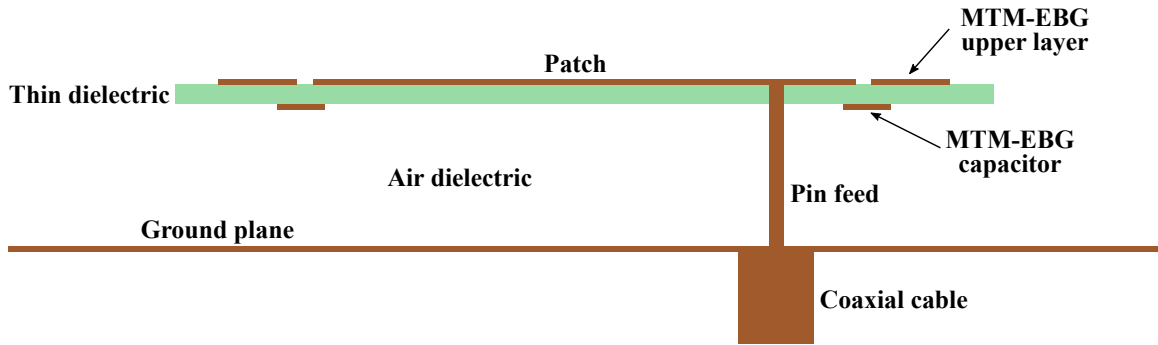


Figure 5.19: Side view of the GPS antenna structure, not to scale.

Structurally, an air dielectric simply consists of a suspended a copper trace above a ground plane, but the copper needs some sort of mechanical stability. Foam dielectrics exists that have a relative permittivity approaching unity, but these can be expensive or not robust, and often do not typically come with affixed copper sheeting. Instead, it is common to suspend a very thin dielectric sheet with the copper etching, since the sheet will have very little impact on the effective dielectric constant of the antenna, but will provide rigidity to mount and etch the copper. Suspension of the thin dielectric/upper conductor can be achieved in several ways, including mounting the thin dielectric on an aforementioned rigid foam sheet or 3D printed insert in between the layers, or with nylon screws near the edges of the structure that have little to no effect on performance.

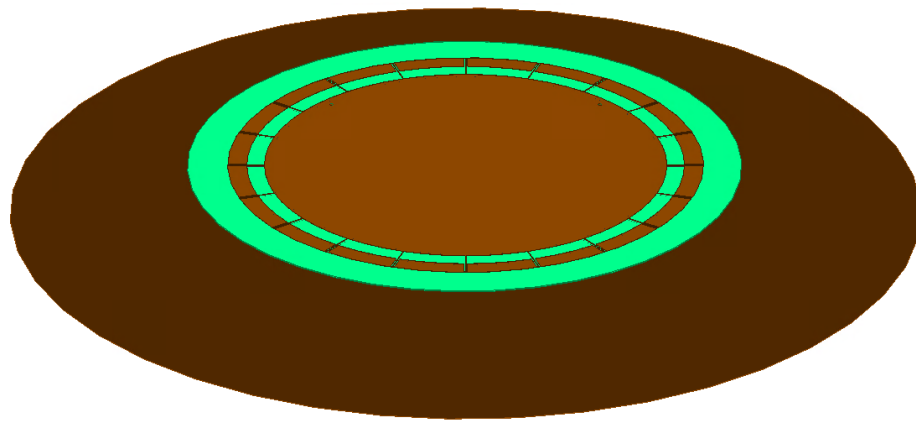
In terms of MTM-EBG design, this approach has an important secondary benefit. Since the upper conductors lie on a thin substrate with both sides available for etching, it is possible to realize the MTM-EBG capacitance in a parallel-plate form. This has the potential to produce much greater capacitance that interdigitations can provide, allowing for more flexible MTM-EBG design, including the larger capacitances needed to provide a bandgap at L1. The achievable capacitance is also influenced by the thin dielectric used, as this will have a minimal effect on antenna performance due to its thickness relative to the air dielectric, but a large effect on the capacitance, since it fills the space between capacitive plates.

A representative side view of the antenna structure with the parallel-plate capacitors is presented in Fig. 5.19, which is not to scale but exaggerated in order to clearly see the layers and pin feed. The thin dielectric chosen for this application is a 0.254 mm thick sheet of Rogers RO3006 ($\epsilon_r = 6.15$, $\tan \delta = 0.0025$) clad in 1/2-oz copper, with the primary patch etched into the upper metallization layer of the thin substrate and capacitive plates on the bottom side. The air dielectric has a height of 14 mm, chosen to provide sufficient bandwidth for the patch lower band to cover L2 and L5.

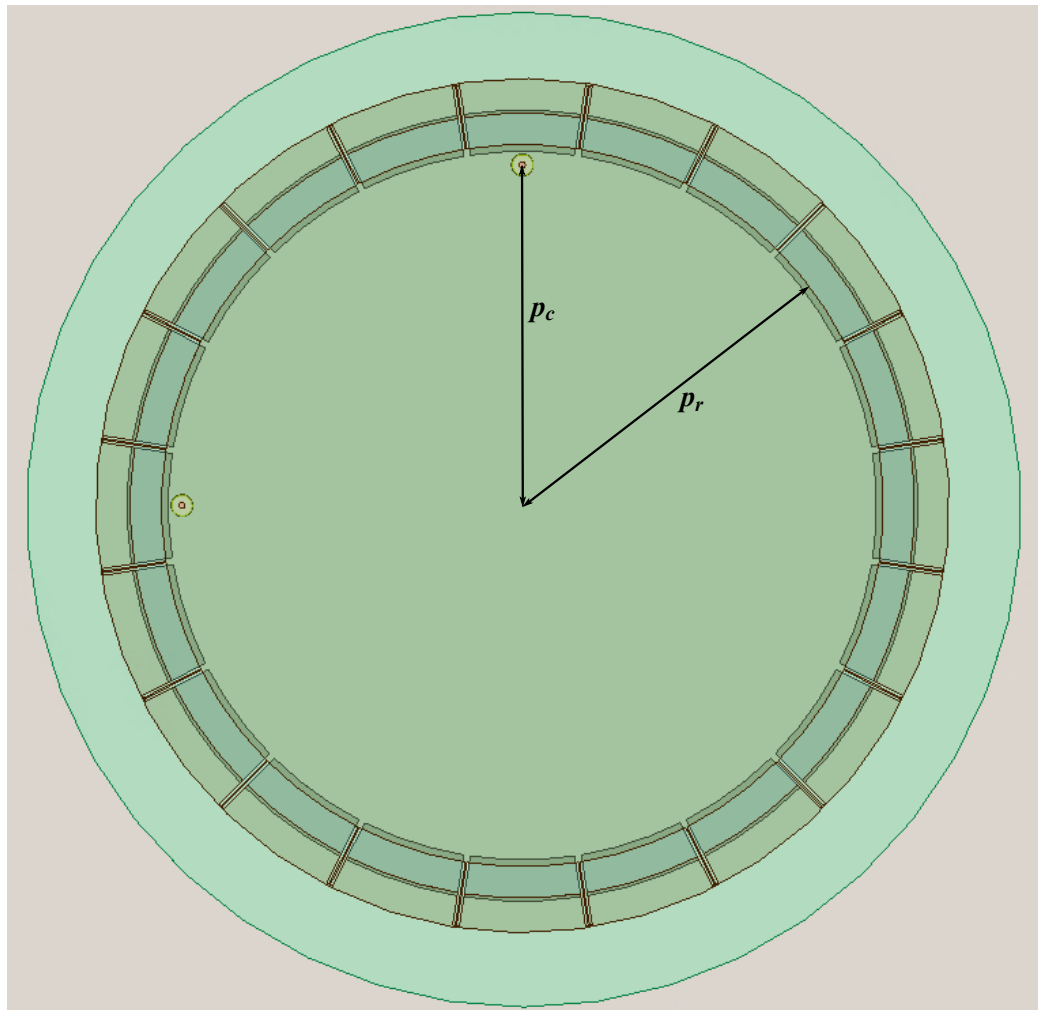
The patch was designed similarly to the DBDPA except with circular geometry, with the lower frequency taken to be the average of L2 and L5, and the upper frequency centered directly on L1. 20 MTM-EBG unit cells are placed azimuthally along the edge of the central patch region (enough that each individual unit cell can be approximated as rectangular), and they are designed to have a bandgap at the upper frequency and transmit with the required phase in the lower band, as usual. A full view of the antenna is presented in Fig. 5.20a, where the thin dielectric above the ground plane is observed. Fig. 5.20b shows a transparent version of the antenna in greater detail, so that the structure can easily be seen. The L1 patch radius is $p_r = 53$ mm with the pin placed a distance of $p_c = 50$ mm from the center, and a standard 50Ω coaxial cable is used as a feed. The ground plane radius is 120 mm.

A clearer view of the MTM-EBG itself is presented in a close-up view of a corner of the patch in Fig. 5.21, where the capacitive plate region, which is on the bottom layer of the thin substrate, is highlighted. The MTM-EBG has a length $l = 9.7$ mm, $g_C = 4.6$ mm, $k_1 = 1.0$ mm, and $k_2 = 0.465$ mm. Other MTM-EBG dimensions, following naming conventions used throughout this work, are $s = 0.2$ mm, $g_L = 0.4$ mm, and $d_3 = 0.3$ mm. The added radius of the thin substrate beyond the outermost edge of the MTM-EBG, r_t , is 20 mm in this case, but has a minor effect on results; it can be expanded to enable nylon screws to hold it in place further from the patch itself.

The MTM-EBG has a height larger than its length or width, and the effect of



(a)



(b)

Figure 5.20: (a) Conventional view of GPS patch antenna above ground plane, and (b) top view with semi-transparent layers.

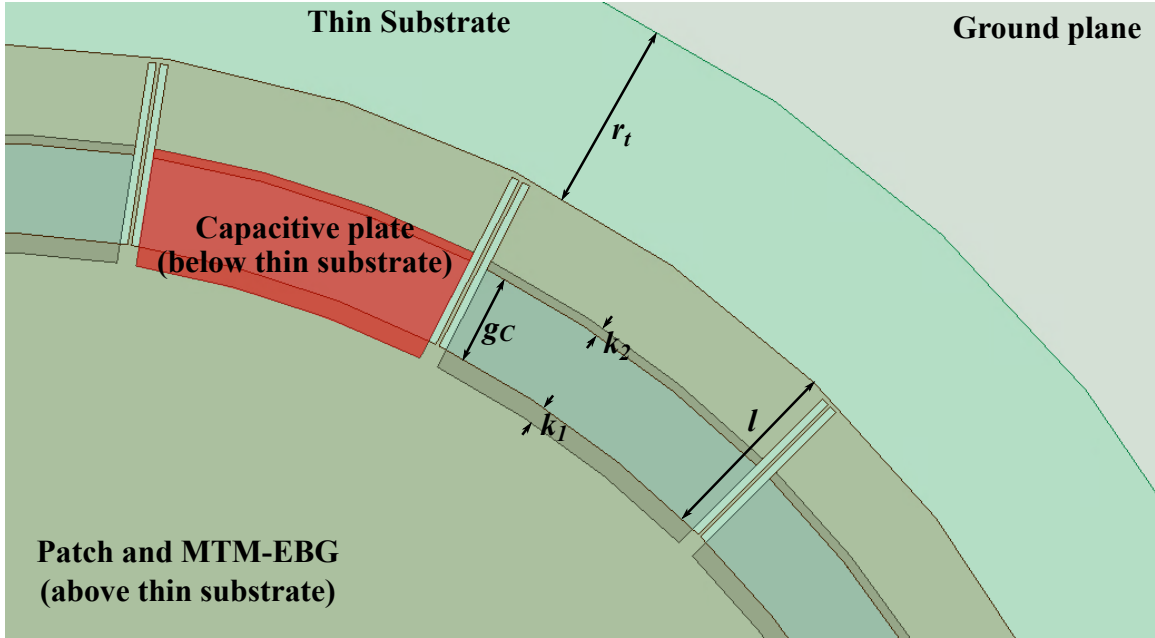


Figure 5.21: Close-up view of a segment of the GPS antenna, showing the MTM-EBG unit cells.

this is weaker modal coupling, and therefore a weaker overall bandgap. Its single-cell insertion loss in a transmission simulation is around 10 dB, which is much weaker than in other unit cells used to this point. The effects of this will be observed shortly. It is also worth noting that the feed location is near the edge of the patch, which was required to match to 50Ω for this geometry. The feed locations could be moved closer to the center of the patch with an appropriate matching network, but the MTM-EBG-based version would require a feed layer below the ground plane to implement this. This could be achieved in the same way it was for the DBDPA, but a direct coaxial connection was preferred for this structure.

5.4.2 Results

The GPS antenna was simulated and tuned in Ansys HFSS, and S -parameter results are presented in Fig 5.22, with operating frequencies indicated. The lower band demonstrates a 70.8 MHz/5.9% 10-dB bandwidth, which is sufficient to cover L2 and L5; the upper frequency is centered on L1 and has a bandwidth of 12.9 MHz/0.8%.

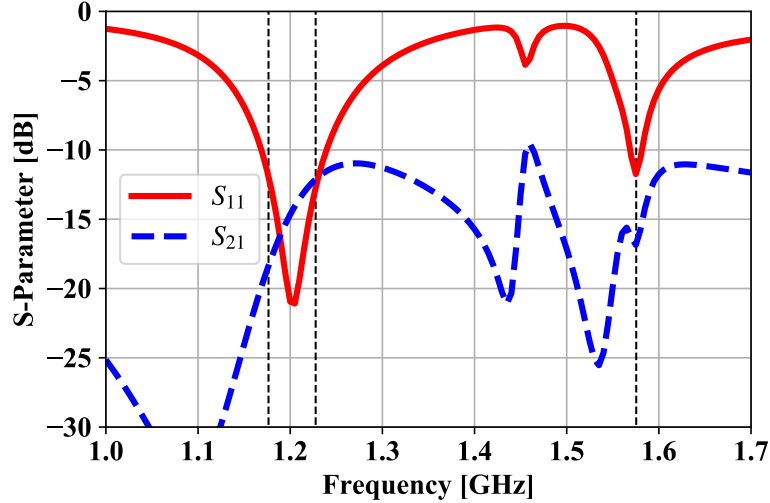


Figure 5.22: S -parameters of the of the GPS antenna, L1, L2, and L5 frequencies indicated by dashed vertical lines.

The increased substrate height and reduced permittivity evidently has a large effect on bandwidth at the lower frequency, but less so in the upper band; this is to be expected, since the upper band bandwidth remains primarily a function of MTM-EBG bandgap bandwidth, the strength of which is reduced by the large substrate height. It is possible that bandwidth could be improved with a matching network, but as discussed, this requires a different feeding configuration, which was not implemented here.

Isolation is also reduced for this antenna, as the substrate height does not enforce such a strong null at the patch center. Despite this, good isolation of over 16 dB is observed at L1 and L5, while isolation greater than 12 dB is produced at L2. Since the antenna is ultimately fed by a single feed with quadrature power division into the two ports, this parameter is less important than in previous designs, but is useful to consider if the bandwidth-enhancement approach was used in other structures, such as the DBDPA. Exact values for return loss and isolation are provided in the first couple rows of Table 5.10.

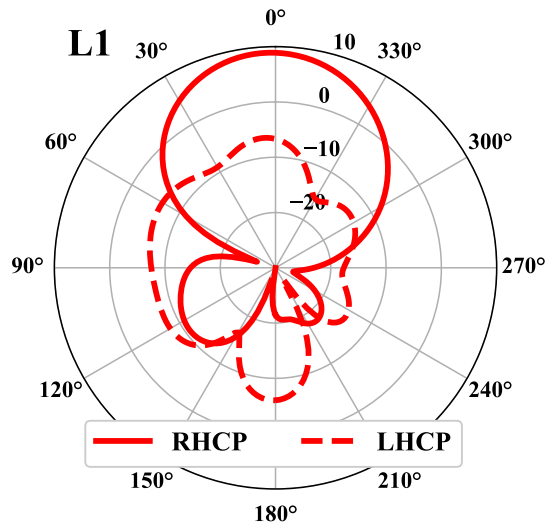
Gain patterns are presented in Fig. 5.23. All three frequencies present nearly 10 dB RHCP gain, much higher than typical GPS antennas that often have values

Table 5.10: Properties of GPS antenna with air dielectric.

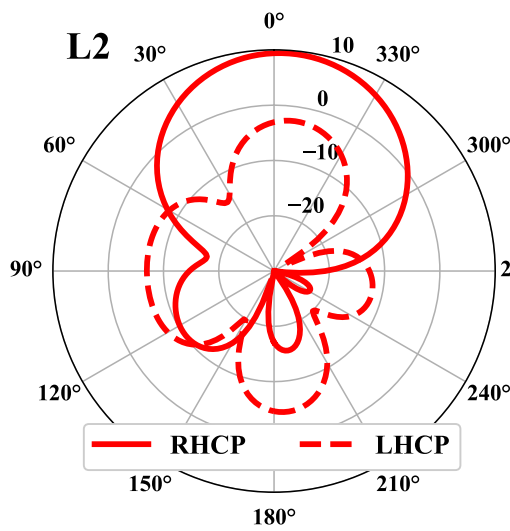
	L1	L2	L5
Return Loss	11.6 dB	12.8 dB	11.9 dB
Isolation	16.8 dB	12.1 dB	18.4 dB
Broadside Gain	8.9 dBi	9.4 dBi	9.6 dBi
Realized Gain	8.5 dBi	8.9 dBi	9.3 dBi
3-dB Beamwidth	49°	54°	58°
Axial Ratio	2.9 dB	4.2 dB	2.8 dB
Efficiency	71.6%	97.5%	98.3%

nearer to 0 dB, and have small backlobes and low gain at the horizon; this last property in particular is important since it reduces multi-path interference. There is a significant amount of cross polarization, although the co-/cross-polarization ratio at broadside is between 12 dB to 18 dB, with L2 performing the worst in this regard. Axial ratio (AR) is relatively poor as a result of the left-hand circular polarization (LHCP) contribution; it is provided in Table 5.10, along with many other relevant properties. There is a solution to this problem, however, that would bring the AR down to nearly 0 dB, and that is to use a four-pin feed, with the additional two being placed symmetrically around the patch; each successive pin would have a phase lag of 90°. This provides an additional degrees of symmetry, and would nearly eliminate broadside LHCP, thus improving AR significantly. Of course, this requires a more complex feed structure as well, but it could be done to improve patch performance.

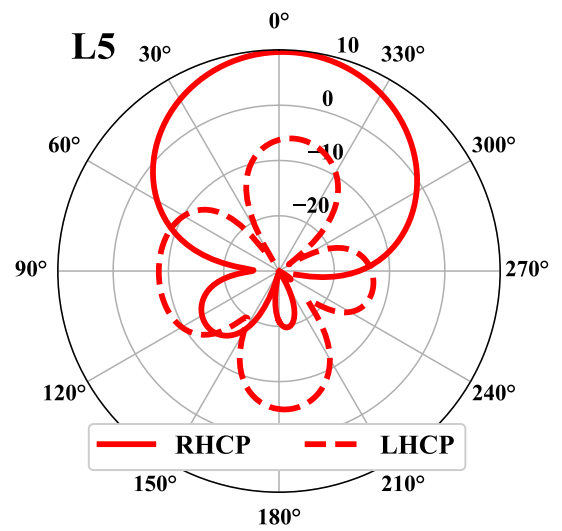
Finally, broadside realized gain, separated again into RHCP and LHCP components, is plotted as a function of frequency in Fig. 5.24. As expected, this peaks in between L2 and L5 where matching is greatest, but 8.5 dB or greater is still observed at all operating frequencies. The design of this GPS antenna, and the generally good performance, demonstrates that it is possible to improve bandwidth of an MTM-EBG-based antenna using conventional techniques, even if just over the



(a)



(b)



(c)

Figure 5.23: GPS gain patterns at (a) L1, (b) L2, and (c) L5.

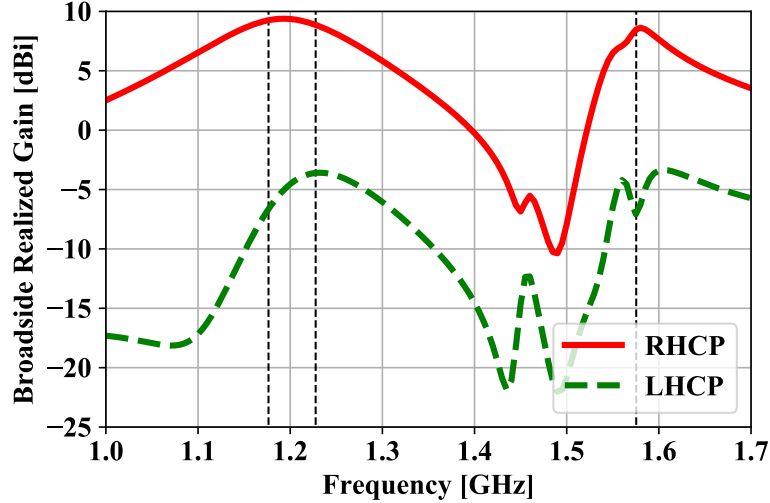


Figure 5.24: Broadside RHCP and LHCP realized gain of the GPS antenna, with the three operating frequencies indicated by dashed vertical lines.

lower operating band. It is likely that performance can be enhanced further through improved feeding or matching techniques, and it is worth noting that improving bandwidth at the lower band somewhat degrades performance in the upper band, as the MTM-EBG is less effective and return loss and efficiency are reduced. Regardless, this design met the initial goal of providing circular polarization with high realized gain and good matching at GPS L1, L2, and L5 bands.

5.5 Tunable DBDPA

5.5.1 Tuning Mechanism

With multi-band antennas now well-established, a further step is to render them tunable. This can be achieved by realizing the capacitances in the MTM-EBG with varactors. The MTM-EBG bandgap region is strongly dependant on the value of the series capacitors, and thus changing the capacitance causes the bandgap location, and therefore the supported higher-frequency resonance, to shift. The lower frequency operates far from the bandgap region of the MTM-EBG and thus a change in capacitance results in only a minor change in phase across the MTM-EBG unit cells, leaving this operating frequency nearly unchanged. Therefore, the upper frequency can be

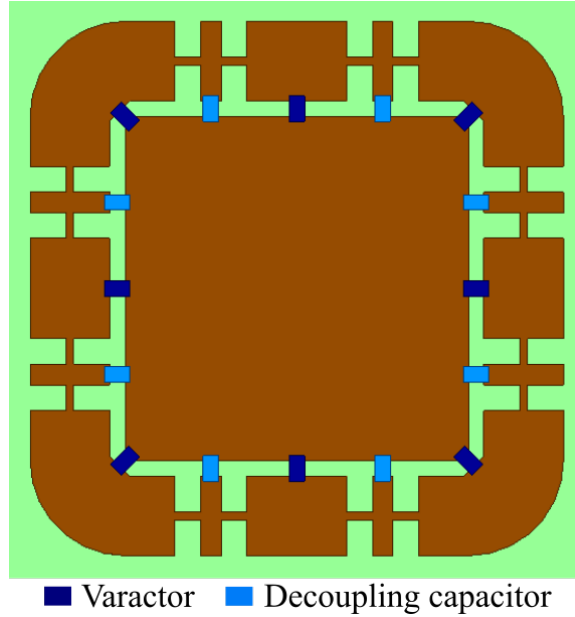


Figure 5.25: Tunable version of the DBDPA, using varactors in the MTM-EBG unit cells rather than interdigitated capacitors, and decoupling capacitors in the MTM-EBG strips.

tuned while the lower frequency remains constant. This could have various applications, for example in CBRS where spectrum is dynamically allocated, or as a dynamic channel that filters out other nearby frequencies, due to its high selectivity. Another possible application is in sensing, where a substance or even ambient conditions cause a change in the MTM-EBG's capacitance, while the constant lower frequency acts as a baseline or data channel.

The tunable antenna is based on the DBDPA, with varactors replacing the printed capacitors. An image of the patch face with varactors included is shown in Fig. 5.25. A problem with this, as discussed in Chapter 3 is that both sides of the MTM-EBG are normally electrically connected. This is resolved by inserting decoupling capacitors into the MTM-EBG strips, which renders the unit cell an OC at DC, but has a minimal effect on dispersion properties at the frequencies of interest. These are also included in the image, and decoupling capacitors of $10 \mu F$ are used.

Patch operation is otherwise unchanged, as the varactors with the same capacitance as the interdigitated capacitors in the DBDPA will result in the same operation. In

order to electrically tune them, however, a full bias network is required.

5.5.2 Bias Network

A voltage must be applied across the varactors to enable tuning, but this creates a major challenge, since any added component to the patch that causes asymmetry will result in poor port isolation and polarization purity. This indicates, first of all, that the voltage source and most of the associated circuitry must be with the feed network, below the patch ground plane. However, metal contacts are needed both to the patch and MTM-EBG edges to apply the DC voltage.

Since the feeding pins already contact the patch, they can be used to apply the DC voltage. The voltage can be applied directly to the feed lines, as long as decoupling capacitors isolate this from the input ports. Next, the MTM-EBG unit cells must be grounded at DC. Consider adding a high-impedance, quarter wavelength shorted stub to the patch layer at the lower patch operating frequency of 3.6 GHz. This stub is directly connected to the MTM-EBG and will provide a DC ground through a via, while at 3.6 GHz, the stub will act as an open circuit and therefore have minimal impact on patch operation (unlike attaching vias directly to the MTM-EBG, which drastically affects all resonances). At the higher operating frequency, the MTM-EBG unit cells will be in their bandgap region and effectively cut off the stubs as well, minimizing their effect on performance at this frequency as well.

An exploded view of the DBDPA with biasing network is shown in Fig. 5.26. The top layer consists of the patch with shorting stubs, two of which were included to preserve some degree of symmetry. Below this, separated by the usual layer of 1.524 mm-thick Rogers RO3003 substrate, is the ground plane, containing holes through which the pins pass. The bottom layer includes the microstrip feed TLs with a decoupling capacitor, and the DC biasing pads which include choke inductors to isolate the area from AC. Simply applying a voltage across the pads biases the varactors.

Note that fabrication complexity increases somewhat to realize the tunable DBDPA

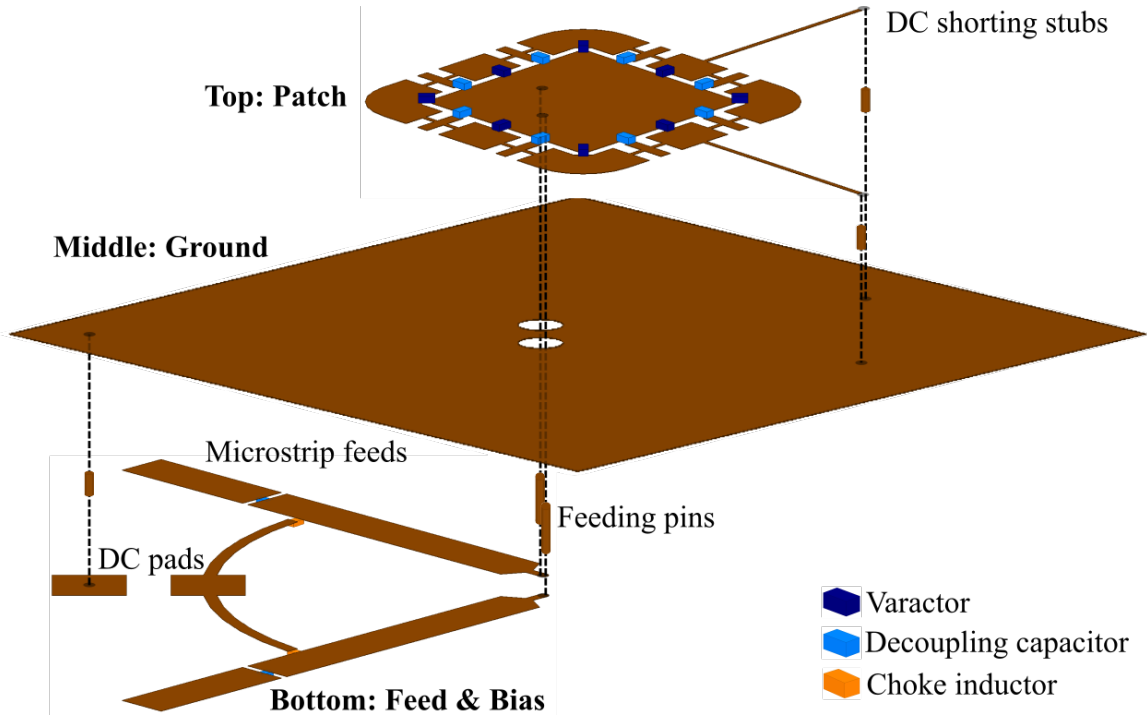


Figure 5.26: Exploded view of the tunable DBDPA. The top layer includes the patch and DC shorting stubs, the bottom layer includes the microstrip feeds with the remainder of the bias network, and a ground plane with holes for the feed pins separate the layers.

Three vias are required, as well as a number of discrete loading elements that must be soldered on to both the top and bottom sides of the board. This is a required trade-off to achieve the required functionality of an antenna that is simultaneously dual-band and dual-polarized, with the upper band being independently tunable of the lower band for both polarizations.

5.5.3 Results

S -parameters of the tunable DBDPA are presented in Fig. 5.27 for a range of different varactor capacitances between 0.44 pF and 0.54 pF. The upper band is swept from 5.60 GHz to 5.97 GHz with excellent matching in all cases, and isolation is at the same level as for the initial DBDPA, although it is not included in the plot. The lower band maintains a reflection coefficient better than -10 dB for all varactor values

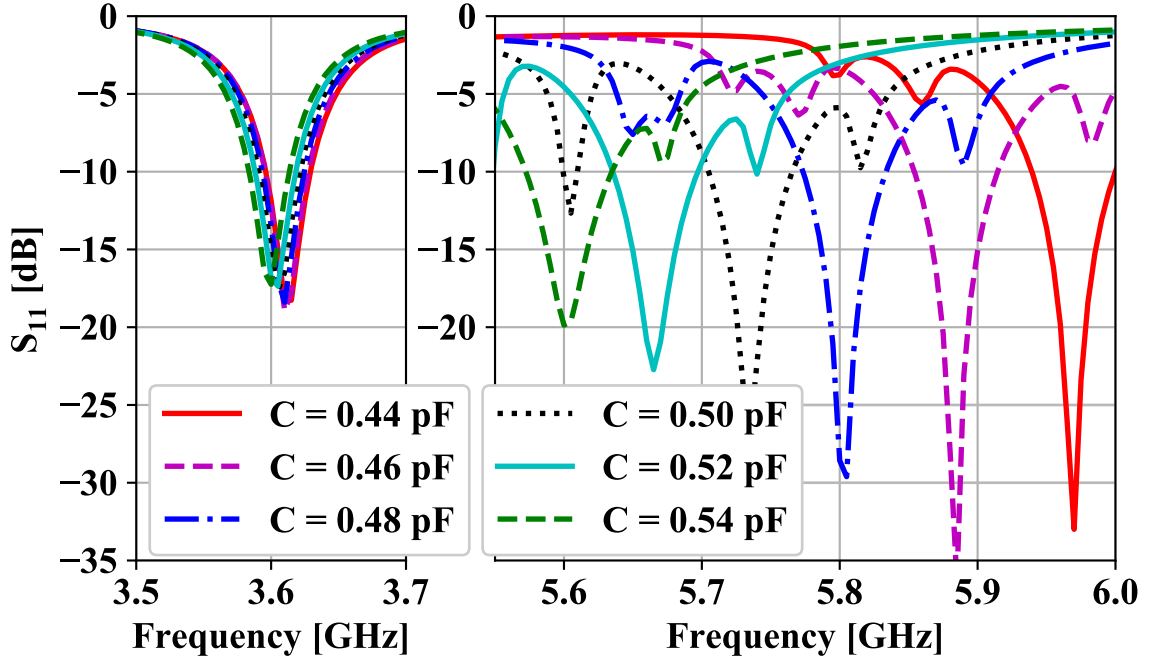


Figure 5.27: S_{11} of the patch antenna for different varactor capacitances, C .

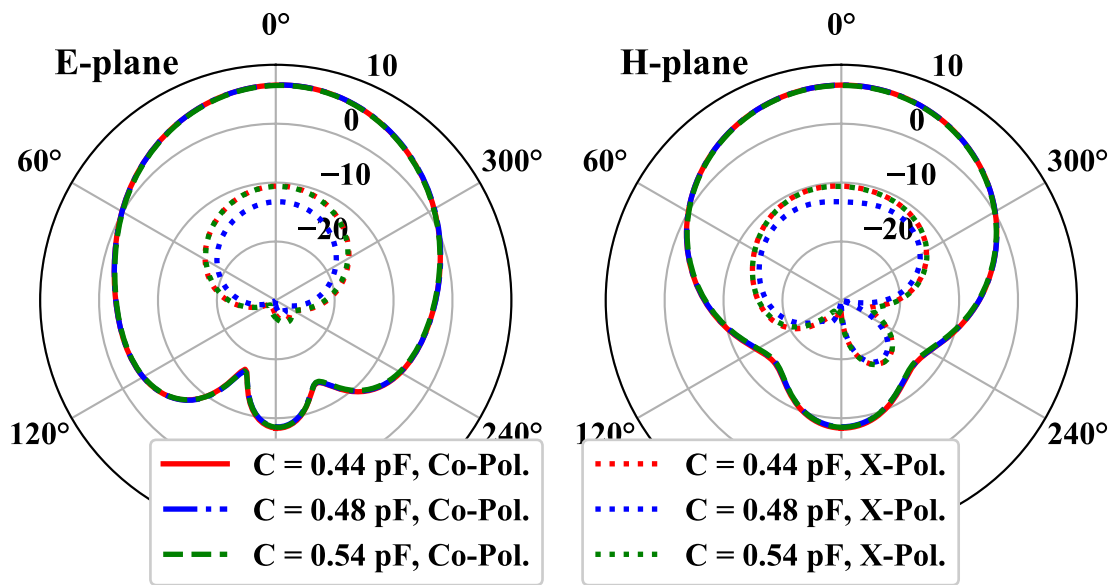
at 3.6 GHz, although a very minor shift of this band is apparent, and keeping the reflection coefficient at this level is what determines the frequency range across which the upper band can be swept.

The voltage required to across sweep the nearly 400 MHz upper-frequency range is typically a few volts or less, but depends on the actual varactors chosen. They are further assumed to be lossless in the simulation, but for varactors of these values loss can be significant, which will degrade antenna gain at all frequencies. Solutions to this are to find low-loss varactors, or else redesign the MTM-EBG unit cell to require larger C values, as varactor losses are typically relatively smaller in this case. Note that the decoupling capacitors in the MTM-EBG are also assumed to be lossless, and realistic modeling will have similarly deleterious effects on gain on efficiency; this is best mitigated by choosing small decoupling capacitors associated with lower loss. Regardless, this antenna acts as a proof of concept for the tunable case.

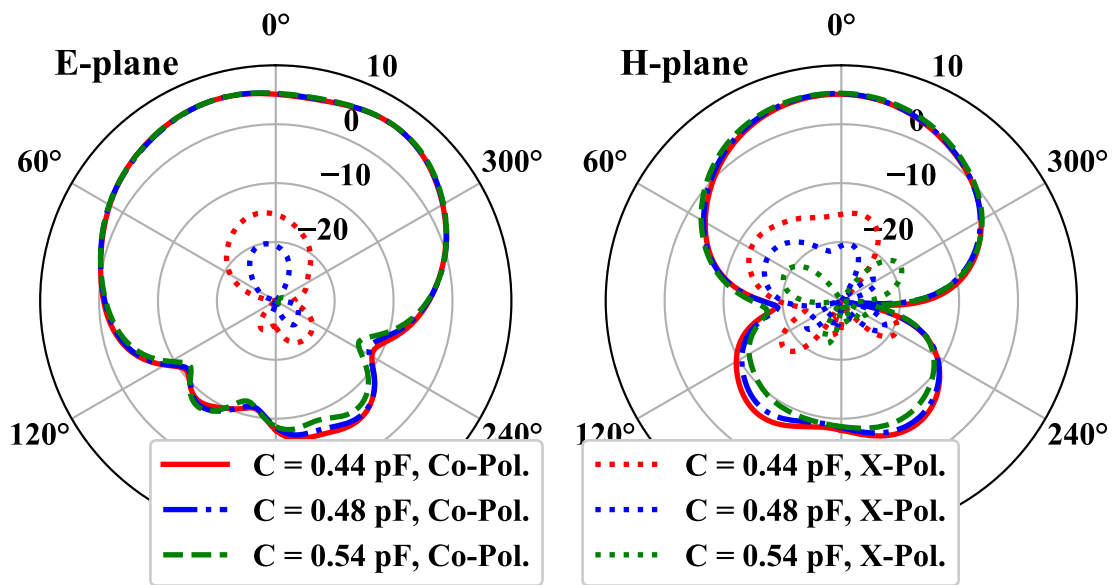
Fig. 5.28 displays the radiation patterns of the tunable DBDPA for three different

varactor values: 0.48 pF, which resonates at 5.8 GHz, and the lower and upper varactor limits, 0.44 pF and 0.54 pF, respectively. Gain patterns at the lower frequency (3.6 GHz) are shown in Fig. 5.28a, while the higher frequency patterns (5.60 GHz, 5.80 GHz, and 5.97 GHz) are shown in Fig. 5.28b. Co- and X-pol in E- and H-planes are included, and note that patterns for both polarizations are identical, although only one excitation is included here.

Neither directivity nor maximum gain change substantially for any of the resonances, demonstrating that this is an effective tuning method where radiation performance is constant across the tuning band, at both frequencies. Final steps for implementation of this antenna are incorporating realistic losses into lumped elements, fabricating the antenna, and measuring its performance. While this remains to be done, the tunable DBDPA provides further evidence of the versatility of the MTM-EBG, by providing a new and unique application based on the same principles.



(a)



(b)

Figure 5.28: (a) E- and H-plane gain patterns for various varactor capacitances C at the lower radiating frequency. (b) Gain patterns at upper frequency resonances.

Chapter 6

Conclusion

6.1 Summary

The main goal of this thesis was to take a newly-developed technology with a number of advantageous physical properties, the MTM-EBG, and apply it to create multi-band version of a wide set of planar microwave antennas and components. Although the invention of TL-MTMs has led to the creation of many novel structures and technologies, few have been developed generally enough to create a suite of different circuit elements and antennas, and none have done so while remaining uniplanar, fully printable, and designed with a theory that allows rapid determination of its dispersion properties.

Chapter 2 begins by investigating current approaches to producing multi-band microwave devices, including recent techniques involving MTMs and EBGs. A comprehensive investigation of multi-band circuit components and antennas follows, with a particular focus on planar structures since these are required in many modern systems, from 5G to IoT to various communication systems and protocols. These devices are categorized, and advantages and drawbacks of individual structures and methods are discussed.

The MTM-EBG is introduced in Chapter 3. While the theory and analysis is not new, a focus is taken on highlighting important characteristics and properties that directly relate to integration into realistic devices. This includes discussions comparing

the properties of individual unit cells to the properties of an infinite periodic array of unit cells, and investigates implementation strategies that rapidly lead to results. Intuition for designing MTM-EBG unit cells for operation at arbitrary frequencies is developed.

Design strategies are finally used to produce a suite of circuit components in Chapter 4, starting with the humble microstrip stub filter. Embedded MTM-EBG unit cells render stub filters dual- and tri-band, and a radial version presents the opportunity to increase filter bandwidth. An impedance matching network is next proposed based on the double-stub tuner, which directly uses design ideas developed in the multi-band stub filters but in a much more complex system. Despite many design options and variables, a simple algorithm is proposed to rapidly produce an optimized solution, and the result is a dual- or tri-band matching network for arbitrary complex and frequency-dependent impedances. Finally, a dual-band WPD serves to illustrate how the MTM-EBG can be integrated in a completely different type of system, and tackles challenges of using extremely small unit cells in a compact area. All devices are uniplanar and fully printed, and most are additionally miniaturized compared to their respective conventional, single-band versions.

Chapter 5 switches the focus to multi-band antennas, starting with a simple dual-band, microstrip-fed patch antenna. An improved and simultaneously dual-band and dual-polarized antenna is next presented, which features four resonances that all radiate in the TM_{10} mode. Two pin feeds excite both frequencies of a single polarization each, and the pin mechanism allows the feed structure to be separated from the antenna itself. This enables easy integration of a matching network with the DBDPA, and the MTM-EBG-based double-stub tuner was combined to the DBDPA to demonstrate this. All of these antennas have small bandwidths, but that was addressed with the design of a GPS antenna that covers L1 in the upper band, and L2 and L5 in a broader lower band. Significant bandwidth enhancement was achieved to produce this antenna while maintaining high RHCP gain, as is required for this

application. Finally, focus returned to the DBDPA as it was taken one step further with the introduction of varactors into the MTM-EBG unit cells, and a bias network was designed to allow them to be electrically tuned. Both polarizations of the upper band of the DBDPA were able to be tuned simultaneously over a broad frequency range, while the lower band remained stable.

The main drawback remains the limited bandwidth that most of the devices display. This was partially addressed in the matching network where reasonably large bandwidths were produced, and the tunable DBDPA may be used in such a way that large bandwidths are not required. The GPS antenna with air dielectric was the most successful in using traditional techniques to improve antenna bandwidth, and while a substantial increase was observed in the lower band that covered L2 and L5, it remains narrowband around L1. This makes these devices particularly suitable to applications where high selectivity is desired, and the bandwidth of the presented structures is still sufficient for many commercial systems.

Advantages of the MTM-EBG-based devices, however, are many. First and foremost, the design of these devices is soundly based on theory, and no ad-hoc design procedures are needed as a result. The diversity of circuit components and antennas demonstrated reinforce the theoretical nature of the work, and suggest that further variability is possible, in terms of both structure and frequency bands. The other main advantages are related to implementation, as nearly all devices are uniplanar and fully printed for easy and scalable fabrication, and compact, with multi-band devices generally taking up less space than their single-band counterparts. These devices also tend to perform well, and are perfectly suited to many existing and emerging multi-band applications.

6.2 Limitations

Taking this work as a whole, advantages of using the MTM-EBG are clear, but reflection on some universal limitations is merited. Limitations on bandwidth have been

well established (and overcome in some cases), but the claim of general applicability should be assessed.

Firstly, do limits exist for the type of devices that can be improved with the MTM-EBG? It is clear that devices which present terminated guided-wave structures present the best opportunities for implementation; that is, stubs, patch antennas, and so on. However, the WPD provided a counter example where transmission through a TL was required at both frequencies. This case is clearly more complex, but the implementation of multi-band versions is limited by the ability to embed MTM-EBG unit cells into small spaces. Signal-routing in this way suggests other opportunities as well, however; for example, the MTM-EBG would be a suitable candidate for creating simple diplexers that divide a signal based on frequency. In fact, this application does not require the MTM-EBG unit cell to be electrically small, so many unit cells could be introduced to create a bandgap response with a steep rolloff.

Generally, limitations on the MTM-EBG will be dependent on how much space there is to implement a unit cell. The use of high-permittivity substrates or the need for an extremely small electrical length places physical limitations on the MTM-EBG size, making fabrication difficult or impossible. These limitations are met more quickly for fully printed unit cells, but ultimately are reached even if discrete chip components are used.

The spacing of adjacent operating bands is similarly limited by the ability to implement an MTM-EBG unit cell in a small physical area. Assuming transmission at one frequency and rejection at the other, an MTM-EBG unit cell generally needs to be implemented in an area related to the difference in guided wavelength at each operating frequency. As this distance shrinks, MTM-EBG unit cells have a decreasing amount of space for implementation. This is compounded by the fact that the transmitting band approaches the MTM-EBG band edge and becomes increasingly dispersive, requiring even physically smaller unit cells to achieve the same electrical length. The limit where it becomes untenable to embed a unit cell is frequency-dependent since

fabrication limits are fixed; in other words, it would be easier to create a unit cell with, for example, 10° of phase when the guided wavelength is on the order of metres rather than centimetres or even millimetres. No specific limit can therefore be given for this limit of nearby frequency spacing, although frequency ratios as small as 1.4 were demonstrated in this work, so the limit lies below this in sub-6 GHz bands.

Note that this same limitation also prevents the creation of wideband devices by merging narrowband responses of adjacent bands. The responses cannot be brought arbitrarily close together due to the need for increasingly small MTM-EBG unit cells to enable this.

The upper limit for band spacing is much more forgiving, since widely-spaced frequencies present the opportunity to implement large and robust MTM-EBG unit cell designs. Furthermore, assuming a bandgap is required at a high frequency far removed from a lower frequency, the MTM-EBG can be expected to have no substantial affect on the lower band, while still providing a bandgap where required. Limitations in this case come more readily from practical design considerations, for example, increased loss in higher bands, or difficulty in feeding an antenna with substantially different resonant lengths. While creative solutions to these problems may be found, it is not an inherent property of the MTM-EBG that limits frequency spacing.

While the magnitude of the S -parameter response of circuit components was typically the primary parameter of interest, the overall phase response merits investigation as well, as this may affect the transmission or reception of modulated signals. Simulations and measurements in the context of such signals should be completed to predict any limitations that may arise in this regard.

Another limitation to consider is the power levels that the MTM-EBG-based devices can handle. Small signals are generally assumed throughout the work, meaning that the presented devices are shown to be suitable as receivers of low power levels rather than as a part of base-station infrastructure. Some potential issues could arise with high power levels. Small gaps in the MTM-EBG unit cells could lead to arcing,

or passive intermodulation could result due to heating of the fine features [204]. Furthermore, heating could result in weakened adhesion between the substrate and trace and delamination may result, particularly in the capacitive interdigitations. These effects should be studied as a part of future work to assess the feasibility of using them in high-power scenarios.

6.3 Future Considerations

A suite of devices based on the MTM-EBG have been presented, but the general design approach means that other applications are possible. This includes designing new devices that incorporate MTM-EBG unit cells, as well as adding more bands to existing devices (e.g., quad-band stub filters and matching networks, or tri-/quad-band antennas). Furthermore, combinations of these devices are required to develop fully multi-band solutions, and while it has been shown that this can be done, there are many cases where the implementation is still required. This could include a fully dual-band antenna array with dual-band antennas, matching networks, and feed structure, or even a tunable version of the same. The full systems should further be investigated in the context of modulated signals to fully understand their range of applicability.

Unique features of the MTM-EBG could render it applicable for more than just multi-banding purposes. Consider using an electrically small MTM-EBG unit cell to isolate patch antenna elements in an array. Existing methods of doing this, for example with EBGs [9], take a large amount of space, but performance could be greatly improved if antenna elements could be isolated without substantial increases to element spacing. As another example, the non-harmonic nature of the MTM-EBG bandgap and dispersion properties could be used to suppress harmonic bands (or a fundamental harmonic) while simultaneously improving performance at the frequency or frequencies of interest.

This work has just scratched the surface of tunability. It has also been demon-

strated in [190] with mechanical tuning, but electrical tuning has proven effective, and this suggests it could be exploited further. A compact and tunable stub filter would be useful, and while a tunable matching network would be more complicated, it could allow for a nearly real-time response to some input, either as frequency or the load itself changes. Adding tunability to antenna feed structures could result in the creation of phased arrays, or applications in beamforming. Before investigating these approaches, however, the realistic tunable DBDPA should be fabricated to ensure that the varactor-based structure operates as predicted.

The main drawback of MTM-EBG structures has consistently been bandwidth, and more creative solutions to this problem merit further investigation. Bandwidth enhancement will likely come from the antenna or circuit element design itself, but MTM-EBG based approaches might also be beneficial; for example, increasing the number of unit cells so that the bandgap bandwidth improves may allow overall improvements. While it is unlikely that broadband techniques will be possible with embedded MTM-EBG unit cells, the limits to how much bandwidth can be gained should be investigated.

The use of MTM-EBG unit cells in different domains should also be studied. This may include different topologies such as stripline or coaxial, in which similar techniques could be employed to improve existing devices. It could also include the expansion into mm-waves, where fully printed solutions are required, and the MTM-EBG-based structures would simply need to be scaled. Decreasing capacitance needed for MTM-EBG unit cells at higher frequency bands suggests that the unit cell structure and its implementation may naturally be simplified for operation in X-/Ku-/K-/Ka-bands (although higher frequencies such as W band present different challenges that may limit MTM-EBG implementation, such as the use of lossy silicon-based substrates). This is an instantly attractive proposition since the MTM-EBG is readily able to overcome some challenges that 5G and even emerging 6G are facing as they progress further into these bands.

All applications of the MTM-EBG have been one-dimensional, in that propagation across only a single axis has been considered. Recently, it has been shown that the MTM-EBG can indeed be characterized using MTL theory in two dimensions, and that this structure is closely related to the UC-EBG [182, 183]. Many new applications could be considered with a 2D MTM-EBG. Consider the linearly-polarized, dual-band patch antenna. Its bandwidth was constrained by the fixed patch width, but a 2D MTM-EBG could be used to render the width frequency-dependent as well as the length. Other structures could take advantage of a unit cell with different x and y propagation properties, for example, to create a uniplanar microstrip crossover (i.e., allowing microstrip lines to cross on the same layer while maintaining high isolation from each other). The most general application of such a structure would be to design a wholly frequency-reconfigurable circuit, such that the same circuit board looks completely different at different operating frequencies. Applications could be as diverse as having a power divider circuit act as an antenna array at some frequency, or connecting to WiFi as well as GPS in the same, overlapping space.

Much remains to be explored, but this work lays the foundation for engineers to understand approaches to MTM-EBG-based design, and use it for a continually expanding number of diverse applications.

Bibliography

- [1] S. Barth, “Theory and applications of a uniplanar transmission-line metamaterial-inspired electromagnetic bandgap structure,” M.S. thesis, Department of Electrical and Computer Engineering, University of Alberta, Edmonton, AB, 2015.
- [2] S. Barth and A. K. Iyer, “A miniaturized uniplanar metamaterial-based EBG for parallel plate mode suppression,” *IEEE Trans. Microw. Theory Techn.*, vol. 64, no. 4, pp. 1176–1185, 2016.
- [3] K. Finkenzeller, *RFID Handbook: Fundamentals and Applications in Contactless Smart Cards and Identification*, 2nd ed. Chichester, West Sussex, England: John Wiley & Sons, 2003.
- [4] L. Zhang, Y.-C. Liang, and M. Xiao, “Spectrum sharing for internet of things: A survey,” *IEEE Wireless Communications*, vol. 26, no. 3, pp. 132–139, 2019.
- [5] Q. Zhao and B. M. Sadler, “A survey of dynamic spectrum access,” *IEEE Signal Processing Magazine*, vol. 24, no. 3, pp. 79–89, 2007.
- [6] M. M. Sohel, M. Yao, T. Yang, and J. H. Reed, “Spectrum access system for the citizen broadband radio service,” *IEEE Communication Magazine*, vol. 53, no. 7, pp. 18–25, 2015.
- [7] M. Grissa, A. A. Yavuz, and B. Hamdaoui, “TrustSAS: A trustworthy spectrum access system for the 3.5 GHz CBRS band,” in *IEEE INFOCOM 2019 - IEEE Conference on Computer Communications*, Paris, France, 2019, pp. 1495–1503.
- [8] N. Engheta and R. W. Ziolkowski, *Metamaterials: Physics and Engineering Explorations*. Hoboken, NJ: John Wiley & Sons, 2006.
- [9] F. Yang and Y. Rahmat-Samii, *Electromagnetic Band Gap Structures in Antenna Engineering*. New York, NY: Cambridge University Press, 2009.
- [10] R. M. Fano, “Theoretical limitations on the broadband matching of arbitrary impedances,” *Journal of the Franklin Institute*, vol. 249, no. 1, pp. 57–83, 1950.
- [11] J. S. McLean, “A re-examination of the fundamental limits on the radiation of electrically small antennas,” *IEEE Trans. Antennas Propag.*, vol. 44, no. 5, pp. 672–676, 1996.
- [12] K.-K. M. Cheng and S. Yeung, “A novel dual-band 3-dB branch line coupler design with controllable bandwidths,” *IEEE Trans. Microw. Theory Techn.*, vol. 60, no. 10, pp. 3055–3061, 2012.

- [13] A. M. Zaidi, T. Khan, M. T. Beg, B. K. Kanaujia, and K. Rambabu, "Dual-band design techniques for microwave passive circuits: A review and applications," *IEEE Microwaves Magazine*, vol. 23, no. 7, pp. 61–77, 2022.
- [14] A. M. Zaidi, B. K. Kanaujia, T. Khan, M. T. Beg, K. Rawat, K. Rambabu, and S. R. Rengarajan, "Multiband design techniques for passive planar microwave circuits: A review," *IEEE Microwaves Magazine*, vol. 23, no. 9, pp. 57–69, 2022.
- [15] F. Elek and G. V. Eleftheriades, "Dispersion analysis of the shielded Sievenpiper structure using multiconductor transmission-line theory," *IEEE Microw. Wireless Compon. Lett.*, vol. 14, no. 9, pp. 434–436, Sep. 2004.
- [16] K. Payandehjoo, A. Tavallaee, and R. Abhari, "Analysis of shielded electromagnetic bandgap structures using multiconductor transmission-line theory," *IEEE Trans. Adv. Packag.*, vol. 33, no. 1, pp. 236–245, 2010.
- [17] C. R. Paul, *Analysis of Multiconductor Transmission Lines*. Hoboken, New Jersey, USA: John Wiley & Sons, Inc., 1994.
- [18] G. V. Eleftheriades, "A generalized negative-refractive-index transmission-line (NRITL) metamaterial for dual-band and quad-band applications," *IEEE Microw. Wireless Compon. Lett.*, vol. 17, no. 6, pp. 415–417, Jun. 2007.
- [19] W. E. Kock, "Metallic delay lenses," *Bell Syst. Tech. J.*, vol. 27, pp. 58–82, Jan. 1948.
- [20] W. Rotman, "Plasma simulation by artificial dielectrics and parallel-plate media," *IRE Trans. Antennas Propag.*, vol. AP-10, no. 1, pp. 82–85, Jan. 1962.
- [21] G. V. Eleftheriades, O. Siddiqui, and A. K. Iyer, "Transmission line models for negative refractive index media and associated implementations without excess resonators," *IEEE Microw. Wireless Compon. Lett.*, vol. 13, no. 2, pp. 51–53, Feb. 2003.
- [22] C. Caloz and T. Itoh, "Application of the transmission line theory of left-handed (LH) materials to the realization of a microstrip "LH line",", in *IEEE Int. Symp. Antennas Propag.*, San Antonio, TX, Jun. 2002, pp. 412–415.
- [23] G. V. Eleftheriades, A. K. Iyer, and P. C. Kremer, "Planar negative refractive index media using periodically L-C loaded transmission lines," *IEEE Trans. Microw. Theory Techn.*, vol. 50, no. 12, pp. 2702–2712, Dec. 2002.
- [24] G. V. Eleftheriades and K. G. Balmain, *Negative-Refraction Metamaterials: Fundamental Principles and Applications*. Hoboken, NJ: John Wiley & Sons, 2005.
- [25] A. Grbic and G. V. Eleftheriades, "Overcoming the diffraction limit with a planar left-handed transmission-line lens," *Phys. Rev. Lett.*, vol. 92, p. 117 403, Mar. 2004.
- [26] A. K. Iyer and G. V. Eleftheriades, "Free-space imaging beyond the diffraction limit using a Veselago-Pendry transmission-line metamaterial superlens," *IEEE Trans. Antennas Propag.*, vol. 57, no. 6, pp. 1720–1727, Jun. 2009.

- [27] A. Grbic and G. V. Eleftheriades, “Dispersion analysis of a microstrip-based negative refractive index periodic structure,” *IEEE Microw. Wireless Compon. Lett.*, vol. 13, no. 4, pp. 155–157, Apr. 2003.
- [28] F. Elek and G. V. Eleftheriades, “A two-dimensional uniplanar transmission-line metamaterial with a negative index of refraction,” *New Journal of Physics*, vol. 7, no. 163, Aug. 2005.
- [29] A. Lai, T. Itoh, and C. Caloz, “Composite right/left-handed transmission line metamaterials,” *IEEE Microwaves Magazine*, vol. 5, no. 3, pp. 34–50, Sep. 2004.
- [30] C. Caloz, “Dual composite right/left-handed transmission (D-CRLH) transmission line metamaterial,” *IEEE Microw. Wireless Compon. Lett.*, vol. 16, no. 11, pp. 585–587, Nov. 2006.
- [31] C. Caloz and T. Itoh, *Electromagnetic Metamaterials: Transmission Line Theory and Microwave Applications*. Hoboken, NJ: John Wiley & Sons, 2006.
- [32] D. Sievenpiper, L. Zhang, R. F. J. Broas, N. G. Alexopolous, and E. Yablonovitch, “High-impedance electromagnetic surfaces with a forbidden frequency band,” *IEEE Trans. Microw. Theory Techn.*, vol. 47, no. 11, pp. 2059–2074, Nov. 1999.
- [33] F. Elek, “Theory and applications of multiconductor transmission line analysis for shielded Sievenpiper and related structures,” Ph.D. dissertation, Graduate Department of Electrical and Computer Engineering, University of Toronto, Toronto, ON, 2010.
- [34] B. A. Munk, *Metamaterials: Critique and Alternatives*. Hoboken, New Jersey, USA: John Wiley & Sons, Inc., 2009.
- [35] A. A. Oliner, “Periodic structures and photonic band-gap terminology: Historical perspectives,” in *29th European Microwave Conference*, Munich, Germany, Oct. 1999, pp. 295–298.
- [36] K. M. Ho, C. T. Chan, and C. M. Soukoulis, “Existence of a photonic gap in periodic dielectric structures,” *Phys. Rev. Lett.*, vol. 65, no. 25, pp. 3152–3155, Dec. 1990.
- [37] P. de Maagt, R. Gonzalo, J. Vardaxoglou, and J.-M. Baracco, “Review of electromagnetic-bandgap technology and applications,” *URSI Radio Science Bulletin*, no. 309, pp. 11–25, Jun. 2004.
- [38] R. E. Collins, *Foundations for Microwave Engineering*, Second. Hoboken, New Jersey, USA: John Wiley & Sons, Inc., 2001.
- [39] E. Yablonovitch, “Inhibited spontaneous emission in solid-state physics and electronics,” *Phys. Rev. Lett.*, vol. 58, no. 20, pp. 2059–2062, May 1987.
- [40] K. M. Ho, C. T. Chan, C. M. Soukoulis, R. Biswas, and M. Sigalas, “Photonic band gaps in three dimensions: New layer-by-layer periodic structures,” *Solid State Communications*, vol. 89, no. 5, pp. 413–416, Feb. 1994.

- [41] G. K. Palikaras, A. P. Feresidis, and J. C. Vardaxoglou, "Cylindrical electromagnetic bandgap structures for directive base station antennas," *IEEE Antennas Wireless Propag. Lett.*, vol. 3, pp. 87–89, 2004.
- [42] S. Enoch, G. Tayeb, and B. Gralak, "The richness of the dispersion relation of electromagnetic bandgap materials," *IEEE Trans. Antennas Propag.*, vol. 51, no. 10, pp. 2659–2666, 2003.
- [43] V. Radisic, Y. Quan, R. Coccioli, and T. Itoh, "Novel 2-D photonic bandgap structure for microstrip lines," *IEEE Microw. Guided Wave Lett.*, vol. 8, no. 2, pp. 69–71, 1998.
- [44] F. Yang and Y. Rahmat-Samii, "Microstrip antennas integrated with electromagnetic band-gap (EBG) structures: A low mutual coupling design for array applications," *IEEE Trans. Antennas Propag.*, vol. 51, no. 10, pp. 2936–2946, 2003.
- [45] L. Yang, M. Fan, F. Chen, J. She, and Z. Feng, "A novel compact electromagnetic-bandgap (EBG) structure and its applications for microwave circuits," *IEEE Trans. Microw. Theory Techn.*, vol. 53, no. 1, pp. 183–190, Jan. 2005.
- [46] F.-R. Yang, K.-P. Ma, Y. Qian, and T. Itoh, "A uniplanar compact photonic-bandgap (UC-PBG) structure and its applications for microwave circuits," *IEEE Trans. Microw. Theory Techn.*, vol. 47, no. 8, pp. 1509–1514, Aug. 1999.
- [47] S. Shahparnia and O. M. Ramahi, "A simple and effective model for electromagnetic bandgap structures embedded in printed circuit boards," *IEEE Microw. Wireless Compon. Lett.*, vol. 15, no. 10, pp. 261–263, Oct. 2005.
- [48] J. Qin and O. M. Ramahi, "Ultra-wideband mitigation of simultaneous switching noise using novel planar electromagnetic bandgap structures," *IEEE Microw. Wireless Compon. Lett.*, vol. 16, no. 9, pp. 487–489, Sep. 2006.
- [49] J. B. Pendry, A. J. Holden, D. J. Robbins, and W. J. Stewart, "Magnetism from conductors and enhanced nonlinear phenomena," *IEEE Trans. Microw. Theory Techn.*, vol. 47, no. 11, pp. 2075–2084, Nov. 1999.
- [50] J. Y. Siddiqui, C. Saha, and Y. M. M. Antar, "Compact srr loaded uwb circular monopole antenna with frequency notch characteristics," *IEEE Trans. Antennas Propag.*, vol. 62, no. 8, pp. 4015–4020, 2014.
- [51] B. Wu, B. Li, T. Su, and C.-H. Liang, "Equivalent-circuit analysis and lowpass filter design of split-ring resonator DGS," *Journal of Electromagnetic Waves and Applications*, vol. 20, no. 14, pp. 1943–1953, 2006.
- [52] H.-M. Kim and B. Lee, "Bandgap and slow/fast-wave characteristics of defected ground structures (DGSs) including left-handed features," *IEEE Trans. Microw. Theory Techn.*, vol. 54, no. 7, pp. 3113–3120, Jul. 2006.
- [53] O. A. Safia, L. Talbi, and K. Hetta, "A new type of transmission line-based metamaterial resonator and its implementation in original applications," *IEEE Trans. Magn.*, vol. 49, no. 3, pp. 968–973, 2013.

- [54] T. Tamir and A. A. Oliner, "Guided complex waves," *Proc. Inst. Elect. Eng.*, vol. 110, pp. 310–334, 1963.
- [55] C. L. Holloway, E. F. Kuester, J. A. Gordon, J. O'Hara, J. Booth, and D. R. Smith, "An overview of the theory and applications of metasurfaces: The two-dimensional equivalents of metamaterials," *IEEE Antennas Propag. Mag.*, vol. 54, no. 2, pp. 10–35, 2012.
- [56] D. M. Pozar, *Microwave Engineering*, Fourth. Hoboken, New Jersey, USA: John Wiley & Sons, Inc., 2005.
- [57] H. A. Atwater, "Microstrip reactive circuit elements," *IEEE Trans. Microw. Theory Techn.*, vol. 31, no. 6, pp. 488–491, 1983.
- [58] F. Giannini, R. Sorrento, and J. Vrba, "Planar circuit analysis of microstrip radial stub," *IEEE Trans. Microw. Theory Techn.*, vol. 32, no. 12, pp. 1652–1655, 1984.
- [59] F. Giannini, M. Ruggieri, and J. Vrba, "Shunt-connected microstrip radial stubs," *IEEE Trans. Microw. Theory Techn.*, vol. 34, no. 3, pp. 363–366, 1986.
- [60] P. K. Singh, A. K. Tiwary, and N. Gupta, "Ultra-compact switchable microstrip band-pass filter–low-pass filter with improved characteristics," *Microwave and Optical Technology Letters*, vol. 59, no. 1, pp. 197–201, 2017.
- [61] L. Smerklo, Y. Rybak, and M. Naumets, "Low pass filter with triangular stubs," in *Proc. Int. Conf. Modern Problems Radio Eng., Telecommun. and Comput. Sci.*, Lviv-Slavsko, Ukraine, Feb. 2004.
- [62] J. J. Yu, S. T. Chew, M. S. Leong, and B. L. Ooi, "New class of microstrip miniaturised filter using triangular stub," *Electronics Letters*, vol. 37, no. 19, pp. 1169–1170, 2001.
- [63] B. Zhang, S. Li, and J. Huang, "Compact lowpass filter with wide stopband using coupled rhombic stubs," *Electronics Letters*, vol. 51, no. 3, pp. 264–266, 2015.
- [64] P. K. Singh, A. K. Tiwary, and N. Gupta, "Microstrip low-pass filter using modified log periodic radial stub," in *IEEE Applied Electromagnetics Conference*, Guwahati, India, Dec. 2015.
- [65] C.-J. Chen, C.-H. Sung, and Y.-D. Su, "A multi-stub lowpass filter," *IEEE Microw. Wireless Compon. Lett.*, vol. 25, no. 8, pp. 532–534, 2015.
- [66] W.-T. Wong, Y.-S. Lin, C.-H. Wang, and C. H. Chen, "Highly selective microstrip bandpass filters for ultra-wideband (UWB) applications," in *Asia-Pacific Microwave Conference Proceedings*, Suzhou, China, Dec. 2005.
- [67] J.-R. Lee, J.-H. Cho, and S.-W. Yun, "New compact bandpass filter using microstrip $\lambda/4$ resonators with open stub inverter," *IEEE Microw. Guided Wave Lett.*, vol. 10, no. 12, pp. 526–527, 2000.
- [68] J. Xu, W. Wu, W. Kang, and C. Miao, "Compact UWB bandpass filter with a notched band using radial stub loaded resonator," *IEEE Microw. Wireless Compon. Lett.*, vol. 22, no. 7, pp. 351–353, 2012.

- [69] X. Deng, K. D. Xu, Z. Wang, and B. Yan, “Novel microstrip ultra-wideband bandpass filter using radial-stub-loaded structure,” *ACES Journal*, vol. 32, no. 12, pp. 1148–1151, 2017.
- [70] K. Ma and K. S. Yeo, “New ultra-wide stopband low-pass filter using transformed radial stubs,” *IEEE Trans. Microw. Theory Techn.*, vol. 59, no. 3, pp. 604–611, 2011.
- [71] W.-H. Tu and K. Chang, “Compact microstrip bandstop filter using open stub and spurline,” *IEEE Microw. Wireless Compon. Lett.*, vol. 15, no. 4, pp. 268–270, 2005.
- [72] S. Fallahzadeh and M. Tayarani, “A new microstrip UWB bandpass filter using defected microstrip structures,” *Journal of Electromagnetic Waves and Applications*, vol. 24, no. 7, pp. 893–902, 2010.
- [73] A. Tirado-Mendez, H. Jardon-Aguilar, R. Flores-Leal, E. Andrade-Gonzalez, and F. Iturbide-Sanchez, “Improving frequency response of microstrip filters using defected ground and defected microstrip structures,” *PIER C*, vol. 10, no. 12, pp. 77–90, 2010.
- [74] R. Li, S. Sun, and L. Zhu, “Synthesis design of ultra-wideband bandpass filters with composite series and shunt stubs,” *IEEE Trans. Microw. Theory Techn.*, vol. 57, no. 3, pp. 684–692, 2009.
- [75] P. Mondal and M. K. Mandal, “Design of dual-band bandpass filters using stub-loaded open-loop resonators,” *IEEE Trans. Microw. Theory Techn.*, vol. 56, no. 1, pp. 150–155, 2008.
- [76] X. Y. Zhang, J.-X. Chen, Q. Xue, and S.-M. Lin, “Dualband bandpass filters using stub-loaded resonators,” *IEEE Microw. Wireless Compon. Lett.*, vol. 17, no. 8, pp. 583–585, 2007.
- [77] S. R. Borjlu and M. S. Khadem, “Novel microstrip dual-band quad-section bandpass filter using radial stub for wireless communication,” *J. Electr. Eng. Technol.*, vol. 14, pp. 1327–1333, 2019.
- [78] C.-F. Chen, “Design of a compact microstrip quint-band filter based on the tri-mode stub-loaded stepped-impedance resonators,” *IEEE Microw. Wireless Compon. Lett.*, vol. 22, no. 7, pp. 357–359, 2012.
- [79] J.-K. Xiao and Y.-F. Zhu, “Multi-band bandstop filter using inner t-shaped defected microstrip structure (DMS),” *AEU – Int. Journal Electron. Commun.*, vol. 68, no. 2, pp. 90–96, 2014.
- [80] F. Wei, P.-Y. Qin, Y. J. Guo, and X.-W. Shi, “Design of multi-band bandpass filters based on stub loaded stepped-impedance resonator with defected microstrip structure,” *IET Microwaves, Antennas, & Propagation*, vol. 10, no. 2, pp. 230–236, 2016.
- [81] I.-H. Lin, M. DeVicentis, C. Caloz, and T. Itoh, “Arbitrary dual-band components using composite right/left-handed transmission lines,” *IEEE Trans. Microw. Theory Techn.*, vol. 52, no. 4, pp. 1142–1149, 2004.

- [82] X. Q. Lin, R. P. Liu, X. M. Yang, J. X. Chen, X. X. Yin, Q. Cheng, and T. J. Cui, "Arbitrary dual-band components using simplified structures of conventional CRLH TLs," *IEEE Trans. Microw. Theory Techn.*, vol. 54, no. 7, pp. 2902–2909, Jul. 2006.
- [83] A. Saxena, D. Banerjee, R. Gupta, and M. Hashmi, "Design of π -structure dual-band matching network with unequal susceptance cancellation stubs," in *IEEE MTT-S Int. Microw. RF Conf.*, Kolkata, India, Nov. 2018.
- [84] O. Manoochchri, A. Asoodeh, and K. Forooraghi, " Π -model dual-band impedance transformer for unequal complex impedance loads," *IEEE Microw. Wireless Compon. Lett.*, vol. 25, no. 4, pp. 238–240, 2015.
- [85] M.-L. Chuang and M.-T. Wu, "Transmission zero embedded dual-band impedance transformer with three shunt stubs," *IEEE Microw. Wireless Compon. Lett.*, vol. 27, no. 9, pp. 788–790, 2017.
- [86] K. Rawat and F. M. Ghannouchi, "Dual-band matching technique based on dual-characteristic impedance transformers for dual-band power amplifiers design," *IET Microwaves, Antennas, & Propagation*, vol. 5, no. 14, pp. 1720–1729, 2011.
- [87] X. Fu, D. T. Bepalko, and S. Boumaiza, "Novel dual-band matching network for effective design of concurrent dual-band power amplifier," *IEEE Trans. Circuits Syst. I*, vol. 61, pp. 293–301, 2014.
- [88] X. Tang, K. Mouthaan, and J. C. Coetzee, "Dual-band decoupling and matching network design for very closely spaced antennas," in *Proc. 42nd European Microwave Conference*, Amsterdam, Netherlands, 2012.
- [89] K.-D. Xu, H. Luyen, and N. Behdad, "A decoupling and matching network design for single- and dual-band two-element antenna arrays," *IEEE Trans. Microw. Theory Techn.*, vol. 68, pp. 3986–3999, 2020.
- [90] M. A. Maktoomi, M. S. Hashmi, and V. Panwar, "A dual-frequency matching network for FDCLs using dual-band $\lambda/4$ -lines," *PIER Letters*, vol. 52, pp. 23–30, 2015.
- [91] W. Liu, Q. Liu, G. Du, G. Li, and D. Cheng, "Dual-band impedance transformer with single shunt stub for complex impedance loads," *Microwave and Optical Technology Letters*, vol. 63, no. 7, pp. 1832–1836, 2021.
- [92] M.-L. Chuang, "Dual-band impedance transformer using two-section shunt stubs," *IEEE Trans. Microw. Theory Techn.*, vol. 58, no. 5, pp. 1257–1263, 2010.
- [93] C. Monzon, "A small dual-frequency transformer in two sections," *IEEE Trans. Microw. Theory Techn.*, vol. 51, no. 4, pp. 1157–1161, 2003.
- [94] Y.-S. Lin and C.-H. Wei, "A novel miniature dual-band impedance matching network for frequency-dependent complex impedances," *IEEE Trans. Microw. Theory Techn.*, vol. 68, no. 10, pp. 4314–4326, 2020.

- [95] M. A. Maktoomi, M. S. Hashmi, A. P. Yadav, and V. Kumar, "A generic tri-band matching network," *IEEE Microw. Wireless Compon. Lett.*, vol. 26, no. 5, pp. 316–318, 2016.
- [96] D. Banerjee, A. Saxena, and M. Hashmi, "A novel compact tri-band matching network utilizing two dual-band transformers at a common reference frequency," in *Proc. Asia Pacific Microwave Conference*, Kuala Lumpur, Malaysia, Nov. 2017.
- [97] R. K. Barik and S. S. Karthikeyan, "A novel design of ultra-high impedance transforming ratio quad-band matching network," *Microwave and Optical Technology Letters*, vol. 59, no. 8, pp. 2021–2026, 2017.
- [98] N. Nallam and S. Chatterjee, "Multi-band frequency transformations, matching networks and amplifiers," *IEEE Trans. Circuits Syst. I*, vol. 60, no. 6, pp. 1635–1647, 2013.
- [99] Z. Zhou and K. L. Melde, "Frequency agility of broadband antennas integrated with reconfigurable RF impedance tuner," *IEEE Antennas Wireless Propag. Lett.*, vol. 6, pp. 56–59, 2007.
- [100] M. J. Park and B. Lee, "A dual-band Wilkinson power divider," *IEEE Microw. Wireless Compon. Lett.*, vol. 18, no. 2, pp. 85–87, 2008.
- [101] K. K. M. Cheng and F. L. Wong, "A new Wilkinson power divider design for dual-band application," *IEEE Microw. Wireless Compon. Lett.*, vol. 17, no. 9, pp. 664–666, 2007.
- [102] Y. H. Pang and Z. H. Li, "Dual-band bandpass Wilkinson power divider of controllable bandwidths," *Electronics Letters*, vol. 52, no. 7, pp. 537–538, 2016.
- [103] L. Wu, Z. Sun, H. Yilmaz, and M. Berroth, "A dual-frequency Wilkinson power divider," *IEEE Trans. Microw. Theory Techn.*, vol. 54, no. 1, pp. 278–284, 2006.
- [104] X. Li, S. X. Gong, L. Yang, and Y. J. Yang, "A novel Wilkinson power divider for dual-band operation," *Journal of Electromagnetic Waves and Applications*, vol. 23, pp. 395–404, 2009.
- [105] Y. Wu, Y. Liu, and Q. Xue, "An analytical approach for a novel coupled-line dual-band Wilkinson power divider," *IEEE Trans. Microw. Theory Techn.*, vol. 59, no. 2, pp. 286–294, 2011.
- [106] M.-J. Park, "Two-section cascaded coupled line Wilkinson power divider for dual-band applications," *IEEE Microw. Wireless Compon. Lett.*, vol. 19, no. 4, pp. 188–190, 2009.
- [107] Z. Lin and Q.-X. Chu, "A novel approach to the design of dual-band power divider with variable power dividing ratio based on coupled lines," *Progress in Electromagnetics Research*, vol. 103, pp. 271–284, 2010.
- [108] Y. C. Li, Q. Xue, and X. Y. Zhang, "Single- and dual-band power dividers integrated with bandpass filters," *IEEE Trans. Microw. Theory Techn.*, vol. 61, no. 1, pp. 69–76, 2013.

- [109] S. Avrillon, I. Pele, A. Chousseaud, and S. Toutain, “Dual-band power divider based on semiloop stepped-impedance resonators,” *IEEE Trans. Microw. Theory Techn.*, vol. 51, no. 4, pp. 1269–1273, 2003.
- [110] R. Gomez-Garcia, R. Loeches-Sanchez, D. Psychogiou, and D. Peroulis, “Single/multi-band Wilkinson-type power dividers with embedded transversal filtering sections and application to channelized filters,” *IEEE Trans. Circuits Syst. I*, vol. 62, no. 6, pp. 1518–1527, 2015.
- [111] K.-K. M. Cheng and F.-L. Wong, “A novel approach to the design and implementation of dual-band compact planar 90° branch-line coupler,” *IEEE Trans. Microw. Theory Techn.*, vol. 52, no. 11, pp. 2458–2463, 2004.
- [112] S. Y. Zheng, S. H. Yeung, W. S. Chan, K. F. Man, S. H. Leung, and Q. Xue, “Dual-band rectangular patch hybrid coupler,” *IEEE Trans. Microw. Theory Techn.*, vol. 56, no. 7, pp. 1721–1728, 2008.
- [113] K.-K. M. Cheng and F.-L. Wong, “A novel rat race coupler design for dual-band applications,” *IEEE Microw. Wireless Compon. Lett.*, vol. 15, no. 8, pp. 521–523, 2005.
- [114] C.-H. Tseng, C.-H. Mou, C.-C. Lin, and C.-H. Chao, “Design of microwave dual-band rat-race couplers in printed-circuit board and GPID technologies,” *IEEE Trans. Compon. Packag. Manuf. Technol.*, vol. 6, no. 2, pp. 262–271, Feb. 2016.
- [115] H. Zhang and K. J. Chen, “A stub tapped branch-line coupler for dual-band operations,” *IEEE Microw. Wireless Compon. Lett.*, vol. 17, no. 2, pp. 106–108, 2007.
- [116] H. Kim, B. Lee, and M.-J. Park, “Dual-band branch-line coupler with port extensions,” *IEEE Trans. Microw. Theory Techn.*, vol. 58, no. 3, pp. 651–655, 2010.
- [117] F. Lin, Q.-X. Chu, and S. W. Wong, “Design of dual-band filtering quadrature coupler using $\lambda/2$ and $\lambda/4$ resonators,” *IEEE Microw. Wireless Compon. Lett.*, vol. 22, no. 11, pp. 565–567, 2012.
- [118] C.-L. Hsu, J.-T. Kuo, and C.-W. Chang, “Miniaturized dual-band hybrid couplers with arbitrary power division ratios,” *IEEE Trans. Microw. Theory Techn.*, vol. 57, no. 1, pp. 149–156, 2009.
- [119] L.-S. Wu, B. Xia, W.-Y. Yin, and J. Mao, “Collaborative design of a new dual-bandpass 180° hybrid coupler,” *IEEE Trans. Microw. Theory Techn.*, vol. 61, no. 3, pp. 1053–1066, 2013.
- [120] M.-J. Park and B. Lee, “Dual-band, cross coupled branch line coupler,” *IEEE Microw. Wireless Compon. Lett.*, vol. 15, no. 10, pp. 655–657, 2005.
- [121] L. K. Yeung, “A compact dual-band 90° coupler with coupled-line sections,” *IEEE Trans. Microw. Theory Techn.*, vol. 59, no. 9, pp. 2227–2232, 2011.

- [122] X. Wang, W.-Y. Yin, and K.-L. Wu, "A dual-band coupled-line coupler with an arbitrary coupling coefficient," *IEEE Trans. Microw. Theory Techn.*, vol. 60, no. 4, pp. 945–951, 2012.
- [123] A. Genc and R. Baktur, "Dual- and triple-band Wilkinson power dividers based on composite right- and left-handed transmission lines," *IEEE Trans. Compon. Packag. Manuf. Technol.*, vol. 6, no. 2, pp. 327–334, Feb. 2011.
- [124] T. K. Prakash, P. H. Rao, and K. T. Selvan, "Complementary split ring resonator loaded reduced size Wilkinson power divider," in *Proc. IEEE Applied Electromagnetics Conference*, Bhubaneswar, India, Dec. 2013, pp. 1–2.
- [125] J. Zhang, B. Cui, J. Z. Gu, and X. W. Sun, "A harmonic suppressed Wilkinson power divider using complementary split ring resonators," *Journal of Electromagnetic Waves and Applications*, vol. 21, no. 6, pp. 811–819, 2007.
- [126] J. Bonache, G. Siso, M. Gil, A. Iniesta, J. Garcia-Rincon, and F. Martin, "Application of composite right/left handed (CRLH) transmission lines based on complementary split ring resonators (CSRRLs) to the design of dual-band microwave components," *IEEE Microw. Wireless Compon. Lett.*, vol. 18, no. 8, pp. 524–526, 2008.
- [127] A. C. Papanastasiou, G. E. Georghiou, and G. V. Eleftheriades, "A quad-band Wilkinson power divider using generalized nri transmission lines," *IEEE Microw. Wireless Compon. Lett.*, vol. 18, no. 8, pp. 521–523, Aug. 2008.
- [128] M. Duran-Sindreu, G. Siso, J. Bonache, and F. Martin, "Planar multi-band microwave components based on a generalized composite right/left handed transmission line concept," *IEEE Trans. Microw. Theory Techn.*, vol. 58, no. 12, pp. 3882–3891, Dec. 2010.
- [129] S. Maci and G. B. Gentili, "Dual-frequency patch antennas," *IEEE Antennas Propag. Mag.*, vol. 39, no. 6, pp. 13–20, 1997.
- [130] D. M. Pozar, "Microstrip antennas," *Proc. IEEE.*, vol. 80, no. 1, pp. 79–91, 1992.
- [131] J. R. James and P. S. Hall, *Handbook of Microstrip Antennas*. London, U.K.: Peter Peregrinus, 1989.
- [132] S. A. Long and M. D. Walton, "A dual-frequency stacked circular-disk antenna," *IEEE Trans. Antennas Propag.*, vol. 27, no. 2, pp. 270–273, 1979.
- [133] Y. Zhou, C.-C. Chen, and J. L. Volakis, "Dual band proximity-fed stacked patch antenna for tri-band GPS applications," *IEEE Trans. Antennas Propag.*, vol. 55, no. 1, pp. 220–223, 2007.
- [134] F. Croq and D. Pozar, "Multifrequency operation of microstrip antennas using aperture coupled parallel resonators," *IEEE Trans. Antennas Propag.*, vol. 40, no. 11, pp. 1367–1374, 1992.
- [135] K. Carver and J. Mink, "Microstrip antenna technology," *IEEE Trans. Antennas Propag.*, vol. 29, no. 1, pp. 2–24, 1981.

- [136] K.-F. Lee and K.-F. Tong, "Microstrip patch antennas—basic characteristics and some recent advances," *Proc. IEEE.*, vol. 100, no. 7, pp. 2169–2180, 2012.
- [137] B. F. Wang and Y. T. Lo, "Microstrip antennas for dual-frequency operation," *IEEE Trans. Antennas Propag.*, vol. 32, no. 6, pp. 938–943, 1984.
- [138] P. Sharma and K. Gupta, "Analysis and optimized design of single feed circularly polarized microstrip antennas," *IEEE Trans. Antennas Propag.*, vol. 31, no. 6, pp. 949–955, 1983.
- [139] W. C. Mok, S. H. Wong, K. M. Luk, and K. F. Lee, "Single-layer single-patch dual-band and triple-band patch antennas," *IEEE Trans. Antennas Propag.*, vol. 61, no. 8, pp. 4341–4344, 2013.
- [140] Y. Chung, S. Jeon, D. Ahn, J. Choi, and T. Itoh, "High isolation dual-polarized patch antenna using integrated defected ground structure," *IEEE Microw. Wireless Compon. Lett.*, vol. 14, no. 1, pp. 4–6, 2004.
- [141] C. Zhou, G. Wang, J. Liang, Y. Wang, and B. Zong, "Broadband antenna employing simplified MTLs for WLAN/WiMAX applications," *IEEE Antennas Wireless Propag. Lett.*, vol. 13, pp. 595–598, 2014.
- [142] D. Schaubert, F. Farrar, A. Sindoris, and S. Hayes, "Microstrip antennas with frequency agility and polarization diversity," *IEEE Trans. Antennas Propag.*, vol. 29, no. 1, pp. 118–123, 1981.
- [143] S. S. Zhong and Y. T. Lo, "Single-element rectangular microstrip antenna for dual-frequency operation," *Electronics Letters*, vol. 19, no. 8, pp. 298–300, 1983.
- [144] W. Richards, S. Davidson, and S. Long, "Dual-band reactively loaded microstrip antenna," *IEEE Trans. Antennas Propag.*, vol. 33, no. 5, pp. 556–561, 1985.
- [145] S. E. Davidson, S. A. Long, and W. F. Richards, "Dual-band microstrip antennas with monolithic reactive loading," *Electronics Letters*, vol. 21, no. 20, pp. 936–937, 1985.
- [146] W. Cao, B. Zhang, A. Liu, T. Yu, D. Guo, and X. Pan, "Multi-frequency and dual-mode patch antenna based on electromagnetic bandgap EBG structure," *IEEE Trans. Antennas Propag.*, vol. 60, no. 12, pp. 6007–6012, Dec. 2012.
- [147] S. Zhu and R. Langley, "Dual-band wearable textile antenna on an EBG substrate," *IEEE Trans. Antennas Propag.*, vol. 57, no. 4, pp. 926–935, 2009.
- [148] H.-X. Xu, G.-M. Wang, and M.-Q. Qi, "A miniaturized triple-band metamaterial antenna with radiation pattern selectivity and polarization diversity," *Prog. Electromagn. Res.*, vol. 137, pp. 275–292, 2013.
- [149] H. Malekpoor and S. Jam, "Design of a multi-band asymmetric patch antenna for wireless applications," *Microw. Opt. Technol. Lett.*, vol. 55, no. 4, pp. 730–734, 2013.

- [150] P. K. Mishra, D. R. Jahagirdar, and G. Kumar, "A review of broadband dual linearly polarized microstrip antenna designs with high isolation," *IEEE Antennas Propag. Mag.*, vol. 56, no. 6, pp. 238–251, 2014.
- [151] S. J. Yang, W. Duan, Y. Y. Liu, H. Ye, H. Yang, and X. Y. Zhang, "Compact dual-band base-station antenna using filtering elements," *IEEE Trans. Antennas Propag.*, vol. 70, no. 8, pp. 7106–7111, 2022.
- [152] E. Aloni and R. Kastner, "Analysis of a dual circularly polarized microstrip antenna fed by crossed slots," *IEEE Trans. Antennas Propag.*, vol. 42, no. 8, pp. 1053–1058, 1994.
- [153] D. H. Choi, Y. J. Cho, and S. O. Park, "Dual-band and dual-polarised microstrip antenna," *Electronics Letters*, vol. 42, no. 2, pp. 68–69, 2006.
- [154] Z.-B. Weng, Y. Song, Y.-C. Jiao, and F.-S. Zhang, "A directive dual-band and dual-polarized antenna with zero index metamaterial," *Microwave and Optical Technology Letters*, vol. 50, no. 11, pp. 2902–2904, 2008.
- [155] O. P. Falade, Y. Gao, X. Chen, and C. Parini, "Stacked-patch dual-polarized antenna for triple-band handheld terminals," *IEEE Antennas Wireless Propag. Lett.*, vol. 12, pp. 202–205, 2013.
- [156] H. Lei, Y. Liu, Y. Jia, Z. Yue, and X. Wang, "A low-profile dual-band dual-circularly polarized folded transmitarray antenna with independent beam control," *IEEE Trans. Antennas Propag.*, vol. 70, no. 5, pp. 3852–3857, 2022.
- [157] A. Sabban, "A new broadband stacked two-layer microstrip antenna," in *Proc. IEEE Antennas Propag. Int. Symp.*, Houston, TX, May 1983, pp. 63–66.
- [158] L. Shafai, W. Chamma, G. Seguin, and N. Sultan, "Dual-band dual-polarized microstrip antennas for SAR applications," in *Proc. IEEE Antennas Propag. Int. Symp.*, Montreal, QC, Canada, Jul. 1997, pp. 1866–1869.
- [159] B. Lindmark, "A dual polarized dual band microstrip antenna for wireless communications," in *IEEE Aerospace Conference Proceedings*, Aspen, CO, Mar. 1998, pp. 333–338.
- [160] S. D. Targonski and D. M. Pozar, "Dual-band dual-polarised printed antenna element," *Electronics Letters*, vol. 34, no. 23, pp. 2193–2194, 1998.
- [161] M. Kaboli, M. S. Abrishamian, S. A. Mirtaheri, and S. M. Aboutorab, "High-isolation XX-polar antenna," *IEEE Trans. Antennas Propag.*, vol. 60, no. 9, pp. 4046–4055, 2012.
- [162] T.-W. Chiou and K.-L. Wong, "A compact dual-band dual-polarized patch antenna for 900/1800-MHz cellular systems," *IEEE Trans. Antennas Propag.*, vol. 51, no. 8, pp. 1936–1940, 2003.
- [163] M. Stanley, Y. Huang, H. Wang, H. Zhou, A. Alieldin, S. Joseph, C. Song, and T. Jia, "A dual-band dual-polarised stacked patch antenna for 28 GHz and 39 GHz 5G millimetre-wave communication," in *European Conference on Antennas and Propagation*, Krakow, Poland, Apr. 2019, pp. 333–338.

- [164] Y. He, Z. Pan, X. Cheng, Y. He, and J. Qiao, "A novel dual-band, dual-polarized, miniaturized and low-profile base station antenna," *IEEE Trans. Antennas Propag.*, vol. 63, no. 12, pp. 5399–5408, 2015.
- [165] K. Moradi and S. Nikmehr, "A dual-band dual-polarized microstrip array antenna for base stations," *Progress in Electromagnetics Research*, vol. 123, pp. 527–541, 2012.
- [166] H. Zhai, K. Zhang, S. Yang, and D. Feng, "A low-profile dual-band dual-polarized antenna with an AMC surface for WLAN applications," *IEEE Antennas Wireless Propag. Lett.*, vol. 16, pp. 2692–2695, 2017.
- [167] J. Lin, Z. Qian, W. Cao, S. Shi, Q. Wang, and W. Zhong, "A low-profile dual-band dual-mode and dual-polarized antenna based on AMC," *IEEE Antennas Wireless Propag. Lett.*, vol. 16, pp. 2473–2476, 2017.
- [168] L. Sabri, N. Amiri, and K. Forooghi, "Dual-band and dual-polarized SIW-fed microstrip patch antenna," *IEEE Antennas Wireless Propag. Lett.*, vol. 13, pp. 1605–1608, 2014.
- [169] Y. X. Sun and K. W. Leung, "Dual-band and wideband dual-polarized cylindrical dielectric resonator antennas," *IEEE Antennas Wireless Propag. Lett.*, vol. 12, pp. 384–387, 2013.
- [170] M.-T. Tan and B.-Z. Wang, "A compact dual-band dual-polarized loop-slot planar antenna," *IEEE Antennas Wireless Propag. Lett.*, vol. 14, pp. 1742–1745, 2015.
- [171] F. J. Herraiz-Martinez, V. Gonzalez-Posadas, L. E. Garcia-Munoz, and D. Segovia-Vargas, "Multifrequency and dual-mode patch antennas partially filled with left-handed structures," *IEEE Trans. Antennas Propag.*, vol. 56, no. 8, pp. 2527–2539, 2008.
- [172] P. Garg and P. Jain, "Metamaterial-based patch antennas—review," in *Advances in System Optimization and Control: Lecture Notes in Electrical Engineering*, vol. 509, Springer, Singapore, 2019, pp. 65–81.
- [173] L. C. Paul, M. S. Hosain, S. Sarkar, M. H. Prio, M. Morshed, and A. K. Sarkar, "The effect of changing substrate material and thickness on the performance of inset feed microstrip patch antenna," *American Journal of Networks and Communications*, vol. 4, no. 3, pp. 54–58, 2015.
- [174] C. A. Balanis, *Antenna Theory: Analysis and Design*, Third. Hoboken, New Jersey, USA: John Wiley & Sons, Inc., 2005.
- [175] H. F. Pues and A. R. Van de Capelle, "An impedance-matching technique for increasing the bandwidth of microstrip antennas," *IEEE Trans. Antennas Propag.*, vol. 37, no. 11, pp. 1345–1354, 1989.
- [176] R. B. Waterhouse and N. V. Shuley, "Dual frequency microstrip rectangular patches," *Electronics Letters*, vol. 28, no. 7, pp. 606–607, 1992.

- [177] P. Loghmannia and M. Manteghi, “Broadband parametric impedance matching for small antennas using the Bode-Fano limit: Improving on Chu’s limit for loaded small antennas,” *IEEE Antennas Propag. Mag.*, vol. 64, no. 5, pp. 55–68, 2022.
- [178] K. Payandehjoo and R. Abhari, “Design of a compact patch antenna backed by a multi-layer EBG structure using multi-conductor transmission line modeling,” in *Proc. Int. Symp. Antennas Propag.*, Chicago, IL, Jul. 2012, pp. 1–2.
- [179] C.-H. Liu, Y.-G. Lu, X.-G. Luo, and C.-L. Du, “The numerical simulation of AMC characteristics for UCPBG on grounded dielectric substrate,” *Journal of Electromagnetic Waves and Applications*, vol. 21, no. 6, pp. 755–768, 2007.
- [180] Y. Tajima and S. Kamihashi, “Multiconductor couplers,” *IEEE Trans. Microw. Theory Techn.*, vol. 26, no. 10, pp. 795–801, 1978.
- [181] F. Bongard, J. Perruisseau-Carrier, and J. R. Mosig, “Enhanced periodic structure analysis based on a multiconductor transmission line model and application to metamaterials,” *IEEE Trans. Microw. Theory Techn.*, vol. 57, no. 11, pp. 2715–2726, 2009.
- [182] S. Barth, “Theory, analysis, and applications of multidimensional, multiconductor transmission-line metamaterials,” Ph.D. dissertation, Department of Electrical and Computer Engineering, University of Alberta, Edmonton, AB, 2015.
- [183] S. Barth and A. K. Iyer, “The MTM-EBG as a rigorous multiconductor model of the UC-EBG and approaches for miniaturization,” *IEEE Trans. Antennas Propag.*, vol. 70, no. 4, pp. 2822–2831, 2022.
- [184] S. Barth, B. P. Smyth, J. A. Brown, and A. K. Iyer, “Theory and design of dual-band microstrip networks using embedded metamaterial-based electromagnetic bandgap structures (MTM-EBGs),” *IEEE Trans. Antennas Propag.*, vol. 68, no. 3, pp. 1761–1772, 2020.
- [185] B. P. Smyth and A. K. Iyer, “Low-profile uniplanar dual-band and dual-polarized microstrip patch antenna using embedded MTM-EBGs,” *IEEE Trans. Antennas Propag.*, vol. 69, no. 7, pp. 3645–3653, 2021.
- [186] J. A. Brown, “Applications of embedded metamaterial-based electromagnetic-bandgap structures for dual-band devices and compact tunable bandstop filtering,” M.S. thesis, Department of Electrical and Computer Engineering, University of Alberta, Edmonton, AB, 2020.
- [187] C. R. Paul, “Decoupling the multiconductor transmission line equations,” *IEEE Trans. Microw. Theory Techn.*, vol. 44, no. 8, pp. 1429–1440, 1996.
- [188] B. P. Smyth, S. Barth, and A. K. Iyer, “Dual-band microstrip patch antenna using integrated uniplanar metamaterial-based EBGs,” *IEEE Trans. Antennas Propag.*, vol. 64, no. 12, pp. 5046–5053, 2016.

- [189] J. A. Brown, S. Barth, B. P. Smyth, and A. K. Iyer, "Dual-band microstrip corporate feed network using an embedded metamaterial-based EBG," *IEEE Trans. Antennas Propag.*, vol. 67, no. 11, pp. 7031–7039, 2019.
- [190] J. A. Brown, S. Barth, B. P. Smyth, and A. K. Iyer, "Compact mechanically tunable microstrip bandstop filter with constant absolute bandwidth using embedded metamaterial-based ebg," *IEEE Trans. Microw. Theory Techn.*, vol. 68, no. 10, pp. 4368–4380, 2020.
- [191] J. K. A. Everard and K. K. M. Cheng, "High performance direct coupled bandpass filters on coplanar waveguide," *IEEE Trans. Microw. Theory Techn.*, vol. 41, no. 9, pp. 1568–1573, 1993.
- [192] G. D. Alley, "Interdigital capacitors and their application to lumped-element microwave integrated circuits," *IEEE Trans. Microw. Theory Techn.*, vol. 18, no. 12, pp. 1028–1033, 1970.
- [193] B. P. Smyth and A. K. Iyer, "Multi-band impedance matching using microstrip-embedded MTM-EBGs," *IEEE Trans. Microw. Theory Techn.*, early access, 2023. doi: 10.1109/TMTT.2023.3251563.
- [194] S. Barth and A. K. Iyer, "A low-profile dual-band circular patch antenna for GPS using metamaterial-based EBGs," in *IEEE Int. Symp. Antennas Propag.*, San Diego, CA, Jul. 2017, pp. 1727–1728.
- [195] B. P. Smyth, S. Barth, and A. K. Iyer, "A low-profile tri-band microstrip GPS circular patch antenna with integrated MTM-EBGs," in *Int. Conf. Electromagn. Adv. Appl.*, Honolulu, HI, 2021, p. 115.
- [196] B. P. Smyth and A. K. Iyer, "Compact tri-band microstrip stub filter using embedded MTM-EBGs," in *IEEE Int. Symp. Antennas Propag.*, Boston, MA, Jul. 2018, pp. 163–164.
- [197] G. Antonini, A. C. Scogna, and A. Orlandi, "De-embedding procedure based on computed/measured data set for PCB structures characterization," *IEEE Trans. Adv. Packag.*, vol. 27, no. 4, pp. 597–602, 2004.
- [198] B. P. Smyth and A. K. Iyer, "Dual-band Wilkinson power divider using uniplanar metamaterial-based EBGs," in *IEEE Int. Symp. Antennas Propag.*, San Diego, CA, Jul. 2017, pp. 457–458.
- [199] J. Gong, K. Gao, and C. Liang, "Synthesis of a miniaturised wireless local area network dual-band microstrip Wilkinson power divider through a general three-step optimisation process," *IET Microw. Antennas Prop.*, vol. 9, no. 12, pp. 1274–1278, 2015.
- [200] M. A. Maktoomi and M. S. Hashmi, "A performance enhanced port extended dual-band Wilkinson power divider," *IEEE Access*, vol. 5, pp. 11 832–11 840, 2017.
- [201] L. I. Basilio, M. A. Khayat, J. T. Williams, and S. A. Long, "The dependence of the input impedance on feed position of probe and microstrip line-fed patch antennas," *IEEE Trans. Antennas Propag.*, vol. 49, no. 1, pp. 45–47, 2001.

- [202] T. Samaras, A. Kouloglou, and J. N. Sahalos, “A note on the impedance variation with feed position of a rectangular microstrip-patch antenna,” *IEEE Antennas Propag. Mag.*, vol. 46, no. 2, pp. 90–92, 2004.
- [203] R. C. Hansen, “Fundamental limitations in antennas,” *Proc. IEEE*, vol. 69, no. 2, pp. 170–182, 1981.
- [204] E. Rocas, C. Collado, N. D. Orloff, J. Mateu, A. Padilla, J. M. O’Callaghan, and J. C. Booth, “Passive intermodulation due to self-heating in printed transmission lines,” *IEEE Trans. Microw. Theory Techn.*, vol. 59, no. 2, pp. 311–322, 2011.

Appendix A: Modeling the MTM-EBG with 2-Conductor Transmission Lines

The goal of this section is to observe the ability of a 2-conductor TL to accurately model a single MTM-EBG unit cell, as compared to the MTL model. A 2-conductor model would not, on its own, be able to recreate the full dispersion information provided by an MTL model, since it would support only a single TEM mode. (A 2-conductor system could be constructed for each individual mode, however, to obtain all relevant data; three individual 2-conductor TLs would be needed for a description of all the MTL modes of the 4-conductor MTM-EBG.) If interest only lies in determining the MS-like mode bandgap, then the recreation of a single mode may be sufficient. As this is often the case, a 2-conductor TL model of a single unit cell (fed by a microstrip TL to ensure the desired mode is excited) can be constructed, and results can be compared to the comparable mode predicted by MTL analysis.

The utility of circuit models is that they are capable of describing any linear system if an accurate enough model is used, and regardless of the complexity of the full model, a simple equivalent circuit results. It can be assumed, therefore, that a 2-conductor TL model (or simply just a TL model, as opposed to an MTL model) for the MTM-EBG exists to describe the microstrip-like mode, and the question that remains is whether it provides an accurate way to analyze the MTM-EBG as compared to the MTL model that has been used thus far. A comparison of simplicity and accuracy of the each model helps determine which one should be used.

First, consider a full-wave simulation of a single MTM-EBG unit cell; this provides a baseline that circuit models will attempt to match, as this simulation is assumed to be well-converged and accurate. The simulation model is shown in Fig. A.1a,

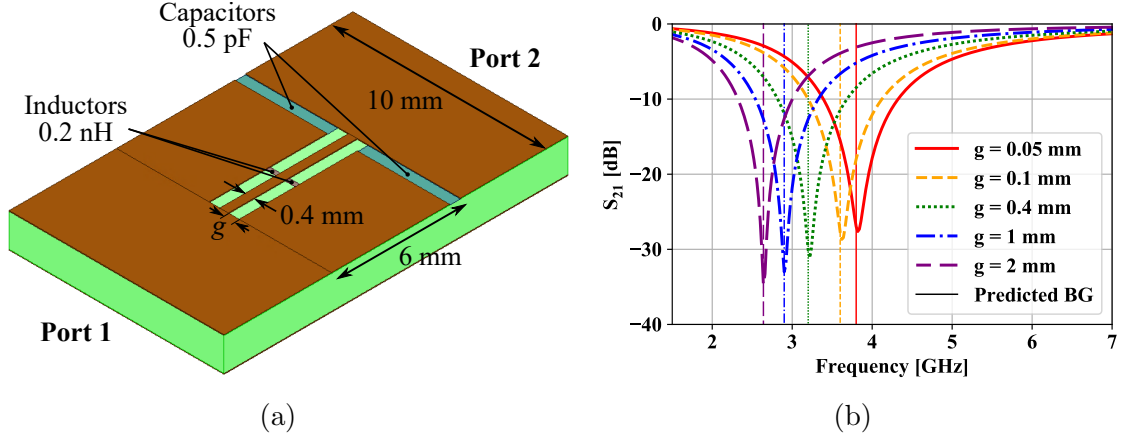


Figure A.1: (a) Simulation model of MTM-EBG unit cell on 60 mil Rogers 3003. (b) S_{21} of the unit cell for various values of g . Also included are vertical lines indicating the lower bandgap edge predicted by MTL analysis.

and dimensions are provided in the figure. Capacitive and inductive sheets are used rather than fully-printed structures to ensure better agreement between this model and comparative circuit models. The gaps of width g are allowed to vary in size as this is known to have an effect on bandgap location. This variable is of particular interest since it will affect coupling between adjacent conductors, which provides the greatest challenge to model in the TL case.

Simulation results of the single unit cell are plotted in Fig. A.1b, specifically S_{21} to easily show the bandgap location. Data for various gap widths g are presented in order to observe the effect this has on bandgap location. This plot shows that as g increases, the bandgap location is shifted downwards. On the same plot, the lower band edge as predicted by MTL analysis is given by thinner vertical lines, with the colours and line styles corresponding to the same g values. It is clear that the bandgap for a single unit cell occurs very near the predicted lower band edge, with very good correlation as g is swept. It can be concluded that the MTL model, while not a perfect model for a single MTM-EBG unit cell, is very useful in predicting bandgap location (and other properties, by extension), and provides an accurate model of the coupling between adjacent conductors.

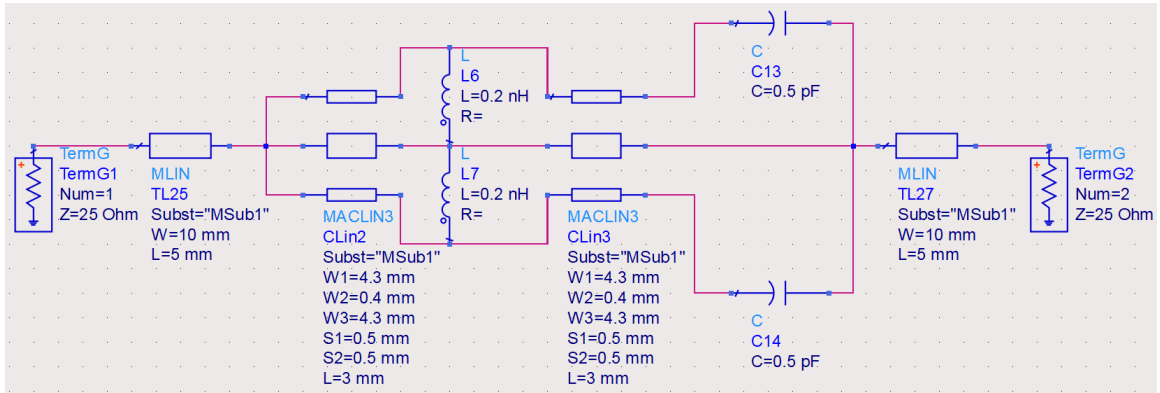
A comparable TL model of MTM-EBG microstrip-like mode should be fed by a single TL, and each individual part of the MTM-EBG unit cell itself separately modeled. Narrow, high-impedance TLs replace the upper three conductors that form

the MTM-EBG unit cell, with lumped capacitors and inductors placed appropriately. What remains to be modeled is the coupling caused by the gaps of width g between the upper three conductors; the previous result demonstrates that they are definitely not isolated from each other. Modeling this is the key to creating an accurate 2-conductor representation of the microstrip-like mode.

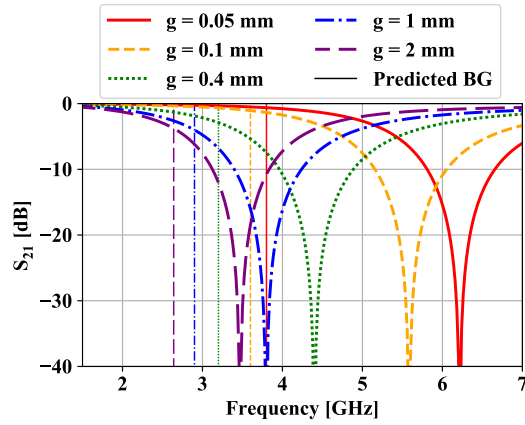
One way in which a TL model predicts this coupling is through coupled-line theory, but this is more complex than simply implementing additional circuit elements; per-unit-length capacitances between conductors must be found, and even for a system of two microstrip lines, numerical or approximate quasi-static solutions are required [56]. This result is similar to the MTL approach, and does not provide any further simplification. An different but intuitive way to model this without requiring such equations is to approximate the coupling with a number of shunt capacitors between adjacent conductors. A single capacitor provides a poor approximation of the expected coupling, but adding many parallel capacitors between the conductor edges would increase accuracy. As more capacitors are added, a discrete reconstruction of MTL theory is approached. This approximation provides little benefit over using MTL theory directly, which accounts for capacitive coupling between all conductors with its per-unit-length matrix.

There are no analytical advantages to these approaches, but a circuit model can still be used with software that simplifies the required design equations. As an example, Pathwave Advanced Design System (ADS) provides a convenient means of modeling coupling between adjacent conductors: a *MACLIN3* component contains the relevant information, as it is designed to model coupling of three adjacent microstrip TLs. Fig. A.2a shows the ADS layout including the *MACLIN3* component. Results of this circuit simulation for various values of g , compared to the lower band edges as determined by MTL theory (which are now known to be located accurately at the strongest rejection frequency), are shown in Fig. A.2b.

This circuit model demonstrates a sensitivity to g , indicating that TL coupling is indeed being modeled; however, the results show a large frequency shift as compared to the full-wave model, by several GHz. This may be due in part to inaccuracies in the *MACLIN3* component, but other deficiencies of the circuit model likely contribute as well, such as poor modeling of parasitics at various junctions. It is clear that



(a)



(b)

Figure A.2: (a) Possible circuit model of a single MTM-EBG unit cell incorporating TL coupling, created in Pathwave ADS. (b) S_{21} of the unit cell for various values of g . Vertical lines indicate the lower bandgap edge predicted by MTL analysis.

this model is approaching the correct solution, but is still insufficiently accurate to be considered as a primary design tool. Increasing its accuracy could be achieved by adding more complexity to the TL model, as more components could be used to correctly model all parasitics of the structure.

MTL theory is much better equipped to deal with the coupling of the various conductors that make up this system, and while it suffers from inaccuracies in the prediction of the properties of a single unit cell, it remains to be the simplest and most accurate method for design of a unit cell with desired dispersion properties. It may be possible to create a circuit model with sufficient accuracy (at least under some conditions) to be a useful aid in the design of a multi-band system, and perhaps the model could even include components for strip inductors or interdigitated/gap capacitors (indeed, ADS has circuit components for these structures). This may be a useful tool, but it should be used only once it is verified that any model agrees with full-wave simulations, and design intuition is still best taken from the MTL model used in this work.

Appendix B: MTM-EBG Host TLs

The use of MTM-EBG unit cells in PPW and microstrip structures has been established, and this will be the focus of applications in this work. It is worth considering whether other TL structures are amenable to MTM-EBG integration, and if similar design principles can therefore be used in these cases. Consider interaction with guided TEM modes in the following structures:

Stripline: Stripline looks like a microstrip TL in a homogeneous substrate, with an additional large shielding conductor above the signal line. While more difficult than a microstrip TL to fabricate, the three CPW conductors of the MTM-EBG could be integrated into the signal line and modeled with MTL theory. The additional conductor would have to be included in the circuit model ($N = 5$ conductor system), which results in an additional mode being supported and larger matrices as a result. MTM-EBG unit cells could be embedded to create novel circuit elements, but antenna applications are limited by the upper shielding conductor.

Co-Planar Waveguide: The MTM-EBG relies on contra-directional coupling of the backward CPW mode with a forward PPW mode, but a CPW TL alone does not support the required PPW mode. While this system could still be modeled as a MTL, it would not be considered a form of the MTM-EBG since any bandgap and phase properties would arise from a different mechanism. A conductor-backed CPW, on the other hand, matches the MTM-EBG host medium geometry, and would more readily support integration.

Coaxial: Considering the central wire of a coaxial cable to be the reference conductor and patterning the outer conductor similarly to a CPW, it is conceivable that MTM-EBG unit cells could be realized in a cylindrical geometry in a coaxial line. An integer number of unit cells would be required azimuthally along the circumference of the cable and fabrication of such a structure would pose challenges, but the funda-

mental TEM coaxial mode in this case would operate as the PPW mode due to the similar field distribution, and coupling with the cylindrical CPW mode could provide the required bandgap. This configuration would be modeled similarly to the planar MTM-EBG, with different per-unit-length matrices for the host medium.

This discussion focuses on MTM-EBG interactions with guided modes, but the interaction with free-space or surface waves can be modeled by the addition of an additional conductor above the plane containing conductors 1, 2 and 3 [1]. Interaction with these modes is not generally considered in this work.